

**Kinetics, Selectivity
and Scale Up of the
Fischer-Tropsch Synthesis**

Gerard P. van der Laan

CIP-GEGEVENS KONINKLIJKE BIBLIOTHEEK, DEN HAAG

Laan, van der, Gerard Pieter

Kinetics, Selectivity and Scale Up of the Fischer-Tropsch Synthesis / G.P. van der Laan. - Groningen:

Thesis University of Groningen. - With ref. - With summary in Dutch.

ISBN 90-367-1011-1

NUGI 813

Subject headings: Fischer-Tropsch / water gas shift / iron catalyst / selectivity / product distribution / slurry bubble column reactor / scale up / reactor design / kinetic model.

©1999 by G.P. van der Laan

All rights reserved. No part of this publication may be reproduced, stored in a retrieval system, or transmitted in any form, or by any means, electronic, mechanical, photocopying, recording, or otherwise, without the prior written permission of the author.

This thesis was set in \LaTeX with font type Times.

The format of this thesis follows the style of the American Chemical Society.

Printed in the Netherlands.

ISBN 90 367 1011 1

RIJKSUNIVERSITEIT GRONINGEN

**Kinetics, Selectivity
and Scale Up of the
Fischer-Tropsch Synthesis**

Proefschrift

ter verkrijging van het doctoraat in de
Wiskunde en Natuurwetenschappen
aan de Rijksuniversiteit Groningen
op gezag van de
Rector Magnificus, dr. D.F.J. Bosscher,
in het openbaar te verdedigen op
vrijdag 9 april 1999
om 14.15 uur

door

Gerard Pieter van der Laan

geboren op 15 juni 1971
te Hoogeveen

Promotor: Prof. dr. ir. A.A.C.M. Beenackers

ISBN 90 367 1011 1

Aan Loeki

Promotiecommissie:

Voorzitter: Rector Magnificus

Promotor: Prof. dr. ir. A.A.C.M. Beenackers

Beoordelingscommissie:

Prof. dr. ir. K.P. de Jong, Universiteit Utrecht

Prof. dr. R. Krishna, Universiteit van Amsterdam

Prof. dr. J.A. Moulijn, Technische Universiteit Delft

Overige leden:

Prof. dr. H. Levinsky, Rijksuniversiteit Groningen

Prof. dr. ir. S.T. Sie, Technische Universiteit Delft

Prof. dr. ir. R.M. Voncken, Rijksuniversiteit Groningen

Prof. ir. J.A. Wesselingh, Rijksuniversiteit Groningen

Het promotieonderzoek is uitgevoerd aan:

Rijksuniversiteit Groningen

Faculteit Wiskunde en Natuurwetenschappen

Vakgroep Technische Scheikunde

Nijenborgh 4

9747 AG Groningen

Summary

In the Fischer-Tropsch (FT) process, synthesis gas, a mixture of predominantly CO and H₂, obtained from either coal, peat, biomass or natural gas is converted to a multicomponent mixture of hydrocarbons. Currently, a promising topic in the energy industry is the conversion of remote natural gas to environmentally clean fuels, specialty chemicals and waxes. Fuels produced with the FT process are of high quality due to a very low aromaticity and absence of sulfur. These fuels can be used as blending stocks for transportation fuels derived from crude oil. Other valuable products besides fuels can be tailor-made with the FT in combination with upgrade processes: for example, ethene, propene, α -olefins, ketones, solvents, alcohols, and waxes.

The FT process is catalyzed by both iron and cobalt at pressures from 10 to 60 bar and temperatures from 200 to 300 °C. The FT synthesis is a surface polymerization reaction. The reactants, CO and H₂, adsorb and dissociate at the surface of the catalyst and react to form chain initiator (CH₃), methylene (CH₂) monomer and water. The hydrocarbons are formed by CH₂ insertion into metal-alkyl bonds and subsequent dehydrogenation or hydrogenation to an α -olefin or paraffin, respectively. Iron catalysts can also use synthesis gas with a H₂/CO ratio below 2, because excess of CO is converted with water to carbon dioxide and hydrogen in the water gas shift (WGS) reaction. The most important aspects for FT reactor development are the high reaction heats and the large number of products (gas, liquid and waxy hydrocarbons). The favorite reactor system for the Fischer-Tropsch synthesis of high molecular weight products is the slurry bubble column reactor. Excellent heat transfer characteristics of this reactor result in isothermal conditions.

An optimal design of a commercial scale reactor requires detailed information of the hydrodynamics, reaction kinetics, catalytic system and FT chemistry. Kinetic information is crucial for reliable design and scale up of commercial Fischer-Tropsch processes. The major aim of this thesis is to study the kinetics and selectivity over a commercial precipitated iron catalyst in laboratory reactors. A detailed multicomponent reaction engineering model for a slurry bubble column reactor on commercial scale with use of these detailed kinetic models is the final aim of this thesis.

A critical literature review on the kinetics and selectivity of the Fischer-Tropsch synthesis is given in Chapter 2. The kinetic equations for CO consumption to FT products do not present a uniform picture. Most studies aim at catalyst improvement and

postulate empirical power law kinetics, both for the carbon monoxide conversion rate and the water gas shift reaction. Relatively few studies aim at understanding the reaction mechanisms. Some authors derived Langmuir-Hinshelwood- Hougen-Watson (LHHW) or Eley-Rideal type of rate expressions for the reactant consumption. In most cases the rate determining step is assumed to be the formation of the building block or monomer, methylene. Simultaneous modeling of the WGS and FT reactions on iron catalysts with WGS activity has hardly been reported. The total product yield decreases exponentially with increasing chain length. Most studies assume the so-called Anderson-Schulz-Flory (ASF) distribution to model the product selectivity. The ASF model describes the entire product range by a single parameter, α , the probability of the addition of a carbon intermediate to a chain. However, significant deviations are reported in literature. It is concluded that the reinsertion or readsorption of α -olefins is the most important secondary reaction and that secondary hydrogenation of α -olefins may occur, depending on the catalytic system and process conditions. Accurate product distribution models must also include the change of the solubility and physisorption energy with carbon number. Until now, none of the available literature models obtains enough details to describe the complete FT product spectrum as a function of operating conditions.

The kinetics and selectivity of the Fischer-Tropsch synthesis over a commercial Fe-Cu-K-SiO₂ catalyst was studied in a gas-solid spinning basket reactor and in a gas-slurry laboratory reactor. For the gas-solid system, a new product distribution model for linear hydrocarbons, based on experiments in the spinning basket reactor, is proposed in Chapter 4 (see Figure 1). The α -Olefin Readsorption Product Distribution Model (ORPDM) can quantitatively describe the deviations from conventional Anderson-Schulz-Flory distributions. The model combines olefin readsorption with chain growth and termination on the same catalytic site. The olefin readsorption rate

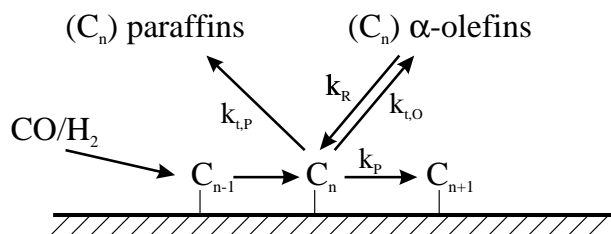


Figure 1 Scheme of the reaction network of the Olefin Readsorption Product Distribution Model.

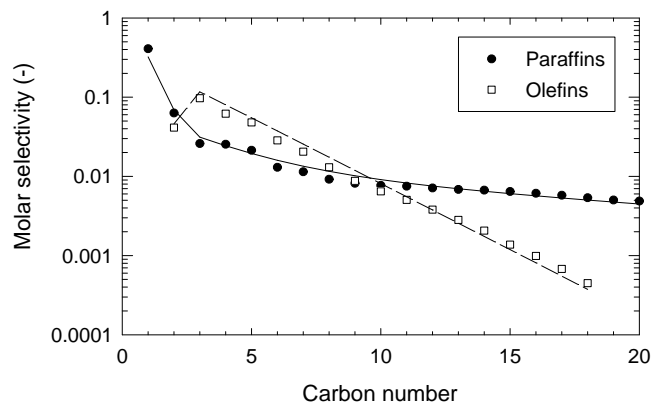


Figure 2 Product distribution for a typical gas-solid experiment (A1) in the spinning basket reactor. Symbols are experimental selectivities. Lines are model predictions.

depends on the chain length due to increasing physisorption strength and increasing solubility in FT-wax with increasing chain length. ORPDM predicts selectivities of linear paraffins and olefins over a wide range of industrially relevant process conditions. For each experimental product distribution three parameters were optimized. An example of a modeled product distribution is shown in Figure 2. The ORPDM parameters could be described successfully with semi-empirical equations containing operating variables only. The novel model, ORPDM, can also predict the selectivity obtained in a gas-slurry reactor accurately (Chapter 6). However, the presence of the slurry liquid appeared to affect both the values of the model parameters and the product selectivity relative to the gas-solid system. The slurry-phase system gives a higher olefin yield at comparable reaction conditions due to a decrease of both the readsorption rate and the termination rate to olefins.

The kinetics of both the Fischer-Tropsch and the water gas shift reactions were modeled simultaneously to experimental data (Chapters 5 and 6). It is generally accepted that the FT and WGS reaction proceed on different active sites on precipitated iron catalysts. A number of Langmuir-Hinshelwood-Hougen-Watson and Eley-Rideal type of rate equations were derived on the basis of a detailed set of possible reaction mechanisms based on the carbide mechanism for the hydrocarbon formation and the formate mechanism for the WGS reaction. Simulations using the optimal kinetic equations derived, showed good agreement both with experimental data and with some

kinetic models from literature. The presence of the slurry liquid appeared to affect the reaction kinetics. The reaction rates are comparable in the gas-solid and the gas-slurry systems at high H_2/CO ratios. However, at low H_2/CO ratios, the reaction rate of the FT reaction appeared to be lower in the slurry system due to CO_2 inhibition. The water gas shift reaction rate is also slower at these reaction conditions.

In Chapter 7, a multicomponent reaction engineering model is presented for a large scale slurry bubble column reactor (SBCR) operating in the heterogeneous or churn-turbulent regime (see Figure 3). Literature data on hydrodynamics and mass transfer are used to describe the performance of the SBCR. The model combines the FT reaction as well as the WGS reaction and the individual paraffin and olefin formation rates (based on original experimental work) with multicomponent vapor-liquid equilibria. Under the operating conditions investigated the SBCR is mainly reaction controlled. This is caused by the limited activity of iron catalysts on the one hand and the large value of the volumetric mass transfer coefficient of the large bubbles due to frequent bubble coalescence and breakup on the other hand. The model predicts the composition of the gaseous and the liquid product streams and the performance of a large scale SBCR. It provides all the data for a reliable design of these FT slurry reactors and for predicting their performance as a function of operating conditions, such as inlet gas velocity, catalyst concentration, and feed composition.

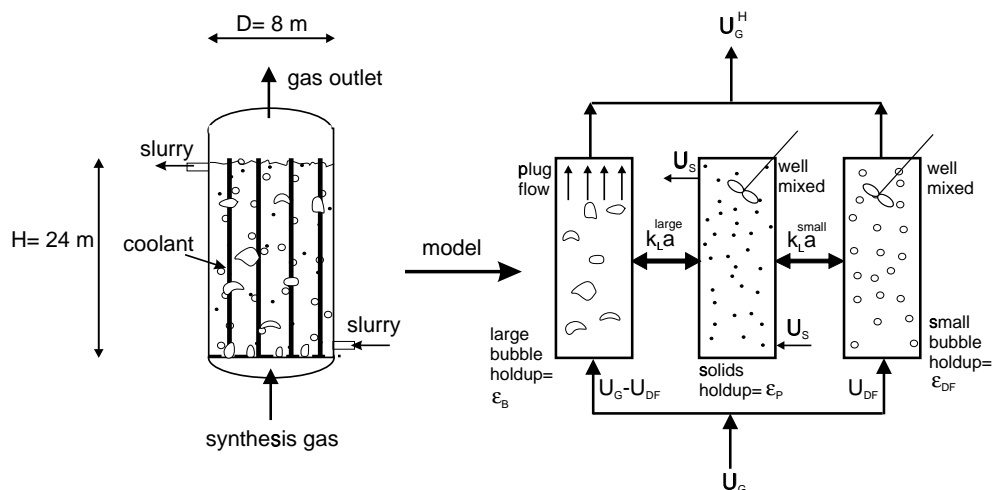


Figure 3 Model for Fischer-Tropsch slurry bubble column reactor in the heterogeneous flow regime.

Contents

Summary	vii
1 Introduction	1
1.1 Fischer-Tropsch (FT) Process	1
1.2 Industrial Fischer-Tropsch Processes	9
1.3 Research on the Fischer-Tropsch Synthesis	13
1.4 Aims and Outline of this Thesis	15
2 Kinetics and Selectivity of the Fischer-Tropsch Synthesis.	
A Literature Review	19
2.1 Introduction	20
2.2 Kinetic experiments	20
2.3 Adsorption	21
2.4 Fischer-Tropsch Catalysis	24
2.5 Mechanism	27
2.6 Selectivity	31
2.7 Product Selectivity Models	38
2.8 Kinetics	60
2.9 Conclusions	78
3 Experimental	93
3.1 Experimental Setup	93
3.2 Catalyst	96
3.3 Product Analysis	98
3.4 Experimental Procedure	104
3.5 Reaction Rates and Selectivities	106
3.6 Catalyst Activity and Selectivity	109
3.7 Catalyst Deactivation	109
4 α-Olefin Readsorption Product Distribution Model for the Gas-Solid Fischer-Tropsch Synthesis	117
4.1 Introduction	118

4.2	α -Olefin Readsorption Product Distribution Model	120
4.3	Experimental	125
4.4	Results and Discussion	126
4.5	Conclusions	140
5	Intrinsic Kinetics of the Gas-Solid Fischer-Tropsch and Water Gas Shift Reactions	145
5.1	Introduction	146
5.2	Theory	147
5.3	Experimental	157
5.4	Results and Discussion	158
5.5	Conclusions	164
6	Kinetics and Selectivity of the Gas-Slurry Fischer-Tropsch Synthesis	169
6.1	Introduction	170
6.2	Experimental	172
6.3	Results and Discussion	173
6.4	Conclusions	184
7	Multicomponent Reaction Engineering Model for Fischer-Tropsch Synthesis in Commercial Scale Slurry Bubble Column Reactors	189
7.1	Introduction	190
7.2	Kinetics and Hydrocarbon Selectivity	192
7.3	Model Equations	193
7.4	Hydrodynamic Parameters	195
7.5	Physical Properties and Flash Calculations	196
7.6	Results and Discussion	198
7.7	Conclusions	203
8	Conclusions and Epilogue	209
	Appendixes A-B	215
	List of Symbols	223
	Samenvatting (Summary in Dutch)	229
	List of Abbreviations	235

CONTENTS

xiii

List of Publications	236
Dankwoord (Acknowledgments)	237
Curriculum Vitae	238

1

Introduction

1.1 Fischer-Tropsch (FT) Process

Coal and natural gas can be utilized as feedstock of the chemical industry and the transportation fuels market. The conversion of natural gas to hydrocarbons (Gas-To-Liquids route) is currently one of the most promising topics in the energy industry due to economic utilization of remote natural gas to environmentally clean fuels, specialty chemicals and waxes. Alternatively, coal or heavy residues can be used on sites where these are available at low costs. The resources of coal and natural gas are very large, see Table 1.1. Coal and natural gas can be converted into synthesis gas, a mixture of predominantly CO and H₂, by either partial oxidation or steam reforming processes. Possible reactions of synthesis gas are shown in Figure 1.1.

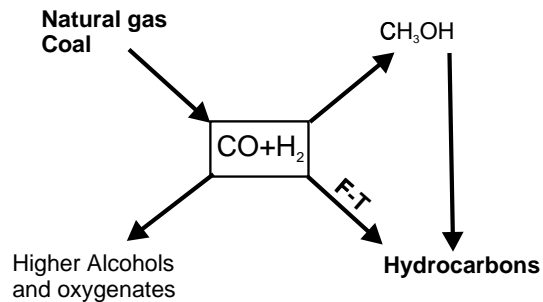


Figure 1.1 Possible reactions from synthesis gas.

Table 1.1 World fossil fuel reserves and consumption (EJ,10¹⁸J) [1].

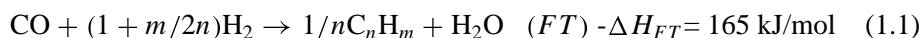
	Reserves	Consumption (1991)
Coal (1991)	27,185	69.91
Crude oil (1992)	6,054	143.67
Natural gas (1992)	4,512	79.44

Table 1.2 Major overall reactions in the Fischer-Tropsch synthesis.

Main reactions	
1. Paraffins	$(2n + 1)H_2 + nCO \rightarrow C_nH_{2n+2} + nH_2O$
2. Olefins	$2nH_2 + nCO \rightarrow C_nH_{2n} + nH_2O$
3. Water gas shift reaction	$CO + H_2O \rightleftharpoons CO_2 + H_2$
Side reactions	
4. Alcohols	$2nH_2 + nCO \rightarrow C_nH_{2n+2}O + (n - 1)H_2O$
5. Boudouard reaction	$2CO \rightarrow C + CO_2$
Catalyst modifications	
6. Catalyst oxidation/reduction	a. $M_xO_y + yH_2 \rightleftharpoons yH_2O + xM$
	b. $M_xO_y + yCO \rightleftharpoons yCO_2 + xM$
7. Bulk carbide formation	$yC + xM \rightleftharpoons M_xC_y$

The conversion of the synthesis gas to aliphatic hydrocarbons over metal catalysts was discovered by Franz Fischer and Hans Tropsch at the Kaiser Wilhelm Institute for Coal Research in Müllheim in 1923 [2, 3]. They proved that CO hydrogenation over iron, cobalt or nickel catalysts at 180-250 °C and atmospheric pressure results in a product mixture of linear hydrocarbons. The Fischer-Tropsch product spectrum consists of a complex multicomponent mixture of linear and branched hydrocarbons and oxygenated products. Main products are linear paraffins and α -olefins. The overall reactions of the Fischer-Tropsch synthesis are summarized in Table 1.2. The hydrocarbon synthesis is catalyzed by metals such as cobalt, iron, and ruthenium. Both iron and cobalt are used commercially these days at a temperature of 200 to 300 °C and at 10 to 60 bar pressure [4, 5].

The reactions of the FT synthesis on iron catalysts can be simplified as a combination of the FT reaction and the water gas shift (WGS) reaction:



where n is the average carbon number and m is the average number of hydrogen atoms of the hydrocarbon products. Water is a primary product of the FT reaction, and CO_2 can be produced by the WGS reaction. The WGS activity can be high over potassium-promoted iron catalysts and is negligible over cobalt or ruthenium catalysts.

Figure 1.2 shows a block diagram of the overall Fischer-Tropsch process configuration. The commercial process involves three main sections, namely: synthesis gas production and purification, Fischer-Tropsch synthesis, and product grade-up. These subjects are described in more detail below. Choi et al. [6] gives a capital cost breakdown of these three individual process sections for a 45,000 bbl/day FT plant. The synthesis gas preparation (that is air separation plant, partial oxidation, steam reforming of natural gas, and syngas cooling) is about 66 % of the total on-site capital costs. The FT synthesis section consisting of FT slurry reactors, CO₂ removal, synthesis gas compression and recycle, and recovery of hydrogen and hydrocarbons is 22 % of the total costs. Finally, the upgrading and refining section of hydrocarbons is about 12 %. Consequently, cost reduction of synthesis gas production is the most beneficial. Note, however, that at a fixed production rate the selectivity of the FT process directly affects the size of the syngas generation section. A high selectivity of the FT process to desired products is of utmost importance to the overall economics.

1.1.1 Synthesis Gas Production

Synthesis gas can be obtained by steam reforming or (catalytic) partial oxidation of fossil fuels: coal, natural gas, refinery residues, biomass or industrial off-gases. The composition of syngas from the various feedstocks and processes is given in Table 1.3 [7, 8]. Synthesis gas can be obtained from reforming of natural gas with either steam or carbon dioxide, or by partial oxidation. The most important reactions are:



Usually, a combination of synthesis gas production processes is used to obtain synthesis gas with a stoichiometric ratio of hydrogen and carbon monoxide.

Synthesis gas produced in modern coal gasifiers (Shell/Koppers or Texaco gasifiers) and from heavy oil residues has a high CO content in comparison to synthesis gas from natural gas. If synthesis gas with a H₂/CO ratio below 2 is used, the composition is not stoichiometric for the Fischer-Tropsch reactions (see Table 1.2). Then the water gas shift reaction is important to change the H₂/CO ratio to 2. Figure 1.3 shows the application ranges for iron (high WGS-activity) and cobalt catalysts (no WGS activity) [10]. Inexpensive iron catalysts in comparison to cobalt can directly convert

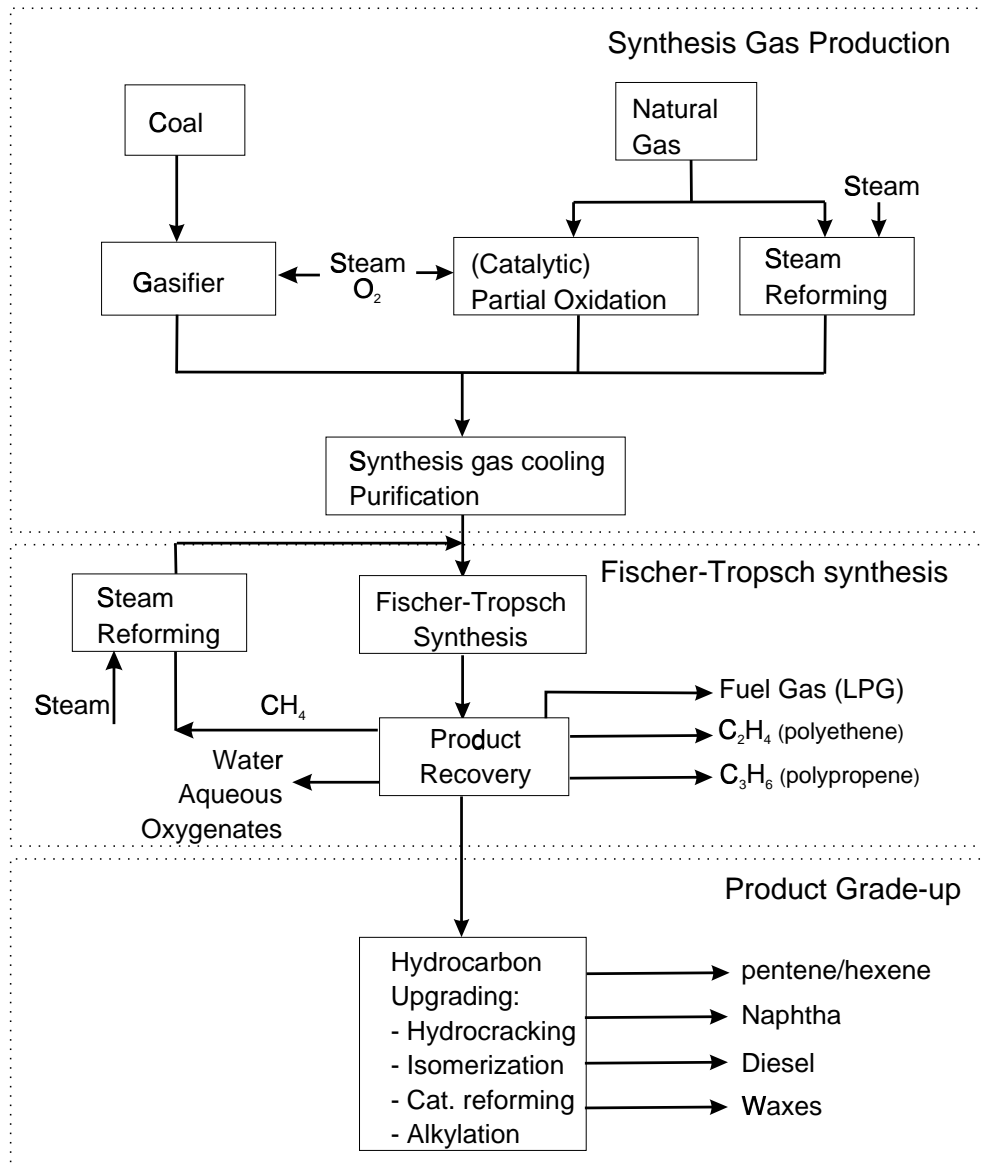


Figure 1.2 Overall process scheme Fischer-Tropsch.

Table 1.3 Synthesis gas compositions.

Feedstock	Process	Component (vol%)			
		H ₂	CO	CO ₂	Other
Natural gas, steam	SR ¹	73.8	15.5	6.6	4.1
Natural gas, steam, CO ₂	CO ₂ - SR ²	52.3	26.1	8.5	13.1
Natural gas, O ₂ , steam, CO ₂	ATR ²	60.2	30.2	7.5	2.0
Coal/heavy oil, steam	Gasification ¹	67.8	28.7	2.9	0.6
Coal, steam, oxygen	Texaco gasifier ¹	35.1	51.8	10.6	2.5
Coal, steam, oxygen	Shell/Koppers gasifier ¹	30.1	66.1	2.5	1.3
Coal, steam, oxygen	Lurgi gasifier ³	39.1	18.9	29.7	12.3

SR= steam reforming, CPO= catalytic partial oxidation, ATR= autothermal reforming

¹ Data from Cybulski et al. [7]

² Data from Basini and Piovesan [9]

³ Data from Perry and Green [8]

low H₂/CO ratio synthesis gas without an external shift reaction [11–13].

New ceramic membranes might become interesting for significant cost reduction of synthesis gas production by 30-50 % [14]. Reduction of the synthesis gas costs could also be accomplished by a decrease of steam/carbon and oxygen/carbon ratios in the feedstock [9]. Basini and Piovesan [9] compared economical evaluations of steam-CO₂ reforming, autothermal reforming, and combined reforming processes. They concluded that combined reforming has the lowest production and investment costs at a H₂/CO ratio of 2.

Although the capital costs predominate, the cost price of natural gas is also an important factor in the overall process economics of GTL (Gas-To-Liquids) Fischer-Tropsch plants. Remote gas fields or natural gas associated with crude oil production has a low cost or a negative value as an undesired by-product. Reduction of flaring of associated natural gas and the unfavorable economics of gas reinjection make the Fischer-Tropsch process economically viable. FT derived fuels are easily transported in standard vessels or pipelines relative to natural gas and LNG.

1.1.2 Fischer-Tropsch Synthesis

The Fischer-Tropsch synthesis section consists of: FT reactors, recycle and compression of unconverted synthesis gas, removal of hydrogen and carbon dioxide, reforming of methane produced and separation of the FT products. The most important aspects

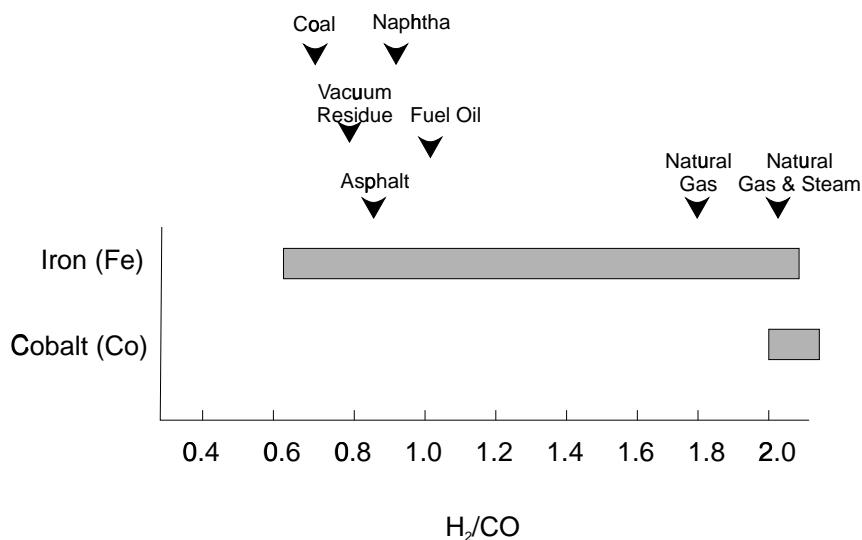


Figure 1.3 Feedstocks and catalysts [10].

for development of commercial Fischer-Tropsch reactors are the high reaction heats and the large number of products with varying vapor pressures (gas, liquid, and solid hydrocarbons). The main reactor types which have been proposed and developed after 1950 are [5, 15, 16]:

1. Three-phase fluidized (ebulliating) bed reactors or slurry bubble column reactors with internal cooling tubes (SSPD: Sasol; GasCat: Energy International, AGC-21: Exxon, see Figure 1.4a)
2. Multitubular fixed bed reactor with internal cooling (Arge: Sasol; SMDS: Shell, see Figure 1.4b)
3. Circulating fluidized bed reactor with circulating solids, gas recycle and cooling in the gas/solid recirculation loop (Synthol: Sasol) (Figure 1.4c)
4. Fluidized bed reactors with internal cooling (SAS: Sasol) (Figure 1.4d)

Sie [5] compared the advantages and disadvantages of the two most favorite reactor systems for the Fischer-Tropsch synthesis of high molecular weight products: that is the multitubular trickle bed reactor and the slurry bubble column reactor. Major drawbacks of the bubble column are requirements for continuous separation between

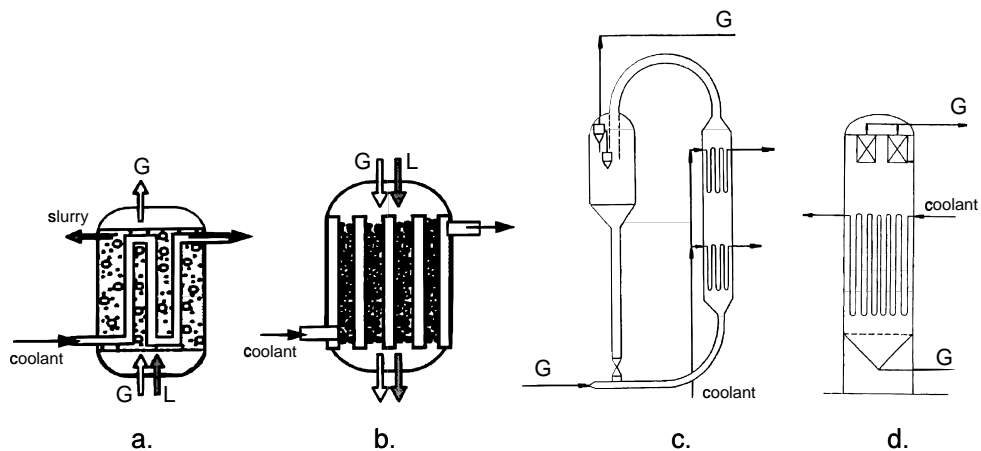


Figure 1.4 Possible reactors for Fischer-Tropsch synthesis [5, 16]. a. Slurry bubble column reactor; b. Multitubular trickle bed reactor; c. Circulating fluidized bed reactor; d. Fluidized bed reactor.

catalyst and liquid products, a smaller scaling-up factor (500) in comparison to the multitubular reactor (max. 10,000), and possible attrition of the catalyst particles. The advantages are [17]: 1) Low pressure drop over the reactor. 2) Excellent heat transfer characteristics resulting in stable reactor temperatures. 3) No diffusion limitations. 4) Possibility of continuous refreshment of catalyst particles. Disadvantages of the multitubular reactor are the larger catalyst particles, the required equal distribution of gas and liquid streams over all tubes, and the large reactor weight due to a large number of tubes for effective heat transfer area. However, the most important disadvantage of the multitubular reactor probably is in the high costs of 10 to 100,000 tubes, typical for commercial scale.

De Swart [18] modeled a cobalt-based FT process both in trickle bed reactors and in slurry bubble column reactors. The major conclusion was that 10 multitubular trickle bed reactors (6 m diameter, 20 m height) or 4 slurry reactors (7.5 m diameter, 30 m height) can produce 5000 tonnes of middle distillates (C_{5+}) per day. Mainly due to the high heat transfer rates occurring in the slurry system, the capital costs of this system reportedly can be 60 % lower than that of the multitubular system [18]. Jager [19] stated that the costs of a single 10,000 bbl/day slurry reactor system is about 25 % of that of a tubular fixed bed reactor. Although these capital cost figures look impressive, it is emphasized again that the C_{5+} selectivity is crucial to overall economics. In other words, if a cheaper reactor delivers a lower C_{5+} selectivity, the larger syngas section needed may off-set the initial advantages.

1.1.3 Product Upgrading and Separation

Conventional refinery processes can be used for upgrading of Fischer-Tropsch liquid and wax products. A number of possible processes for FT products are: wax hydrocracking, distillate hydrotreating, catalytic reforming, naphtha hydrotreating, alkylation and isomerization [6, 20]. Fuels produced with the FT synthesis are of a high quality due to a very low aromaticity and zero sulfur content. The product stream consists of various fuel types: LPG, gasoline, diesel fuel, jet fuel. The definitions and conventions for the composition and names of the different fuel types are obtained from crude oil refinery processes and are given in Table 1.4.

Table 1.4 Conventions of fuel names and composition [1].

Name	Synonyms	Components
Fuel gas		C ₁ - C ₂
LPG		C ₃ - C ₄
Gasoline		C ₅ - C ₁₂
Naphtha		C ₈ -C ₁₂
Kerosene	Jet fuel	C ₁₁ -C ₁₃
Diesel	Fuel oil	C ₁₃ -C ₁₇
Middle distillates	Light gas oil	C ₁₀ -C ₂₀
Soft wax		C ₁₉ - C ₂₃
Medium wax		C ₂₄ - C ₃₅
Hard wax		C ₃₅ +

The diesel fraction has a high cetane number resulting in superior combustion properties and reduced emissions (see Table 1.5). New and stringent regulations may promote replacement or blending of conventional fuels by sulfur and aromatic free FT products [21, 22]. Also, other products besides fuels can be manufactured with Fischer-Tropsch in combination with upgrading processes, for example, ethene, propene, α -olefins, alcohols, ketones, solvents, specialty waxes, and so forth. These valuable by-products of the FT process have higher added values, resulting in an economically more attractive process economy. The value of Fischer-Tropsch products used as blending stocks for transportation fuels (kerosene and diesel) is higher than crude oil derived fuels due to their excellent properties (see Table 1.5). Choi et al. [6] assumed the FT gasoline and FT diesel to be 10.07 \$/bbl (0.24 \$/gallon) and 7.19 \$/bbl (0.17 \$/gallon) more expensive than transportation fuels derived from crude oil.

Table 1.5 Product quality, adapted from Sie [5] and Gregor [22].

Product	Property	SMDS products	Hydrocracked Arge FT-wax	Specification
Diesel	Cetane number	70	> 74	min. 40
	Cloud point, °C	-10	-7	-20 to +20
Kerosene	Smoke point, mm	> 100	> 50	min. 19-25
	Freezing point, °C	-47	-43	max. -47 to -40

1.2 Industrial Fischer-Tropsch Processes

Below, the major industrial Fischer-Tropsch processes are discussed briefly. The emphasis is on processes developed after 1980. Table 1.6 gives an overview of the major companies and their patents divided in the following sections: 1. FT catalyst development; 2. process design and development; 3. upgrading of specific FT products. A comparison of the several industrial Fischer-Tropsch companies is presented in Table 1.7.

Table 1.6 Estimate of patents of the major companies active in Fischer-Tropsch (April 1998).

Company	Catalyst development	Process development	Separation and product grade-up
BP	13	4	0
Exxon	71	15	5
Rentech	1	8	0
Sasol	2	3	3
Shell	45	27	13
Statoil	5	3	1
Syntroleum	0	1	0

Energy International

Energy International (Pittsburgh) is owned by Williams International Corp. (formerly owned by Gulf Oil Corp.) which is promoting slurry bubble column reactors for the FT process. They claim the major advantage of their process to be low capital costs in comparison to other processes. Highly active cobalt catalyst on alumina carriers

Table 1.7 Comparison of the major companies active in Fischer-Tropsch (October 1998).

Company	Synthesis gas preparation ¹	FT reactor	Capacity (bbl/day)	Catalyst
Energy Int.	PO with O ₂	slurry	-	Co
Exxon	CPO (O ₂)	slurry	200	Co
Rentech	PO with O ₂ , SR, ATR	slurry	235	Fe
Sasol	PO with O ₂ , SR, coal gasification	slurry fluidized	2,500 110,000	Fe, Co
Shell ²	PO with O ₂	fixed	12,500	Co
Syntroleum	ATR with air	fixed	2	Co

¹ (C)PO= (Catalytic) Partial Oxidation, SR= Steam Reforming, ATR= Autothermal Reforming

² Capacity until December 1997

(GasCat catalyst) produce a high liquid fuel yield relative to other cobalt catalysts [23]. Energy International performs a US Department of Energy funded study for the concept of a 25,000 bbl/day floating Fischer-Tropsch plant for the deep waters of the Gulf of Mexico (Remote Gas Strategies, October 1997).

Exxon

The Exxon's process is known as AGC 21 (Advanced Gas Conversion 21st Century) [24]. The process consists of the following steps: 1. Fluidized bed synthesis gas production; 2. Slurry phase FT reactor; 3. Hydro-isomerization process. Exxon has a 200 bbl/day GTL pilot plant in Baton-Rouge, USA, that has been operating until 1996. The AGC-process can be scaled up to commercial plants producing 50,000-100,00 bbl/day at a location in Qatar [25]. A significant number of patents (about 70) between 1980-1993 of Exxon deal with the development of new formulations of catalysts. Main emphasis is on cobalt and ruthenium-based catalysts. Recent licenses (after 1993) are also dealing with slurry-phase processes [26, 27].

Rentech Inc.

Rentech licenses an iron based catalyst [28] and a slurry phase process [29–31] for the production of high quality FT diesel. Rentech built 0.038 m and 0.15 m diameter slurry reactors on laboratory scale. A 1.8 m diameter and 16.7 m high slurry reactor producing 235 bbl/day was built in Pueblo, Colorado, U.S in 1992. Recently, this plant

was dismantled and transported to Arunachal, India where it is expected to produce 350 bbl/day of waxes in 1999 in cooperation with the Indian company Donyi Polo Petrochemicals Ltd.

Sasol

Sasol has operated commercial Fischer-Tropsch plants since 1955. A detailed review of Sasol's commercial plants from 1950 to 1979 is given by Dry [32]. A commercial plant in Sasolburg (South Africa) (Sasol 1) use multitubular (2050 tubes, 50 mm ID) fixed bed and entrained bed Kellogg reactors. Synthesis gas is predominantly produced with Lurgi coal gasifiers. Sasol 2 and Sasol 3 plants in Secunda went on stream in the beginning of the eighties. These plants use circulating fluidized bed reactors (Synthol, Figure 1.4c) for the production of fuels and low molecular weight olefins. Currently, Sasol has two new processes for the Fischer-Tropsch synthesis. A process at high temperatures (HTFT: 330-350 °C) for the production of gasoline and light olefins and a process for wax production at lower temperatures (LTFT: 220-250 °C). The HTFT is performed in Synthol circulating fluidized bed (CFB) reactors, but a more efficient Sasol Advanced Synthol (SAS) reactor with gas-solid fluidization was developed recently [16]. The Synthol reactors will be replaced by the new SAS reactors. Conventionally, ARGE tubular fixed bed reactors were used for the LTFT process. In 1990, a slurry bubble column reactor (Sasol Slurry Phase Distillate; SSPD) with a diameter of 1 m was commissioned [15]. A commercial-scale slurry reactor is in operation since 1993 and has a diameter of 5 m and a height of 22 m with a capacity of about 2,500 bbl/day. Table 1.8 shows an overview of different Sasol reactors [15, 19]. Further scale up of the SSPD reactor is planned to 20,000 bbl/day per reactor.

Table 1.8 Sasol Fischer-Tropsch commercial reactors (bbl/day), adapted from Jager [19].

	CFB	SAS	ARGE	SSPD
Total installed capacity	110,000	11,000	3,200	2,500
Capacity per reactor	6,500	11,000	500-700	2,500
Potential per reactor	7,500	20,000	3,000	20,000

Phillips Petroleum, Sasol, and Qatar General Petroleum Corp. signed a memorandum of understanding to build a 20,000 bbl/day GTL plant at Ras Laffan, Qatar. The new complex will use Sasol's Slurry Phase Distillate Process. Start-up is planned for 2002 (Remote Gas Strategies, August 1998). Sasol and Chevron announced plans (May 1998) to build a 20,000 bbl/day GTL (Gas-To-Liquids) plant based on the SSPD

technology in Nigeria. The estimated cost price of this complex is \$ 500-600 million (Remote Gas Strategies, May 1998). Most patents of Sasol (see Table 1.6) concern the development of a slurry reactor with continuous in-situ wax-solid separation [33] and grade-up of olefins by hydroformulation [34].

Shell

In 1993, Shell started up a \$ 850 million FT synthesis plant in Bintulu, Malaysia. The Shell Middle Distillate Synthesis (SMDS) process [5, 35] produces heavy paraffins on a cobalt catalyst in multitubular trickle bed reactors. Part of these products are sold as wax specialties; another part is hydro-cracked over a noble metal catalyst into clean transportation fuels (see Table 1.5). The plant converts 100 million cubic feet/day of natural gas from off-shore fields by non-catalytic partial oxidation into 12,500 bbl/day hydrocarbons. The air separation plant of the SMDS plant in Bintulu exploded in December 1997. Shell Oil wants to reopen the SMDS plant in 1999 (Remote Gas Strategies, April 1998). Most Shell patents focus on either catalyst development or on the way the SMDS process is preferably carried out, for example, see patents [36, 37]. Some patents for improving a slurry process have been filed as well [38–40].

Statoil

Patents of Statoil involve slurry reactor design and continuous catalyst-wax separations with the use of filtration [41]. Recent patents with respect to Fischer-Tropsch catalysis concern the development of cobalt catalysts promoted with Rh, Pt, Ir, or Re on alumina (for example, [42]). Statoil formed an alliance with Sasol for the development of floating Fischer-Tropsch plants on ships or floating production systems. These floating off-shore plants can be used to utilize natural gas associated with oil production [43].

Syntroleum

Syntroleum is a small research firm in Tulsa, Oklahoma, USA, which has signed licensing agreements with Texaco, ARCO, Kerr-McGee, and Enron. A laboratory pilot plant (2 bbl/day) is used to demonstrate their FT process. They claim that their process eliminates a costly air separation unit, since their Autothermal Reformer (ATR) produces nitrogen-diluted synthesis gas from natural gas [44]. Nitrogen can be used to remove some of the generated heat during the FT reaction. The Syntroleum process is the basis of an agreement between Texaco, Brown & Root and Syntroleum to develop

a 2,500 bbl/day GTL plant, starting end 1999 (Remote Gas Strategies, January 1998). Recently, Syntroleum and Enron announced final agreement to build a 8,000 bbl/day GTL plant in Wyoming, USA. The plant is expected to operate in 2001 [45].

1.3 Research on the Fischer-Tropsch Synthesis

An optimal design with respect to product yield and selectivity of a large scale reactor requires a deep understanding of hydrodynamics, reaction kinetics, catalytic system and FT chemistry (see Figure 1.5). Research on the various aspects of the FT process will be discussed briefly. A detailed review on kinetics and selectivity of the Fischer-Tropsch process is given in Chapter 2.

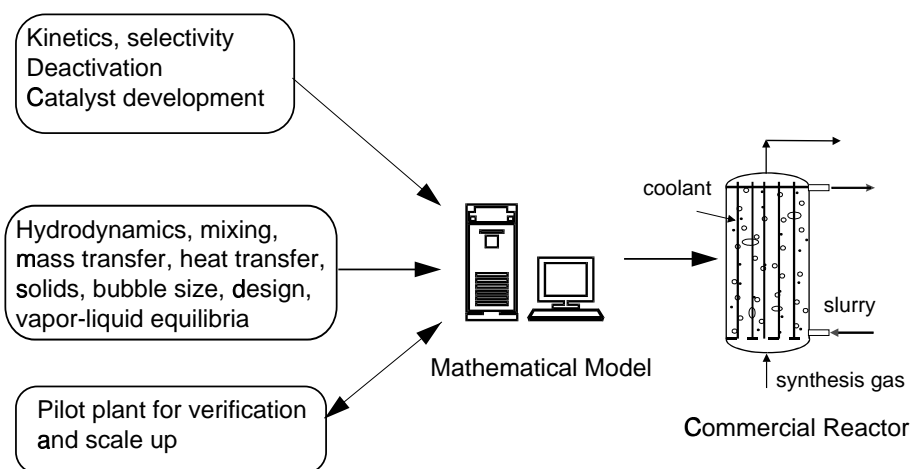


Figure 1.5 Modeling of a large scale Fischer-Tropsch reactor.

Reaction Kinetics

The complexity of the FT reaction mechanism and the large number of species involved is the major problem for development of reliable kinetic expressions. Most catalyst studies aim at catalyst improvement and postulate empirical power law kinetics for both the carbon monoxide conversions and the carbon dioxide formation rate [46, 47]. Langmuir-Hinshelwood-Hougen-Watson (LHHW) type of rate equations have been applied in literature (see Chapter 2.8). The water gas shift reaction can play a dominant role on iron catalysts. Only a few studies report on WGS kinetics on

iron catalysts under FT conditions. A thorough comparison of the available literature models is presented in Chapter 2.

Product Selectivity

The products from the Fischer-Tropsch synthesis form a complex multicomponent mixture with substantial variation in carbon number and product type. Main products are linear paraffins and α -olefins. According to Anderson [48], the product distribution of hydrocarbons can be described by the Anderson-Schulz-Flory (ASF) equation: $m_n = (1 - \alpha)\alpha^{n-1}$ with m_n the mole fraction of a hydrocarbon with chain length n and the growth probability factor α independent of n . α determines the total carbon number distribution of the FT products. The range of α depends on reaction conditions and catalyst type. Dry [49] reported typical ranges of α on Ru, Co, and Fe of: 0.85-0.95, 0.70-0.80, and 0.50-0.70, respectively. More recent references report Co catalysts with chain growth factors between 0.85-0.95 [5]. Significant deviations from the ASF distribution are reported in literature: i) Relatively high yield of methane. ii) Relatively low yield of ethene. iii) Change in chain growth parameter α and exponential decrease of the olefin to paraffin ratio with increasing carbon number. These deviations are predominantly caused by secondary reactions of α -olefins, which may readsorb on growth sites of the catalyst surface and continue to grow via propagation with monomer or terminate as hydrocarbon product. Details on the characteristics of the product selectivity and on modeling of the selectivity are discussed in Chapter 2.

Reactor Engineering Model

Mathematical modeling of FT slurry bubble columns was reviewed by Saxena et al. [17] and more recently by Saxena [50]. He showed that none of the available models is accurate enough for a reliable reactor design. The bottleneck appears to be the lack of reliable kinetic equations for all products and reactants based on realistic reaction mechanisms. Until now, none of the available literature models obtain enough details to describe the complete product distribution of the Fischer-Tropsch synthesis at industrial conditions (high temperature and pressure) as a function of overall consumption of synthesis gas components and operating conditions. Either the product distribution model (ASF behavior) or the kinetic scheme (no WGS and rates equations with first order in hydrogen) is oversimplified, or the hydrodynamic situation is unrealistic under industrial (churn-turbulent or heterogeneous flow regime) operating conditions. The features of the models available will be compared in Chapter 7.

1.4 Aims and Outline of this Thesis

The problem to be dealt with in this thesis is the lack of accurate models for product distributions and reaction kinetics, necessary for reliable design and scale up of industrial Fischer-Tropsch processes.

Therefore, the major aim of this thesis is the development of a product distribution model and a kinetic model both in gas-slurry as well as in gas-solid reactors over a commercial precipitated iron catalyst based on own experimental work. The product distribution model should be able to explain the deviations from the ASF distribution observed experimentally. It should include a mechanistic model of olefin readsorption and kinetics of chain growth and termination on the same catalytic sites. Accurate intrinsic rate expressions for the CO conversion to Fischer-Tropsch products and for the water gas shift (WGS) reaction over a precipitated iron catalyst on the basis of reliable mechanisms are another aim. A detailed multicomponent mathematical model for a large scale slurry bubble column reactor with use of our detailed models is the final aim of this thesis.

Chapter 2 presents a literature review on the kinetics and selectivity of the Fischer-Tropsch synthesis. The focus is on the reaction mechanisms and kinetic models of the water gas shift and Fischer-Tropsch reactions. Literature product selectivity models are reviewed as well. Here the areas which require further research will be defined.

Chapter 3 describes the experimental setup of the kinetic experiments both in a gas-solid and gas-slurry laboratory kinetic reactor and the catalyst applied. The analytical section and the experimental procedures are described as well.

The development of a new α -Olefin Readsorption Product Distribution Model (ORPDM) based on own experiments for the gas-solid FT synthesis, over a precipitated iron catalyst is presented in Chapter 4. The effect of variation of process conditions on the selectivity is described as well.

Chapter 5 presents the kinetic experiments and kinetic modeling of the CO hydrogenation and the water gas shift reaction of gas-solid Fischer-Tropsch synthesis over the precipitated iron catalyst.

The influence of the slurry liquid on the product selectivity and the reaction kinetics is presented in Chapter 6. The product selectivity model developed for the gas-solid system will be applied for the description of the product selectivity at industrially relevant conditions over a precipitated iron catalyst suspended in the slurry phase. Furthermore, Chapter 6 describes kinetic modeling of the gas-slurry Fischer-Tropsch synthesis based on a methodology derived in Chapter 5.

The models obtained in Chapters 4-6 and literature data on hydrodynamics and mass transfer in the heterogeneous flow regime are incorporated in a multicomponent reaction engineering model for a large scale Fischer-Tropsch slurry bubble column reactor in Chapter 7. The main novel aspect of this model is that, for the first time, multicomponent vapor-liquid equilibria with detailed kinetic expressions for all reactants and products (based on original experimental work) are combined to predict the compositions of the gaseous and liquid streams and the performance of a slurry bubble column reactor.

References

- [1] Kroschwitz, I.; Howe-Grant, M., *Kirk-Othmer encyclopedia of chemical technology*, Wiley & Sons, New York, fourth edn. **1996**.
- [2] Fischer, F.; Tropsch, H., Über die Herstellung synthetischer ölgemische (Synthol) durch Aufbau aus Kohlenoxyd und Wasserstoff, *Brennst. Chem.* **1923**, *4*, 276–285.
- [3] Fischer, F.; Tropsch, H., *German Patent 484337* **1925**.
- [4] Jager, B.; Espinoza, R., Advances in low-temperature Fischer-Tropsch synthesis, *Catal. Today* **1995**, *23*, 17–28.
- [5] Sie, S.T., Process development and scale up: IV Case history of the development of a Fischer-Tropsch synthesis process, *Rev. Chem. Eng.* **1998**, *14*, 109–157.
- [6] Choi, G.N.; Kramer, S.J.; Tam, S.T.; Fox, J.M., Design/economics of a natural gas based Fischer-Tropsch plant, in *Spring National Meeting*, American Institute of Chemical Engineers, Houston, 1996 .
- [7] Cybulski, A.; Edvinsson, R.; Irandoust, S.; Andersson, B., Liquid-phase methanol synthesis: modelling of a monolithic reactor, *Chem. Eng. Sci.* **1993**, *48*, 3463–3478.
- [8] Perry, R.H.; Green, D., *Perry's chemical engineers' handbook*, McGraw-Hill, New York, 6th edn. **1984**.
- [9] Basini, L.; Piovesan, L., Reduction on synthesis gas costs by decrease of steam/carbon and oxygen/carbon ratios in the feedstock, *Ind. Eng. Chem. Res.* **1998**, *37*, 258–266.
- [10] Rentech, Gas to liquids home page, <http://www.gastoliquids.com/tech2.htm> (accessed December 1998).
- [11] Rao, V.U.S.; Stiegel, G.J.; Cinquegrane, G.J.; Srivastave, R.D., Iron-based cat-

- alysts for slurry-phase Fischer-Tropsch process: Technology review, *Fuel Process. Technol.* **1992**, *30*, 83–107.
- [12] Xu, L.; Bao, S.; R.J., O'Brien; Raje, A.; Davis, B.H., Don't rule out iron catalysts for Fischer-Tropsch synthesis, *CHEMTECH* **1998**, *8*, 47–53.
- [13] Raje, A.P.; Davis, B.H., Fischer-Tropsch synthesis: process considerations based on performance of iron-based catalysts, *Fuel* **1997**, *76*, 273–280.
- [14] Udovich, C.A., Ceramic membrane reactors for the conversion of natural gas to syngas, *Stud. Surf. Sci. Catal.* **1998**, *119*, 417–422.
- [15] Jager, B., Developments in Fischer-Tropsch technology, *Stud. Surf. Sci. Catal.* **1997**, *107*, 219–224.
- [16] Jager, B.; Dry, M.E.; Shingles, T.; Steynberg, A.P., Experience with a new type of reactor for Fischer-Tropsch synthesis, *Catal. Lett.* **1990**, *7*, 293–302.
- [17] Saxena, S.C.; Rosen, M.; Smith, D.N.; Ruether, J.A., Mathematical modeling of Fischer-Tropsch slurry bubble column reactors, *Chem. Eng. Commun.* **1986**, *40*, 97–151.
- [18] De Swart, J.W.A., *Scale-up of a Fischer-Tropsch reactor*, Ph.D. thesis, University of Amsterdam, Amsterdam, The Netherlands **1996**.
- [19] Jager, B., Developments in Fischer-Tropsch technology, *Stud. Surf. Sci. Catal.* **1998**, *119*, 25–34.
- [20] Choi, G.N.; Kramer, S.J.; Tam, S.T.; Fox, J.M.; Carr, N.L.; Wilson, G.R., Design/economics of a once-through natural gas based Fischer-Tropsch plant with power co-production, in *Coal liquefaction and solid fuels*, Pittsburgh, 1997 .
- [21] Fox, III, J.M., The different catalytic routes for methane valorization: an assessment of processes for liquid fuels, *Catal. Rev.-Sci. Eng.* **1993**, *35*, 169–212.
- [22] Gregor, J.H., Fischer-Tropsch products as liquid fuels or chemicals. An economical evaluation, *Catal. Lett.* **1990**, *7*, 317–332.
- [23] Singleton, A.H., Advances make gas-to-liquids process competitive for remote locations, *Oil Gas J.* **1997**, 68–72.
- [24] Eisenberg, B.; Fiato, R.A.; Mauldin, C.H.; Say, G.R.; Soled, S.L., Exxon's advanced gas-to-liquids technology, *Stud. Surf. Sci. Catal.* **1998**, *119*, 943–948.
- [25] Davis, B.H., Fischer-Tropsch conversion of gas to liquid, *Appl. Catal. A* **1997**, *155*, N4–N7.
- [26] Behrmann, W.C.; Mauldin, C.H.; Pedrick, L.E., Patent WO 9414735 **1994**, Exxon.
- [27] Koros, R.B., US Patent 5384336 **1995**, Exxon.
- [28] Benham, C.B.; Bohn, M.S.; Yakobson, D.L., US Patent 5504118 **1996**, Rentech.

- [29] Benham, C.B.; Bohn, M.S.; Yakobson, D.L., US Patent 5620670 **1997**, Rentech.
- [30] Benham, C.B.; Bohn, M.S.; Yakobson, D.L., US patent 5621155 **1997**, Rentech.
- [31] Benham, C.B.; Bohn, M.S.; Yakobson, D.L., US Patent 5534437 **1996**, Rentech.
- [32] Dry, M.E., The Fischer-Tropsch synthesis, in J.R. Anderson; M. Boudart, eds., *Catalysis-Science and technology*, vol. 1, Springer-Verlag, New York, 1981 pp. 160–255.
- [33] Inga, J.R.; Jager, B.; Kelfkens, R.C.; Malherbe, F.E.J.; Smith, M.A.; Steynberg, A.P., Eur. Patent 609079, US patent 5599849 **1994**, Sasol.
- [34] Betts, M.J. Dry, M.E.; Geertsema, A.; Rall, G.J.H., Patent WO 9701521 **1997**, Sasol.
- [35] Sie, S.T.; Senden, M.M.G.; Van Wechum, H.M.H., Conversion of natural gas to transportation fuels via the Shell Middle Destillate Synthesis process (SMDS), *Catal. Today* **1991**, 8, 371–394.
- [36] Bode, D.; Sie, S.T., Eur. Patent 188304 **1986**, Shell.
- [37] Post, M.F.M.; Sie, S.T., Eur. Patent 167215 **1984**, Shell.
- [38] Engel, D.C.; Van der Honing, G., Patent WO 9731693 **1997**, Shell.
- [39] Wijn, E.F.; Danckaarts, A.M., Eur. Patent 694325 **1996**, Shell.
- [40] McEwan, M.W.; Teekens, M.B., US Patent 694325 **1978**, Shell.
- [41] Lorentzen, G.B.; Myrstad, T.; Westvik, A., US Patent 5520890 **1995**, Statoil.
- [42] Eri, S.; Goodwin, J.G.; Marcelin, G.; Riis, T., US Patent 4801573 **1989**, Statoil.
- [43] Statoil, Press release April 14, **1997**.
- [44] Agee, K.L.; Willingham, F.Y., WO Patent 9733847 **1997**, Syntroleum.
- [45] Syntroleum, Press release February 24, **1998**.
- [46] Bub, G.; Baerns, M., Prediction of the performance of catalytic fixed bed reactors for Fischer-Tropsch synthesis, *Chem. Eng. Sci.* **1980**, 35, 348–355.
- [47] Newsome, D.S., The water-gas shift reaction, *Catal. Rev.-Sci. Eng.* **1980**, 21, 275–318.
- [48] Anderson, R.B., *Catalysts for the Fischer-Tropsch synthesis*, vol. 4, Van Nostrand Reinhold, New York **1956**.
- [49] Dry, M.E., Catalytic aspects of industrial Fischer-Tropsch synthesis, *J. Mol. Catal.* **1982**, 17, 133–144.
- [50] Saxena, S.C., Bubble column reactors and Fischer-Tropsch synthesis, *Catal. Rev.-Sci. Eng.* **1995**, 37, 227–309.

2

Kinetics and Selectivity of the Fischer-Tropsch Synthesis. A Literature Review

Abstract

A critical review is given on the kinetics and selectivity of the Fischer-Tropsch synthesis. The focus is on reaction mechanisms and kinetics of the water gas shift and Fischer-Tropsch reactions. New developments in the product selectivity as well as the overall kinetics are reviewed. It is concluded that the development of rate equations for the FTS should be based on realistic mechanistic schemes. Qualitatively, there is agreement that the product distribution is affected by the occurrence of secondary reactions (hydrogenation, isomerization, reinsertion, and hydrogenolysis). At high CO and H₂O pressures, the most important secondary reaction is readsorption of olefins resulting in initiation of chain growth processes. Secondary hydrogenation of olefins may occur at high hydrogen pressures and on certain catalytic systems, such as cobalt- and ruthenium-based catalysts. The rates of the secondary reactions increase exponentially with chain length. Much controversy exists whether these chain length dependencies stem from differences in physisorption, solubility or diffusivity. Preferential physisorption of longer hydrocarbons and increase of the solubility with chain length influences the product distribution and results in a decreasing olefin to paraffin ratio with increasing chain length. Process development and reactor design should be based on reliable kinetic expressions and detailed selectivity models.

2.1 Introduction

Literature on the kinetics and selectivity of the Fischer-Tropsch synthesis can be divided into two classes. Most studies aim at catalyst improvement and postulate empirical power law kinetics for the carbon monoxide and hydrogen conversion rates and assume a simple polymerization reaction following an Anderson-Schulz-Flory (ASF) distribution for the total hydrocarbon product yield. This distribution describes the entire product range by a single parameter, α , the probability of the addition of a carbon intermediate (monomer) to a chain. Relatively few kinetic studies under industrial conditions aim at understanding the reaction mechanisms. Some authors derived Langmuir-Hinshelwood-Hougen-Watson (LHHW) or Eley-Rideal type of rate expressions for the reactant consumption and proposed quantitative formulations to describe the product distribution of linear and branched paraffins and olefins, and alcohols. Models which combine the prediction of the overall consumption of the reactants with a prediction of the product distribution are very scarce in literature, despite their utmost value for understanding and modeling the FT process.

Recently, interest in the distribution of the Fischer-Tropsch products raised from improvements of the analysis of all isomers and products which can not be described with the classical ASF distribution. Also the mechanism of CO hydrogenation has remained a subject of immense controversy and uncertainty. A critical review on the various reaction mechanisms and on the kinetic relations proposed is the subject of this chapter. Areas which require further research will be defined.

2.2 Kinetic experiments

Diffusion limitation of one of the reactants results in an incomplete utilization of the catalyst particles and leads to changes in reactivity and selectivity. Zimmerman and Bukur [1] assumed first order kinetics with respect to hydrogen and proved transport limitations of H_2 to occur at particle diameters greater than 0.2 mm ($T > 235$ °C) with a fused iron ammonia synthesis catalyst. Post et al. [2] also used first order behavior and observed transport limitations of hydrogen at high temperatures ($T > 220$ °C; $d_p > 0.4$ mm) with a number of iron- and cobalt-based catalysts in a fixed bed micro-reactor. A common feature of these studies [1, 2] is the assumption that H_2 is the limiting reactant and the overall FT reaction rates are described as first order in H_2 . Iglesia et al. [3] showed that under FT conditions CO becomes diffusion-limited. The relative transport rates of H_2 and CO within liquid-filled pores has been described by

the dimensionless quantity γ_0 [3]:

$$\gamma_0 = \frac{D_{H_2}/H_{H_2}}{D_{CO}/H_{CO}} \quad (2.1)$$

where D and H are the diffusivity coefficient and Henry coefficient, respectively. Under typical Fischer-Tropsch conditions (200 °C, 2.1 MPa), γ_0 is about 1.9 [3–5]. Intrinsic FT kinetic measurements should be performed with small ($d_p < 0.2$ mm) catalyst particles in order to eliminate diffusion limitations of one of the reactants.

2.3 Adsorption

2.3.1 H₂ Adsorption

Hydrogen molecules react either in molecular state or via dissociative adsorption. Most transition metals are able to dissociate hydrogen on the catalyst surface [6, 7]. Heats of chemisorption of H₂ on Group VIII unsupported metals increases in the order: Co, Ni, Fe. [8, 9], see Figure 2.1. Dissociative adsorption follows the weak molecular physisorbed state of dihydrogen:



where s is a catalytic site.

Most adsorption studies of hydrogen are carried out on pure metals. However, Fischer-Tropsch catalysts are generally supported and promoted metals. Under FT process conditions the catalysts consist of mixtures of catalytic materials (metal, metal oxides and carbides). Dry et al. [10] measured the heats of adsorption of CO, CO₂ and H₂ on unpromoted and on K₂O-promoted reduced magnetite. The initial heat of adsorption of H₂ (80 kJ/mol) on unpromoted reduced magnetite is significantly lower than of CO (113 kJ/mol) and of H₂ on a clean iron film (about 135-150 kJ/mol) [8]. Promoters influence the bond strength of hydrogen to metal. Addition of alkali metals (usually K₂O) to iron catalysts promotes electron transfer to the iron and inhibits hydrogen adsorption, since adsorption of hydrogen induces electron donation to the iron surface [10–13].

Curtis Conner and Falconer [14] reviewed the influence of spillover in heterogeneous catalysis. Spillover proceeds by surface diffusion of adsorbed species from a surface to a different surface that does not adsorb the active species under the same conditions. Spillover of hydrogen from an oxide or a carbon surface is important

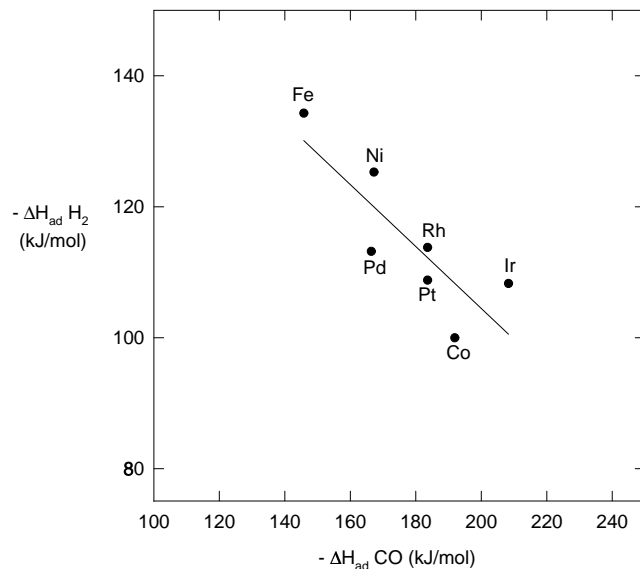


Figure 2.1 Variation of H_2 chemisorption with CO chemisorption on group VIII metals (Vannice [8]).

because the majority of the metal catalysts consists of metal particles supported on oxidic supports. Hydrogen usually dissociates on a metal surface and then spills over to the support. In this way, the catalyst support can act as a hydrogen atom reservoir [14, 15]. The influence of spilt-over hydrogen has never been quantified in kinetic rate equations of the FT synthesis, but can play a significant role.

Hydrogen reacts either in the molecular state or adsorbed dissociated state during the FTS, depending on catalyst, reaction conditions and more important co-adsorption of other species.

2.3.2 CO Adsorption

Both associative and dissociative adsorption of CO occurs. The role of CO adsorption in FTS has been discussed for a long time in literature. Reactions of dissociated CO as well as associated CO with hydrogen are reported. Therefore, adsorption measurements of CO (and H_2) on supported FT catalysts are extremely valuable for mechanistic schemes.

Dissociative adsorption of CO has been demonstrated by X-ray photo-electron spectroscopy (XPS) or pulse techniques for Ni, Co, Ru, and Fe at elevated temperatures ($T > 350$ K) [16]. Associated adsorption of CO via a carbon metal bond is the precursor state to dissociation [6, 7, 17, 18]. CO may be dissociated to a carbidic species according to:



At room temperature, CO adsorption is dissociative for metals more to the left of the periodic system (Cr, Mn, Fe), while other metals adsorb CO molecularly (Co, Ni, Ru). At high temperatures and pressures, CO dissociates on most transition metals [15]. Dissociation of CO occurs without activation ($\Delta E_{CO,G} < 0$) on Fe(110) according to Shustorovich [19]. However, various types of CO will be present on a catalyst (molecular, dissociative, and associative adsorbed CO) depending on process conditions [15, 20].

Figure 2.1 shows the general trend for the heats of adsorption of CO and H₂ on Group VIII unsupported metals. An increase of the adsorption strength of H₂ corresponds to a decrease of the strength of CO adsorption on the same metal. Van Santen and Neurock [21] explained the selectivity differences observed on different metals on the basis of potential energies of the CO dissociation and of the metal-carbon bond. E.g. methanol formation will easily be performed on metals such as Cu, which do not dissociate CO ($\Delta E_{CO,G} = 163$ kJ/mol [19]) and will not form any methane. On Ni, much methane is formed due to easy dissociation of CO ($\Delta E_{CO,G} = 25$ kJ/mol [19]). On Co and Fe, typical excellent Fischer-Tropsch catalysts, stronger metal-carbon bonds will lead to C₂₊ formation. Alkali promoters on iron catalysts increase the d-electron density distribution in iron and will result in an increase of CO adsorption [10–13, 20].

Above 350 K, CO is adsorbed more strongly than H₂ on group VIII metals [10, 16, 20, 22, 23]. In conclusion, in the temperature range of interest various states of CO (molecular, dissociative, and associative adsorbed CO) are present on the metal which displace hydrogen from the surface.

2.4 Fischer-Tropsch Catalysis

2.4.1 Catalysts

The most common Fischer-Tropsch catalysts are group VIII metals (Co, Ru, and Fe). Iron catalysts are commonly used, because of their low costs (see Table 2.1) in comparison to other active metals. Most early FT catalysts were prepared with precipitation techniques [24]. Novel catalyst preparation methods are sintering and fusing metal oxides with desired promoters. Alkali-promoted iron catalysts have been applied industrially for the Fischer-Tropsch synthesis during many years [25]. These catalysts have a high water gas shift activity, high selectivity to olefins and appear to be stable when synthesis gas with a high H₂/CO ratio is converted [26, 27].

Table 2.1 Relative prices of metals (March 1989) adapted from Rao et al. [25].

Metal	Price ratio
Iron	1
Cobalt	230
Nickel	250
Ruthenium	31,000
Rhodium	570,000

Cobalt catalysts give the highest yields and longest life-time and produce predominantly linear alkanes [28]. A precipitated cobalt catalyst on kieselguhr (Ruhchemie) became the standard catalyst for commercial purposes in the second world war in Germany [29]. Disadvantages are the high costs of cobalt and low water gas shift activity. Therefore, cobalt catalysts are viable for natural-gas based Fischer-Tropsch processes for the production of middle distillates and high-molecular weight products [30–32]. Cobalt catalysts are not inhibited by water, resulting in a higher productivity at a high synthesis gas conversion [33].

Ruthenium is a very active but expensive catalyst for the Fischer-Tropsch synthesis relative to Co and Fe. At relatively low pressures ($P < 100$ bar) ruthenium produces much methane while at low temperatures and high pressures it is selective towards high molecular waxes [13, 34]. The molecular mass of polymethylene could reach one million at low temperature (100 °C) and high pressure (1000-2000 bar) [34]. Vannice [35] determined the activity of group VIII metals supported on Al₂O₃ and reported a decrease in activity in the order Ru, Fe, Co, Rh, Pd, Pt, and Ir. The activities of Cr and Mo catalysts were measured at Sasol [13], but were found to be significantly lower than of iron.

2.4.2 Catalyst Pretreatment

The catalysts, synthesized in the form of a metal oxide, are subjected to an activation treatment to become active for FT synthesis. Cobalt, nickel, and ruthenium are almost always reduced in H₂ at temperatures between 473 and 723 K and remain in the metallic state under process conditions [24]. Recently, Ernst et al. [36] reported the behavior of a cobalt silica catalyst both during reduction and for Fischer-Tropsch reaction. Before reduction the cobalt is present as Co₃O₄ spinel phase. A two-step reduction by H₂ at 673 K of Co₃O₄ to CoO and to Co⁰ was observed.

The pretreatment for iron is not as straightforward. The common activation treatments for iron catalysts are H₂ reduction, CO reduction or reduction in synthesis gas (induction). Reduction of Fe₃O₄ by hydrogen to the zero-valent state is reported by, for example, Rao et al. [37] and Bukur et al. [38]. Lox et al. [39] reported that H₂ reduction at 220 °C results in 20 % metallic iron. After pretreatment of Fe-SiO₂ with CO or synthesis gas, the χ -carbide is the dominant iron phase [37, 38, 40, 41]. Pretreatment with synthesis may also result in formation of ε' -carbide [40]. More details on the composition and catalytic activity of the different iron phases is given below.

Iron catalysts are often promoted with Cu, which increase the rate of reduction enabling a lower reduction temperature [12, 13, 24]. Bukur et al. [38, 42–45] studied several reducing gases (CO, H₂ and H₂/CO=0.68) in a fixed bed and concluded that activation in CO (at 280 °C and 1 bar for 24 h) led to catalysts with higher initial activity and better selectivity towards higher hydrocarbons than H₂-activated catalysts. Shroff et al. [46] determined the effect of activation conditions on catalyst behavior. They also studied the micro-structure of the catalyst by electron microscopy and other bulk and surface characterization techniques. They observed that magnetite crystals transform to smaller carbide crystallites. Deposition of carbon on these crystallites causes further segregation of the particles.

2.4.3 Fischer-Tropsch Activity

Cobalt, nickel, and ruthenium remain in the metallic state under FT conditions [24]. Ernst et al. [36] concluded that a completely reduced cobalt remains in the metallic state during CO/H₂ reaction by *in situ* EXAFS (extended X-ray absorption fine structure).

The composition of iron-based catalysts changes during Fischer-Tropsch synthesis. Characterization of the several phases with *in situ* laser Raman spectroscopy [47], *in situ* magnetic measurements [48] or Mössbauer spectroscopy [37, 48] may give ev-

idence of the reactivity of the several active species. Several phases of iron are known in iron-based catalysts subjected to FT synthesis conditions. These include metallic iron (α -Fe), iron oxides (hematite, α -Fe₂O₃; magnetite Fe₃O₄, and Fe_xO), and five different forms of iron carbides O-carbides (carbides with carbon atoms in octahedral interstices, ϵ -Fe₂C, ϵ' -Fe_{2.2}C, and Fe_xC), and TP-carbides (carbides with carbon atoms in trigonal prismatic interstices, χ -Fe_{2.5}C and Fe₃C) [13, 37, 39, 46, 47]. The formation and composition of these iron phases depends on the process conditions, catalyst deactivation and catalyst composition. The catalytic activity of each of these phases with respect to the Fischer-Tropsch reaction is still controversial [13, 44, 46].

There are a number of studies on iron catalysts concerning the role of iron phases in FT synthesis. Raupp and Delgass [49] and Niemantsverdriet et al. [50] proposed that iron carbide formation is needed for a high FT activity. Based on X-ray diffraction, Dictor and Bell [51] concluded that a mixture of χ - and ϵ' -carbides are the active phase on iron catalysts. Bukur et al. [44] showed with Mössbauer spectroscopy that the FT activity of H₂-activated catalysts coincided with the conversion of metallic iron to ϵ' -carbide. They concluded that the active phase of CO-pretreated catalyst was the χ -carbide [44].

Zhang and Schrader [47] concluded that two active sites operated simultaneously on the surface of iron catalysts: Fe⁰/Fe-carbides and Fe-oxide (Fe₃O₄). The carbide phase is active towards dissociation of CO and formation of hydrocarbons, while the oxide phase adsorbs CO associatively and produces predominantly oxygenated products. Lox et al. [39] and Shroff et al. [46] concluded that the magnetite phase has negligible catalytic activity towards FT reactions whereas carbide formation resulted in a high FT activity. Several studies have shown that the ϵ' -carbide phase is the active form for CO hydrogenation on iron catalysts [49, 50, 52]. More recent studies show that the χ -carbide can also be the active phase for the FT synthesis [37, 44, 53].

2.4.4 Water Gas Shift Activity

Cobalt and ruthenium catalysts are not very active towards the WGS reaction in contrast to most iron-based Fischer-Tropsch catalysts [54]. The water gas shift (WGS) reaction is important when synthesis gas with non-stoichiometric amounts of hydrogen is used. The WGS reaction is an equilibrium reaction and may reach equilibrium at high temperatures ($T > 250$ °C) on catalysts with a high water gas shift activity [55, 56]. Several authors proposed that magnetite (Fe₃O₄) is the most active phase for the WGS reaction [37, 47, 54, 57, 58] on iron catalysts. Rao et al. [37] studied the

iron phase of Fe/Cu/K/SiO₂ catalysts from the demonstration unit at LaPorte, Texas (August, 1992) with Mössbauer spectroscopy. The changes of the magnetite phase corresponded to the WGS reaction activity during time-on-stream. Lox et al. [39] showed that Fe₃O₄ coexists with various iron carbides on the catalyst during synthesis gas reactions. It is generally assumed that the WGS reaction and the FT reaction proceed on different active sites.

2.5 Mechanism

2.5.1 Fischer-Tropsch Synthesis

The mechanism of the hydrocarbon and oxygenate formation in the FTS has been reviewed by several authors [13, 16, 18, 24, 59]. Recent reviews are given by Hindermann et al. [60], Dry [61], Dry [62], and Adesina [63]. Here we give a summary of the mechanisms for the formation of linear hydrocarbons which are supported by experiments. The FTS is a polymerization reaction with the following steps [63]: 1. reactant adsorption; 2. chain initiation; 3. chain growth; 4. chain termination; 5. product desorption; 6. readsorption and further reaction.

A variety of surface species were proposed to describe chain initiation and chain growth. Figure 2.2, adapted from Schulz et al. [64] and Rofer-De Poorter [7], gives an overview of observed and postulated species on the catalyst surface during Fischer-Tropsch synthesis. Reactants: **1,2,3,4,5**; oxygen containing intermediates: **6,7,8** and hydrocarbon intermediates: **9,10,11,12**. Several compounds are possible monomers for chain growth.

The most important growth mechanism for the hydrocarbon formation on cobalt [28], iron [51, 65], and ruthenium catalysts [65, 66] is the surface carbide mechanism by CH₂ insertion [13, 22, 67, 68]. Figure 2.3 shows a schematic representation of the initiation, growth and termination of chains according to this mechanism. The monomer of the carbide mechanism is a methylene (CH₂) species (see Figure 2.2: nr. **10**). CO and H₂ are assumed to adsorb dissociatively. Several species like CH (**9**), CH₂ (**10**) and CH₃ (**11**) can be formed this way. Chain growth occurs by insertion of the monomer in a growing alkyl species (**12**). Termination can take place by abstraction of hydrogen to an olefin or addition of a CH₃ species (**11**) or hydrogen to form a paraffin. The presence of methylene has been identified with use of isotopic-tracer techniques on Ru/SiO₂ [69], on unsupported Co, Ni/SiO₂, and Ru/Al₂O₃ [65, 70] and on Fe/Al₂O₃ [71]. Several authors mentioned a mechanism where CH₂ is formed by hydrogen assisted CO dissociation [11, 22, 72]. Undissociated adsorbed CO re-

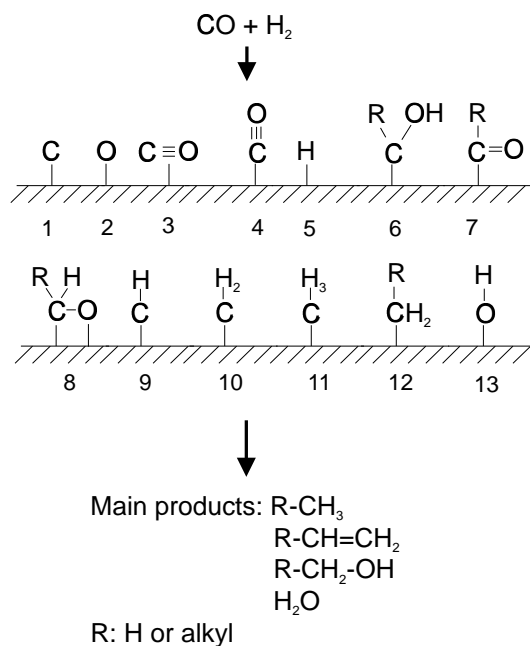


Figure 2.2 Observed and postulated chemisorbed species during Fischer-Tropsch synthesis (adapted from Schulz et al. [64]).

acts with hydrogen before the CH_2 species is formed. After that, the enolic (HCOH) species is dissociated in water and a methylene species, while chain growth proceeds in a similar way.

The carbide mechanism by CH_2 insertion is the most plausible mechanism for the hydrocarbon formation reactions on ruthenium, cobalt, and iron. It is uncertain if the monomer formation proceeds via hydrogenation of dissociated or undissociated CO . The set of elementary reactions proposed for the formation of linear hydrocarbons is given in Table 2.2 [18, 22, 75, 76].

Secondary reactions occur when primary products desorb from a site and interact with another catalytic site before leaving the reactor. Novak et al. [77, 78] listed possible secondary reactions of α -olefins: (i) hydrogenation to give n-paraffins, (ii) isomerization, (iii) cracking and hydrogenolysis, (iv) insertion into growing chains, mostly effective for C_2H_4 and C_3H_6 , and (v) readsorption and initiation of hydrocarbon chains. Schulz et al. [68, 74] showed a possible reaction mechanism for the readsorption of olefins followed by hydrogenation to paraffins or isomerization to internal olefins via double bond shift reactions (Figure 2.4). Secondary reactions can influence the type and molecular weight of the hydrocarbon products as will be proved later.

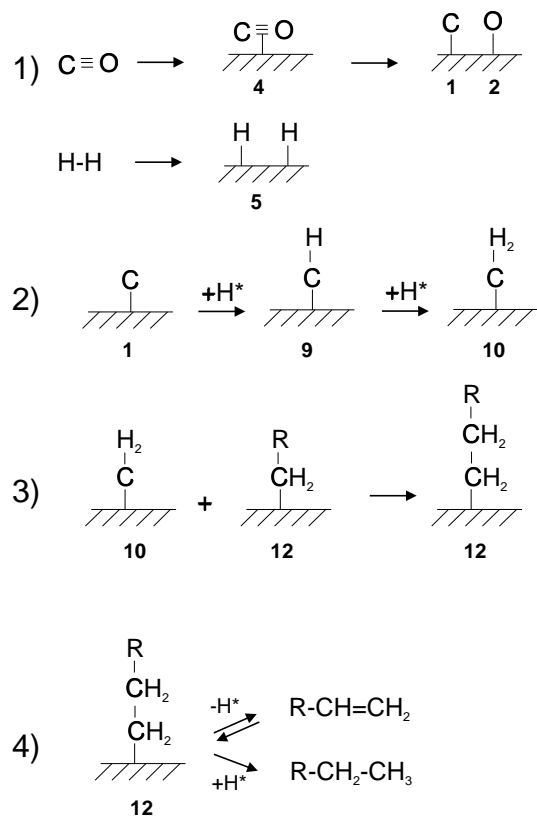


Figure 2.3 Carbide mechanism for the Fischer-Tropsch synthesis [18, 73].

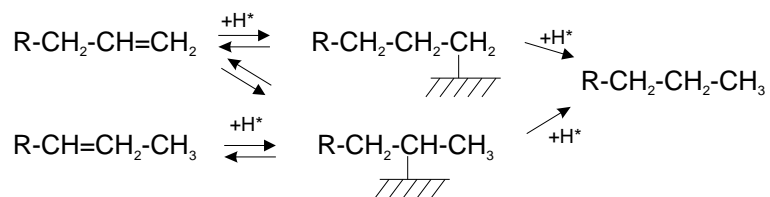


Figure 2.4 Secondary reactions of olefins (Schulz et al. [74]).

Table 2.2 Proposed mechanism of the hydrocarbon synthesis from CO and H₂ [18, 22, 75, 76].

<i>Adsorption</i>	
1	$\text{CO} + \text{s} \rightleftharpoons \text{COs}$
2	$\text{COs} + \text{s} \rightleftharpoons \text{Cs} + \text{Os}$
3	$\text{H}_2 + 2\text{s} \rightleftharpoons 2\text{Hs}$
<i>Surface reactions</i>	
<i>Water formation</i>	
4	$\text{Os} + \text{Hs} \rightarrow \text{HOs} + \text{s}$
5	$\text{HOs} + \text{Hs} \rightarrow \text{H}_2\text{O} + 2\text{s}$
or	$\text{Os} + \text{H}_2 \rightarrow \text{H}_2\text{O} + \text{s}$
<i>Chain initiation</i>	
6	$\text{Cs} + \text{Hs} \rightleftharpoons \text{CHs} + \text{s}$
7	$\text{CHs} + \text{Hs} \rightleftharpoons \text{CH}_2\text{s} + \text{s}$
8	$\text{CH}_2\text{s} + \text{Hs} \rightleftharpoons \text{CH}_3\text{s} + \text{s}$
or	$\text{COs} + \text{H}_2 \rightleftharpoons \text{CHOHs}$
	$\text{CHOHs} + \text{H}_2 \rightleftharpoons \text{CH}_2\text{s} + \text{H}_2\text{O}$
<i>Methanation</i>	
9	$\text{CH}_3\text{s} + \text{Hs} \rightarrow \text{CH}_4 + \text{s}$
<i>Chain growth</i>	
10	$\text{C}_n\text{H}_{2n+1}\text{s} + \text{CH}_2\text{s} \rightarrow \text{C}_{n+1}\text{H}_{2n+3}\text{s} + \text{s}$
<i>Hydrogenation to paraffins</i>	
11	$\text{C}_n\text{H}_{2n+1}\text{s} + \text{Hs} \rightarrow \text{C}_n\text{H}_{2n+2} + 2\text{s}$
<i>β-dehydrogenation to olefins</i>	
12	$\text{C}_n\text{H}_{2n+1}\text{s} \rightleftharpoons \text{C}_n\text{H}_{2n} + \text{Hs}$

2.5.2 Water Gas Shift Reaction

Several mechanisms for the water gas shift reaction are proposed in the literature. Single studies of the water gas shift reaction over supported iron and cobalt shift catalysts suggest the appearance of formate species [54]. A mechanism based on a reactive formate intermediate is shown in Figure 2.5 [58, 75, 79–82]. The formate species can be formed by the reaction between a hydroxy species or water and carbon monoxide in the gas phase or in the adsorbed state. The hydroxy intermediate can be formed by the decomposition of water. The formate intermediate is reduced to adsorbed or gaseous carbon dioxide. Rofer-De Poorter [7] suggested that a mechanism with direct oxidation of adsorbed or gas-phase CO to CO₂ [58, 83–87], presented in Figure 2.6, is more plausible in conjunction with the Fischer-Tropsch synthesis on iron catalysts. The oxygen intermediate can be formed from the dissociation of water. Direct oxidation of CO proceeds via a regenerate or redox mechanism where H₂O oxidizes the surface with formation of H₂, and CO subsequently reduces the surface with the formation of CO₂ [58]. Rethwisch and Dumesic [58] studied the water gas shift reaction on several supported and unsupported iron oxide and zinc oxide catalysts. They suggested that the WGS reaction over unsupported magnetite proceeds via a direct oxidation mechanism, while all supported iron catalysts operate via a mechanism with formate species due to limited change of oxidation state of the iron cations. From the above considerations, we conclude that the water gas shift reaction on supported iron catalysts during the FTS proceeds on the magnetite phase (see before) by reaction of undissociated CO via a formate intermediate.

2.6 Selectivity of the Fischer-Tropsch Synthesis

2.6.1 Introduction

The products from the FTS on Co, Fe, and Ru show the following characteristics [22, 32, 59]:

1. The carbon-number distributions for hydrocarbons gives the highest concentration for C₁ and decreases monotonically for higher carbon numbers, though around C₃-C₄ often a local maximum is observed. Examples of these distributions for iron [88], cobalt [89] and ruthenium catalysts [32] are plotted in Figure 2.7.
2. Monomethyl-substituted hydrocarbons are present in moderate amounts while

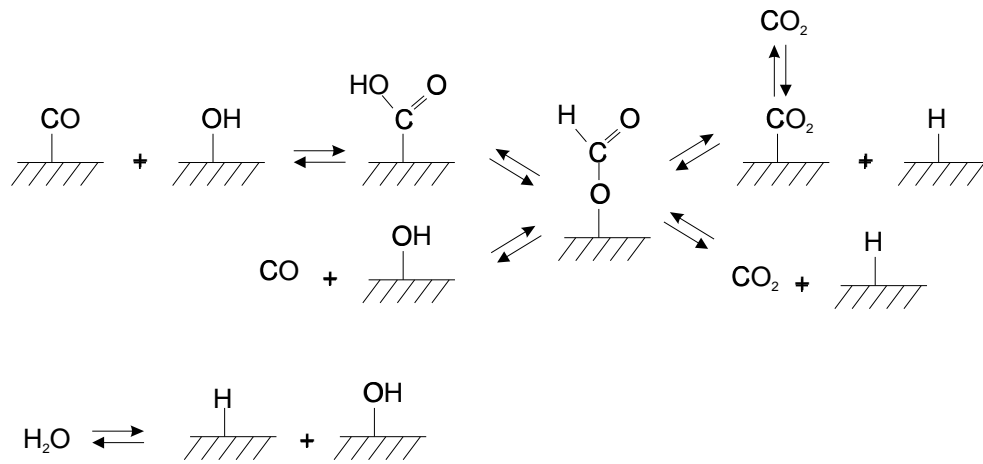


Figure 2.5 Water gas shift reaction mechanism via formate species (Lox and Froment [75]).

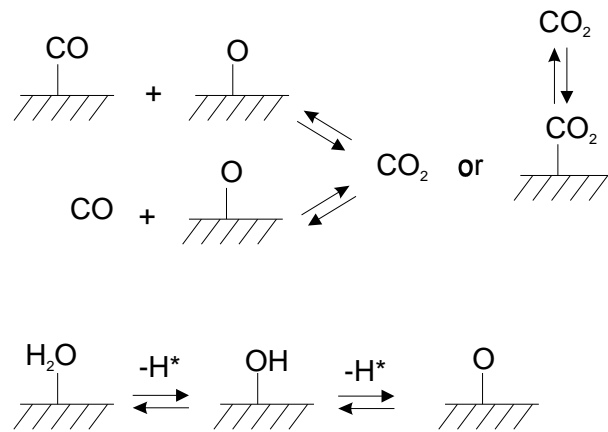


Figure 2.6 Water gas shift mechanism via direct oxidation (Lox and Froment [75]).

dimethyl products are present in significantly smaller amounts than monomethyl. None of these branched products contain quaternary carbon atoms on Co, Fe, and Ru [59].

3. Olefins from iron catalysts exceed 50% of the hydrocarbon products at low carbon numbers, and more than 60% of these are α -olefins. The ethene selectivity is low in comparison to propene. The olefin content decreases asymptotically to zero with increasing carbon number on Co, Ru, and Fe catalysts. For cobalt catalysts both the fraction of total olefins and α -olefins are smaller, and both decrease with carbon number (see Figure 2.8).
4. A change in chain growth parameter in the distribution is only observed for linear paraffins and not for olefins (see Figure 2.9).
5. Yields of alcohols are maximal at C₂ and decrease with carbon number. Low yields of methanol are probably the result of thermodynamic limitations (see Figure 2.9).

2.6.2 Influence of Process Conditions on the Selectivity

The process conditions as well as the catalyst influence the product selectivity. The effect of temperature, partial pressures of H₂ and CO, time on stream, composition and reduction of the catalyst will be discussed briefly. Table 2.3 shows the general influence of different parameters on the selectivity. The effect of the reactor temperature as well as the hydrogen to carbon monoxide ratio on the chain growth probability factor will be described in more detail in the next chapter. The influence of the synthesis gas conversion on the product selectivity is strongly related to the influence of the process conditions (see also paragraph on the influence of space velocity). Donnelly and Satterfield [90] and Dictor and Bell [51] reported that the chain growth factor was insensitive to conversion over a wide range.

Temperature

Increase of temperature results in a shift towards products with a lower carbon number on iron [51, 90], ruthenium [13], and cobalt [13] catalysts. Donnelly and Satterfield [90], Dictor and Bell [51], and Anderson [24] observed an increase of the olefin to

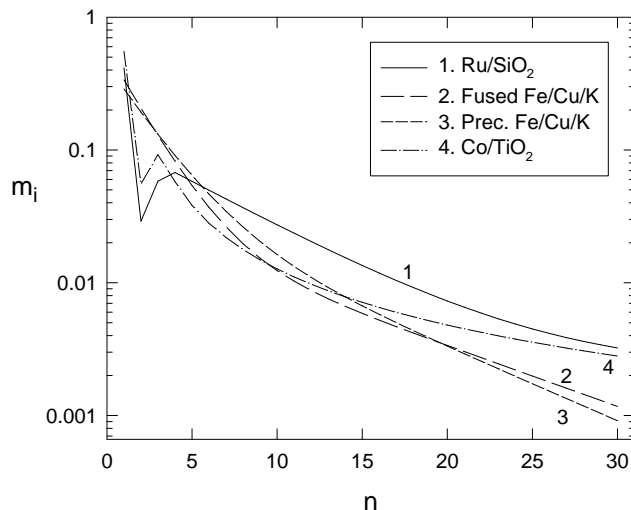


Figure 2.7 Total hydrocarbon selectivity on Co/TiO₂ ($T=473$ K, $H_2/CO=2.1$, $P=2.0$ MPa, data from Iglesia et al. [89]), Ru/SiO₂ ($T=485$ K, $H_2/CO=2$, $P=0.51$ MPa, data from Madon et al. [32]), and fused and precipitated Fe/Cu/K (data from Donnelly et al. [88]).

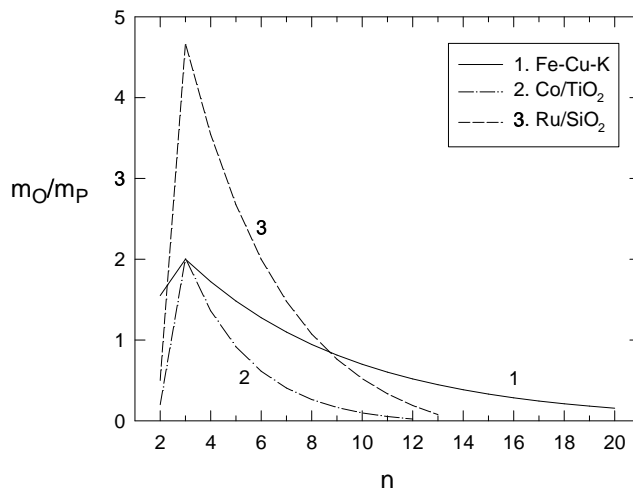


Figure 2.8 Olefin to paraffin ratio on Co/TiO₂ ($T=473$ K, $H_2/CO=2.1$, $P=2.0$ MPa, data from Iglesia et al. [89]), Ru/SiO₂ ($T=485$ K, $P=0.51$ MPa, $H_2/CO=2$, data from Madon et al. [32]), and precipitated Fe/Cu/K ($T=489$ K, $P=1.62$ MPa, $H_2/CO=2$, data from Madon et al. [32]).

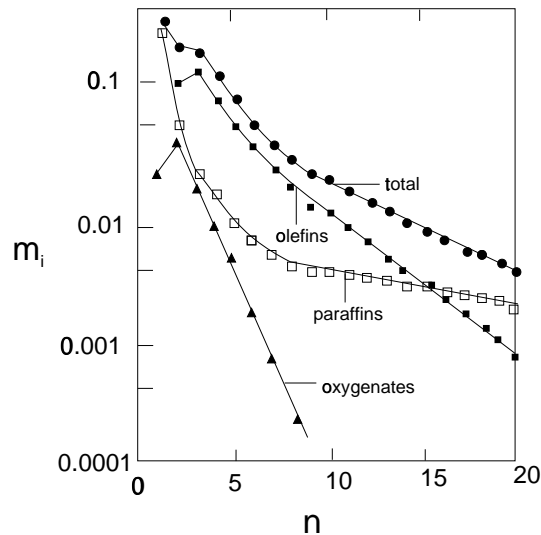


Figure 2.9 Overall product distribution on precipitated Fe/Cu/K catalyst, $H_2/CO = 0.7$, $T = 263$ °C, $P = 2.4$ MPa (from Donnelly and Satterfield [90]).

paraffin ratio on potassium-promoted precipitated iron catalysts with increasing temperature. However, Dictor and Bell [51] reported a decrease of the olefin selectivity with increasing temperature for unalkalized iron oxide powders.

Partial pressure of H_2 and CO

Most studies show that the product selectivity shifts to heavier products and to more oxygenates with increasing total pressure [13]. Increasing H_2/CO ratios in the reactor result in lighter hydrocarbons and a lower olefin content [51, 90]. Donnelly and Satterfield [90] observed a decrease of the olefin to paraffin ratio from 6 to 1 by increasing the H_2/CO ratio from 0.3 to 4. Dry [13] proved a relation between the methane selectivity and the factor $P_{H_2}^{1/2}/(P_{CO} + P_{CO_2})$ for alkaline-promoted fused iron catalysts in a fluidized bed reactor. This indicates that CO_2 appears to play an important role. Increasing CO_2 pressures result in a decrease of the methane selectivity.

Space velocity

The influence of the space velocity of the synthesis gas (residence time) on the selectivity has been investigated [91–93]. Increase of the olefin to paraffin ratio with increasing space velocity (thus a decrease of the conversion) was observed by Kuipers

Table 2.3 Selectivity control in Fischer-Tropsch synthesis by process conditions and catalyst modifications (from Röper [12]).

Parameter	Chain length	Chain branching	Olefin select.	Alcohol select.	Carbon deposition	Methane select.
Temperature	↓	↑	*	↓	↑	↑
Pressure	↑	↓	*	↑	*	↓
H ₂ /CO	↓	↑	↓	↓	↓	↑
Conversion	*	*	↓	↓	↑	↑
Space velocity	*	*	↑	↑	*	↓
Alkali content iron catalyst	↑	↓	↑	↑	↑	↓

Increase with increasing parameter: ↑

Decrease with increasing parameter: ↓

Complex relation: *

et al. [92] on a poly-crystalline cobalt foil (Goodfellow, 99.9 % purity, thickness 0.25 mm), Bukur et al. [91] on a commercial (Ruhchemie) supported iron catalyst (Fe/Cu/K/SiO₂), and Iglesia et al. [93] on TiO₂-supported ruthenium catalysts. Bukur et al. [91] measured no effect of the space velocity on the molecular weight of the hydrocarbons, while Iglesia et al. [93] observed an increase of the average molecular weight of the products with decrease of the space velocity. The selectivity to methane and olefins decreases with a decrease of the space velocity, while the selectivity towards paraffins remains unchanged (see Figure 2.10, obtained from Iglesia et al. [3]). The effect of the space velocity on the secondary reactions of olefins will be discussed more detailed below.

Time on stream

Deactivation of catalysts during the FTS may affect the activity and selectivity to hydrocarbon products. Increase of the selectivity to oxygenates is reported by Donnelly and Satterfield [90] after a period of 1300 hours time on stream with a precipitated

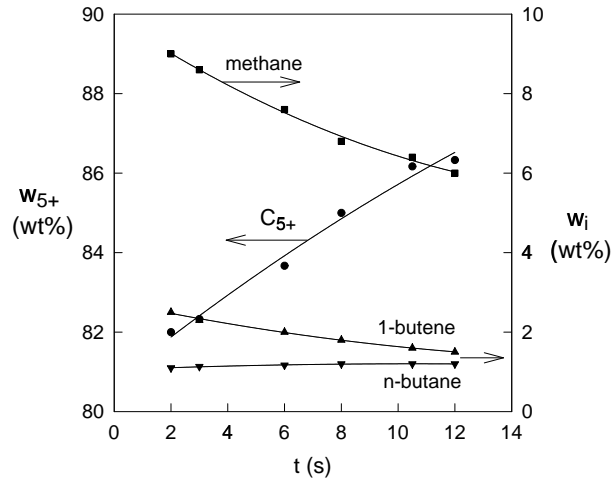


Figure 2.10 Residence time effect on methane, C₅₊, n-butane, and 1-butene selectivity on Co/TiO₂ (473 K, 2.0 MPa, H₂/CO= 2.1, 9.5-72 % CO conversion [3]).

promoted iron catalyst. An increase of the methane selectivity and low-molecular products is observed on iron catalysts [90, 91, 94]. It is known that selectivity changes with time can be caused by the formation of carbonaceous deposits on sites with potassium promoters [13]. Dry [13] showed that these deposits can be removed from a fused iron catalyst by hydrogen treatment at temperatures higher than 350 °C. Sintering of precipitated iron catalysts lead to reduction of the surface area from 300 m²/g for a fresh catalyst to about 90 m²/g for a used catalyst [13, 39, 44]. Agglomeration of initially small crystallites is enhanced by high water pressures.

Reduction of the catalyst

Bukur and co-workers studied the effect of pretreatment conditions of promoted iron catalysts on the hydrocarbon selectivity and activity [38, 42–45]. The hydrocarbon selectivity appeared to relate strongly on the pretreatment procedure. Figure 2.11 shows the effect of pretreatment on the hydrocarbon selectivity [38]. Low methane and C₂-C₄ selectivities and high diesel fuel and wax (C₁₂₊) selectivities were observed at pretreatments with CO and CO/H₂. The figure also shows the influence of reduction temperature with H₂ pretreatment. Reduction at 280 °C causes a shift to products with higher carbon number relative to 250 °C. Olefin selectivities are reported to decrease after hydrogen reduction in comparison to reduction with CO or synthesis gas.

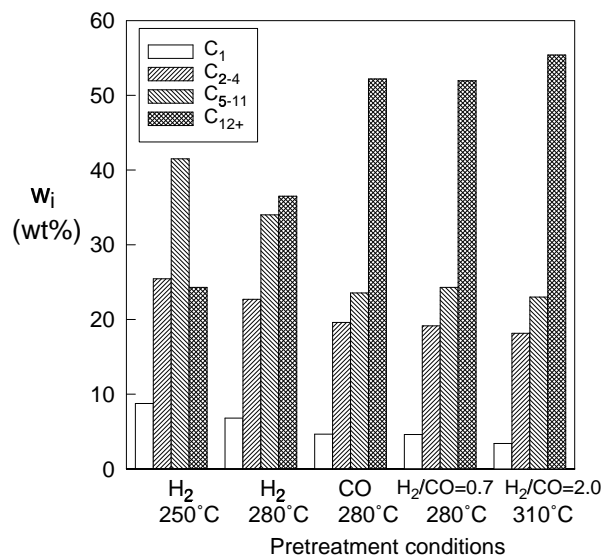


Figure 2.11 Effect of pretreatment conditions on the hydrocarbon selectivity at 250 °C, 1.48 MPa, $H_2/CO = 0.67$, $5.5 \cdot 10^{-4} \text{ Nm}^3 \text{ kg}_{cat}^{-1} \text{ s}^{-1}$ from Bukur et al. [38].

2.7 Product Selectivity Models

2.7.1 Anderson-Schulz-Flory Distribution

According to Anderson [24] the distribution for n-paraffins can be described by the Anderson-Schulz-Flory (ASF) equation:

$$m_n = (1 - \alpha)\alpha^{n-1}, \quad \frac{w_n}{n} = \frac{(1 - \alpha)^2}{\alpha} \alpha^n \quad (2.5)$$

where the growth probability factor α is independent of n and m_n is the mole fraction of a hydrocarbon with chain length n . α is defined by:

$$\alpha = \frac{R_p}{R_p + R_t} \quad (2.6)$$

where R_p and R_t are the rate of propagation and termination, respectively. α determines the total carbon number distribution of the FT products, see Figure 2.12. The range of α is dependent on the reaction conditions and catalyst type. Dry [95]

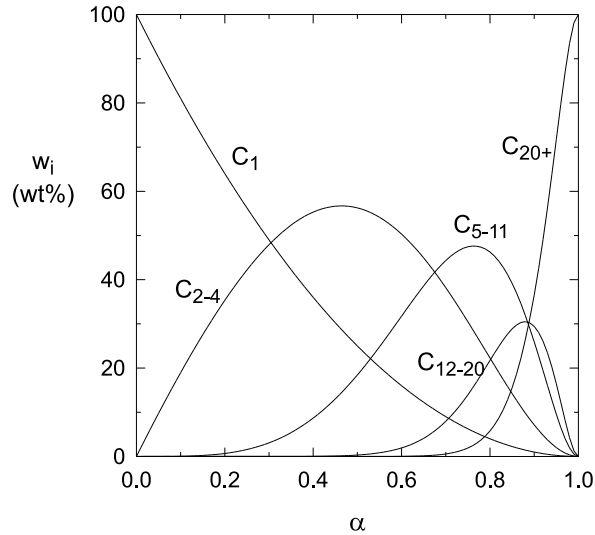


Figure 2.12 Hydrocarbon selectivity as function of the chain growth probability factor α , calculated with eq 2.5.

reported typical ranges of α on Ru, Co, and Fe of: 0.85-0.95, 0.70-0.80, and 0.50-0.70, respectively. The effect of the reactor temperature is shown in Figure 2.13. The chain growth probability, α , decreases with an increase of the reactor temperature [51, 57, 90, 95, 96]. A large variation in α is observed at temperatures higher than 280 °C [57, 95, 96]. Figure 2.14 shows that the values of α depend on the H_2/CO ratio in the reactor. It must be noted that reported values of α from Lox and Froment [57] and Dictor and Bell [51] were obtained with a constant partial pressure of H_2 and a varying CO pressure. The data of Dictor and Bell [51] on a Fe_2O_3/K catalyst depend very little on the H_2/CO ratio in contrast to other studies on Fe, Fe/Cu/K, and Ru catalysts. A decrease of α is observed at higher H_2/CO ratios [18, 51, 57, 90].

Figure 2.15a shows the growing mechanism for a constant α . The ASF equation does not distinguish between different product types. A semi-logarithmic plot of the mole fraction against carbon number yields the well-known Schulz-Flory diagram (fig. 2.16a), where the slope of the straight line yields the chain growth probability α .

In practice, a multicomponent product mixture is formed. Main products are paraffins and olefins. Dependent on process conditions and catalysts, oxygenated prod-

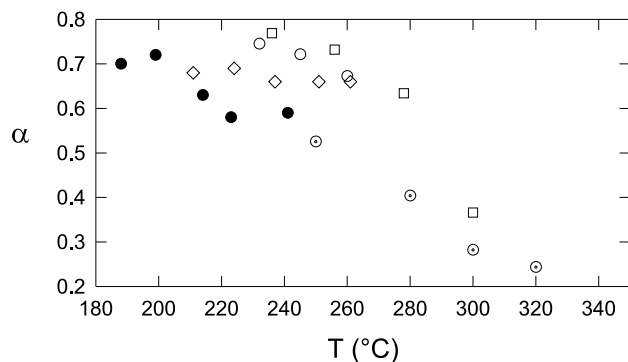


Figure 2.13 Chain growth probability factor as a function of temperature. \circ : Fe/Cu/K commercial Ruhrchemie catalyst, gas-slurry system, $(\text{H}_2/\text{CO})_{\text{feed}} = 0.7$, 2.72 MPa, $0.33 \cdot 10^{-4} \text{ Nm}^3 \text{ kg}^{-1} \text{ s}^{-1}$ [90]; \bullet : Fe₂O₃ catalyst, gas-solid system, $(\text{H}_2/\text{CO})_{\text{feed}} = 3$, 0.8 MPa [51]; \diamond : Fe₂O₃/K catalyst, gas-solid system, $(\text{H}_2/\text{CO})_{\text{feed}} = 3$, 0.8 MPa [51]; \square : Ru catalyst, gas-solid system, $(\text{H}_2/\text{CO})_{\text{feed}} = 3$, 0.8 MPa [95, 96]; \odot : Fe/Cu/K commercial Ruhrchemie catalyst, gas-solid system, $(\text{H}_2/\text{CO})_{\text{feed}} = 3$, 2.0 MPa, [57].

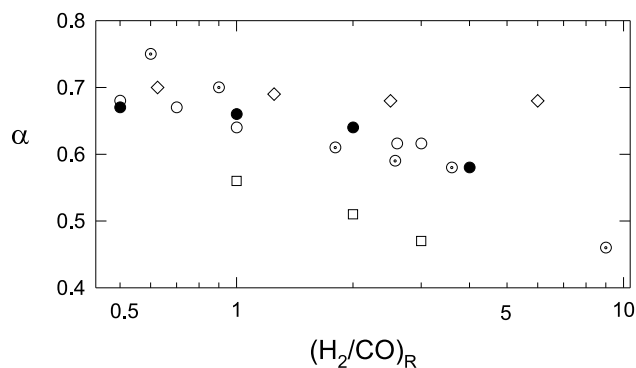


Figure 2.14 Chain growth probability factor as a function of hydrogen to carbon monoxide ratio. \circ : Fe/Cu/K catalyst, gas-slurry system, 1.48 MPa, 260 °C [90]; \bullet : Fe₂O₃ catalyst, 212 °C, gas-solid system, 0.5 - 1.2 MPa [51]; \diamond : Fe₂O₃/K catalyst, 240 °C, gas-solid system, 0.8 MPa, [51]; \square : Ru catalyst, 275 °C, gas-solid system, 0.8 MPa [18]; \odot : Fe/Cu/K commercial Ruhrchemie catalyst, gas-solid system, 250 °C, 1.0 - 2.5 MPa [57].

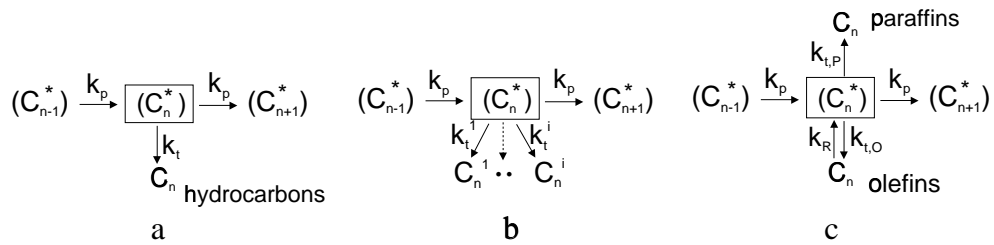


Figure 2.15 Reaction growth schemes Fischer-Tropsch synthesis from Glebov and Kliger [97]. a. Classical Anderson-Schulz-Flory model with one termination constant for all products. b. Multiple termination probabilities originating from a single intermediate. c. Termination to paraffins and olefins, whereas the latter can be re-adsorbed on the catalytic surface.

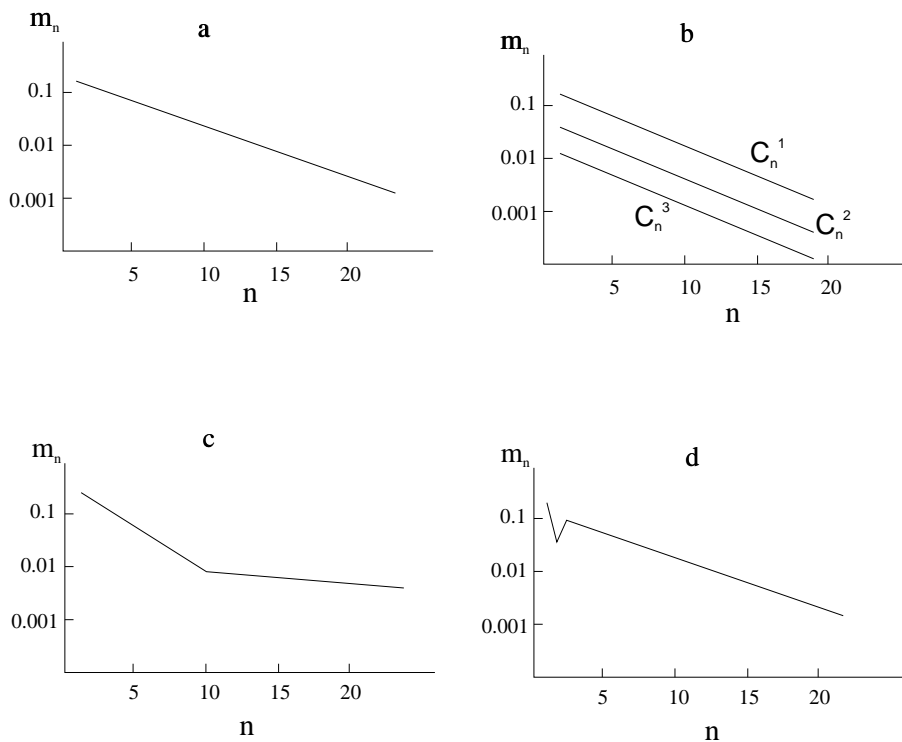


Figure 2.16 Schematic product distribution graphs of the Fischer-Tropsch hydrocarbons from Glebov and Kliger [97]. a. Classical Anderson-Schulz-Flory distribution of all products. b. Multiple termination probabilities yield several parallel straight distributions. c. Distribution graph with two different chain growth probabilities. d. Classical distribution with anomalies at C_1 and C_2 products.

ucts (for-example alcohols, aldehydes), branched hydrocarbons, and β -olefins can be formed as well. Glebov and Kliger [97] showed that the original Anderson-Schulz-Flory equation (eq 2.5) can be modified for the description of multicomponent FT products. Figure 2.15b shows the reaction scheme for this model, while the ASF diagram is presented in Figure 2.16b. Glebov and Kliger [97] assumed all products to be formed from the same intermediate. The mole fraction of a product, component type (paraffins, olefins, alcohols, and so forth) i with carbon number n can be calculated from:

$$\sum^i m_n^i = (1 - \alpha)\alpha^{n-1} \quad (2.7)$$

with α :

$$\alpha = \frac{k_p}{k_p + \sum_i k_t^i} \quad (2.8)$$

Because Glebov and Kliger [97] assume α to be the same for the different product types, a semi-logarithmic plot of the mole fractions against carbon number show straight parallel lines (see Figure 2.16b). However, most product distributions show lines with varying slopes (see Figure 2.7) and more comprehensive models are necessary to describe these deviations from the simplified ASF distribution.

2.7.2 Deviations from ASF Distribution

2.7.2.1 Introduction

Significant deviations from the Anderson-Schulz-Flory distribution are reported in literature. The deviations were sometimes assigned to analytical difficulties [98] and non-steady state conditions of the reactor system [99]. Both effects are still important potential sources of artifacts, however, novel analytical techniques usually rule out these explanations as the major source for the observed deviations. More fundamental explanations will be discussed below.

Relatively high yield of methane

Several mechanisms have been proposed to explain the experimentally observed (see Figure 2.7) relatively high methane contents. Wojciechowski [22] and Sarup and Wojciechowski [100] modeled the distribution of linear and branched paraffins with the

use of termination probabilities. This way, the excess methane yield was described with a separate parameter for the increased termination probability of C_1 precursors. The methane termination probability parameter appears to be between 5 to 20 times larger than the termination probability to paraffins [100].

Schulz et al. [68] assumed a different catalytic site for the methanation reaction for the description of excessive methane formation on a cobalt catalyst in a slurry reactor. The authors did not specify the exact nature of these sites.

Heat and mass transfer limitations are reported in literature as possible reasons for high methane yields. Dry [95] reported that mass transfer limitations will result in an increase of the thermodynamically favored products, that is methane. The existence of hot spots, due to high reaction heats, may result in a decrease of the chain growth parameter and a higher yield of methane [51, 95].

Secondary hydrogenolysis by demethylation which may occur on FT catalysts [92, 101]:



Kuipers et al. [92] modeled the hydrogenolysis of paraffins on Co catalysts. However, hydrogenolysis decreases strongly with increasing CO and H_2O pressures [93] and for reactor temperatures lower than 275 °C.

On common FT-catalysts it is difficult to point at one process responsible for the increased methane production under all circumstances. Under the absence of mass and heat transfer limitations and common H_2/CO ratios and reactor temperatures, the increased methane yield is most probably due to increased surface mobility of the methane precursor [22, 100]. Furthermore, several active sites present on most FT catalysts may result in a site which favors methane formation in comparison to chain growth [16, 68].

Anomalies of ethane and ethene (Figure 2.7)

In agreement with deviations for methane, Wojciechowski [22] used a higher surface mobility or reactivity of C_2 precursors to predict the increased production of ethane. Dependent on the reaction conditions, the termination probability to ethane is 0.5 to 2 times the value to paraffins [100].

Secondary reactions are often reported as the most possible reason for the anomalies of C_2 products: i) incorporation of ethene in growing chains [77, 78], ii) rapid readsorption of ethene [93, 101, 102]. iii) hydrogenolysis of ethene [101], and iv)

hydrogenation of ethene to ethane [92, 102, 103]. If ethene is used as monomer or building block during the FTS, an oscillating product distribution should be observed with maxima at even carbon numbers. However, such behavior has not been observed [97]. Therefore, it is not plausible that ethene is used as a building block. Secondary reactions will be discussed in more detail below. Readsorption of ethene will result in a decrease of the ethene yield and increase of ethane and higher hydrocarbons. Komaya and Bell [101] modeled the elementary reactions in FTS over a Ru/TiO₂ catalyst. Ethene could be hydrogenolyzed to methyl and methylene (monomer), with the readsorption constant of ethene approximately four orders of magnitude larger than higher olefins. Iglesia et al. [93] showed that ethene and propene obtain a higher reactivity and larger readsorption constant (factor 10) than other olefins. Secondary hydrogenation can be important over Co and Ru catalysts at high H₂/CO ratios in the reactor and a low H₂O pressure [102, 103].

Change in chain growth parameter α_n (Figure 2.7 and 2.9) and exponential decrease of the olefin to paraffin ratio (Figure 2.8)

At a carbon number of about 10, the slope of the semi-logarithmic mole fractions of hydrocarbons against carbon number increases. This phenomenon has been observed on iron [32, 51, 72, 104, 105], cobalt [22, 32, 100, 106], and ruthenium catalysts [32, 107, 108]. Suggestions for the increased chain growth parameter or two probabilities of chain growth are the occurrence of different catalytic sites [51, 109, 110] or the existence of different chain termination reactions [22, 100]. Several attempts to model the hydrocarbon distribution with two different values of α have been reported. However, analysis of detailed product distributions shows that the distribution of paraffins are curved instead of the linear distribution of olefins, [90, 91, 106]. Furthermore, the assumption of multiple catalytic sites cannot explain the decrease of the O/P ratio with increasing chain length, decreasing space velocity and increasing H₂/CO ratios in the reactor.

An example of the variation of the chain growth probability, α_n , with chain length is given in Figure 2.17 for several catalysts [32, 88, 93]. Except for carbon number two, the chain growth probability increases to a maximum value. The initial value of α is low for iron catalysts. The asymptotical value of α is between 0.85 and 0.92 in Figure 2.17.

It is widely considered that the occurrence of secondary reactions (hydrogenation, reinsertion, hydrogenolysis, isomerization) gives the most reasonable explanation

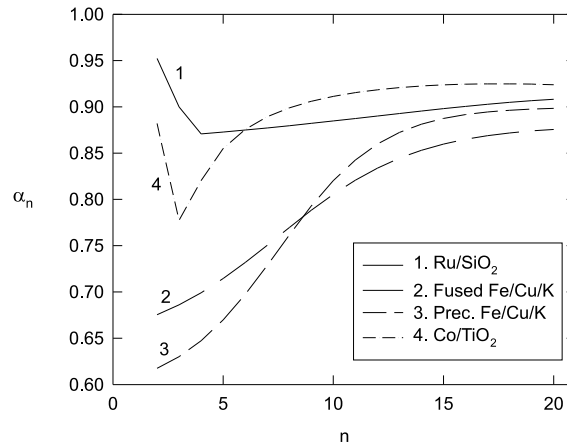


Figure 2.17 Chain growth probability factor (α_n) as function of chain length n , data from Madon et al. [32] (Ru/SiO₂, and Co/TiO₂) and Donnelly et al. [88] (fused and precipitated Fe/Cu/K).

tion for these deviations of the ASF distribution [78, 89, 92, 103, 111]. If a product is terminated by a reaction on an FT growth site to a paraffin or olefin it is called a primary product. Readsorption of olefins on growth sites may also lead to primary products whereas adsorption on other sites will produce secondary products due to hydrogenation or isomerization reactions. Secondary reactions as well as readsorption are directly influenced by space velocity. It is generally accepted that secondary reactions of olefins depend on the chain length, resulting in a decrease of the (O_n/P_n) ratio (see Figure 2.8) and increase of the growth probability α_n with chain length (see Figure 2.17). Three different proposals for chain length dependent processes in the FTS were given by Kuipers et al. [103]:

1. n -dependent diffusion limitations [89, 93, 112, 113]
2. n -dependent solubility in the FT-wax [64, 92, 103, 114, 115]
3. n -dependent physisorption [64, 92, 101, 103]

Therefore, the interfacial effects of reactive olefins near the gas-wax and wax-catalyst surfaces are important. Figure 2.18 (obtained from Kuipers et al. [103]) gives a schematic representation of the olefin concentration profile on a catalyst with a wax

layer. The concentration of the olefins dissolved in the wax phase ($x = d$) can be related to the vapor-phase concentration. Steady state production of olefins results in a concentration gradient over the wax film, which depends on the production rate of olefins, film thickness (d) and the diffusivity of product with chain length n (D_n). At the wax-catalyst interface ($x = -\delta$) n -dependent physisorption will take place. The chain length dependencies of physisorption, solubility, and diffusivities will be discussed below. First, we will consider possible secondary reactions that can take place on FT catalysts.

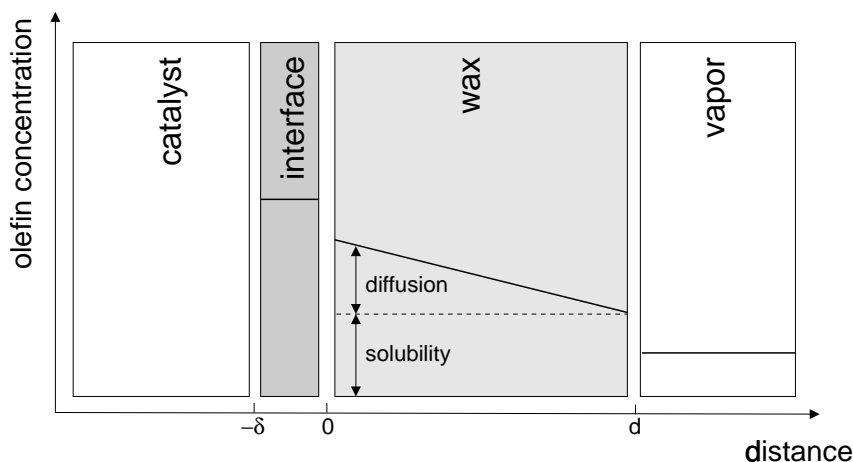


Figure 2.18 Schematic olefin concentration profile on a wax-coated catalyst (from Kuipers et al. [103]).

2.7.2.2 Secondary Reactions

In general, the extent of secondary reactions increases in the order: Fe, Ru, Co [93, 116, 117]. Because of the relatively low tendency of Fe for secondary reactions, high olefin yields can be obtained with alkali promoted iron catalysts. The extent of secondary reactions can also be observed from the dependency of the (O_n/P_n) ratio or olefin content on chain length, see Figure 2.8. On Fe-, Ru-, and Co-based catalysts an exponential decrease with chain length is observed [103]:

$$\frac{m_{O_n}}{m_{P_n}} \propto e^{-Cn} \quad (2.10)$$

Table 2.4 Carbon number dependencies on olefin to paraffin ratio ($n > 3$) according to $m_{O_n}/m_{P_n} \propto e^{-Cn}$.

Catalyst	C	T (K)	P (MPa)	H_2/CO	Conversion	Ref.
Uncoated cobalt foil	0.59	493	0.10	2		[103]
Wax-coated cobalt foil	0.24	493	0.10	2		[103]
Co/TiO ₂	0.49	473	2.0	2.1	X_{CO} 9.5 %	[3]
Co/TiO ₂	0.25	473	2.0	2.1	X_{CO} 72 %	[3]
Ru/TiO ₂	0.38	476	0.56	2.1	X_{CO} 5 %	[3]
Co/TiO ₂	0.19	476	0.56	2.1	X_{CO} 60 %	[3]
Fe/Cu/K	0.15	489	1.62	2		[32]

where m_{O_n} and m_{P_n} are the production rates or mole fractions of olefins and paraffins with carbon number n and C is a constant. See Table 2.4 for several literature values of C . The ratio of olefins to paraffins depends on catalyst type and structure, and reaction conditions. Iglesia et al. [3] observed a two-fold decrease of the exponential factor, C , for cobalt and ruthenium catalysts, when the residence time in a packed bed reactor decreased from 12 to 2 seconds corresponding to 9.5 % and 72 % CO conversion, respectively (see Table 2.4).

A direct indication of secondary reactions can be obtained from co-feeding of olefins (see Table 2.5 for a summary of references). In studies with carbon-labeled olefins, low concentrations can be used. Non-labeled co-fed olefins must have higher concentrations (5-10 mol %) to observe significant effects of possible secondary reactions. Different from co-fed olefins, an olefin produced on a growth site obtains physisorbed interactions with the catalyst surface, at least for some time. Therefore, reactivity of co-fed olefins may differ from the adsorbed olefin intermediate products. This makes interpretation of such experiments complicated and tricky.

In Table 2.5, the selectivity of secondary reactions: i) hydrogenation, ii) isomerization, iii) reinsertion, and iv) cracking or hydrogenolysis is calculated as the fraction of the co-fed olefin converted by a specific reaction relative to the total conversion of that olefin added.

Most olefin co-feeding studies were performed at atmospheric pressure. Under real FTS reaction conditions (high CO and H₂O pressures), secondary reactions can be inhibited. Almost all results of co-feeding of olefins show a significant amount of secondary hydrogenation [89, 102, 114, 116, 118–121]. Added olefins are hydrogenated to the corresponding paraffin.

Table 2.5 Summary of co-feeding studies olefins.

Reference	Component	Selectivity of co-fed olefins (%)			
		Hydr.	Reins.	Isom.	Cracking
Schulz et al. [116]	ethene	67	29	-	4
	propene	51	31	-	12
	1-hexadecene	79	6	-	14
Schulz et al. [116]	ethene	88	12	-	< 1
	propene	96	3	-	< 1
Schulz et al. [118]	1-octene	15	33	52	-
		20	30	50	-
		10	35	55	-
		5	35	60	-
Hanlon and Satterfield [119]	ethene	92	8	-	-
		94	6	-	-
	1-butene	31	67	2	-
Tau et al. [114]	ethene ³	64-73	18 (C ₅₊)	-	-
	1-pentene	-	-	-	-
	1-decene	43	-	57	-
Jordan and Bell [102] ²	ethene	95	4.2	-	-
		58	42	-	-
		50	50	-	-
		51	49	-	-
		38	62	-	-
Jordan and Bell [120] ²	propene	98	2.1	-	-
		92	8.1	-	-
		89	11	-	-
		90	10	-	-
		92	8.1	-	-
Jordan and Bell [121] ²	1-butene	62	4.2	34	-
		48	4.8	52	-
		38	5.2	57	-
		20	6.6	74	-
		21	6.6	72	-
Iglesia et al. [89]	ethene	50.5	49.5	-	-
		11.5	88.5	-	-
Iglesia et al. [89]	ethene	70.5	29.5	-	-
		22.0	78.0	-	-

Notation: Hydr.= Hydrogenation, Reins.= Reinsertion, Isom.= Isomerization

¹ First line gives general operating conditions. Following lines denotes the parameters changed

² Selectivity of reinsertion and hydrogenolysis are added in column Reins. The influence of CO pressure is presented only.

³ Selectivity of co-fed ethene to 1-propanol is about 9-18 %.

Table 2.5 Continued from previous page; operating conditions and catalyst applied.

Reference	Catalyst, Reactor	Operating conditions ¹
[116]	Co/ThO ₂ /K, fixed bed	$T = 185\text{-}190\text{ }^{\circ}\text{C}$, $H_2/\text{CO}=2$, $P = 0.1\text{ MPa}$
[116]	Iron, fixed bed	$T = 220\text{ }^{\circ}\text{C}$, $H_2/\text{CO}=2$, $P = 2.0\text{ MPa}$
[118]	Cobalt, slurry	$T = 180\text{ }^{\circ}\text{C}$, $P_{H_2}=0.5\text{ MPa}$, $P_{CO}=0.5\text{ MPa}$ $P_{CO}=1.0\text{ MPa}$ $P_{CO}=1.5\text{ MPa}$ $P_{CO}=2.0\text{ MPa}$
[119]	Fe/K, slurry	$T = 248\text{ }^{\circ}\text{C}$, $P_{CO}=0.08\text{ MPa}$, $P_{H_2}=0.23\text{ MPa}$ $P_{CO}=0.34\text{ MPa}$, $P_{H_2}=0.33\text{ MPa}$ $P_{CO}=0.071\text{ MPa}$, $P_{H_2}=0.27\text{ MPa}$
[114]	Iron, slurry	$T=260\text{ }^{\circ}\text{C}$, $P=0.70\text{ MPa}$, $H_2/\text{CO}=1.2$
[102] ²	Ruthenium, micro reactor	$T=493\text{ K}$, $P_{H_2}=0.04\text{ MPa}$, $P_{CO}=0.00\text{ MPa}$ $P_{CO}=0.02\text{ MPa}$ $P_{CO}=0.05\text{ MPa}$ $P_{CO}=0.10\text{ MPa}$ $P_{CO}=0.20\text{ MPa}$
[120] ²	Ruthenium, micro reactor	$T=493\text{ K}$, $P_{H_2}=0.03\text{ MPa}$, $P_{CO}=0.00\text{ MPa}$ $P_{CO}=0.01\text{ MPa}$ $P_{CO}=0.05\text{ MPa}$ $P_{CO}=0.10\text{ MPa}$ $P_{CO}=0.20\text{ MPa}$
[121] ²	Ruthenium, micro reactor	$T=493\text{ K}$, $P_{H_2}=0.04\text{ MPa}$, $P_{CO}=0.00\text{ MPa}$ $P_{CO}=0.02\text{ MPa}$ $P_{CO}=0.05\text{ MPa}$ $P_{CO}=0.12\text{ MPa}$ $P_{CO}=0.20\text{ MPa}$
[89]	Ruthenium, fixed bed	$T = 465\text{ K}$, $P = 2.07\text{ MPa}$, $H_2/\text{CO}=2$ 15 mol% H ₂ O
[89]	Cobalt, fixed bed	$T=465\text{ K}$, $P=2.07\text{ MPa}$, $H_2/\text{CO}=2$ 15 mol% H ₂ O

Secondary hydrogenation is inhibited by CO [89, 102, 118–121] suggesting competitive adsorption of olefins and CO for the same catalytic sites. For example, Hanlon and Satterfield [119] observed a decrease of the added ethene conversion from 59 % to 9.2% when the CO pressure was increased from 0.08 MPa to 0.34 MPa on a potassium-promoted fused magnetite catalyst.

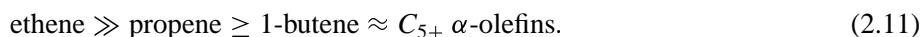
Schulz and Gökcebay [117] mentioned secondary hydrogenation as the most important process for the selectivity of the FT products on iron catalysts promoted with one of the transition metals Mn, Ti, Cr, Zr, or V. They concluded that secondary hydrogenation increases with carbon number due to increased adsorption strength. Ethene appeared very reactive for hydrogenation relative to propene and butene. Mechanistic conclusions from their results are that FT catalyst sites produce preferably olefins and to a smaller extent paraffins and that olefins can be adsorbed and hydrogenated on hydrogenation sites which are of another type than the Fischer-Tropsch growth sites. The authors stated that these hydrogenation sites can be inactivated in matrix catalysts, but no direct evidence on the nature of these sites was given.

No cracking or hydrogenolysis reactions of co-fed olefins (ethene, 1-butene, 1-hexene, 1-decene) was observed by Hanlon and Satterfield [119]. Also Dwyer and Somorjai [122] did not observe any cracking products from added ethene or propene. Schulz et al. [116] reported less than 1% cracking of added ethene or propene on an iron catalyst. However, cracking of added olefins was observed by Jordan and Bell [102, 120, 121] on a ruthenium catalyst at low total pressure. Cracking is promoted by high hydrogen pressures and high temperatures ($T > 300$ °C) and is strongly inhibited by CO pressure [13, 123] and H₂O pressures [113]. Therefore, we conclude that cracking is unimportant under normal FT synthesis conditions on Co and Fe catalysts [116, 124]. Under certain conditions, for example, high temperatures (hot spot) or a high degree of CO conversion (large catalyst pellets or low H₂/CO ratio), cracking of hydrocarbons may occur [89].

Insertion or readsorption of co-fed olefins was observed by many authors [89, 102, 114, 116, 118–121]. Insertion of olefins reverses the chain termination step to olefins and causes an increase of the chain growth probability and decrease of the olefin content of the products. Hanlon and Satterfield [119] observed an increased selectivity of C₃₊ hydrocarbons with addition of ethene on an Fe/K catalyst. Likewise, addition of 1-butene or 1-hexene resulted in a minor increase of the yield of high-molecular products, suggesting olefins to act as chain initiators. Addition of ethene and ethanol also resulted in a lower methane selectivity and increased olefin to paraffin ratio for C₃ and C₄ according to Hanlon and Satterfield [119]. Ethanol and ethene reduced the

hydrogenation of olefins on the catalyst. Addition of olefins and ethanol did not result in a change of the chain growth factor, α .

Iglesia et al. [89] showed the difference between co-fed ethene and *in situ* formed ethene on Ru and Co catalysts. Studies of the variation of bed residence time showed that 95% of the *in situ* formed ethene is consumed as chain initiator, while less than 5% appears as hydrogenated product. Co-feeding of ethene resulted in much higher selectivities towards ethane ($\approx 50\%$). They also found that the reactivity of added α -olefins in chain initiation reactions on Ru catalysts decreased in the order [93]:



Iglesia et al. [3] showed an increase of the olefin selectivity with increasing flow rate on a Co/TiO₂ catalyst, due to secondary reactions. The paraffin selectivity remained independent of the bed residence time for small paraffins, suggesting that hydrogenation is not the most important secondary reaction. The selectivity to higher molecular weight paraffins decreased with increasing flow rate due to accumulation and high surface concentration of smaller alkyl chains. The selectivity to methane increases, while the selectivity to C₅₊ products decreases with increasing space velocity (decreasing residence time) (see Figure 2.10). Therefore, they suggested that olefins are not consumed in secondary cracking or hydrogenation reactions. The same observations were reported by Komaya and Bell [101] for C₂ and C₄ products on a Ru/TiO₂ catalyst at 523 K. Iglesia et al. [3, 89], Madon et al. [32], and Komaya and Bell [101] concluded that readsorption of α -olefins and chain initiation is the most important secondary reaction for Ru, Co, and Fe resulting in deviations from the ASF distribution instead of hydrogenation or hydrogenolysis reactions.

Secondary hydrogenation is strongly inhibited by CO. Table 2.5 shows that the rates of isomerization and reinsertion are less inhibited by CO [89, 102, 113, 119, 120]. At high CO pressures, reinsertion of olefins becomes more important. Some data on the influence of H₂O on secondary reactions was reported by Iglesia et al. [89]. Addition of 15 mol% H₂O to synthesis gas ($T = 465$ K, $H_2/CO = 2$, $P = 2.07$ MPa) on a ruthenium and cobalt catalyst resulted in reinsertion of ethene to be the most important secondary reaction (see Table 2.5). Also, Hall et al. [125] observed a strong decrease of secondary hydrogenation of added ethene, with addition of 1.6 % water vapor on a Zr/Fe/Al₂O₃ catalyst.

Co-fed α -olefins can also isomerize to internal olefins (cis- and trans- β -olefins). Isomerization of 1-octene on a cobalt catalyst is favored by high CO pressure, while secondary olefin hydrogenation is inhibited [118].

From this discussion, we conclude that secondary reactions of olefins on iron, cobalt, and ruthenium catalysts are responsible for the observed selectivities. The most important secondary reaction is readsorption of olefins resulting in initiation of chain growth processes. Secondary hydrogenation of olefins is observed for added olefins but seems to be a minor reaction for *in situ* formed olefins. Moreover, high CO and H₂O pressures inhibit hydrogenation and cracking reactions in comparison to olefin readsorption. Secondary hydrogenation may occur under certain conditions, depending on the catalytic system and the process conditions (high H₂ pressures).

2.7.2.3 Chain Length Dependency of the Secondary Reactions

Secondary reactions of olefins depend on the chain length, resulting in a decrease of the (O_n/P_n) ratio and increase of the growth probability α_n with chain length. The influence of three possible chain length dependent processes are discussed below.

Diffusivity

Both diffusion limitation of reactants to the catalytic sites, and of products from the sites may occur. Slow removal of reactive products (for example, α -olefins) due to a decrease of diffusion coefficients with increasing chain length can influence the FTS reaction rate and selectivity. Measurements of these coefficients at FT operating conditions are scarce. Erkey et al. [126] measured the molecular diffusion coefficients of three paraffins (n-octane, n-dodecane and n-hexadecane) in FT-wax with an average chain length of C₂₈ (see Figure 2.19). Using the correlation proposed by Wilke-Chang [127] to predict the molecular diffusivity of hydrocarbons in a heavy paraffinic Fischer-Tropsch product (viscosity wax with $M = 300$ g/mol, at $T = 504$ K: $\mu = 0.6 \times 10^{-3}$ N s m⁻²) we found a chain length dependency of $D_n \propto n^{-0.5}$. The calculated values for the diffusivities of C₁ to C₁₇ are also plotted in Figure 2.19.

Iglesia and co-workers studied the influence of chain length dependent diffusion coefficients on secondary reactions [3, 32, 89, 93, 112, 113, 128]. They reported an empirical equation describing a strong influence of chain length on diffusivity for olefins and paraffins $D_n \propto e^{-0.3n}$, which was not verified by experimental data. This carbon number dependency is a factor of three higher than determined by Erkey et al. [126] and apparently is wrong (see Figure 2.19).

Iglesia et al. [89] modeled diffusion-limited removal of olefins and diffusion limitation of CO on a cobalt and ruthenium catalyst in a packed bed reactor. No reactant depletion was observed at particle diameters smaller than 0.2 mm. However, selectivity changes due to product limitations are still present. They concluded that olefin

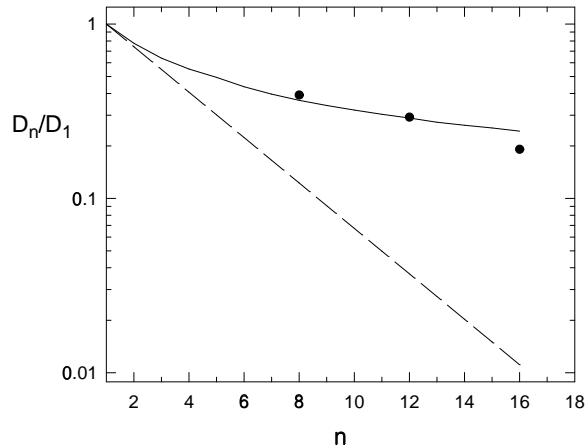


Figure 2.19 Diffusivities of n-paraffins in FT-wax; • experimental data at $T = 504$ K from Erkey et al. [126], — Wilke-Chang correlation at $T = 540$ K, - - - correlation Iglesia et al. [89].

readsorption and chain initiation is the most important secondary reaction. Their transport model includes the rate of diffusion-enhanced olefin readsorption and its effect on detailed product distributions. However, Iglesia et al. [89] were not able to explain the strong exponential decrease of the (O_n/P_n) ratio on their catalyst ($C = 0.19-0.49$ in eq 2.10) with diffusion effects only. Especially, when the more realistic lower dependency of the diffusion coefficients with chain length, as observed by Erkey et al. [126] (see Figure 2.19), is used their model underestimates the olefin to paraffin ratio.

Furthermore, Kuipers et al. [103] measured the (O_n/P_n) ratio for the FTS on a polycrystalline cobalt-foil (without diffusion limitations) and still obtained an exponential decrease of this ratio with chain length. So, we can conclude that the chain length dependency of the olefin to paraffin ratio can hardly be due to diffusion effects only, but that preferential physisorption and increase of the solubility with chain length influences the selectivity as well.

Solubility

Values of the vapor-liquid equilibria (VLE) of reactants and products in high-boiling solvents are necessary for an optimal design of gas-slurry processes and kinetic modeling. Experimental data of solubilities at high pressures are scarce in open literature.

Solubilities are often expressed in terms of Henry's constants of a solute in a solvent:

$$H_{1,2} = \lim_{x_1 \rightarrow 0} \frac{f_1}{x_1} \quad (2.12)$$

where f_1 is the fugacity of the solute and x_1 is its mole fraction in the liquid phase.

Breman et al. [129] studied 1533 VLE for 60 binary systems of the reactants: carbon monoxide, hydrogen and products: water, carbon dioxide, C₁-C₆ alcohols and C₂-C₆ paraffins in the solvents tetraethylene glycol, hexadecane, octacosane, 1-hexadecanol, and phenantrene. Experimental conditions were varied from 293 to 553 K and from 0.06 to 5.5 MPa. Measurements of the VLE of reactants and products in octacosane closely resemble FTS operating conditions.

Chappelow and Prausnitz [130] measured the solubilities of n-paraffinic gases C₁-C₄ in high-boiling hydrocarbon solvents at low-pressures in an equilibrium cell. A gas-chromatographic technique was used by Donohue et al. [131] to measure the solubilities of n-paraffins (C₅-C₉) in solvents. Figure 2.20 shows the logarithm of the Henry's constant as a function of the carbon number of the solute in eicosane (C₂₀). Henry's coefficients obtained from Donohue et al. [131] are interpolated to $T = 325$ K. At this temperature, the Henry's coefficients appear to decrease exponentially with carbon number, indicating an increase of the solubility with carbon number. VLE measured by Breman et al. [129] contain data for ethane, propane, pentane, and hexane in octacosane (C₂₈). Henry's constants were determined between $T = 423 - 518$ K. Figure 2.20 also shows these constants as a function of carbon number at three temperatures. As expected, the solubility decreases with increase in temperature for all components. The available VLE data show that carbon number dependency decreases with increasing temperature (Figure 2.20).

A rough estimate of the ideal solubility can be found using Raoult's law [127] and vapor pressure data of hydrocarbons. Caldwell and van Vuuren [132] found that the vapor pressures of n-paraffins C₉ to C₂₉ ($T = 452-553$ K) can be described with the following equation:

$$P_n = P_0 \beta^n \quad (2.13)$$

where P_n is the vapor pressure of a paraffin with a chain length n and $P_0 = 17.8382$ MPa and $\beta = \exp[-427.218(1/T - 1.029807 \times 10^{-3})]$. The vapor pressure (and solubility), calculated with eq 2.13, as function of temperature is also plotted in Figure 2.20. It can be seen that the exponential chain length dependency of the vapor pressure ($\exp\beta$) is in good agreement with the experimental VLE data [129] although these experimental values were obtained with short-chain hydrocarbons ($n < 6$).

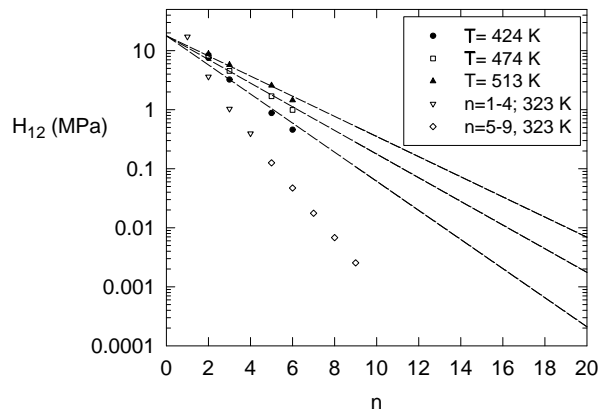


Figure 2.20 Henry's constants of n-paraffins in eicosane at $T = 323\text{K}$ (Chappelow and Prausnitz [130] and Donohue et al. [131]) and in octacosane at $T = 424, 474,$ and 513K (Breman et al. [129]), dotted lines are calculated with the vapor pressure correlation for $\text{C}_9\text{-C}_{29}$ (Caldwell and van Vuuren [132]).

Much controversy exists on the effect of the solubility on the reaction rate of secondary reactions. Schulz et al. [74], Tau et al. [114], Zimmerman et al. [115] and Kuipers et al. [103] stated that a greater solubility of larger hydrocarbons results in an increase of the residence time and higher readsorption rates. Madon and Iglesia [112] and more recently Iglesia [133] rejected the arguments of solubility stating that the presence of a liquid does not influence chemical potentials. They concluded that the presence of a liquid phase in absence of transport limitations, cannot increase the rate of secondary reactions. They accounted the deviations from the ASF distribution completely to diffusion-enhanced readsorption of α -olefins. However, as seen above, this is not convincing.

According to our opinion, indeed an "ideal" liquid does not influence the reaction rate. Here, "ideal" means an inert, non-adsorbing, non-polar liquid with all activity coefficients equal to unity whilst no mass transfer effects are apparent. This follows from transition-state theory, where the chemical potential (fugacity at standard state) of any component is the same in the gaseous, liquid, and adsorbed state.

However, in real cases the liquid may affect the reaction rate. Eckert [134] considered a bimolecular reaction between two gases on a solid catalyst in presence of a liquid-phase. A reaction, $A + B \rightarrow \text{product}$, in a system with thermodynamic non-

idealities, can be described with the Brønsted-Bjerrum equation:

$$k = \frac{k_0 \gamma_A \gamma_B}{\gamma_I} \quad (2.14)$$

where k_0 is the rate constant in an ideal reference state. The presence of a liquid may alter the activity coefficients of the reactants on the surface, γ_A or γ_B , and of the activated complex γ_I . To evaluate the effect of a liquid, Eckert [134] used regular solutions theory for dilute, non-polar solutions

$$RT \ln \gamma_A = V_2(\delta_A - \delta_1)^2 \quad (2.15)$$

Here subscripts A and 1 refer to the solute A and solvent, respectively. δ is the solubility parameter. Substitution into eq 2.14 gives

$$\ln k = \ln k_0 + \frac{V_A}{RT}(\delta_1 - \delta_A)^2 + \frac{V_B}{RT}(\delta_1 - \delta_B)^2 - \frac{V_I}{RT}(\delta_1 - \delta_I)^2 \quad (2.16)$$

There are two possible assumptions to evaluate the non-ideality of the system. The first assumption is that all surface species are in equilibrium with the activities in the bulk, which is given in the foregoing equation. The other possibility is that the reactants on the surface are in equilibrium with the bulk, while the activated complex is not. Then the activity of the complex might be independent of the liquid and its activity coefficients are constant. If so, we have [134]:

$$\ln k = \ln \left(\frac{k_0}{\gamma_I} \right) + \frac{V_A}{RT}(\delta_1 - \delta_A)^2 + \frac{V_B}{RT}(\delta_1 - \delta_B)^2 \quad (2.17)$$

Eckert [134] evaluated hydrogenation experiments and concluded that the second assumption is valid for heterogeneous reactions. If so, the rate of reaction is proportional to the concentration of the activated complex instead of its thermodynamic activity. eq 2.17 shows that the reaction rate is enhanced, compared to the rate in the ideal liquid or gas phase, if the solvent is similar to the reactants (high solubility) and vice versa.

Moreover, comparison of the increase of the transport rates of olefins with varying carbon number in analogy with eq 2.1 [3] shows:

$$\gamma_n = \frac{D_{O_n}/H_{O_n}}{D_{O_{n-1}}/H_{O_{n-1}}} \approx \frac{H_{O_{n-1}}}{H_{O_n}} \quad (2.18)$$

since solubility effects overrule the weak chain-length dependency of the diffusivity.

This discussion has a great impact on the rate of readsorption of olefins during the FTS. The solubility increases exponentially with carbon number. Consequently, the rate of readsorption of long-chain olefins is enhanced in comparison to smaller olefins (according to eq 2.17), because actual concentrations are necessary instead of activities. Kuipers et al. [103] also stated that the olefin concentration at the catalyst interface has to be taken into account for the readsorption rate, which is not in equilibrium with the chemisorbed phase at the catalyst surface.

Physisorption

Physisorption of hydrocarbons may change the extent of secondary reactions. The physisorbed state is a transition state between the chemisorbed and the vapor phase and is governed by Van der Waals attraction and repulsion forces [15]. These forces depend on the structure of the adsorbates and the adsorbents. Here, we focus on the influence of carbon number on the adsorption of hydrocarbons on adsorbents. Measurements of gas-solid adsorption of hydrocarbons on several adsorbents are reported in literature [135–137]. The logarithm of the adsorption equilibrium constant increases linearly with carbon number. Komaya and Bell [101] used a chain-length dependent Henry constant at 523 K for the readsorption of olefins on a ruthenium catalyst under FT conditions: $H_n \propto e^{1.2n}$.

Keldsen et al. [138] measured the enthalpies of adsorption of linear paraffins with different chain length on a clay. The enthalpy of adsorption and the strength of the physisorbed bond appeared to increase with carbon number. We used a linear regression of their experimental enthalpies of adsorption as a function of carbon number, n :

$$-\Delta H_{ad} = 12.6 + 8.7n \quad (\text{kJ/mol}) \quad (2.19)$$

This relation suggests a simple group-additive quantity for linear paraffins, as also mentioned by Ruthven [139] (originally from Kiselev and Shcherbakova [140]) for a homologous series of paraffins on silica:

$$-\Delta H_{ad} = 12.5 + 4.0n \quad (\text{kJ/mol}) \quad (2.20)$$

Ruthven [139] also reviewed a group contribution method for estimating the heat of adsorption on 5 Å zeolites. The presence of double bonds appears to give rise to a higher dipole moment for the adsorbed species resulting in a higher increment of the heat of adsorption.

Xia and Landman [141] reported the results of molecular dynamic calculations of the preferential adsorption of n-hexadecane and n-hexane on a Au(001) surface.

Starting with an equimolar mixture of the components resulted in a layer at the interface with high concentration of long-chain molecules due to a better packing and intermolecular ordering at steady state.

Rofer-De Poorter [7] schematically described the FT catalyst surface as a very active layer at the metal surface containing C,O, H atoms, adsorbed CO and growing alkyl chains; further away from the surface are physisorbed CO, H₂, and desorbing products. Reaction intermediates are also present in the surface layer. From the above, we conclude that the adsorption equilibrium constants increase exponentially with chain length resulting in an increase of the contact time and an enrichment of long-chain hydrocarbons at the catalyst surface.

Komaya and Bell [101] and Pichler and Schulz [124] reported the effect of stronger physisorption for larger olefins to predict the increase of the chain growth probabilities with chain length. Komaya and Bell [101] developed a model where desorption of chemisorbed products proceeds through a physisorbed layer. Transient kinetic experiments with labeled carbon were performed in a packed bed reactor at 523 K. Equations for labeled carbon in the monomer pool, the pool of alkyl chains, and the pool of physisorbed hydrocarbons were optimized to experimental data. The fractional coverage of products in the physisorbed layer, θ_n , was calculated with the chain length dependent Henry constant. The authors stated that for olefins with $n > 8$, readsorption becomes more important than removal of physisorbed hydrocarbons from the reactor.

We conclude from this discussion that the solubility and physisorption are crucial for the reaction rates in the FTS. Secondary reactions of olefins can be influenced by the chain length dependent solubility in a liquid and by preferential physisorption.

2.7.3 Comprehensive Product Distribution Models

The distribution of paraffins was firstly described by Herrington [142]. His approach used individual chain termination probabilities for each chain size, β_n ,

$$\beta_n = \frac{R_{t,n}}{R_{p,n}} = m_n / \sum_{i=n+1}^{\infty} m_i \quad (2.21)$$

The chain growth probability, α_n can easily be calculated from eq 2.21:

$$\alpha_n = 1/(1 + \beta_n) = \sum_{i=n+1}^{\infty} m_i / \sum_{i=n}^{\infty} m_i \quad (2.22)$$

Iglesia et al. [93] used the same approach and expressed the total termination probability ($\beta_{t,n}$) as a combination of individual terminations:

$$\beta_{t,n} = \beta_{t,O} + \beta_{t,P} - \beta_{R,n} \quad (2.23)$$

where $\beta_{t,O}$ and $\beta_{t,P}$ is the termination probability to olefins and paraffins, respectively. We showed above that Iglesia et al. [93] stated incorrectly that the readsorption of olefins ($\beta_{R,n}$) is chain length dependent due to diffusion effects alone. The chain termination probability in eq 2.23 and the O/P ratio decrease with increasing carbon number until all olefins are consumed. The asymptotical value of $\beta_{t,n}$ or α_n corresponds to propagation and termination to paraffins alone. However, the increased readsorption rate is not completely due to diffusion effects, increased solubility and physisorption with increasing carbon number should be taken into account.

Kuipers et al. [103] modeled the experimental data of the olefin to paraffin ratio synthesized on wax-coated and uncoated cobalt foils at atmospheric pressures and a temperature of 493 K. Mass balances over the film layer were given to obtain the concentration of olefins in the physisorbed layer, wax phase and vapor phase. According to the authors, the concentration of the olefins dissolved in the wax phase ($x = d$, see Figure 2.18) can be related to the vapor-phase concentration by Raoult's law and is proportional to $(C_{n,vap}^s V_{n,wax}^m)^{-1}$, where $C_{n,vap}^s$ is the saturated vapor phase concentration and $V_{n,wax}^m$ is the molar volume of hydrocarbons with carbon number n . They used the following exponential increase for the solubility, $1/C_{n,vap}^s \propto e^{(0.55 \pm 0.10)n}$ at 493 K and a linear increase of $V_{n,wax}^m$ with n . Above, we described experimental and calculated data on the solubility of hydrocarbons. At a temperature of 493 K, the correlation of Caldwell and van Vuuren [132] shows that the solubility is proportional to $e^{0.43n}$. Kuipers et al. [103] described the increase of physisorption strength of hydrocarbons at the catalyst interface with increasing chain length by $e^{n\Delta G_{1phys}/RT}$. On uncoated foils without transport limitations (diffusion), their model predicts that $m_{O_n}/m_{P_n} \propto n \exp[-(\Delta G_{1phys}/RT + 0.55)n]$. Kuipers et al. [103] measured a carbon number dependency of $C = 0.55$ according to eq 2.10 on an uncoated cobalt foil. It can easily be seen that the authors stated incorrectly that the preferential physisorption is $\propto e^{0.2n}$, because in that case the exponent in eq 2.10 would be $C = 0.75$. This dependency is not the same as their experimental determined value of $C = 0.55$.

For small olefins and a wax-layer on the cobalt foil a much weaker chain length dependency was observed by Kuipers et al. [103] (see Table 2.4). Their model predicts the following chain length dependency on the O_n/P_n ratio when diffusion limitations

($D_n \propto n^{-0.6}$) are dominant:

$$O_n/P_n \propto e^{-n\Delta G_{1 \text{ phys}}/RT} D_n \propto e^{(-0.2 \pm 0.1)n} n^{-0.6} \quad (2.24)$$

In a more recent article, Kuipers et al. [92] concluded that the main secondary reaction on the same cobalt foil is secondary hydrogenation of primary α -olefins. With 50 nm Co particles on a SiO₂ wafer, Kuipers et al. [92] reported reinsertion of α -olefins as the most important secondary reaction.

We can conclude that any comprehensive product distribution model for the selectivity to olefins and paraffins should incorporate readsorption of olefins and the effect of physisorption and solubility on the actual olefin concentration at the catalyst surface. These models have to predict the selectivity to olefins and paraffins on porous FT catalysts at industrial conditions.

2.8 Kinetics

2.8.1 Introduction

The major problem in describing the FT reaction kinetics is the complexity of its reaction mechanism and the large number of species involved. As discussed above, the mechanistic proposals for the FTS used a variety of surface species and different elementary reaction steps, resulting in empirical power law expressions for the kinetics [8, 143]. However, also Langmuir-Hinshelwood-Hougen-Watson (LHHW) and Eley-Rideal type of rate equations have been applied, based on a reaction mechanism for the hydrocarbon forming reactions [22, 75, 144]. In most cases the rate determining step was assumed to be the formation of the monomer [22, 73, 145, 146]. These rate expressions for the consumption of synthesis gas mainly differ in the nature of the monomer and of the adsorption of CO, H₂ and products (H₂O and CO₂) on the catalyst surface.

Kellner and Bell [147] and Takoudis [148] modeled the production rates of hydrocarbons without assumptions on a rate determining step. However, several assumptions were introduced to solve the resulting set of equations. Lox and Froment [75] and Hovi et al. [76] examined whether the incorporation of the monomer or the termination reaction to hydrocarbons are rate limiting. Ideally, the development of kinetic rate expressions should be based on each possible rate determining process in a well-defined mechanistic scheme in the hydrocarbon-forming reactions.

Kinetic studies of the consumption of synthesis gas on iron and cobalt catalysts will be discussed in more detail, as well as kinetic studies of the WGS on iron cata-

lysts. Finally, kinetic models which describe the rate of formation of products will be reviewed.

2.8.2 Overall Conversion of Synthesis Gas

Kinetic equations can be based on the overall synthesis gas consumption ($-R_{H_2+CO} = -R_{CO} - R_{H_2}$), which is independent of the WGS equilibrium, or based on CO consumption to hydrocarbon products ($R_{FT} = -R_{CO} - R_{WGS}$). The rate of synthesis gas consumption only differs from the FT reaction rate by reaction stoichiometry, $-R_{H_2+CO} = (2 + m/2n)R_{FT}$. Reaction rate equations use to be expressed in either liquid phase concentrations or, preferably, in gas phase partial pressures. Since Henry's constants are temperature dependent, activation energies will also be influenced by the use of either liquid or gas concentration terms [56, 145].

The kinetic rate equations presented for the synthesis gas consumption [24, 56, 72, 149] do not present a uniform picture. Table 2.7 gives an overview. A few, mainly older, kinetic studies are performed in fixed-bed reactors at high synthesis gas conversions. Integral kinetic studies of the FTS in plug flow reactors (PFR) are not easily interpreted because the partial pressure of CO and H₂ as well as the composition of the catalyst vary along the axis of the reactor [22]. Extra complications occur due to possible heat and mass transfer effects, secondary reactions, and product inhibition. In general, catalyst composition as well as reaction conditions determine the numerical values of the intrinsic rate parameters. Moreover, the rate equations are not identical, thus k can be composed of different combinations of kinetic and adsorption constants. There is experimental evidence that the Fischer-Tropsch activity of Fe and Co depends on the preparation method, metal loading of the catalyst, and catalyst support [103, 150–154].

2.8.2.1 Iron Based Catalysts

Reviews of kinetic equations for iron catalysts are given by Huff and Satterfield [72] and Zimmerman and Bukur [56]. Kinetic studies of the FTS on iron catalysts are tabulated in Table 2.7.

In general for iron catalysts, the FT reaction rate increases with H₂ partial pressure and decreases with partial pressure of water. Satterfield et al. [164] observed a reversible decrease of the catalyst activity by addition of 12 and 27 mol% water to the feed gas. However, after addition of 42 mol% water the catalyst did not regain its initial activity.

Table 2.6 Reaction rate equations overall synthesis gas consumption rate, proposed in the studies mentioned in Table 2.7.

	Kinetic expression	References
(a)	$k P_{H_2}$	[24, 56, 155]
(b)	$k P_{H_2}^a P_{CO}^b$	[143]
(c)	$\frac{k P_{H_2} P_{CO}}{P_{CO} + a P_{H_2O}}$	[24, 56, 156–158]
(d)	$\frac{k P_{H_2}^2 P_{CO}}{P_{CO} P_{H_2} + a P_{H_2O}}$	[72, 158–160]
(e)	$\frac{k P_{H_2}^2 P_{CO}}{1 + a P_{CO} P_{H_2}^2}$	[24]
(f)	$\frac{k P_{H_2} P_{CO}}{P_{CO} + a P_{CO_2}}$	[56, 145, 159, 161]
(g)	$\frac{k P_{H_2} P_{CO}}{P_{CO} + a P_{H_2O} + b P_{CO_2}}$	[56, 145, 161]
(h)	$\frac{k P_{CO}^{1/2} P_{H_2}^{1/2}}{(1 + a P_{CO}^{1/2} + b P_{H_2}^{1/2})^2}$	[73]
(i)	$\frac{k P_{CO} P_{H_2}^{1/2}}{(1 + a P_{CO} + b P_{H_2}^{1/2})^2}$	[22]
(j)	$\frac{k P_{CO} P_{H_2}}{(1 + b P_{CO})^2}$	[144, 162, 163]

Table 2.7 Kinetic studies for the FTS on cobalt and iron catalysts.

Catalyst	Reactor	Operating conditions			Kinetic expression	E_A (k) (kJ/mol)	$-\Delta H_{ad}$ (a) (kJ/mol)	Ref.
		T, °C	P, MPa	H ₂ /CO _{feed}				
Fused Fe/K	Fixed bed	225-265	1.0-1.8	1.2-7.2	(a)	71	-	[155]
Prec. Fe/K/Cu	Slurry	235-265	1.5-3.0	0.6-1.0	(a)	86	-	[56] ¹
Prec. Fe/K/Cu	Slurry	250	1.5-3.0	0.6-1.0	(c)	-	-	[56]
Iron	fixed bed	?	?	?	(c)	-	-	[24]
Fused Fe/K	Gradientless, fixed bed	250-315	2.0	2.0	(c)	85	8.8	[157]
Fused iron	slurry	232-263	0.4-1.5	0.5-1.8	(d)	83	100	[72]
Prec. iron	slurry	220-260	1.0	0.5-0.6	(f)	103	0	[161] ²
Prec. iron	slurry	220-280	0.5-1.2	0.5-3.5	(c)	89	-	[145] ²
Fused iron	slurry	210-270	0.5-5.5	0.5-3.5	(f)	81	-	[145] ²
Co/Kieselguhr	Berty	190	0.2-1.5	0.5-8.3	(h,i)	-	-	[22, 73] ³
Co/MgO/SiO ₂	slurry	220-240	1.5-3.5	1.5-3.5	(j)	-	-	[163]
Co/Zr/SiO ₂	slurry	220-280	2.1	0.5-2.0	(d)	97	-	[160]
Prec. Fe/Cu/K	Gradientless	230-264	1.0-2.6	1.1-2.4	(d)	56	-62	[158]
Prec. Fe/Cu/K	Gradientless	230-264	1.0-2.6	1.1-2.4	(c)	56	-60	[158]
Prec. iron	slurry	220-260	-	0.5-0.8	(f)	105	0	[159] ²
Prec. iron	slurry	220-260	-	0.8-2.0	(c)	80	55	[159] ²
Prec. iron	Fixed bed	250-350	0.6-2.1	3.0-6.0	-	-	-	[75] ⁴

¹No temperature dependence of optimal rate equations (c) (Fe/Cu/K) and (g) (100 Fe/0.3 Cu/0.2 K) is given

²Rate equations expressed in liquid concentrations

³Only measurements at 190 °C are reported. Conversions and space velocities are not mentioned by Sarup and Wojciechowski [73]

⁴Kinetic expressions not mentioned in Table 2.6

The mechanistic kinetic rate expressions for iron catalysts are all based on the formation of the monomer species as the rate determining step in the consumption of synthesis gas. Several theories for the formation of the monomer species are postulated in literature: i) **Carbide mechanism**: here CO dissociates on the surface and the adsorbed carbon hydrogenates to a methylene species [18]. ii) **Combined enol/carbide mechanism**: here a methylene species is formed by hydrogenation of the hydroxylated enolic CO-H₂ complex [11]. Both mechanisms were discussed above (see Chapter 2.5). Huff and Satterfield [72] derived and reviewed kinetic equations 2.25 and 2.29 based on the formation of the monomer, methylene. The assumptions for the rate equations were: 1) The rate determining step is the reaction of dihydrogen and a carbon intermediate. 2) Carbon monoxide and water are strongly adsorbed on the catalyst surface. 3) Hydrogen is assumed to react molecularly via the gaseous phase or via the associated adsorbed state [18, 155].

Anderson [24] proposed a rate equation which included water inhibition:

$$R_{FT} = \frac{k P_{CO} P_{H_2}}{P_{CO} + a P_{H_2O}} \quad (2.25)$$

Dry [156] and Huff and Satterfield [72] derived the same equation from the combined enol/carbide mechanism, assuming strong adsorption of CO and water relative to H₂ and CO₂. Atwood and Bennett [157] used eq 2.25 to describe the kinetics on a fused nitrated iron catalyst. The activation energy was determined as $E_A = 85$ kJ/mol for the kinetic constant k and an adsorption enthalpy of $-\Delta H_{ad} = 8.8$ kJ/mol for the adsorption parameter a :

$$k = k_{\infty} \exp(-E_A/RT) \quad (2.26)$$

$$a = a_{\infty} \exp(-\Delta H_{ad}/RT) \quad (2.27)$$

Shen et al. [158] modeled their data with the same rate expression and reported an activation energy of 56 kJ/mol for k and an adsorption enthalpy of $-\Delta H_{ad} = -60$ kJ/mol for a on a precipitated commercial Fe/Cu/K catalyst. The observed activation energy for the kinetic constant is low in comparison to most activation energies for Fischer-Tropsch reaction rates which are between 70 and 105 kJ/mol [56, 72]. Boudart [165] gives a list of the physical meaning of the most common rate parameters. For the adsorption enthalpy: $-\Delta H_{ad} > 0$. The adsorption constant is a combination of the adsorption constant of carbon monoxide and for water. Consequently, the heat of adsorption for water is 60 kJ/mol larger than for carbon monoxide adsorption.

At conversions of $H_2 + CO$ conversion lower than 60% and in the case of a high shift activity of the catalyst, eq 2.25 can be simplified to a first order dependency in H_2 , due to low partial pressures of water [24, 156]:

$$R_{FT} = k P_{H_2} \quad (2.28)$$

Dry et al. [155] measured FT kinetics on a fused, promoted iron catalyst in a differential fixed bed reactor, and found the behavior described by eq 2.28 with an activation energy of 71 kJ/mol.

Huff and Satterfield [72] observed a linear decrease in the adsorption parameter a in eq 2.25 with hydrogen pressure on a fused iron catalyst and incorporated this by modifying eq 2.25 to:

$$R_{FT} = \frac{k P_{CO} P_{H_2}^2}{P_{CO} P_{H_2} + a' P_{H_2O}} \quad (2.29)$$

note that a' in eq 2.29 equals a/P_{H_2} in eq 2.25. Equation 2.29 can be obtained from the carbide theory as well as from the enol/carbide theory which have identical mathematical descriptions (see Huff and Satterfield [72] for the derivation of these rate equations). Deckwer et al. [159] used eq 2.29 to describe the kinetic results for H_2/CO feed ratios between 0.8-2.0 on a potassium-promoted iron catalyst in the slurry phase. However, at low H_2 to CO feed ratios this equation was not able to describe the results due to high water gas shift activity. Shen et al. [158] used eq 2.29 to model their data and reported an activation energy of 56 kJ/mol for k and an adsorption enthalpy of $-\Delta H_{ad} = -62$ kJ/mol for a on a precipitated commercial Fe/Cu/K catalyst. The authors did not discriminate between the models in eq 2.25 and 2.29 on the basis of goodness of fit.

The water gas shift can increase or decrease the Fischer-Tropsch synthesis reaction rate by altering the concentrations of the reactants and products. Generally, CO_2 inhibition is not as strong as water inhibition due to the large difference in adsorption coefficients [10, 56]. However, iron catalysts with a high activity of the water gas shift reaction convert a significant amount of water into CO_2 . Ledakowicz et al. [161], Nettelhoff et al. [145] and Deckwer et al. [159] reported the following equation including CO_2 inhibition:

$$R_{FT} = \frac{k P_{CO} P_{H_2}}{P_{CO} + a P_{CO_2}} \quad (2.30)$$

Ledakowicz et al. [161] used a precipitated iron catalyst (100 Fe/1.3 K) with high WGS activity and Nettelhoff et al. [145] a commercial fused iron ammonia synthesis

catalyst (BASF S6-10). Ledakowicz et al. [161] proposed a generalized rate expression for iron catalysts with high and low WGS activity:

$$R_{FT} = \frac{kP_{CO}P_{H_2}}{P_{CO} + aP_{H_2O} + bP_{CO_2}} \quad (2.31)$$

However, co-feeding of CO₂ to the feed gas showed that the CO₂ addition does not alter the reaction rate of the synthesis gas consumption significantly [166, 167]. Yates and Satterfield [167] suggested that the inhibition attributed to CO₂ [145, 159, 161] on catalysts with a high shift activity is caused by H₂O, since the reaction is at or close to equilibrium on these catalysts:

$$P_{CO_2} = K_P \frac{P_{CO}P_{H_2O}}{P_{H_2}} \quad (2.32)$$

where K_P is the equilibrium constant for the water gas shift reaction.

Figure 2.21 shows the response of the reported rate equations to a change in partial pressure of H₂, CO, H₂O, and CO₂, respectively. All equations observe an increase with partial pressure of H₂ and CO, while the other components inhibit the reaction rate. The large variation in the predictions is due to different inhibition effects and functional forms of the rate equations. The water gas shift activity of iron catalysts is of great importance for the inhibiting effects of water and possibly CO₂. Therefore, kinetic expressions can only be compared accurately if the optimal kinetic expression for the WGS is included. Only a CSTR model for the reactants as well as the products CO₂ and H₂O is adequate to compare different expressions. Kinetic expressions and mass balances have to be solved simultaneously. Figure 2.22 compares the results of FT and WGS kinetic expressions of three studies with iron catalysts [56, 158]. The overall conversion of synthesis gas is calculated as a function of the space velocity at 1.5 MPa, 523 K, H₂/CO feed ratio=1 in a CSTR. The kinetic equations applied are also shown in Figure 2.22. The kinetic study of Shen et al. [158] was performed in a gas-solid Bertly reactor in contrast to the study with a slurry reactor used by Bukur et al. [91].

All proposed rate expressions were developed with the assumption that the rate determining step is the reaction of undissociated hydrogen with a carbon intermediate. The rate equations are valid only for the specific catalysts with WGS activity and for the process conditions used to develop the expressions. Therefore, we conclude that the development of FT kinetic equations still requires additional research. Detailed LHHW rate expressions tested both in gas-slurry and gas-solid reactors are needed for an accurate description of the consumption rates of the reactants during the Fischer-Tropsch synthesis on iron catalysts.

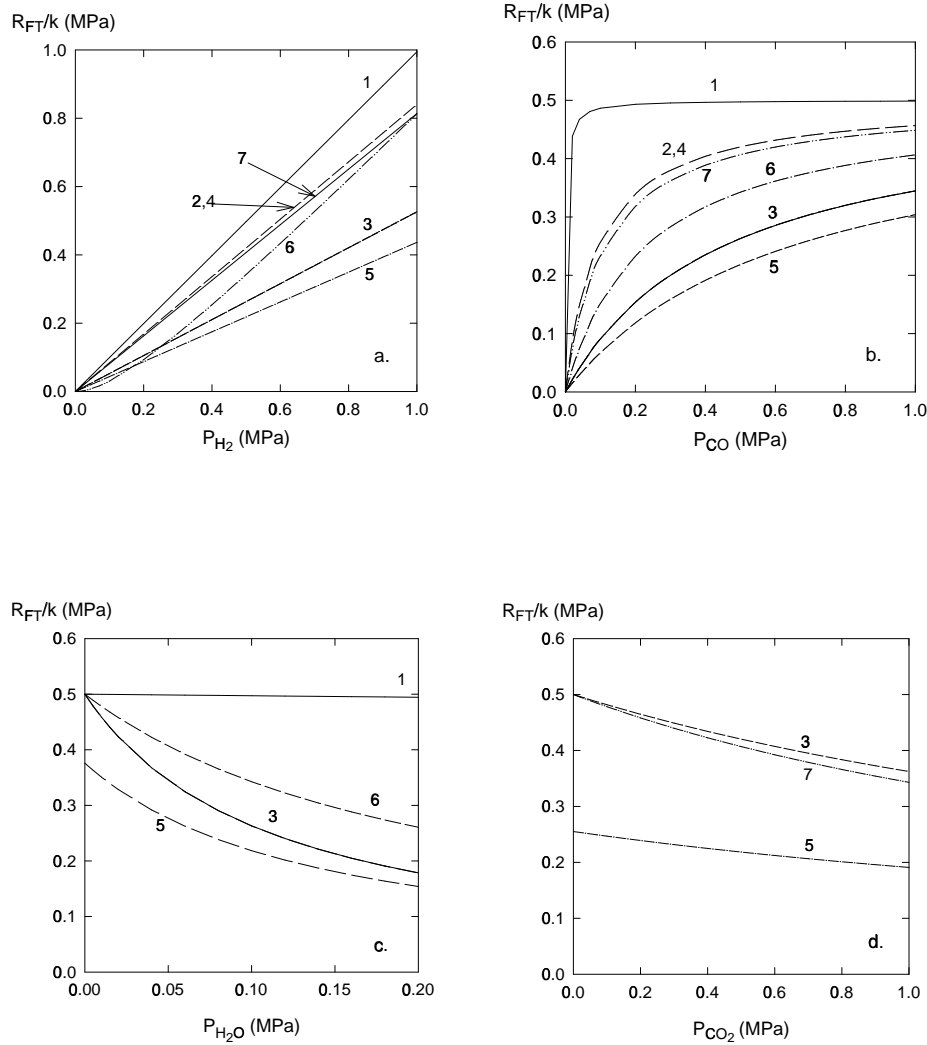


Figure 2.21 Relative reaction rates of synthesis gas consumption on iron catalysts. Kinetics expressions refer to Table 2.6. a) Influence of P_{H_2} : $P_{CO}=0.5$ MPa, $P_{CO_2}=0.5$ MPa, $P_{H_2O}=0.1$ MPa. b) Influence of P_{CO} : $P_{H_2}=0.5$ MPa, $P_{CO_2}=0.5$ MPa, $P_{H_2O}=0.1$ MPa. c) Influence of P_{H_2O} : $P_{H_2}=0.5$ MPa, $P_{CO}=0.5$ MPa, $P_{CO_2}=0.5$ MPa. d) Influence of P_{CO_2} : $P_{H_2}=0.5$ MPa, $P_{CO}=0.5$ MPa, $P_{H_2O}=0.1$ MPa. 1) Atwood and Bennett [157], 250 °C, $a=0.028$, eq c 2) Nettelhoff et al. [145], 270 °C, $a=4.51$, eq c (prec. Fe) 3) Nettelhoff et al. [145], 240 °C, $b=0.19$, eq f (fused Fe) 4) Zimmerman and Bukur [56], 250 °C, $a=4.5$, eq c (commercial Fe) 5) Zimmerman and Bukur [56], 250 °C, $a=4.8$, $b=0.33$ eq g (prec. Fe) 6) Huff and Satterfield [72], 248 °C, $a=1.15$ MPa, eq d (prec. Fe) 7) Ledakowicz et al. [161], 250 °C, $b=0.229$, eq f (prec. Fe).

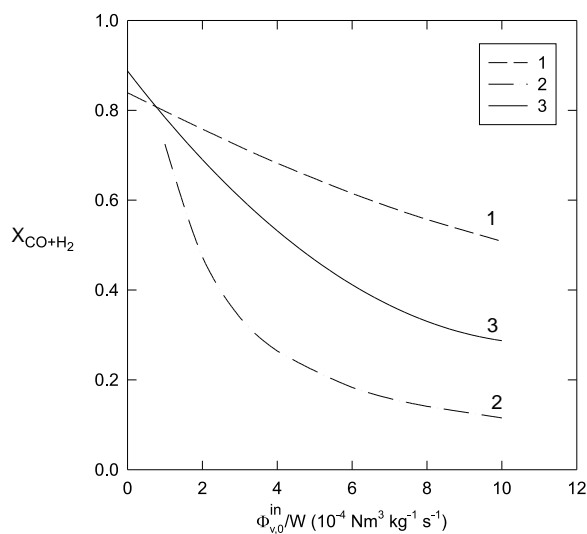


Figure 2.22 Activity comparison at different space velocities on iron catalysts at 1.5 MPa, 523 K, H_2/CO feed ratio= 1. 1) 100 Fe/0.3 Cu/0.2 K catalyst; R_{FT} eq g (Table 2.6) $k=0.0222 \text{ mol kg}_{cat}^{-1} \text{ s}^{-1} \text{ MPa}^{-1}$, $a=4.8$, $b=0.33$; R_{WGS} eq 2.37 $k_w=0.0133 \text{ mol kg}_{cat}^{-1} \text{ s}^{-1} \text{ MPa}^{-1}$ (Zimmerman and Bukur [56]) 2) Fe/Cu/K commercial catalyst; R_{FT} eq c (Table 2.6) $k=0.00753 \text{ mol kg}_{cat}^{-1} \text{ s}^{-1} \text{ MPa}^{-1}$ $a=0.472$; R_{WGS} eq 2.39: $k_w=0.0987 \text{ mol kg}_{cat}^{-1} \text{ s}^{-1}$, $a=0.692 \text{ MPa}$ (Shen et al. [158]) 3) Fe/Cu/K commercial catalyst; R_{FT} eq c (Table 2.6) $k=0.0106 \text{ mol kg}_{cat}^{-1} \text{ s}^{-1} \text{ MPa}^{-1}$ $a=4.5$; R_{WGS} eq 2.39 $k_w=0.0122 \text{ mol kg}_{cat}^{-1} \text{ s}^{-1}$, $a=0 \text{ MPa}$ (Zimmerman and Bukur [56]).

2.8.2.2 Cobalt Based Catalysts

Only a few kinetic studies on cobalt based catalysts are available, see Table 2.7. Remarkably, nearly all kinetic expressions developed for cobalt based catalysts have a different form than for iron based catalysts. Generally, these kinetic equations are based on a rate determining step which involves a dual-site surface reaction, resulting in a quadratic denominator in the rate expression. Furthermore, inhibition terms of H_2O on cobalt catalysts are not reported in literature. Because the WGS reaction hardly plays a role on cobalt, no CO_2 is formed.

Wojciechowski [22] and Sarup and Wojciechowski [73] developed six different rate equations for the formation of the monomer (CH_2), based on both the carbide mechanism and the enol/carbide mechanism. The reaction rates were measured in a

Berty internally recycled reactor at 190 °C for P_{H_2} ranging from 0.07 to 0.68 MPa and P_{CO} between 0.003 and 0.93 MPa. All six rate expressions can be generalized as:

$$-R_{CO} = \frac{k P_{CO}^a P_{H_2}^b}{\left(1 + \sum_i K_i P_{CO}^{c_i} P_{H_2}^{d_i}\right)^2} \quad (2.33)$$

where k is a kinetic rate constant, a and b are the reaction orders of the rate determining step, K_i is the adsorption constant for the i th adsorption term, and c_i and d_i represent the dependency of surface coverage on the reactant pressure of the i th adsorption term. All six different models involve a bimolecular rate determining surface reaction step between a dissociated hydrogen species and a carbon intermediate. Testing of the kinetic models on their experimental data reduced the six to two equations:

$$-R_{CO} = \frac{k P_{CO}^{1/2} P_{H_2}^{1/2}}{\left(1 + K_1 P_{CO}^{1/2} + K_2 P_{H_2}^{1/2}\right)^2} \quad (2.34)$$

$$-R_{CO} = \frac{k P_{CO} P_{H_2}^{1/2}}{\left(1 + K_1 P_{CO} + K_2 P_{H_2}^{1/2}\right)^2} \quad (2.35)$$

In eq 2.34, the first hydrogenation of an adsorbed carbon atom and the first hydrogenation of an adsorbed oxygen atom are slower than the other reaction steps. The assumed rate determining step of eq 2.35 is the hydrogenation of adsorbed CO to form adsorbed formyl. However, after optimization of the parameters of eqs 2.34 and 2.35, the relative variance of experimental and calculated reaction rates was over 40 %, indicating a large lack of fit.

Yates and Satterfield [163] measured the kinetics of a cobalt catalyst in a slurry reactor. A Langmuir-Hinshelwood equation which also involves a bimolecular surface reaction, can accurately describe their results:

$$-R_{CO} = \frac{k P_{CO} P_{H_2}}{(1 + K_1 P_{CO})^2} \quad (2.36)$$

This equation was previously derived by Sarup and Wojciechowski [73] assuming hydrogenation of adsorbed formyl to form carbon and water to be rate determining. However, the number of inhibition terms was larger. Eq 2.36 fitted their data also best, but was rejected because one of the adsorption constants was negative. Yates and Satterfield [163] were able to fit the data of Sarup and Wojciechowski [73] well with the linearized form of the kinetic expression in eq 2.36.

The FT kinetics on a cobalt carbonyl catalyst in slurry-phase was measured by Whithers et al. [160]. They correlated the rate of CO and H₂ consumption to several kinetic equations used for the kinetics on iron catalysts (eqs 2.25 and 2.29). The best fit was obtained for eq 2.29 with an activation energy of 97 kJ/mol for the rate constant.

Recently, Ribeiro et al. [150] reviewed kinetic studies over cobalt FT catalysts in order to explain the differences in turnover rates. The available kinetic data were corrected to 473 K. Furthermore, the effects of partial pressure were corrected to a total pressure of 10 atm and H₂/CO= 2 with the use of a simple power law equation: $-R_{CO} = k P_{H_2}^{0.7} P_{CO}^{-0.2}$ which provided the best fit. The corrected turnover rates vary by a factor of 20, according to the authors due to the effect of a wide range of CO conversion and water concentration.

In comparison to iron catalyst is the kinetic research on cobalt catalysts more comprehensive. In the first place is the situation on cobalt catalysts easier due to the absence of the water gas shift reaction and less different catalytic sites. Secondly, Wojciechowski and co-workers [22, 73, 100, 168] described detailed LHHW equations based on a reliable mechanistic scheme for the CO consumption on cobalt catalysts. This approach is a good example of modeling complex reaction systems like the Fischer-Tropsch synthesis.

2.8.3 Water Gas Shift Kinetics

Cobalt catalysts are not active towards the WGS reaction in contrast to iron-based Fischer-Tropsch catalysts [54]. The water gas shift can increase or decrease the Fischer-Tropsch synthesis rate. Since these reactions share the same components, adsorption and desorption reactions as well as dissociation of H₂, H₂O, and CO₂ and reactions of formate species must be shared [169]. The individual WGS kinetics is studied extensively [54, 58, 81, 86], sometimes in combination with the methanation reaction [85] or methanol synthesis [82, 87]. Only a few studies reported the WGS kinetics of iron catalysts under FTS conditions. Table 2.8 gives an overview.

Based on unpublished results, Dry [156] reported the first (empirical) kinetic expression for the WGS reaction under FTS conditions which is independent of the water concentration:

$$R_{WGS} = k_w P_{CO} \quad (2.37)$$

The same equation was used by Feimer et al. [170] on a precipitated Fe/Cu/K catalyst, with an activation energy of 124 kJ/mol.

Table 2.8 Summary of kinetic studies of the WGS reaction (see also Table 2.7).

Kinetic expression	E_A (k_w) (kJ mol ⁻¹)	Reference
$R_{WGS} = k_w (P_{H_2O} P_{CO} - P_{CO_2} P_{H_2} / K_P)$		[56]
$R_{WGS} = k_w P_{CO}$	124 ¹	[56, 156, 170]
$R_{WGS} = \frac{k_w (P_{H_2O} P_{CO} - P_{CO_2} P_{H_2}^{1/2} / K_P)}{(1 + a P_{H_2O} / P_{H_2}^{1/2})^2}$	27.7	[75]
$R_{WGS} = \frac{k_w (P_{H_2O} P_{CO} - P_{CO_2} P_{H_2} / K_P)}{P_{CO} P_{H_2} + a P_{H_2O}}$	88 ²	[56, 158]
$R_{WGS} = \frac{k_w (P_{H_2O} P_{CO} - P_{CO_2} P_{H_2} / K_P)}{P_{CO} + a P_{H_2O} + b P_{CO_2}}$	125 ²	[56, 158]

¹Activation energy Feimer et al. [170]

²Activation energy Shen et al. [158]

Since the WGS reaction is an equilibrium reaction at or close to equilibrium under Fischer-Tropsch reaction conditions the reverse reaction has to be taken into account. For the temperature dependency of the equilibrium constant of the WGS reaction, K_P , the following relation can be used [171]:

$$\log K_P = \log \left(\frac{P_{CO_2} P_{H_2}}{P_{H_2O} P_{CO}} \right)_{eq} = \left(\frac{2073}{T} - 2.029 \right) \quad (2.38)$$

Zimmerman and Bukur [56] measured the kinetics of the WGS reaction at 250 °C both on a home-made iron catalyst (100 Fe/0.3 Cu/0.2 K) and a commercial precipitated iron catalyst (Ruhchemie LP 33/81). The experimental conditions are mentioned in Table 2.7. The 100 Fe/0.3 Cu/0.2 K catalyst obtained a higher WGS activity in comparison to the commercial catalyst, resulting in a higher extent of equilibrium and higher rate constants. The authors tested several kinetic models to their experimental WGS rates. Some of their kinetic equations contain the same functional form of the denominator as used in their kinetic equations of the FTS:

$$R_{WGS} = \frac{k_w (P_{H_2O} P_{CO} - P_{CO_2} P_{H_2} / K_P)}{P_{CO} P_{H_2} + a P_{H_2O}} \quad (2.39)$$

They also derived a kinetic expression with the denominator from the FT rate expres-

sion of Huff and Satterfield [72]:

$$R_{WGS} = \frac{k_w (P_{H_2O} P_{CO} - P_{CO_2} P_{H_2} / K_P)}{P_{CO} + a P_{H_2O} + b P_{CO_2}} \quad (2.40)$$

This implies that the reaction takes place on the same catalytic sites as the FT. No temperature dependency is given. The estimates of the adsorption constants were significantly different in comparison to the constants for the FT synthesis. If these reactions take place on the same catalytic sites, the adsorption constant may not differ. However, the authors stated that they were not able to derive reliable kinetic equations for the WGS kinetics under FT conditions and their results are largely empirical. For both catalysts applied, the adsorption constant b for CO_2 in eq 2.40 was not significantly different from zero. The modeling of the WGS kinetics for the 100 Fe/0.3 Cu/0.2 K catalyst was equally good with eq 2.39 and 2.40 and slightly better with the simple expression of eq 2.37. The reaction rate of the WGS for the commercial catalyst was best described with eq 2.39 with the adsorption coefficient a of H_2O equal to zero.

Shen et al. [158] measured the WGS kinetics on the same commercial catalyst in a gas-solid Berty reactor. See Table 2.7 for the experimental conditions. They fitted their data with the same equations and found activation energies for k_w in eq 2.39 and 2.40 of 88 kJ/mol and 125 kJ/mol, respectively. The adsorption constants appearing in the denominator were chosen equally to those in the FT kinetic equations, indicating that the authors also assumed that the two reactions proceed on the same catalytic sites.

Lox and Froment [75] also studied the FTS and WGS kinetics on the commercial precipitated iron catalyst (Ruh Chemie LP33/81). Discrimination between rival LHHW kinetic models resulted in the following optimal equation:

$$R_{WGS} = \frac{k_w (P_{H_2O} P_{CO} - P_{CO_2} P_{H_2}^{1/2} / K_P)}{(1 + a P_{H_2O} / P_{H_2}^{1/2})^2} \quad (2.41)$$

In agreement with the statement of Rethwisch and Dumesic [58], the slowest step is the reaction between adsorbed CO and adsorbed hydroxyl species, resulting from the dissociation of water. They assumed the WGS reaction to proceed on a different catalytic site than the FTS. As discussed above, it is generally assumed for supported iron catalysts that magnetite is the most active phase for the WGS while the FT reactions proceed on iron carbides. The reported activation energy of 27.7 kJ/mol is relatively low in comparison to other kinetic studies, but consists of the contribution of adsorption enthalpies of reactants and products and a real activation energy. The

adsorption enthalpy of a was not significantly different from zero. It should be noted that these results were obtained in a packed bed reactor at high conversions, relatively high temperatures of 523-623 K, and high H₂/CO feed ratios between 3.0-6.0.

We conclude that the WGS kinetics under FT conditions still requires additional research. Lox and Froment [75] derived detailed LHHW rate expressions which should be tested on other studies with iron catalysts at common FT conditions both in slurry and gas-solid recycle reactors. Furthermore, knowledge about the active sites of the FTS and the WGS should provide more information for the kinetic modeling of this reaction network.

2.8.4 Hydrocarbon Production Rate

The hydrocarbon production rates on a potassium-promoted Fe₂O₃ catalyst have been correlated empirically by Dictor and Bell [51] as power law kinetics:

$$R_{C_n} = k_n P_{H_2}^a P_{CO}^b \quad (2.42)$$

The rate of formation of the hydrocarbons appeared to increase with P_{H_2} . The observed H₂ dependency of methane production was 1.01 and decreased with increasing carbon number to 0.84 for C₇ hydrocarbon. The observed CO dependency was -0.4 for methane and increased slightly with increasing carbon number. Assuming ASF of the distribution of the small-chain hydrocarbons, the chain growth probability α appeared to increase with increasing CO pressure and decreasing H₂ pressure. The reaction rates for $n=2-7$ could be calculated with:

$$R_{C_n} = R_{CH_4} \alpha^{n-1} \quad (2.43)$$

The dependence of the chain growth probability factor α on CO and H₂ pressures has been correlated empirically [51, 143, 147, 172]. α increases with CO pressure, whereas an increase in H₂ pressure results in a minor or slight decrease of α . Empirical power law kinetics for paraffins as well as olefins have been proposed by Kellner and Bell [147], Bub and Baerns [143], and Anikeev et al. [172].

Several attempts to model these production rates more fundamentally have been reported [22, 73, 75, 101, 115, 118, 147, 148, 173]. Non-steady state kinetics obtained from step-concentration transients of (isotopic) feed components were used to measure absolute values of surface intermediates and intrinsic rate parameters [101, 173, 174]. Also steady state kinetic rates can be used to measure kinetic rate constants [18, 22, 75,

147]. Both approaches require a well-defined mechanistic scheme for the elementary reactions in the Fischer-Tropsch synthesis.

Bell [18] and Kellner and Bell [147] proposed a mechanism shown in Table 2.2. The kinetics were studied over an alumina-supported Ru catalyst. They assumed that CO is first adsorbed molecularly and subsequently gets dissociated. The Ru catalyst surface is assumed to be saturated with CO. It was assumed that the rate of methane formation is controlled by the hydrogenation of methyl, whereas chain growth and termination to higher paraffins and olefins are irreversible, and independent of the carbon number. The other reaction steps are at equilibrium. The probability of chain growth was given as

$$\alpha = \frac{k_p \theta_{CH_2}}{k_p \theta_{CH_2} + k_{t,O} \theta_v + k_{t,P} \theta_H} \quad (2.44)$$

Several simplifying assumptions were proposed in order to solve the kinetic equations and surface fraction of oxygen (θ_O) analytically. The olefin to paraffin ratio equaled $O/P \propto P_{H_2}^{-0.5}$. The authors observed a dependence of the O/P ratio with carbon number which they could not describe with their model. According to our opinion these discrepancies are due to readsorption or secondary reactions which were not taken into account. However, their kinetic expression for methane formation was approximately equal to the empirical dependency: $R_{CH_4} \propto P_{H_2}^{3/2} P_{CO}^{-1}$.

By assuming polymerization kinetics, Sarup and Wojciechowski [73] were able to derive kinetic rate expressions for the methanation and a mechanistic formulation for the paraffin formation based on the optimized model for the rate of CO consumption [168]. They made use of the polymerization kinetics where the rate of initiation must be equal to the rate of termination at steady state. The rate of initiation was equal to the hydrogenation of methylene to chain initiator methyl:

$$R_i = k_i \theta_H \theta_{CH_2} \quad (2.45)$$

and the rate of termination in their model was equal to the termination to paraffins due to hydrogenation (k_3) and reaction with a methyl species (k_4):

$$R_t = k_3 \theta_H \sum_1^{\infty} \theta_i + k_4 \theta_{CH_3} \sum_1^{\infty} \theta_i \quad (2.46)$$

Surface coverages of dissociated hydrogen (θ_H), methyl (θ_{CH_3}), alkyl chains (θ_i), and methylene (θ_{CH_2}) species were obtained using the assumption that the rate constant

for propagation as well as the rate constant for termination to paraffins is independent of chain length. Several other assumptions were introduced in order to derive dependencies of ratios of specific rates on P_{H_2} and P_{CO} . The approach of Sarup and Wojciechowski [73] is a good example how to combine the overall consumption rate of CO and a product distribution model. However, they use the concept of growth "locations" which is a number of sites in close proximity. E.g. formation of paraffins proceeds on three sites, the first site contains the growing alkyl chains, another the monomer and a final site contains a hydrogen atom that will result in termination and desorption of a paraffin. These locations are invariant with time and only small species can migrate towards the specific sites. Their approach involves a situation where a site can only contain one type of intermediate. In general, competitive adsorption of components on sites and surface diffusion of intermediates to sites will result in indistinguishable sites, without preference for certain types of intermediates. They also assumed two termination possibilities for paraffins to predict the "break" in the ASF distribution of paraffins. Rice and Wojciechowski [175] rejected the possibility of readsorption of olefins. However, several authors proved that olefins show a high tendency for secondary reactions and readsorption (see Chapter 2.7.2.2).

Zimmerman et al. [115] and Zimmerman [176] proposed a kinetic model for both the formation of linear olefins and paraffins and the water gas shift reaction. The model accounts for secondary readsorption of olefins on FT sites and the possibility of secondary hydrogenation of olefins on separate hydrogenation sites. The model was tested for a single experiment obtained with a commercial iron-based catalyst in a laboratory slurry reactor but showed significant deviations between model and experiments, specially for the methane and ethene content [115]. Their model predicts a decrease of the olefin to paraffin ratio and an increase of the chain growth factor with increasing chain length. The decrease is caused by the higher olefin concentration in the liquid. Zimmerman et al. [115] reported the following kinetic equations:

$$\text{Initiation: } R_i = k_p \theta_{CO} \theta_H^2 \quad (2.47)$$

$$\text{Propagation: } R_{p,i} = k_p \theta_i \theta_{CO} \theta_H \quad (i = 1 \rightarrow N) \quad (2.48)$$

Termination:

$$\text{methane } R_{t,p,1} = (k_{t,p} \theta_H + k_{t,o}) \theta_1 \quad (2.49)$$

$$\text{paraffins } R_{t,p,i} = k_{t,p} \theta_i \theta_H \quad (i = 2 \rightarrow N) \quad (2.50)$$

$$\text{olefins } R_{t,o,i} = k_{t,o} (\theta_i - P_{C_i H_{2i}} \theta_H / K_\ell) \quad (i = 2 \rightarrow N) \quad (2.51)$$

$$\text{Water gas shift: } R_{WGS} = k_w(P_{CO}P_{H_2O} - P_{CO_2}P_{H_2}/K_p) \quad (2.52)$$

$$\text{Olefin hydrogenation: } R_{s,i} = \frac{k_s P_{H_2} P_{C_i H_{2i}}}{1 + (K_{H_2} P_{H_2})^{1/2} \left(1 + \sum_{i=1}^N K_e P_{C_i H_{2i}} \right)^2} \quad (2.53)$$

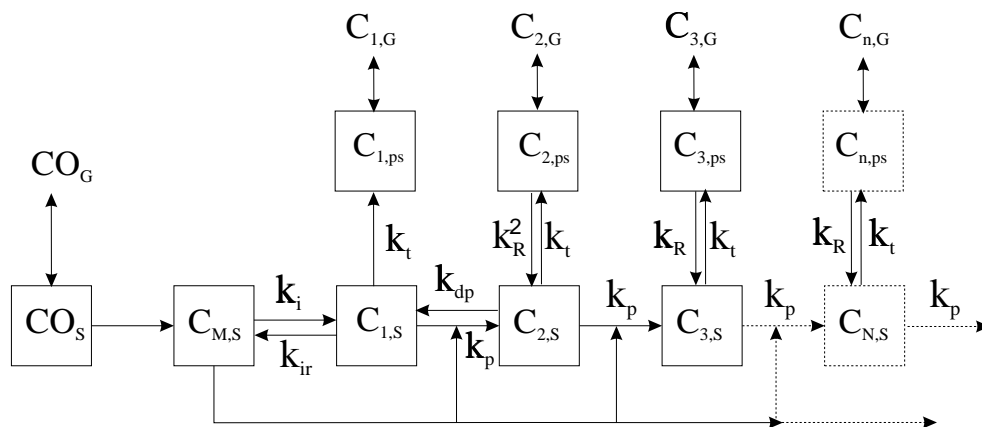


Figure 2.23 Chain growth model on Co catalyst (adapted from Komaya and Bell [101]).

Komaya and Bell [101] and Krishna and Bell [173] determined the pseudo reaction rate constants of the elementary FTS reactions over Ru/TiO₂ ($T = 523$ K) using both steady-state and transient-response kinetic experiments. Their pseudo rate constants contain surface concentrations of surface species and *real* kinetic rate constants. These pseudo kinetic rate constants will not only depend on temperature but also on pressure and composition. The chain growth model in Figure 2.23 was used as a basis for their kinetic models. In contrast to Krishna and Bell [173], Komaya and Bell [101] accounted for the effect of chain length dependent readsorption of olefins (k_R), as well as depolymerization of adsorbed ethylene (k_{dp}) and dehydrogenation of methyl to form a methylene monomer species (k_{ir}). Their explanation for increasing readsorption rates with carbon number is an increase of the physisorption strength with increasing carbon number. The observed rate coefficient of readsorption of ethene (k_R^2) is four orders of magnitude larger than for higher olefins. The authors did not specify separate termination reactions for the formation of paraffins and olefins from adsorbed alkyl species, but lumped the termination reactions in a single termination rate constant. Therefore, no influence of the partial pressures of CO and H₂ on the olefin to paraffin ratio was predicted.

Lox and Froment [75] developed a reaction network for the formation of linear hydrocarbons on a commercial precipitated iron catalyst. For each reaction path one or more elementary reaction steps were assumed to be slower than the other steps. On basis of the carbide mechanism they developed several kinetic models. Their experimental product distributions obtained at $T= 523\text{-}623$ K and $H_2/CO= 3\text{-}6$ in a fixed bed reactor at a high level of conversion fitted well with the Anderson-Schulz-Flory distribution. Their model predicts the desorption of products and adsorption of CO to be rate determining. The rate of formation for the paraffins is given by:

$$R_{C_nH_{2n+2}} = \frac{k_5 P_{H_2} \left(\frac{k_1 P_{CO}}{k_1 P_{CO} + k_5 P_{H_2}} \right) \alpha^{n-1}}{1 + \frac{1}{1 - \alpha} \left(\frac{k_{HC1} P_{CO}}{k_1 P_{CO} + k_{HC5} P_{H_2}} \right)} \quad (2.54)$$

and for olefins:

$$R_{C_nH_{2n}} = \frac{k_6 \left(\frac{k_1 P_{CO}}{k_1 P_{CO} + k_5 P_{H_2}} \right) \alpha^{n-1}}{1 + \frac{1}{1 - \alpha} \left(\frac{k_{HC1} P_{CO}}{k_1 P_{CO} + k_5 P_{H_2}} \right)} \quad (2.55)$$

with α given by:

$$\alpha = \frac{k_1 P_{CO}}{k_1 P_{CO} + k_5 P_{H_2} + k_6} \quad (2.56)$$

The growth probability factor α and the formation rates of the products depend on the partial pressure of CO and H_2 but are independent of the carbon number n . Their kinetic model predicts a constant ratio of the production rate of olefins to paraffins independent of the carbon number equal to:

$$\frac{R_{C_nH_{2n}}}{R_{C_nH_{2n+2}}} = \frac{m_{O_n}}{m_{P_n}} = \frac{k_6}{k_5 P_{H_2}} \quad (2.57)$$

Unfortunately, their experiments were performed in an integral packed bed reactor at high synthesis gas conversions, which is unsuitable for fundamental kinetic studies. Their product formation rates and models do not predict the well-known deviations observed in the nearly all FT product distributions.

Neither of the above-mentioned overall models is able to describe a detailed product distribution as a function of reactant pressures and operating conditions.

2.9 Conclusions

From the above we conclude that further research should concentrate on development of mechanistic rate expressions based on reliable mechanistic proposals. Coupling of the CO consumption and product distribution is an important feature of this new development. Until now, none of the available literature models obtains enough details to describe the complete product distribution of the Fischer-Tropsch synthesis at industrial conditions (high temperature and pressure) as a function of overall consumption of synthesis gas components and operating conditions. Either the product distribution model is oversimplified (Anderson-Schulz-Flory behavior), or the mechanistic proposals for the elementary reactions are unrealistic.

Rate equations for CO consumption to FT products show a great variety of inhibitor terms and are based on different mechanistic proposals. Also, many rate equations were proposed which are strongly influenced by the catalyst type and reaction conditions. The proposed FT kinetic equations on iron catalysts show inhibiting effects of CO_2 and H_2O , dependent on the WGS activity. However, close to equilibrium, a strong correlation between the inhibiting terms of CO_2 and H_2O occur. Rate equations based on a single-site rate determining reaction step between undissociated hydrogen and a carbon intermediate are presented for iron catalysts. On cobalt catalysts, dual-site elementary reactions between dissociated hydrogen and a carbon intermediate are considered to be the rate determining step. The majority of the kinetic rates under industrial conditions are reported per mass unit of catalyst. However, the preferred way to present rate data is in the form of specific activity, such as turnover rates (TOR) or frequencies (TOF). This way, different catalysts can be compared appropriately. Therefore, preparation and characterization procedures and calculations of surface area and metal dispersion should be reported in detail.

The WGS reaction is important for potassium-promoted iron catalysts at low H_2/CO ratios. Only a few authors reported on the WGS kinetics on iron catalysts under FT conditions. Therefore, development of WGS kinetic expressions from intrinsic kinetic experiments requires additional research.

The product distribution of the FTS shows significant deviations from the Anderson-Schulz-Flory distribution on iron, cobalt, and ruthenium catalysts. The ASF product distribution is changed by the occurrence of secondary reactions (hydrogenation, isomerization, reinsertion, and hydrogenolysis). Due to high CO and H_2O pressures present at FTS conditions, reinsertion of olefins appears to be the most important secondary reaction. The rates of these secondary reactions increase exponentially with

chain length. There is controversy in the literature about the fundamentals of these chain length dependency. Several possibilities for a chain length dependent contact time are physisorption, solubility and diffusivity. The chain length dependency of the olefin to paraffin ratio can hardly be due to diffusion effects only. Changes in the solubility and physisorption strength must be included in a proper model description. Reliable and independent measurements of these quantities on FT catalysts are necessary for the development of more accurate product distribution models.

Measured kinetic rates should not be influenced by deactivation of the catalyst. Experiments should be carried out in continuous perfectly mixed reactors (slurry or gas-solid) or differential fixed bed reactors over a wide range of independently varied experimental conditions. Kinetic experiments should preferably be accompanied by characterization measurements of the catalyst (for example different phases and texture). Process optimization and improvement of the FTS should result from kinetic equations for all products and reactants based on realistic mechanistic schemes. The development of new catalysts with high stability, activity and selectivity to the desired products is important. A model for a commercial reactor, which combines reliable kinetic expressions with hydrodynamics and mass transfer in a slurry bubble column should lead to improved scale up and development for industrial processes.

References

- [1] Zimmerman, W.H.; Bukur, D.B., Effect of particle size on the activity of a fused iron Fischer-Tropsch catalyst, *Ind. Eng. Chem. Res.* **1989**, *28*, 406–413.
- [2] Post, M.F.M.; van't Hoog, A.C.; Minderhoud, J.K.; Sie, S.T., Diffusion limitations in Fischer-Tropsch catalysts, *AIChE J.* **1989**, *35*, 1107–1114.
- [3] Iglesia, E.; Reyes, S.C.; Soled, S.L., Reaction-transport selectivity models and the design of Fischer-Tropsch catalysts, in E.R. Becker; C.J. Pereira, eds., *Computer-aided design of catalysts*, Marcel Dekker, New York, 1993 pp. 199–257.
- [4] Matthews, M.A.; Rodden, J.B.; Akgerman, A., High-temperature diffusion of hydrogen, carbon monoxide and carbon dioxide in liquid n-heptane, n-dodecane, and n-hexadecane, *J. Chem. Eng. Data* **1987**, *32*, 319–322.
- [5] Albal, R.S.; Shah, Y.T.; Carr, N.L.; Bell, A.T., Mass transfer coefficients and solubilities for hydrogen and carbon monoxide under Fischer-Tropsch conditions, *Chem. Eng. Sci.* **1984**, *39*, 905.

- [6] Ponec, V.; Van Barneveld, W.A., The role of chemisorption in Fischer-Tropsch synthesis, *Ind. Eng. Chem. Prod. Res. Des.* **1979**, *4*, 268–271.
- [7] Rofer-De Poorter, C.K., A comprehensive mechanism for the Fischer-Tropsch synthesis, *Chem. Rev.* **1981**, *81*, 447–474.
- [8] Vannice, M.A., The catalytic synthesis of hydrocarbons from H₂/CO mixtures over the group VIII metals. II. The kinetics of the methanation reaction over supported metals, *J. Catal.* **1975**, *37*, 462–473.
- [9] Bond, G.C., *Catalysis by metals*, Academic Press, New York **1962**.
- [10] Dry, M.E.; Shingles, T.; Boshoff, L.J.; Oosthuizen, G.J., Heats of adsorption on promoted iron surfaces and the role of alkali in Fischer-Tropsch synthesis, *J. Catal.* **1969**, *15*, 190–199.
- [11] Vannice, M.A., The catalytic synthesis of hydrocarbons from carbon monoxide and hydrogen, *Catal. Rev.-Sci. Eng.* **1976**, *14*, 153–191.
- [12] Röper, M., Fischer-Tropsch synthesis, in W. Keim, ed., *Catalysis in C₁ chemistry*, D. Reidel, Dordrecht, The Netherlands, 1983 pp. 41–88.
- [13] Dry, M.E., The Fischer-Tropsch synthesis, in J.R. Anderson; M. Boudart, eds., *Catalysis-Science and technology*, vol. 1, Springer-Verlag, New York, 1981 pp. 160–255.
- [14] Curtis Conner, Jr., W.; Falconer, J.L., Spillover in heterogeneous catalysts, *Chem. Rev.* **1995**, *95*, 759–788.
- [15] Masel, R.I., *Principles of adsorption and reaction on solid surfaces*, Wiley & Sons, New York **1996**.
- [16] Ponec, V., Some aspects of the methanation and Fischer-Tropsch synthesis, *Catal. Rev.-Sci. Eng.* **1978**, *18*, 151–171.
- [17] Muetterties, E.L.; Stein, J., Mechanistic features of catalytic carbon monoxide hydrogenation reactions, *Chem. Rev.* **1979**, *79*, 479–490.
- [18] Bell, A.T., Catalytic synthesis of hydrocarbons over group VIII metals. A discussion on the reaction mechanism, *Catal. Rev.-Sci. Eng.* **1981**, *23*, 203–232.
- [19] Shustorovich, E., Metal effects in the Fischer-Tropsch synthesis: bond-order-conservation-morse-potential approach, *Catal. Lett.* **1990**, *7*, 107–118.
- [20] Vannice, M.A., Catalytic activation of CO on metal surfaces, in J.R. Anderson; M. Boudart, eds., *Catalysis-Science and technology*, vol. 3, Springer-Verlag, New York, 1982 pp. 139–198.
- [21] Van Santen, R.A.; Neurock, M., Concepts in theoretical heterogeneous catalytic reactivity, *Catal. Rev.-Sci. Eng.* **1995**, *37*, 557–698.
- [22] Wojciechowski, B.W., The kinetics of the Fischer Tropsch synthesis, *Catal.*

- Rev.-Sci. Eng.* **1988**, *30*, 629–702.
- [23] Biloen, P.; Sachtler, W.M.H., Mechanism of hydrocarbon synthesis over Fischer-Tropsch catalysts, *Adv. Catal.* **1981**, *30*, 165–216.
- [24] Anderson, R.B., *Catalysts for the Fischer-Tropsch synthesis*, vol. 4, Van Nostrand Reinhold, New York **1956**.
- [25] Rao, V.U.S.; Stiegel, G.J.; Cinquegrane, G.J.; Srivastava, R.D., Iron-based catalysts for slurry-phase Fischer-Tropsch process: Technology review, *Fuel Process. Technol.* **1992**, *30*, 83–107.
- [26] Jager, B.; Espinoza, R., Advances in low-temperature Fischer-Tropsch synthesis, *Catal. Today* **1995**, *23*, 17–28.
- [27] Kölbel, H.; Ralek, M., The Fischer-Tropsch synthesis in the liquid phase, *Catal. Rev.-Sci. Eng.* **1980**, *21*, 225–274.
- [28] Chaumette, P.; Courty, Ph.; Kiennemann, A.; Ernst, B., Higher alcohol and paraffin synthesis on cobalt based catalysts: comparison of mechanistic aspects, *Top. in Catal.* **1995**, *2*, 117–126.
- [29] Frohning, C.D.; Kölbel, H.; Ralek, M.; Rottig, W.; Schuur, F.; Schulz, H., Fischer-Tropsch-Synthese, in J. Falbe, ed., *Chemierohstoffe aus Kohle*, Georg Thieme Verlag, Stuttgart, 1977 pp. 219–299.
- [30] Van der Burgt, M.J.; Van Leeuwen, C.J.; delÁmico, J.J.; Sie, S.T., The Shell Middle Distillate Synthesis process, in D.M. Bibby; C.D. Chang; R.F. Howe; S. Yurchak, eds., *Methane Conversion*, Elsevier Science, New York, 1988 pp. 473–482.
- [31] Sie, S.T.; Senden, M.M.G.; Van Wechum, H.M.H., Conversion of natural gas to transportation fuels via the Shell Middle Distillate Synthesis process (SMDS), *Catal. Today* **1991**, *8*, 371–394.
- [32] Madon, R.J.; Iglesia, E.; Reyes, S.C., Non-Flory product distributions in Fischer-Tropsch synthesis catalyzed by Ruthenium, Cobalt, and Iron, in S.L. Suib; M.E. Davis, eds., *Selectivity in Catalysis*, ACS Symposium Series, American Chemical Society, 1993 pp. 382–396.
- [33] Berge van, P.J.; Everson, R.C., Cobalt as an alternative Fischer-Tropsch catalyst to iron for the production of middle distillates, *Stud. Surf. Sci. Catal.* **1997**, *107*, 207–212.
- [34] Schulz, H., Polymethylen aus Synthesegas, in J. Falbe, ed., *Chemierohstoffe aus Kohle*, Georg Thieme Verlag, Stuttgart, 1977 pp. 335–355.
- [35] Vannice, M.A., The catalytic synthesis of hydrocarbons from CO and H₂ over group VIII metals. V. The catalytic behavior of silica-supported metals, *J. Catal.*

- 1977**, 50, 228.
- [36] Ernst, B.; Bensaddik, A.; Jilaire, L.; Chaumette, P.; Kienemann, A., Study on cobalt silica catalyst during reduction and Fischer-Tropsch reaction: In situ EXAFS compared to XPS and XRD, *Catal. Today* **1998**, 39, 329–341.
- [37] Rao, K.R.P.M.; Huggins, F.E.; Mahajan, V.; Huffman, G.P.; Rao, V.U.S.; Bhatt, B.L.; Bukur, D.B.; Davis, B.H.; O'Brien, R.J., Mössbauer spectroscopy study of iron-based catalysts used in Fischer-Tropsch synthesis, *Top. Catal.* **1995**, 2, 71–78.
- [38] Bukur, D.B.; Koranne, M.; Lang, X.; Rao, K.R.P.M.; Huffman, G.P., Pre-treatment effect studies with a precipitated iron Fischer-Tropsch catalyst, *Appl. Catal. A* **1995**, 126, 85–113.
- [39] Lox, E.S.; Marin, G.B.; de Graeve, E.; Bussiere, P., Characterization of a promoted precipitated iron catalyst for Fischer-Tropsch synthesis, *Appl. Catal. A* **1988**, 40, 197–218.
- [40] Rao, K.R.P.M.; Huggins, F.E.; Huffman, G.P.; Gormley, R.J.; O'Brien, R.J.; Davis, B.H., Mössbauer spectroscopy study of iron Fischer-Tropsch catalysts during activation and synthesis, *Energy Fuels* **1996**, 10, 546–551.
- [41] Rao, K.R.P.M.; Huggins, F.E.; Mahajan, V.; Huffman, G.P.; Davis, B.; O'Brien, R.J.; Xu, L.; Rao, V.U.S., Effect of pre-heat treatment on a Fischer-Tropsch iron catalyst, *Hyperfine Interact.* **1994**, 93, 1755–1758.
- [42] Bukur, D.B.; Lang, X.; Rossin, J.A.; Zimmerman, W.H.; Rosynek, M.P.; Yeh, E.B.; Li, C., Activation studies with a promoted precipitated iron Fischer-Tropsch catalyst, *Ind. Eng. Chem. Res.* **1989**, 28, 1130–1140.
- [43] Bukur, D.B.; Okabe, K.; Rosynek, M.P.; Li, C.; Wang, D.; Rao, K.R.P.M.; Huffman, G.P., Activation studies with a precipitated iron catalyst for Fischer-Tropsch synthesis. 1. Characterization studies, *J. Catal.* **1995**, 155, 353–365.
- [44] Bukur, D.B.; Nowicki, L.; Manne, R.K.; Lang, X., Activation studies with a precipitated iron catalyst for Fischer-Tropsch synthesis 2. Reaction studies, *J. Catal.* **1995**, 155, 366–375.
- [45] Bukur, D.B.; Nowicki, L.; Patel, S.A., Activation studies with an iron Fischer-Tropsch catalyst in fixed bed stirred tank reactors, *Can. J. Chem. Eng.* **1996**, 74, 399–404.
- [46] Shroff, M.D.; Kalakkad, D.S.; Coulter, K.E.; Köhler, S.D.; Harrington, M.S.; Jackson, N.B.; Sault, A.G.; Datye, A.K., Activation of iron precipitated Fischer-Tropsch catalysts, *J. Catal.* **1995**, 156, 185–207.
- [47] Zhang, H.-B.; Schrader, G.L., Characterisation of a fused iron catalyst for

- Fischer-Tropsch synthesis by in situ laser Raman spectroscopy, *J. Catal.* **1985**, *95*, 325–332.
- [48] Van de Loosdrecht, J., *Preparation and properties of supported Fischer-Tropsch catalysts*, Ph.D. thesis, University of Utrecht, Utrecht, The Netherlands **1995**.
- [49] Raupp, G.B.; Delgass, W.N., Mössbauer investigation of supported Fe catalysts. III In situ kinetics and spectroscopy during Fischer-Tropsch synthesis, *J. Catal.* **1979**, *58*, 361–369.
- [50] Niemantsverdriet, J.W.; Van der Kraan, A.M.; Van Dijk, W.L.; Van der Baan, H.S., Behavior of metallic iron catalysts during Fischer-Tropsch synthesis studied with Mössbauer spectroscopy, X-ray diffraction, carbon content determination, and reaction kinetic measurements, *J. Phys. Chem.* **1980**, *84*, 3363–3370.
- [51] Dictor, R.A.; Bell, A.T., Fischer-Tropsch synthesis over reduced and unreduced iron oxide catalysts, *J. Catal.* **1986**, *97*, 121–136.
- [52] Amelse, J.A.; Butt, J.B.; Schwartz, L.H., Carburization of supported iron synthesis catalysts, *J. Phys. Chem.* **1978**, *82*, 558–563.
- [53] Rao, K.R.P.M.; Huggins, F.E.; Mahajan, V.; Huffman, G.P.; Rao, V.U.S., Mössbauer spectroscopy study of CO-precipitated Fischer-Tropsch iron catalysts, *Hyperfine Interact.* **1994**, *93*, 1751–1754.
- [54] Newsome, D.S., The water-gas shift reaction, *Catal. Rev.-Sci. Eng.* **1980**, *21*, 275–318.
- [55] Satterfield, C.N.; Huff, Jr., G.A., Usefulness of a slurry-type Fischer-Tropsch reactor for processing synthesis gas of low hydrogen-carbon monoxide ratios, *Can. J. Chem. Eng.* **1982**, *60*, 159–162.
- [56] Zimmerman, W.H.; Bukur, D.B., Reaction kinetics over iron catalysts used for the Fischer-Tropsch synthesis, *Can. J. Chem. Eng.* **1990**, *68*, 292–301.
- [57] Lox, E.S.; Froment, G.F., Kinetics of the Fischer-Tropsch reaction on a precipitated promoted iron catalyst. 1. Experimental procedure and results, *Ind. Eng. Chem. Res.* **1993**, *32*, 61–70.
- [58] Rethwisch, D.G.; Dumesic, J.A., Adsorptive and catalytic properties of supported metal oxides. III. Water-gas shift over supported iron and zinc oxides, *J. Catal.* **1986**, *101*, 35–42.
- [59] Anderson, R.B., *The Fischer-Tropsch synthesis*, Academic Press, New York **1984**.
- [60] Hindermann, J.P.; Hutchings, G.J.; Kiennemann, A., Mechanistic aspects of the formation of hydrocarbons and alcohols from CO hydrogenation, *Catal. Rev.-Sci. Eng.* **1993**, *35*, 1–127.

- [61] Dry, M.E., Conversion of syngas to fuels and chemicals, in *Int. Conf. on Catal. & Catal. Proc.*, Cape Town, South Africa, 1993 pp. 57–66.
- [62] Dry, M.E., Practical and theoretical aspects of the catalytic Fischer-Tropsch process, *Appl. Catal. A* **1996**, *138*, 319–344.
- [63] Adesina, A.A., Hydrocarbon synthesis via Fischer-Tropsch reaction: travails and triumphs, *Appl. Catal. A* **1996**, *138*, 345–367.
- [64] Schulz, H.; Beck, K.; Erich, E., Mechanism of the Fischer-Tropsch process, in D.M. Bibby; C.D. Chang; R.F. Howe; S. Yurchak, eds., *Methane Conversion*, Elsevier Science, 1988 pp. 457–471.
- [65] Biloen, P.; Helle, J.N.; Sachtler, W.M.H., Incorporation of surface carbon into hydrocarbons during Fischer-Tropsch synthesis: mechanistic implications, *J. Catal.* **1979**, *58*, 95–107.
- [66] Chuang, S.C.; Thian, Y.H.; Goodwin, Jr., J.G.; Wender, I., The use of probe molecules in the study of CO hydrogenation over SiO₂-supported Ni, Ru, Rh, and Pd, *J. Catal.* **1985**, *96*, 396–407.
- [67] Fischer, F.; Tropsch, H., Über die Herstellung synthetischer Ölgemische (Synthol) durch Aufbau aus Kohlenoxyd und Wasserstoff, *Brennst. Chem.* **1923**, *4*, 276–285.
- [68] Schulz, H.; Van Steen, E.; Claeys, M., Olefin formation, hydrogenation and isomerization in the kinetic regime of Fischer-Tropsch synthesis, in *Selective hydrogenation and dehydrogenation*, DGMK, Kassel, Germany, 1993 .
- [69] Kobori, Y.; Yamasaki, H.; Naito, S.; Onishi, T.; Tamaru, K., *J. Chem. Soc., Faraday Trans. 1* **1982**, *78*, 473.
- [70] Biloen, P.; Helle, J.N.; van den Berg, F.G.A.; Sachtler, W.M.H., Mechanism of hydrocarbon synthesis over Fischer-Tropsch catalysts, *J. Catal.* **1983**, *81*, 450.
- [71] Bianchi, D.; Tau, L.M.; Borcar, S.; Bennett, C.O., Nature of the species on supported iron during CO/H₂ reaction, *J. Catal.* **1983**, *84*, 358–374.
- [72] Huff, Jr., G.A.; Satterfield, C.N., Intrinsic kinetics of the Fischer-Tropsch synthesis on a reduced fused-magnetite catalyst, *Ind. Eng. Chem. Process Des. Dev.* **1984**, *23*, 696–705.
- [73] Sarup, B.; Wojciechowski, B.W., Studies of the Fischer-Tropsch synthesis on a cobalt catalyst. II. Kinetics of carbon monoxide conversion to methane and to higher hydrocarbons, *Can. J. Chem. Eng.* **1989**, *67*, 62–74.
- [74] Schulz, H.; Beck, K.; Erich, E., Kinetics of Fischer-Tropsch selectivity, *Fuel Process. Technol.* **1988**, *18*, 293–304.
- [75] Lox, E.S.; Froment, G.F., Kinetics of the Fischer-Tropsch reaction on a precip-

- itated promoted iron catalyst. 2. Kinetic modeling, *Ind. Eng. Chem. Res.* **1993**, *32*, 71–82.
- [76] Hovi, J.-P.; Lahtinen, J.; Liu, Z.S.; Nieminen, R.M., Monte Carlo study of CO hydrogenation on cobalt model catalysts, *J. Chem. Phys.* **1995**, *102*, 7674–7682.
- [77] Novak, S.; Madon, R.J.; Suhl, H., Models of hydrocarbon product distributions in Fischer-Tropsch synthesis, *J. Chem. Phys.* **1981**, *74*, 6083–6091.
- [78] Novak, S.; Madon, R.J.; Suhl, H., Secondary effects in the Fischer-Tropsch synthesis, *J. Catal.* **1982**, *77*, 141–151.
- [79] Oki, S.; Mezaki, R., Identification of rate controlling steps for the water gas shift reaction over an iron catalyst, *J. Phys. Chem.* **1973a**, *77*, 447.
- [80] Oki, S.; Mezaki, R., Mechanistic structure of the water gas shift reaction in the vicinity of chemical equilibrium, *J. Phys. Chem.* **1973b**, *77*, 1601.
- [81] Grenoble, D.C.; Edstadt, M.M.; Ollis, D.F., The chemistry and catalysis of the water gas shift reaction, *J. Catal.* **1981**, *67*, 90–102.
- [82] Graaf, G.H.; Winkelman, J.G.M.; Stamhuis, E.J.; Beenackers, A.A.C.M., Kinetics of the three-phase methanol synthesis, *Chem. Eng. Sci.* **1988**, *43*, 2161–2168.
- [83] Chinchin, G.C.; Mansfield, K.; Spencer, M.S., The methanol synthesis: How does it work?, *CHEMTECH* **1990**, 241.
- [84] Sachtler, W.H.M., Mechanismus der katalysierten Synthese von Kohlenwasserstoffen, *Chem.-Ing.-Tech.* **1982**, *54*, 901–907.
- [85] Xu, J.; Froment, G.F., Methane steam reforming, methanation and water-gas shift: I. Intrinsic kinetics, *AIChE J.* **1989**, *35*, 88–96.
- [86] Ovesen, C.V.; Clausen, B.S.; Hammershøi, B.S.; Steffensen, G.; Askgaard, T.; Chorkendorff, I.; Norskø, J.K.; Rasmussen, P.B.; Stoltze, P.; Taylor, P., A microkinetic analysis of the water-gas-shift reaction under industrial conditions, *J. Catal.* **1996**, *158*, 170–180.
- [87] Vandenbussche, K.M.; Froment, G.F., A steady-state kinetic model for methanol synthesis and the water gas shift reaction on a commercial Cu/ZnO/Al₂O₃ catalyst, *J. Catal.* **1996**, *161*, 1–10.
- [88] Donnelly, T.J.; Yates, I.C.; Satterfield, C.N., Analysis and prediction of product distributions of the Fischer-Tropsch synthesis, *Energy Fuels* **1988**, *2*, 734–739.
- [89] Iglesia, E.; Reyes, S.C.; Madon, R.J.; Soled, S.L., Selectivity control and catalyst design in the Fischer-Tropsch synthesis: sites, pellets, and reactors, in E.E. Eley; H. Pines; P.B. Weisz, eds., *Advances in Catalysis*, vol. 39, Academic Press, New York, 1993 pp. 221–302.

- [90] Donnelly, T.J.; Satterfield, C.N., Product distributions of the Fischer-Tropsch synthesis on precipitated iron catalysts, *Appl. Catal. A* **1989**, *52*, 93–114.
- [91] Bukur, D.B.; Patel, S.A.; Lang, X., Fixed bed and slurry reactor studies of Fischer-Tropsch synthesis on precipitated iron catalyst, *Appl. Catal. A* **1990**, *61*, 329–349.
- [92] Kuipers, E.W.; Scheper, C.; Wilson, J.H.; Oosterbeek, H., Non-ASF product distributions due to secondary reactions during Fischer-Tropsch synthesis, *J. Catal.* **1996**, *158*, 288–300.
- [93] Iglesia, E.; Reyes, S.C.; Madon, R.J., Transport-enhanced α -olefin readsorption pathways Ru-catalyzed hydrocarbon synthesis, *J. Catal.* **1991**, *129*, 238–256.
- [94] Pichler, H.; Schulz, H., Neuere Erkenntnisse auf dem Gebiet der Synthese von Kohlenwasserstoffen aus CO und H_2 , *Chem.-Ing.-Tech.* **1970**, *32*, 1162–1174.
- [95] Dry, M.E., Catalytic aspects of industrial Fischer-Tropsch synthesis, *J. Mol. Catal.* **1982**, *17*, 133–144.
- [96] Everson, R.C.; Woodburn, E.T.; Kirk, A.R.M., Fischer-Tropsch reaction studies with supported ruthenium catalysts I. product distributions at moderate pressures and catalyst deactivation, *J. Catal.* **1978**, *53*, 186–197.
- [97] Glebov, L.S.; Kliger, G.A., The molecular weight distribution of the products of the Fischer-Tropsch synthesis, *Russ. Chem. Rev.* **1994**, *63*, 185–194.
- [98] Puskas, I.; Hurlbut, R.S.; Pauls, R.E., Telomerization model for cobalt-catalyzed Fischer-Tropsch products, *J. Catal.* **1993**, *139*, 591–601.
- [99] Huff, Jr., G.A.; Satterfield, C.N., Liquid accumulation in a Fischer-Tropsch fixed-bed reactor, *Ind. Eng. Chem. Process Des. Dev.* **1985**, *24*, 986–995.
- [100] Sarup, B.; Wojciechowski, B.W., Studies of the Fischer-Tropsch synthesis on a cobalt catalyst. I. Evaluation of product distribution parameters from experimental data, *Can. J. Chem. Eng.* **1988**, *66*, 831–842.
- [101] Komaya, T.; Bell, A.T., Estimates of rate coefficients for elementary processes occurring during Fischer-Tropsch synthesis over Ru/TiO₂, *J. Catal.* **1994**, *146*, 237–248.
- [102] Jordan, D.S.; Bell, A.T., Influence of ethene on the hydrogenation of CO over ruthenium, *J. Phys. Chem.* **1986**, *90*, 4797–4805.
- [103] Kuipers, E.W.; Vinkenburg, I.H.; Oosterbeek, H., Chain length dependence of α -olefin readsorption in Fischer-Tropsch synthesis, *J. Catal.* **1995**, *152*, 137–146.
- [104] König, L.; Gaube, J., Fischer-Tropsch-Synthese. Neuere Untersuchungen und Entwicklungen, *Chem.-Ing.-Tech.* **1983**, *55*, 14–22.

- [105] Egiebor, N.O.; Cooper, W.C.; Wojciechowski, B.W., Carbon number distribution of Fischer-Tropsch CO-hydrogenation products from precipitated iron catalysts, *Can. J. Chem. Eng.* **1985**, *63*, 826–834.
- [106] Yates, I.C.; Satterfield, C.N., Hydrocarbon selectivity from cobalt Fischer-Tropsch catalysts, *Energy Fuels* **1992**, *6*, 308–314.
- [107] Inoue, M.; Miyake, T.; Inui, T., Alcohol synthesis from syngas on ruthenium-based composite catalysts, *J. Catal.* **1987**, *105*, 266.
- [108] Iglesia, E.; Vroman, H.; Soled, S.L.; Baumgartner, J.E.; Fiato, R.A., Selective catalysts and their preparation for catalytic hydrocarbon synthesis, *US Patent 5,036,032* **1991**.
- [109] Huff, Jr., G.A.; Satterfield, C.N., Some kinetic design considerations in the Fischer-Tropsch synthesis on a reduced fused-magnetite catalyst, *Ind. Eng. Chem. Process Des. Dev.* **1984**, *23*, 851–854.
- [110] Stenger, H.G.; Satterfield, C.N., Effect of liquid composition on the slurry Fischer-Tropsch synthesis. 1. Rate of reaction, *Ind. Eng. Chem. Process Des. Dev.* **1985**, *24*, 407–411.
- [111] Bianchi, C.L.; Ragaini, V., Experimental evidence of α -olefin readsorption in Fischer-Tropsch synthesis on ruthenium-supported ETS-10 titanium silicate catalysts, *J. Catal.* **1997**, *168*, 70–74.
- [112] Madon, R.J.; Iglesia, E., The importance of olefin readsorption and H₂/CO reactant ratio for hydrocarbon chain growth on ruthenium catalysts, *J. Catal.* **1993**, *139*, 576–590.
- [113] Madon, R.J.; Reyes, S.C.; Iglesia, E., Primary and secondary reaction pathways in ruthenium-catalyzed hydrocarbon synthesis, *J. Phys. Chem.* **1991**, *95*, 7795–7804.
- [114] Tau, L.-M.; Dabbagh, A.; Davis, B.H., Fischer-Tropsch synthesis: ¹⁴C tracer study of alkene incorporation, *Energy Fuels* **1990**, *4*, 94–99.
- [115] Zimmerman, W.H.; Bukur, D.B.; Ledakowicz, S., Kinetic model of Fischer-Tropsch selectivity in the slurry phase, *Chem. Eng. Sci.* **1992**, *47*, 2707–2712.
- [116] Schulz, H.; Rao, B.R.; Elstner, M., ¹⁴C-Studien zum Reaktionsmechanismus der Fischer-Tropsch-Synthese, *Erdöl Kohle* **1970**, *23*, 651–655.
- [117] Schulz, H.; Gökcebay, H., Fischer-Tropsch CO-hydrogenation as a means for linear olefins production, in J.R. Kosak, ed., *Catalysis of organic reactions*, Marcel Dekker, 1984 pp. 153–169.
- [118] Schulz, H.; Steen van, E.; Claeys, M., Specific inhibition as the kinetic principle of the Fischer-Tropsch synthesis, *Top. Catal.* **1995**, *2*, 223–234.

- [119] Hanlon, R.T.; Satterfield, C.N., Reactions of selected 1-olefins and ethanol added during the Fischer-Tropsch synthesis, *Energy Fuels* **1988**, *2*, 196–204.
- [120] Jordan, D.S.; Bell, A.T., The influence of butene on CO hydrogenation over ruthenium, *J. Catal.* **1987**, *108*, 63–76.
- [121] Jordan, D.S.; Bell, A.T., The influence of propylene on CO hydrogenation over silica-supported ruthenium, *J. Catal.* **1987**, *107*, 338–350.
- [122] Dwyer, D.J.; Somorjai, G.A., The role of readsorption in determining the product distribution during CO hydrogenation over Fe single crystals, *J. Catal.* **1979**, *56*, 249–257.
- [123] Dalla Betta, R.A.; Piken, A.G.; Shelef, M., Heterogeneous methanation: initial rate of CO hydrogenation on supported ruthenium and nickel, *J. Catal.* **1974**, *35*, 54.
- [124] Pichler, H.; Schulz, H. Elstner, M., Gesetzmässigkeiten bei der Synthese von Kohlenwasserstoffen aus Kohlenoxide und Wasserstoff, *Brennst. Ch.* **1967**, *48*, 78–87.
- [125] Hall, W.K.; Kokes, R.J.; Emmett, P.H., Mechanism studies of the Fischer-Tropsch synthesis: the incorporation of radioactive ethylene, propionaldehyde and propanol, *J. Am. Chem. Soc.* **1960**, *82*, 1027–1037.
- [126] Erkey, C.; Rodden, J.B.; Akgerman, A., Diffusivities of synthesis gas and n-alkanes in Fischer-Tropsch wax, *Energy Fuels* **1990**, *4*, 275–276.
- [127] Reid, R.C.; Prausnitz, J.M.; Poling, B.E., *The properties of gases and liquids*, McGraw-Hill, New York, fourth edn. **1987**.
- [128] Madon, R.J.; Iglesia, E., Hydrogen and CO intrapellet diffusion effects in ruthenium-catalyzed hydrocarbon synthesis, *J. Catal.* **1994**, *149*, 428–437.
- [129] Breman, B.B.; Beenackers, A.A.C.M.; Rietjens, E.W.J.; Stege, R.J.H., Gas-liquid solubilities of carbon monoxide, carbon dioxide, hydrogen, water, 1-alcohols ($1 \leq n \leq 6$), and n-paraffins ($1 \leq n \leq 6$) in hexadecane, octacosane, 1-hexadecanol, phenantrene, and tetraethylene glycol at pressures up to 5.5 MPa and temperatures from 293 to 552 K, *J. Chem. Eng. Data* **1994**, *39*, 647–666.
- [130] Chappelow, C.C.; Prausnitz, J.M., Solubilities of gases in high-boiling hydrocarbon solvents, *AIChE J.* **1974**, *20*, 1097–1103.
- [131] Donohue, M.C.; Shah, D.S.; Connally, K.G.; Venkatachalam, V.R., Henry's constants for C₅ to C₉ hydrocarbons in C₁₀ and larger hydrocarbons, *Ind. Eng. Chem. Fundam.* **1985**, *24*, 241–246.
- [132] Caldwell, L.; van Vuuren, D.S., On the formation and composition of the liquid phase in Fischer-Tropsch reactors, *Chem. Eng. Sci.* **1986**, *41*, 89–96.

- [133] Iglesia, E., Fischer-Tropsch synthesis on cobalt catalysts: structural requirements and reaction pathways, *Stud. Surf. Sci. Catal.* **1997**, *107*, 153–162.
- [134] Eckert, C.A., Molecular thermodynamics of chemical reactions, *Ind. Eng. Chem.* **1967**, *59*, 20–32.
- [135] Rybolt, T.R.; Wall, M.D.; Thomas, H.E.; Bramblett, J.W.; Phillips, M., Gas-solid chromatography and virial analysis of hydrocarbon adsorption on 13X zeolite, *J. Colloid Interface Sci.* **1990**, *138*, 113–121.
- [136] Miyabe, K.; Suzuki, M., Solvent effect on adsorption phenomena in reversed-phase liquid chromatography, *AIChE J.* **1995**, *41*, 536–547.
- [137] Miyabe, K.; Suzuki, M., Chromatographic study on liquid-phase adsorption on octadecylsilyl-silica gel, *AIChE J.* **1995**, *41*, 548–558.
- [138] Keldsen, G.L.; Nicholas, J.B.; Carrado, K.A.; Winans, R.E., Molecular modeling of the enthalpies of hydrocarbons on smectite clay, *J. Phys. Chem.* **1994**, *98*, 279–284.
- [139] Ruthven, D.M., *Principles of adsorption and adsorption processes*, Wiley & Sons, New York **1984**.
- [140] Kiselev, A.V.; Shcherbakova, K.D., in *Molecular Sieves*, Proceedings of the First International Conference on Zeolites, Soc. Chem. Ind., London, 1967 .
- [141] Xia, T.K.; Landman, U., Molecular dynamics of adsorption and segregation from an alkane mixture, *Science* **1993**, *261*, 1310–1312.
- [142] Herrington, E.F.G., The Fischer-Tropsch synthesis considered as a polymerization reaction, *Chem. Ind.* **1946**, *65*, 346.
- [143] Bub, G.; Baerns, M., Prediction of the performance of catalytic fixed bed reactors for Fischer-Tropsch synthesis, *Chem. Eng. Sci.* **1980**, *35*, 348–355.
- [144] Dixit, R.S.; Tavlarides, L.L., Kinetics of the Fischer-Tropsch synthesis, *Ind. Eng. Chem. Process Des. Dev.* **1983**, *22*, 1–9.
- [145] Nettelhoff, H.; Kokuun, R.; Ledakowicz, S.; Deckwer, W.-D., Studies on the kinetics of Fischer-Tropsch synthesis in slurry phase, *Ger. Chem. Eng.* **1985**, *8*, 177–185.
- [146] Huff, Jr., G.A.; Satterfield, C.N., Stirred autoclave apparatus for study of the Fischer-Tropsch synthesis in a slurry bed. 2. Analytical procedures, *Ind. Eng. Chem. Fundam.* **1983**, *22*, 258–263.
- [147] Kellner, C.S.; Bell, A.T., The kinetics and mechanism of carbon monoxide hydrogenation over alumina-supported ruthenium, *J. Catal.* **1981**, *70*, 418–432.
- [148] Takoudis, C.G., Power rate law studies in heterogeneously catalyzed reactions, *Ind. Eng. Chem. Prod. Res. Dev.* **1984**, *23*, 149–153.

- [149] Falbe, J.; Frohning, C.D., The raw materials future: critical examination of the role played by catalysis, *J. Mol. Catal.* **1982**, *17*, 117–132.
- [150] Ribeiro, F.H.; Schach von Wittenau, A.E.; Bartholemew, C.H.; Somorjai, G.A., Reproducibility of turnover rates in heterogeneous metal catalysis: compilation of data and guidelines for data analysis, *Catal. Rev.-Sci. Eng.* **1997**, *39*, 49–76.
- [151] Martin-Martinez, J.M.; Vannice, M.A., Carbon-supported iron catalysts: Influence of support porosity and preparation techniques on crystallite size and catalytic behavior, *Ind. Eng. Chem. Res.* **1991**, *30*, 2263–2275.
- [152] Snel, R., Supported iron catalysts in Fischer-Tropsch synthesis: Influence of the preparation method, *Ind. Eng. Chem. Res.* **1989**, *28*, 654–659.
- [153] Roe, G.M.; Ridd, M.J.; Cavell, K.J.; Larkins, F.P., Role of supports for cobalt-based catalysts used in Fischer-Tropsch synthesis of hydrocarbons, in D.M. Bibby; C.D. Chang; R.F. Howe; S. Yurchak, eds., *Methane Conversion*, Elsevier Science, 1988 pp. 509–515.
- [154] Iglesia, E.; Soled, S.L.; Fiato, R.A., Fischer-Tropsch synthesis on cobalt and ruthenium. Metal dispersion and support effects on reaction rate and selectivity, *J. Catal.* **1992**, *137*, 212–224.
- [155] Dry, M.E.; Shingles, T.; Boshoff, L.J.; Oosthuizen, G.J., Rate of the Fischer-Tropsch reaction over iron catalysts, *J. Catal.* **1972**, *25*, 99–104.
- [156] Dry, M.E., Advances in Fischer-Tropsch chemistry, *Ind. Eng. Chem. Prod. Res. Dev.* **1976**, *15*, 282–286.
- [157] Atwood, H.E.; Bennett, C.O., Kinetics of the Fischer-Tropsch reaction over iron, *Ind. Eng. Chem. Process Des. Dev.* **1979**, *18*, 163–170.
- [158] Shen, W.J.; Zhou, J.L.; Zhang, B.J., Kinetics of Fischer-Tropsch synthesis over precipitated iron catalyst, *J. Nat. Gas Chem.* **1994**, *4*, 385–400.
- [159] Deckwer, W.-D.; Kokuun, R.; Sanders, E.; Ledakowicz, S., Kinetic studies of Fischer-Tropsch synthesis on suspended Fe/K catalyst. Rate inhibition by CO₂ and H₂O, *Ind. Eng. Chem. Process Des. Dev.* **1986**, *25*, 643–649.
- [160] Whitters, Jr., H.P.; Eleizer, K.F.; Mitchell, J.W., Slurry-phase Fischer-Tropsch synthesis and kinetic studies over supported cobalt carbonyl derived catalysts, *Ind. Eng. Chem. Res.* **1990**, *29*, 1807–1814.
- [161] Ledakowicz, S.; Nettelhoff, H.; Kokuun, R.; Deckwer, W.-D., Kinetics of the Fischer-Tropsch synthesis in the slurry phase on a potassium-promoted iron catalyst, *Top. Catal.* **1985**, *24*, 1043–1049.
- [162] Chanenchuk, C.A.; Yates, I.C.; Satterfield, C.N., The Fischer-Tropsch synthesis with a mechanical mixture of a cobalt catalyst and a copper-based water gas

- shift catalyst, *Energy Fuels* **1991**, 5, 847–855.
- [163] Yates, I.C.; Satterfield, C.N., Intrinsic kinetics of the Fischer-Tropsch synthesis on a cobalt catalyst, *Energy Fuels* **1991**, 5, 168–173.
- [164] Satterfield, C.N.; Hanlon, R.T.; Tung, S.E.; Zou, Z.; Papaefthymiou, G.C., Effect of water on the iron-catalyzed Fischer-Tropsch synthesis, *Ind. Eng. Chem. Prod. Res. Dev.* **1986**, 25, 407–414.
- [165] Boudart, M., Two-step catalytic reactions, *AIChE J.* **1972**, 18, 465–478.
- [166] Boelee, J.H., *The Fischer-Tropsch synthesis in slurry phase reactors. Kinetics and mass transfer*, Ph.D. thesis, University of Eindhoven, Eindhoven, The Netherlands **1988**.
- [167] Yates, I.C.; Satterfield, C.N., Effect of carbon dioxide on the kinetics of the Fischer-Tropsch synthesis on iron catalysts, *Ind. Eng. Chem. Res.* **1989**, 28, 9–12.
- [168] Sarup, B.; Wojciechowski, B.W., Studies of the Fischer-Tropsch synthesis on a cobalt catalyst. III. Mechanistic formulation of the kinetics of selectivity for hydrocarbon formation, *Can. J. Chem. Eng.* **1989**, 67, 620–627.
- [169] Rofer-De Poorter, C.K., Untangling the water gas shift from Fischer-Tropsch: a gordian knot?, in R.G. Herman, ed., *Catalytic conversion of synthesis gas and alcohols to chemicals*, Plenum Press, New York, 1984 .
- [170] Feimer, J.L.; Silveston, P.L.; Hudgins, R.R., Steady-state study of the Fischer-Tropsch reaction, *Ind. Eng. Chem. Prod. Res. Dev.* **1981**, 20, 609–615.
- [171] Graaf, G.H.; Sijtsema, P.J.J.M.; Stamhuis, E.J.; Joosten, G.E.H., Chemical equilibria in methanol synthesis, *Chem. Eng. Sci.* **1986**, 41, 2883–2890.
- [172] Anikeev, V.I.; Yermakova, A.; Gudkov, A.Y., Energy-chemical coal processing. 3. Fischer-Tropsch synthesis of light and heavy hydrocarbon fuels from coal gasification products, *Chem. Sust. Dev.* **1996**, 4, 119–129.
- [173] Krishna, K.R.; Bell, A.T., Estimates of the rate coefficients for chain initiation, propagation, and termination during Fischer-Tropsch synthesis over Ru/TiO₂, *J. Catal.* **1993**, 139, 104–118.
- [174] Zhang, X.; Biloen, P., A transient kinetic observation of chain growth in the Fischer-Tropsch synthesis, *J. Catal.* **1986**, 98, 468–476.
- [175] Rice, N.M.; Wojciechowski, B.W., On interpreting FT product distribution data, *Can. J. Chem. Eng.* **1987**, 65, 102–112.
- [176] Zimmerman, W.H., *Kinetic modeling of the Fischer-Tropsch synthesis*, Ph.D. thesis, Texas A&M University, College Station TX, USA **1990**.

3

Experimental

3.1 Experimental Setup

Continuous laboratory reactors are used to measure reaction kinetics and product distributions of the Fischer-Tropsch synthesis. Most studies were performed in atmospheric gas-solid packed bed reactors. Packed beds at higher pressures were applied by, for example, Lox et al. [1], Bub and Baerns [2], and Bukur et al. [3]. Wojciechowski [4] showed that integral reactors are unsuitable for fundamental studies of the FTS. Continuous recycle reactors are to be preferred for gas-solid kinetic measurements: for example, the Berty reactor [5, 6] or the spinning basket reactor [7]. Slurry phase Fischer-Tropsch experiments are performed in slurry reactors with either a continuous gas-phase and a liquid batch of FT-wax or a high-boiling solvent. These reactor systems commonly are perfectly mixed recycle reactors with turbine impellers [8] or gas-inducing stirrers.

Measurements used for the development of kinetic expressions and selectivity models were carried out in several experimental setups. The equipment for the experiments of the gas-solid and gas-slurry Fischer-Tropsch synthesis as well as the product analysis and the experimental procedures are described below. Fischer-Tropsch experiments were carried out in a gas-continuous Spinning Basket Reactor (SBR) [9] and in a slurry reactor (SR), both in a setup shown in Figure 3.1. H_2 (**1**) and CO (**2**) (purities of 99.999 % and 99.8 %, respectively) were fed with separate mass flow controllers (**5,6**) (range: $0\text{--}4.2 \cdot 10^{-3} \text{ Nm}^3 \text{ s}^{-1}$). Two purification columns (**7**) were used to remove possible catalyst poisons like iron carbonyl, sulfides, and oxygen. The columns were packed with BASF R3-11 and BASF R5-10 catalysts at 473 K and 323 K, respectively. Synthesis gas was preheated at 523 K (**12**). To prevent product condensation, the product tubes from the reactor down to the high-pressure gas-liquid separator and condenser (**19**) ($P=P_R$, $T=423 \text{ K}$) were heated at 473 K. Condensed wax products were removed periodically (**20**). The reactor pressure was measured (**13**) (range: 0.1–10.0 MPa; accuracy 0.01 MPa) and kept constant via a PID-controlled pneumatic needle valve (**22**). The remaining gaseous stream was reduced to atmospheric pres-

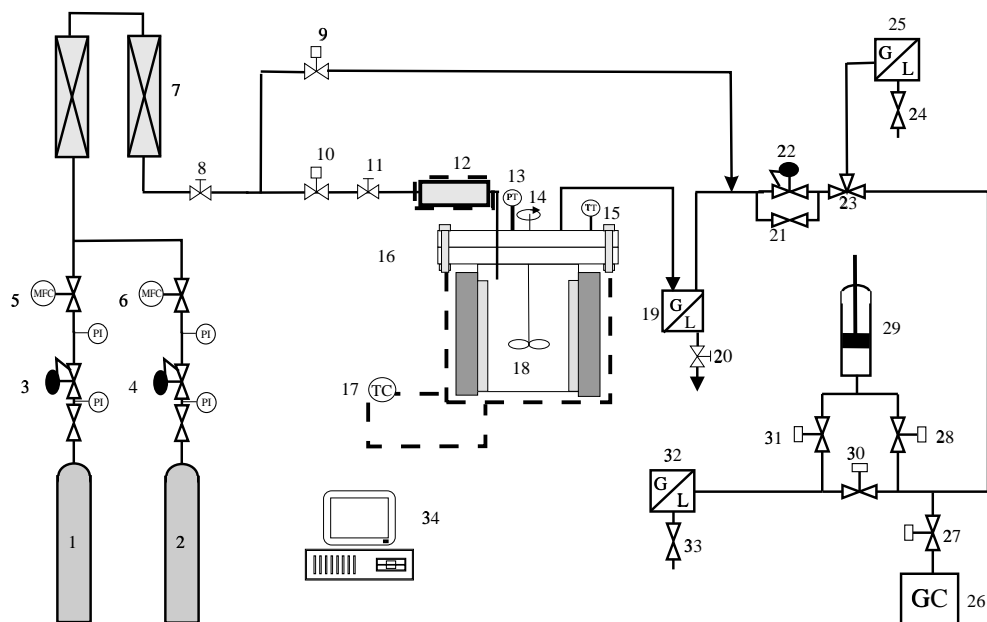


Figure 3.1 Experimental set-up.

1, 2: gas cylinders CO and H₂, respectively; 3, 4: pressure reducers; 5, 6: mass flow controllers; 7: purification columns; 8, 11, 20, 21, 24, 33: valves; 9, 10, 27, 28, 30, 31: magnetic valves; 12: pre-heater; 13: pressure transmitter; 14: magnetic stirrer; 15: temperature transmitter; 16: reactor; 17: reactor temperature control; 18: slurry or spinning basket reactor; 19: high-pressure condenser; 22: pressure reducer; 23: three-way valve; 25, 32: low-pressure condensers; 26: on-line GC analysis; 29: flow meter; 34: personal computer; 35: baffles.

sure. A small sample flow was split from the main flow and led to a heated injection valve of an on-line gas chromatograph (26). The volumetric flow rate of the gaseous stream was determined with a thermostated flow meter (29) (373 K). The flow was measured via the displacement of a mercury-sealed piston in a glass tube. Finally, the product stream was transported to a low-pressure condenser at 273 K (25, 32). The condensed products from this condenser were separated manually into an aqueous and an oil phase (24, 33).

3.1.1 Spinning Basket Reactor

The spinning basket reactor shown in Figure 3.2 is a stainless steel reactor ($V = 285 \text{ cm}^3$, $H = 8.6 \text{ cm}$, $D = 6.5 \text{ cm}$) with the catalyst particles placed in four baskets (3)

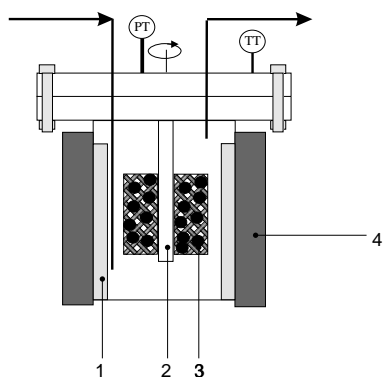


Figure 3.2 Spinning basket reactor.
1: baffles; 2: stirrer shaft; 3: baskets with catalyst particles; 4: electrical heating.

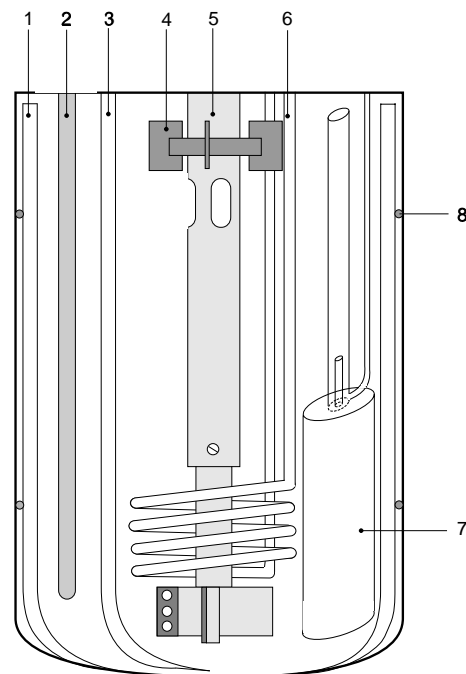


Figure 3.3 Slurry reactor.
1: baffles; 2: temperature measurement; 3: liquid drain; 4: turbine impeller gas phase; 5: self-inducing stirrer; 6: cooling coil; 7: continuous filtering unit; 8: distance ring.

mounted on the stirrer shaft (2). A stirrer speed of 33 s^{-1} ensured complete mixing of the gas phase, and resulted in high mass and heat transfer rates. Preliminary experiments showed that the conversion of synthesis gas and the hydrocarbon selectivity did not change by varying the stirrer speed between 20 and 33 s^{-1} . Vortex formation was prevented by four vertical baffles (1) with a width of 8 mm each. The reactor was electrically heated (4), and the temperature was measured with a PT-100 resistance thermometer (TT) (range: 373-773 K; accuracy: 0.2 K).

3.1.2 Slurry Reactor

The slurry reactor is a 1.8 dm^3 autoclave ($H = 18.2 \text{ cm}$, $D = 12.0 \text{ cm}$) made by Medimex (Figure 3.3). The autoclave was connected to a magnetic stirrer (5). The shaft of

the impeller was hollow with small holes in the stirrer blades and sleeves in the top of the shaft. This enabled the vapor in the reactor to be recycled through the liquid by the suction created by the impeller. Above 15 s^{-1} strong circulation of the gas phase in the autoclave was observed. The impeller was always driven at 25 s^{-1} to ensure complete mixing of the liquid phase, uniform distribution of the catalyst, and high mass and heat transfer rates [10]. A turbine impeller (**4**) mounted on the top of the shaft was applied to obtain a homogeneous gas phase. Four vertical baffles (**1**) (width 10 mm) were used to prevent the formation of vortices. A distance ring of 3 mm (**8**) was applied to prevent undesired catalyst accumulation between the reactor wall and the baffles. The temperature of the reactor was controlled by the combination of a 3000 W electric heating mantle with air cooling and a cooling coil (air) in the slurry phase (**6**). The temperature was measured with a PT-100 resistance thermometer (range 273-773 K; accuracy: 0.2 K) inserted in the liquid phase (**2**).

During the Fischer-Tropsch reaction, liquid products can be formed. The level of the slurry was maintained constant using a home-made filtering unit (**7**). The liquid products were removed via a filter (sintered metal $5 \mu\text{m}$), whereas the catalyst particles remained inside the reactor. The liquid and gas phase volumes applied were 730 and 985 cm^3 , respectively.

Initially, the reactor was filled with FT wax (Sasol-Schumann type 4110) mainly consisting of paraffins with carbon number between 21 and 36. The product distribution of the wax was bell-shaped with a maximum at carbon number 28. The liquid density of the applied wax was determined volumetrically as:

$$\rho_L = 820.0 - 0.569(T - 273.15) \quad [\text{kg m}^{-3}] \quad (3.1)$$

3.2 Catalyst

The catalyst applied was a commercial precipitated iron catalyst (type LP 33/81) synthesized by Ruhrchemie AG (Oberhausen, Germany). The synthesis procedure was described by Frohning et al. [11]. The Fe, Cu, and K content was measured by atomic absorption spectroscopy and the SiO_2 gravimetrically. The elemental composition was found to be 74.3 % Fe, 3.7 % Cu, 3.1 % K, and 18.6 % SiO_2 . The composition of this catalyst was also determined by Bukur et al. [12], Lox et al. [1], and by Donnelly and Satterfield [13]. Their results are in reasonable agreement with ours. The catalyst pellets were calcined in air at 573 K for 5 h and crushed and sieved to the appropriate particle diameter range.

3.2.1 BET Measurements

The specific surface areas and the texture of the catalysts were determined by nitrogen physisorption according to the Braun-Emmett-Teller (BET) method. The measurements were performed with a Micromeritics ASAP 2400. Sieve fractions between 140 and 150 μm were out-gassed at 525 K for 2 hours before the actual measurements.

Table 3.1 Texture of the catalyst (BET).

	Surface area (m^2/g)	Pore volume (cm^3/g)	Average mesopore diameter (nm)
As received	323	0.64	8.0
Calcined	309	0.61	7.9
After FT reaction ¹	88	0.31	13.9

¹ After SBR experiments (1800 hrs time-on-stream)

3.2.2 Scanning Electron Microscopy (SEM)

SEM studies of both the fresh catalyst and the catalyst subjected to FT synthesis for 1800 hours on stream are shown in Figure 3.4a and Figure 3.4b, respectively. The catalyst particles are composed of agglomerated crystals. We observed a substantial increase of crystal size after 1800 hrs of duty, relative to virgin catalyst (Figure 3.4b). The SEM micrograph in Figure 3.4b shows a different (more smooth) surface structure with white-colored edges on the crystals in comparison to the fresh catalyst sample (Figure 3.4a).

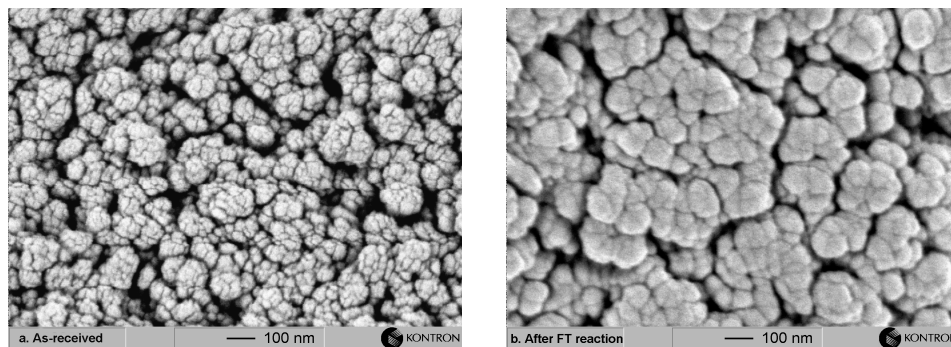


Figure 3.4 SEM micrographs of the Ruhrchemie catalyst samples. a. As-received catalyst; b. Catalyst after 1800 FT synthesis.

3.3 Product Analysis

Kinetic research of the FTS requires an accurate product analysis. The analytical section has to measure the complete product distribution of at least C_{1-30} paraffins and olefins as well as the reactants (CO and H_2) and CO_2 and H_2O . Analysis of isomers (branched products) and oxygenates is necessary if the concentration of these components is significant. Most gas chromatographic systems have a complex arrangement of multiple columns and detectors [14–16]. However, on-line single column gas chromatographic analysis are reported as well [17, 18]. In most studies the reactants and non-condensable products (CO_2 and C_{1-5} hydrocarbons) are analyzed on-line, while the condensed products (C_{6+} hydrocarbons, and H_2O) are collected, weighed, separated in two phases and analyzed off-line, see for example [3, 4, 13]. Some disadvantages of this approach are [14, 19, 20]: 1) Difficult quantification; components appear in more phases and samples. 2) Reactors must run at high conversions or high catalyst load in order to accumulate condensates. 3) Long analysis times. In contrast, on-line analysis of all products is rapid and accurate, so this is the preferred method.

The analysis system used in this study is illustrated in Figure 3.5. The total product stream was split in three flows: on-line gaseous, oil phase (low-pressure condenser), and wax phase (high-pressure condenser).

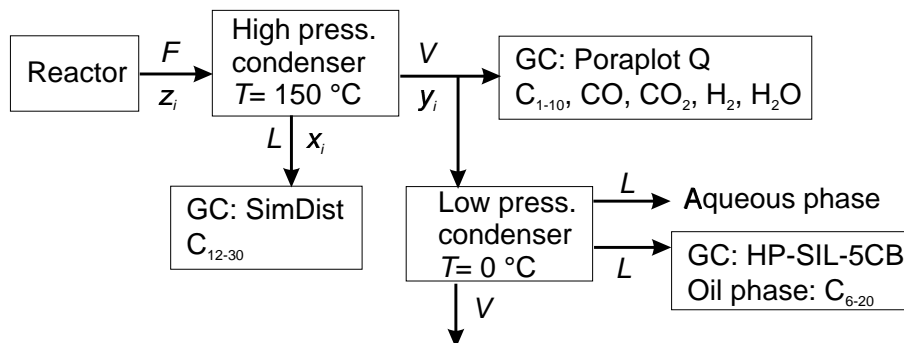


Figure 3.5 Scheme of the liquid and gaseous streams in the condensers and analysis system.

The gaseous phase was analyzed with a Hewlett-Packard 5980A Gas Chromatograph (GC). The gaseous components were linear paraffins C_1-C_{10} , α -olefins C_2-C_{10} , 1-alcohols C_1-C_4 , CO_2 , H_2O , CO , and H_2 . The gas chromatograph was equipped with a heated (473 K) 10-port gas injection valve, with a sample loop and a loop for the Deferred Standard (DS), methane. The DS method for on-line gas chromatographic

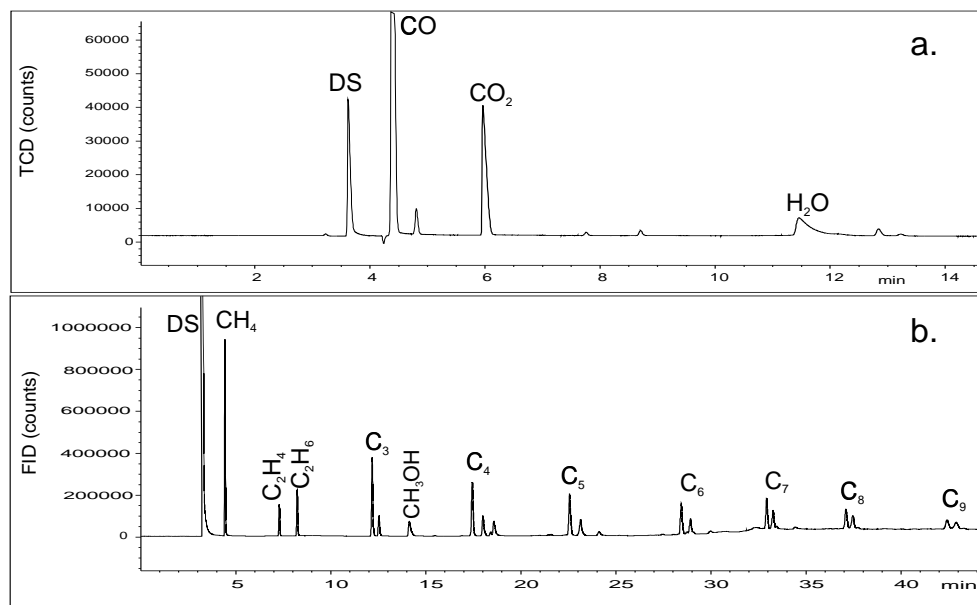


Figure 3.6 Typical on-line gas chromatograms for an SBR experiment (523 K, 1.50 MPa, $(\text{H}_2/\text{CO})_{\text{feed}}=2$, $\Phi_{v,0}/W=1.51 \cdot 10^{-3} \text{ Nm}^3 \text{ kg}_{\text{cat}}^{-1} \text{ s}^{-1}$). a. TCD signal; b. FID signal.

analysis was reported by Marsman et al. [21]. The relative DS technique improves the reliability of the analysis and reduces the calibration efforts. Sample injection on the column was performed after the injection of the DS. The DS and sample were subsequently injected at an initial temperature of the GC of 303 K. The initial temperature was maintained for 8 min, after which the oven temperature was increased to 393 K at the rate of 20 K/min. After 5 min at 393 K the temperature was increased with 10 K/min to 453 K. After another 5 min the temperature was increased at the rate of 10 K/min to the final temperature of 523 K. This temperature was maintained until all the components of interest had eluted. The complete on-line analysis time was 60 min. The components were separated on a capillary column (25 m x 0.53 mm i.d. coated with 0.020 mm Poraplot Q, carrier flow, 0.017 ml s^{-1}). H_2 , CO, CO_2 , and H_2O were detected with a Thermal Conductivity Detector (TCD, see Figure 3.6a) (548 K) and the hydrocarbon products with a Flame Ionization Detector (FID, see Figure 3.6a) (548 K; hydrogen flow, 0.53 ml s^{-1} ; air flow, 7.5 ml s^{-1}) placed in series. Both detectors were connected to an integrator and a personal computer for peak integration and data storage. Since the thermal conductivity of hydrogen almost equals that of

helium, detection is very difficult due to negative peaks, non-linearity, and poor sensitivity. Therefore, the mole fraction of hydrogen was determined in a separate analysis with nitrogen as a carrier gas. Peaks were identified using a gas chromatograph-mass spectrometer (GC-MS) Hewlett Packard 5890A combination and taking into account the logical sequence of retention times of homologous series of hydrocarbons.

The mole fractions of all detected components i were calculated from the integrated peak areas (A_i), according to:

$$y_i = C_i \frac{A_i}{A_{DS}} \quad (3.2)$$

where C_i is the calibration factor for component i and A_{DS} is the integrated area of the deferred standard. Calibration of H_2 , CO , CO_2 , paraffins C_1 - C_5 , olefins C_2 - C_4 , and CH_3OH was performed with calibration mixtures supplied by Scott Specialty Gases (Breda, The Netherlands). For the remaining hydrocarbon components C_{5+} , a correlation for the calibration factors proposed by Dierickx et al. [22] was used. It is based on the standard Gibbs energy change ($-\Delta G_{ox}^0$) at 298 K for complete oxidation to CO_2 and H_2O . The calibration constants were calculated relative to pentane using relative molar response factors $RMR(i)$:

$$C_i = C_{\text{pentane}} \frac{RMR(\text{pentane})}{RMR(i)} \quad (3.3)$$

The thermal conductivity detector was calibrated for water by injection of a gas flow with a known concentration of water. The concentration of water in the carrier gas nitrogen was adjusted with two mass flow controllers and a continuous evaporator mixer from Bronkhorst (Ruurlo, The Netherlands).

The hydrocarbons in the oil phase of the low-pressure condenser (C_{10} - C_{20}) were separated on an HP-SIL 5-CB capillary column with a Hewlett Packard 5890A gas chromatograph (see Figure 3.7a). For these components the mass response factors of the flame ionization detector were taken as constant.

The wax samples of the high-pressure condenser contain C_{15+} hydrocarbons and were analyzed with a 10 m HT-SimDist column on a Hewlett Packard 5890A gas chromatograph. The wax samples were dissolved in CS_2 (0.5-1 mass%) and were injected on-column to the capillary column to prevent splitter discrimination [4] at an initial temperature of 313 K. The temperature was raised with an optimized program to 673 K to eluate components until C_{40} see Figure 3.7b). Peak identification was performed using injection of pure components.

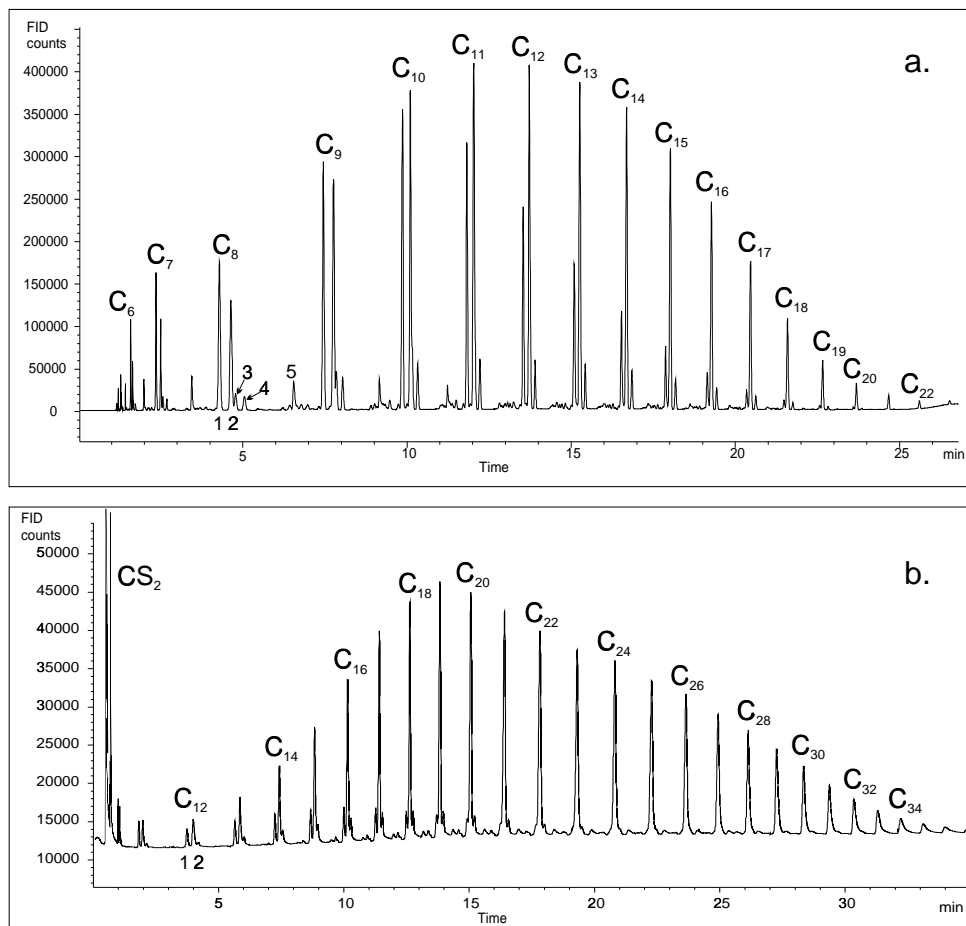


Figure 3.7 Typical off-line analysis of an SBR experiment at 523 K, 1.50 MPa, $(\text{H}_2/\text{CO})_{\text{feed}}=2$ and a space velocity of $1.51 \cdot 10^{-3} \text{ Nm}^3 \text{ kg}_{\text{cat}}^{-1} \text{ s}^{-1}$. a. Hydrocarbon analysis of the low-pressure condensate, 1: 1-octene, 2: octane, 3: cis-2-octene, 4: trans-2-octene, 5: 1-hexanol. b. Wax analysis of high-pressure condenser, 1: 1-dodecene, 2: dodecane.

3.3.1 Flash Calculations

The product composition of the reactor outlet flow (F) at reactor pressure and temperature was obtained by combining the analysis of several samples, see Figure 3.5. The composition and flow rate (L) of the liquid phase (x_i) were determined by GC analysis of the wax samples and gravimetrically, respectively. The composition of the gas phase from the high-pressure condenser was determined by combining the on-line analysis (C_{1-10}) and the oil phase of the low-pressure condenser (C_{10-20}). The flow rate (V) was calculated using a thermostated volumetric flow meter, whereas the liquid flow rate (L) was calculated from the weighed mass and the analyzed composition of the high-pressure condensate. The liquid phase was assumed to obey Raoult's law and the gas phase the ideal gas law. Furthermore, it was assumed that the hydrocarbon products behave like paraffins. The vapor pressures of the pure paraffins at a given temperature were calculated using the method of Caldwell and van Vuuren [23]:

$$P_n = P_0 \beta^n \quad (3.4)$$

where

$$\beta = \exp(-427.218(1/T - 1.029807 \cdot 10^{-3})) \quad (3.5)$$

The equilibrium constant was calculated using Raoult's law:

$$K_i \equiv y_i/x_i = P_i/P \quad (3.6)$$

A molar balance for component i gives:

$$Fz_i = Lx_i + Vy_i \quad (3.7)$$

and the total molar balance:

$$F = L + V \quad (3.8)$$

Solving eqs 3.4-3.8 gives the molar composition of the outlet stream of the reactor (F, z_i). Figure 3.8 shows an example of the GC analysis from the on-line and off-line (wax and fuel) samples resulting in a complete product distribution using vapor-liquid equilibria and flash calculations.

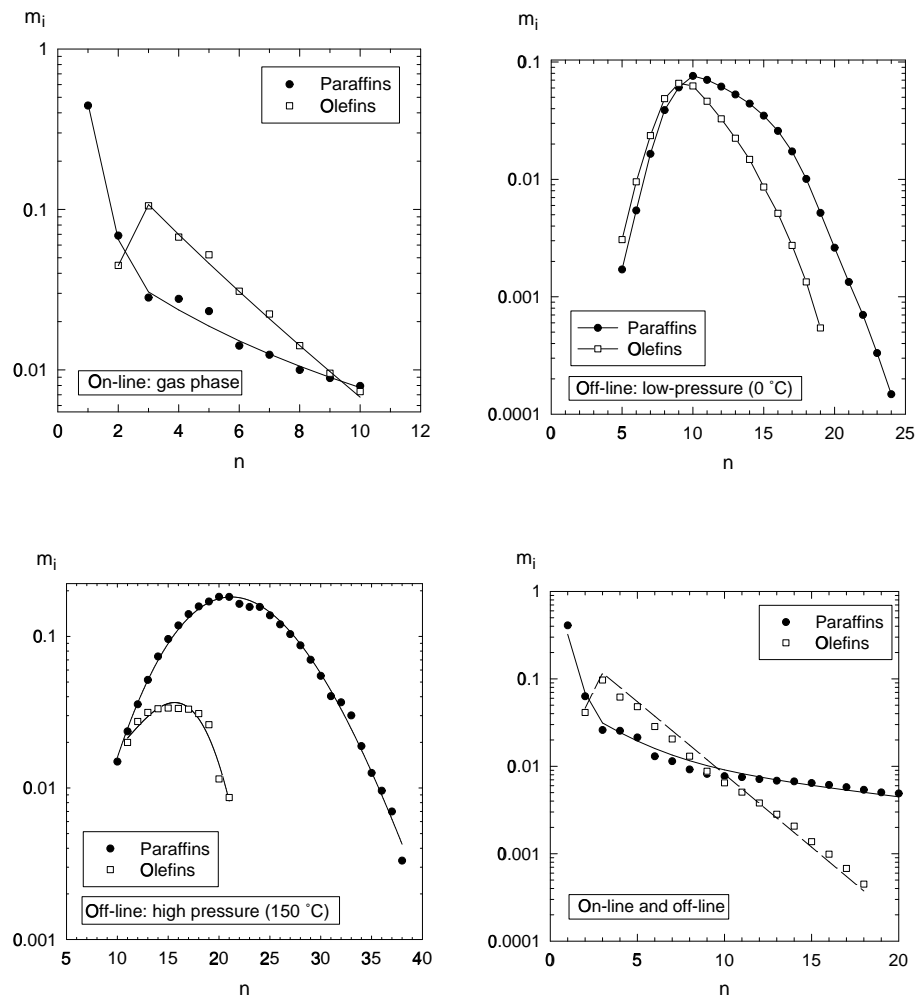


Figure 3.8 Product distributions of on-line and off-line GC analysis and vapor-liquid equilibria and flash calculations for a typical SBR experiment (A1).

3.4 Experimental Procedure

Blank experiments showed that the packed purification columns and the reactor, without catalyst, caused no significant conversion of the synthesis gas. The catalyst was pretreated with hydrogen at a flow rate of $0.83 \cdot 10^{-3} \text{ Nm}^3 \text{ kg}_{cat}^{-1} \text{ s}^{-1}$ according to Bukur et al. [24] in all experiments. The gas space velocity was based on the total mass of the unreduced catalyst. The reactor temperature, T , was increased linearly from 293 K to 553 K by 0.017 K s^{-1} . T remained at 553 K for 24 hours at atmospheric pressure. The reactor pressure in the slurry reactor was maintained at 1.0 MPa to prevent excessive solvent evaporation. After reduction, synthesis gas was fed to the reactor at reference conditions. For the kinetic experiments in the spinning basket reactor these conditions were: 523 K, 1.50 MPa, $(\text{H}_2/\text{CO})_{feed}=2$ and a space velocity of $1.51 \cdot 10^{-3} \text{ Nm}^3 \text{ kg}_{cat}^{-1} \text{ s}^{-1}$. For the slurry reactor they were: 523 K, 1.50 MPa, $(\text{H}_2/\text{CO})_{feed}=0.67$ and a space velocity of $0.50 \cdot 10^{-3} \text{ Nm}^3 \text{ kg}_{cat}^{-1} \text{ s}^{-1}$.

The experimental conditions for the experiments in both the spinning basket reactor and the slurry reactor are summarized in Table 3.2. A summary of relevant experimental data is given in Appendixes A and B.

Table 3.2 Experimental conditions.

Series	A	B	C
Reactor	SBR	SR	SR
T (°C)	225-275	250	250
P (MPa)	0.8-4.0	1.2-4.0	1.2-4.0
Φ_v^{in} / W ($10^{-3} \text{ Nm}^3 \text{ kg}_{cat}^{-1} \text{ s}^{-1}$)	0.5-2.0	0.25-0.50	0.17-0.77
F (-)	0.25-4.0	0.25-4.0	0.5-4.0
W (10^{-3} kg)	2.34	7.32	7.26
d_p (μm)	125-160	40-50	40-50

Liquid products were accumulated in high and low-pressure condensers for a typical period of 6-8 hours during steady state of the reactor system. The products were collected and weighed before analysis. Several on-line GC analysis were performed during this period. After changing the process conditions the reactor operated undisturbed before a new mass balance period was started. The stabilization time for the SBR between two subsequent experiments was taken as 4 gas residence times:

$$t_{\text{steady}} = 4 \frac{1.013 \cdot 10^5 PV}{RT \Phi_{v,0} C_{G,0}} \quad (3.9)$$

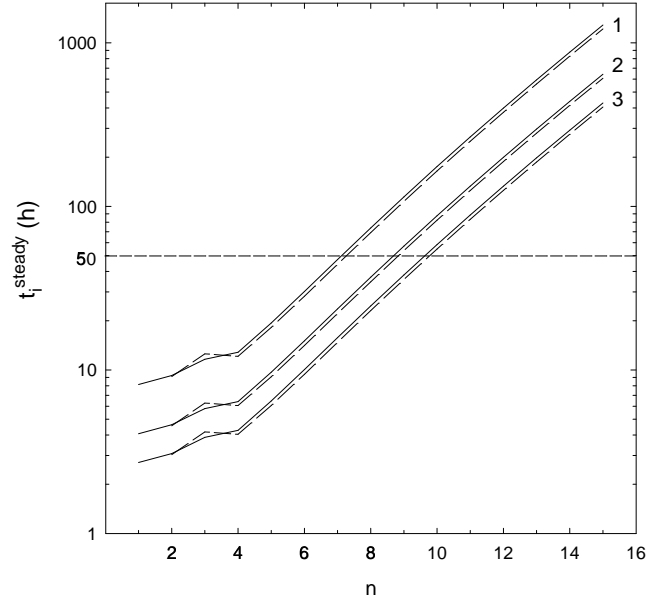


Figure 3.9 Stabilization time in gas-slurry reactor (t_i^{steady} , eq 3.10) for paraffins (solid lines) and olefins (dashed lines) as a function of carbon number (n) at: 1. $P_R = 40$ bar and $\Phi_{v,0} = 2 \cdot 10^{-4} \text{ Nm}^3 \text{ s}^{-1}$, 2. $P_R = 20$ bar and $\Phi_{v,0} = 2 \cdot 10^{-4} \text{ Nm}^3 \text{ s}^{-1}$, 3. $P_R = 20$ bar and $\Phi_{v,0} = 3 \cdot 10^{-4} \text{ Nm}^3 \text{ s}^{-1}$.

where $\Phi_{v,0}$ and $C_{G,0}$ are the flow rate and gas concentration at normal conditions ($T_0 = 273 \text{ K}$, $P_0 = 0.1013 \text{ MPa}$). The maximum time for achieving steady state was 7.9 hours. Therefore, minimal 12 h waiting time between two experiments was applied in the spinning basket reactor experiments.

The stabilization time of component i leaving the reactor in the gas phase after changing the reactor conditions takes into account the gas-liquid solubility of products in the slurry liquid:

$$t_i^{\text{steady}} = 4 \frac{1.013 \cdot 10^5 (P V_G + m_i^{GL} P V_L)}{RT \Phi_{v,0} C_{G,0}} \quad (3.10)$$

where V_G and V_L are the gas and liquid volume, respectively and m_i^{GL} is the solubility (C_L/C_G) of component i . The stabilization time is a function of carbon number and increases rapidly with chain length due to increasing solubility. Figure 3.9 shows the

required stabilization time for several experimental conditions as a function of carbon number, as calculated with eq 3.10. The relevant gas-liquid solubilities of paraffins and olefins were obtained from Marano and Holder [25]. A minimum stabilization time of 48 hours was applied in the slurry reactor experiments. Several on-line GC analysis were performed to ensure steady state in the gas flow from the reactor.

The consistency and accuracy of both the analysis and the reactor system was checked regularly using atomic balances for the components H, C, and O. For example, the carbon balance gives:

$$\Delta C = \frac{(y_{CO})_{in}}{(y_{CO} + y_{CO_2} + \sum_{n=1} n y_{C_n H_{2n+2}} + \sum_{n=2} n y_{C_n H_{2n}})_{out}} \frac{\Phi_{v,0}^{in}}{\Phi_{v,0}} \quad (3.11)$$

Mass and atomic balances were typically within 80-100 %.

Internal diffusion is insignificant for $d_p < 0.16$ mm [26, 27]. Calculation of the criteria of Weisz and Prater [28] for the reactants CO and H₂ also proved that no intra-particle diffusion limitations occurred at the highest rates observed in both the slurry and the spinning basket reactor, assuming the catalyst pores to be filled with long-chain (C₂₈) hydrocarbon waxes.

3.5 Reaction Rates and Selectivities

The formation rate of a product, R_i , follows from a material balance over the reactor, assuming ideal gas behavior:

$$R_i = y_i \frac{\Phi_{v,0}}{W} \frac{P_0}{RT_0} \quad (3.12)$$

where y_i is the mole fraction of component i in the reactor effluent, P_0 and T_0 correspond to normal conditions at 0.1013 MPa and 273 K, W is the weight of the catalyst, and $\Phi_{v,0}$ is the reactor outlet flow at normal conditions. Reaction rates of the reactants H₂ and CO follow from:

$$-R_i = (y_i^{in} \Phi_{v,0}^{in} - y_i \Phi_{v,0}) \frac{P_0}{RT_0 W} \quad (3.13)$$

The corresponding conversions of H₂ and CO are:

$$X_i = 1 - \frac{y_i \Phi_{v,0}}{y_i^{in} \Phi_{v,0}^{in}} \quad (3.14)$$

and the total synthesis gas conversion:

$$X_{CO+H_2} = 1 - \frac{(y_{H_2} + y_{CO})\Phi_{v,0}}{(y_{H_2}^{in} + y_{CO}^{in})\Phi_{v,0}^{in}} \quad (3.15)$$

The synthesis reactions can be considered as a combination of the Fischer-Tropsch (FT) and the water gas shift (WGS) reactions (see eqs. 1.1-1.2). Water is a primary product of the FT reaction, and CO₂ can be produced by the water gas shift reaction ($R_{WGS} = R_{CO_2}$). The reaction scheme neglects formation of oxygenated products. The selectivity to alcohols was lower than 5 wt% for the on-line products in our experiments. No alcohols were detected in the waxeous fractions, leading to a much lower selectivity in the total product yield. The CO consumption to hydrocarbons follows from:

$$R_{FT} = -R_{CO} - R_{WGS} \quad [\text{mol kg}_{cat}^{-1} \text{ s}^{-1}] \quad (3.16)$$

The molar selectivity to product i was calculated from the experimental mole fractions relative to all products (n) considered:

$$m_i = \frac{y_i}{\sum_{j=1}^n y_j} \quad (3.17)$$

The mass selectivity of a single product or of a product range was calculated from the corresponding selectivity or mole fraction y_i and molar mass M_i :

$$w_i = \frac{y_i M_i}{\sum_{j=1}^n y_j M_j} \quad (3.18)$$

$$w_{2-4} = \frac{\sum_{i=2}^4 w_i}{\sum_{i=1}^n w_i} \quad (3.19)$$

3.5.1 Model Parameters

The adjustable model parameters for the several kinetic and selectivity models in Chapters 4-6 were calculated by minimizing the χ^2 function with the Levenberg-Marquardt method [29]:

$$\chi^2 = \sum_i \frac{(x_i^{exp} - x_i^{mod})^2}{\sigma^2} \quad (3.20)$$

where x_i^{exp} and x_i^{mod} are the experimental and model value of the selectivity or the reaction rate, respectively, σ^2 is the relative variance of the experimental data point. The Levenberg-Marquardt method makes use of a combination between the steepest descent and the inverse hessian method.

The accuracy of the fitted model relative to the experimental data was obtained from the *MARR* (Mean Absolute Relative Residual) function

$$MARR = \sum_i^n \left| \frac{x_i^{exp} - x_i^{mod}}{x_i^{exp}} \right| \frac{1}{n} \times 100 \quad (3.21)$$

where n is the total number of optimized data points, x_i^{exp} is the experimental selectivity or reaction rate of the i th data point, and m_i^{mod} is the model prediction of the selectivity or reaction rate.

The relative variance (s_{rel}) was used to compare several models with different numbers of model parameters:

$$s_{rel} = \left(\sum_i^n \left(\frac{x_i^{exp} - x_i^{mod}}{x_i^{exp}} \right)^2 \frac{1}{n - m} \right)^{\frac{1}{2}} \times 100 \quad (3.22)$$

with n , the number of data points included and m , the number of optimized parameters.

The relative residual (*RR*) between experimental and predicted data will be used to show the deviations between model and experiment:

$$RR = \frac{x_i^{exp} - x_i^{mod}}{x_i^{exp}} \times 100 \quad (3.23)$$

Bartlett's test was used to investigate whether the differences in accuracy of the various kinetic models were statistically significant [30]. For a number of H competitive models, the Bartlett's test calculates a critical χ_c^2 value:

$$\chi_c^2 = \frac{\ln S_{av}^2 \sum_{h=1}^H df_h - \sum_{h=1}^H df_h S_h^2}{1 + \frac{1}{3(H-1)} \left(\sum_{h=1}^H df_h^{-1} - \left(\sum_{h=1}^H df_h \right)^{-1} \right)} \quad (3.24)$$

where S_h^2 is the total variance between the experiments and model h and S_{av}^2 is the average total variance of H models:

$$S_h^2 = df_h^{-1} \sum_{i=1}^n (R_i^{exp} - R_i^{mod})^2 \quad (3.25)$$

$$S_{av}^2 = \frac{\sum_{h=1}^H df_h S_h^2}{\sum_{h=1}^H df_h} \quad (3.26)$$

df_h is the degrees of freedom for the h th model predictions and is equal to $df_h = n - m_h$, n is the number of data points and m_h is the number of optimized parameters of the h th model. Bartlett's test compares χ_c^2 with a tabulated $\chi_r^2(H - 1)$ value [31]. Models were subsequently rejected, until χ_c^2 was below the tabulated value.

3.6 Catalyst Activity and Selectivity

A detailed description of the activity and selectivity of the commercial Ruhrchemie iron catalyst is given in Chapters 4-6. A brief comparison between our catalyst tests and available literature data with the same catalyst is presented here.

In Table 3.3 the catalyst activity and selectivity is compared to that reported by Bukur et al. [3] in a fixed bed reactor and of Donnelly and Satterfield [13] in a slurry reactor at approximately similar conditions and the same commercial Ruhrchemie catalyst. Since the results of Bukur et al. [3] were obtained in an integral fixed bed reactor, reaction rates and conversions vary with position and cannot be compared directly. The selectivity to gaseous hydrocarbon products is similar. The olefin content in our experiments is slightly lower than in their study. The observed differences can probably be attributed to the differences in activation procedures, different catalyst aging patterns and to the different reactor types applied. The data of Donnelly and Satterfield [13] are obtained at a higher reactor temperature and in a slurry reactor. The reactor type influences the activity as well as the selectivity of the process. Both the conversion and the reaction rate of synthesis gas are higher in our experiments, whereas the hydrocarbon selectivity is higher to low-molecular hydrocarbons.

3.7 Catalyst Deactivation

Dry [32] mentioned four factors responsible for FT catalyst aging: (1) conversion of active phase, (2) sintering, (3) deposition of carbonaceous material, and (4) chemical poisoning by, for example, sulfur. The BET surface areas of the catalyst before and after FT reaction in an SBR test were determined by N₂-physisorption (see Table 3.1). The BET area of the fresh and calcined catalyst was 323 and 309 m² g⁻¹, respectively.

Table 3.3 Ruhrchemie catalyst comparison: activity and selectivity.

Experiment	A3	A16	C3	C15	[3]	[13]
Time-on-stream (h)	290	985	443	1550	528	-
T (K)	523	523	523	523	523	538
F	1	0.5	1	0.5	1	0.70-0.78
P (MPa)	1.6	2.4	1.5	2.4	1.5	2.4
$\Phi_{v,0}^{in}/W$ ($10^{-3} \text{ Nm}^3 \text{ kg}_{cat}^{-1} \text{ s}^{-1}$)	1.0	0.5	0.5	0.5	0.56	0.56
$\text{H}_2 + \text{CO}$ conversion (%)	47.5	55.5	53.7	53.5	56.0	33.6
Reaction medium	Gas	Gas	Slurry	Slurry	Gas	Slurry
Hydrocarbon selectivities ¹ (wt%)						
w_1	14.4	10.3	14.8	8.5	13.4	7.8
w_{2-4}	39.5	40.6	37.4	40.7	46.7	37.1
w_{5-10}	46.1	49.0	47.7	50.8	39.9	55.0
Olefin selectivity (wt%)						
$w_{O,2-4}$	66.1	75.3	55.9	79.1	75.0	-
$w_{O,5-10}$	60.7	72.9	45.4	76.8	70.0	-

¹ Selectivities based on carbon number $n \leq 10$

After FT reaction for more than 1800 hours the BET surface area decreased to $88 \text{ m}^2 \text{ g}^{-1}$. Previous studies with the same catalyst showed similar results [1, 12, 33]. Prior to N_2 -physisorption, the spent catalyst sample was heated with hexane under reflux conditions and degassed to remove waxy deposits from the pores. Gas chromatographic analysis of the extracted hydrocarbons revealed that the mixture consisted of linear paraffins with a carbon number in the range of 20 to 60. The decrease in the BET surface area results from sintering [1], formation of carbonaceous deposits resulting in blocking of pores [12] or increase of the skeletal density of the catalyst [1]. In agreement with previous literature studies, the average pore diameter as determined by BET, increased from 8 to 14 nm (see Table 3.1) and the pore size distribution shifted to larger sized pores.

3.7.1 Gas-solid Experiments

For accurate kinetic measurements, the catalyst activity has to be stable. Periodically standard experiments are necessary to check for possible deactivation effects on

activity and selectivity of the catalyst [3, 13]. During the catalyst tests in the SBR (Appendix A), 6 reference experiments were performed (see Table 3.4). After an initial period of 100 h (4 days) steady state was achieved. The catalyst activity, reaction rate to hydrocarbon products (R_{FT}) and of the water gas shift (R_{WGS}), changed slowly over 1200 h time-on-stream (see Figure 3.10a). The selectivity of the Ruhrchemie catalyst is plotted in Figure 3.10b. The selectivity to lighter products increases slightly with time-on-stream, whereas the olefin content decreases.

Table 3.4 Effect of time-on-stream on the catalyst activity and selectivity in the spinning basket reactor (Appendix A).

Run ¹	A1	A5	A11	A12	A17	A20
Time-on-stream (h)	240	388	699	862	1011	1224
H ₂ + CO conversion (%)	35.9	31.7	30.7	26.7	33.7	35.8
R_{FT} (10 ⁻³ mol kg _{cat} ⁻¹ s ⁻¹)	7.5	8.0	7.9	7.1	8.5	8.7
R_{WGS} (10 ⁻³ mol kg _{cat} ⁻¹ s ⁻¹)	2.9	2.7	2.6	2.0	3.4	3.6
STY (10 ⁻³ mol kg _{cat} ⁻¹ s ⁻¹)	21.1	21.3	20.6	17.9	22.6	24.0
Hydrocarbon selectivities (wt%)						
w_1	17.5	18.2	20.2	20.5	21.5	21.2
w_{2-4}	35.3	39.8	46.8	43.3	42.9	41.5
w_{5-10}	47.2	42.0	33.1	36.2	35.6	37.2
Olefin selectivity (wt%)						
$w_{O,2-4}$	65.9	66.2	62.2	66.8	61.2	61.7
$w_{O,5-10}$	63.8	63.5	58.7	62.9	58.1	58.8

¹ $P=1.50$ MPa, $T=523$ K, $F=2$, $\Phi_{v,0}^{in}/W=1.5 \cdot 10^{-3}$ Nm³ kg_{cat}⁻¹ s⁻¹

3.7.2 Slurry Experiments

The possible effects of catalyst aging on activity and selectivity was determined in both slurry reactor runs (Appendix B). At regular time intervals, reference experiments were repeated. The major results of the reference experiments in both runs are given in Table 3.5. Remarkably, the reaction rate of CO to hydrocarbons is higher in Run C resulting in higher synthesis gas conversions and space time yields. The selectivities of the hydrocarbon groups in reference experiment C4 are different due to analysis problems with the C₁₀ hydrocarbons, which could not be determined accurately. A sharp decrease of the C₅₋₁₀ selectivity was observed in Run C between reference experiment C10 and C13.

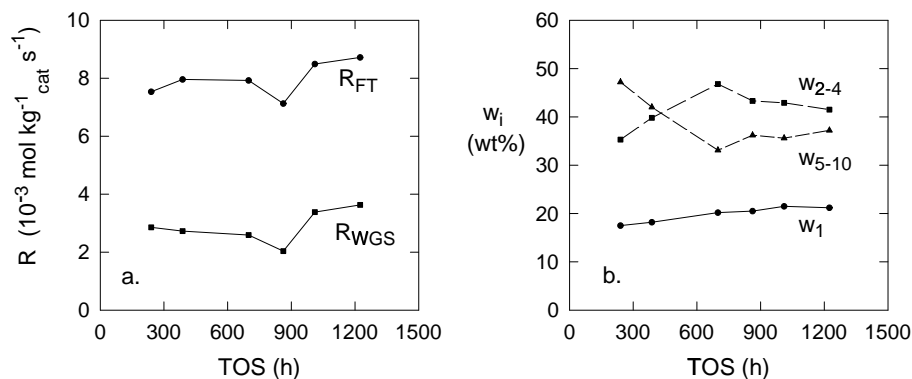


Figure 3.10 Effect of time-on-stream (TOS) on catalyst activity (a) and selectivity (b). Experimental conditions: $T = 523 \text{ K}$, $F = 2$, $P = 1.50 \text{ MPa}$, $\Phi_{v,0}^{in}/W = 1.51 \cdot 10^{-3} \text{ Nm}^3 \text{ kg}_{\text{cat}}^{-1} \text{ s}^{-1}$. Run: A1, A5, A11, A12, A17, A20.

Table 3.5 Effect of time-on-stream on the catalyst activity and selectivity in slurry reactor runs (Appendix B).

Run ¹	B1	B4	B8	C1	C4 ²	C6	C10	C13
Time-on-stream (h)	156	577	643	345	552	802	1056	1395
H ₂ + CO conversion (%)	32.0	32.8	40.1	46.8	53.2	50.8	49.1	41.9
R_{FT} ($10^{-3} \text{ mol kg}_{\text{cat}}^{-1} \text{ s}^{-1}$)	2.1	2.3	2.9	4.0	4.3	4.1	3.4	3.2
R_{WGS} ($10^{-3} \text{ mol kg}_{\text{cat}}^{-1} \text{ s}^{-1}$)	1.9	1.8	1.8	2.3	1.9	2.2	2.4	1.6
STY ($10^{-3} \text{ mol kg}_{\text{cat}}^{-1} \text{ s}^{-1}$)	7.3	7.5	9.1	10.7	12.2	11.6	11.3	9.6
Hydrocarbon selectivities (wt%)								
w_1	9.5	9.6	9.7	16.0	12.1	10.0	9.4	10.9
w_{2-4}	38.3	36.0	39.7	38.0	38.8	35.9	36.1	48.0
w_{5-10}	52.2	54.5	50.6	46.0	49.1	54.2	54.5	41.1
Olefin selectivity (wt%)								
$w_{O,2-4}$	78.8	77.2	79.5	69.0	65.7	77.7	79.5	79.2
$w_{O,5-10}$	79.2	74.9	78.2	63.1	62.9	75.0	78.0	71.6

¹ $P = 1.50 \text{ MPa}$, $T = 523 \text{ K}$, $F = 0.67$, $\Phi_{v,0}^{in}/W = 0.5 \cdot 10^{-3} \text{ Nm}^3 \text{ kg}_{\text{cat}}^{-1} \text{ s}^{-1}$

² On-line analysis $n \leq 9$

References

- [1] Lox, E.S.; Marin, G.B.; de Graeve, E.; Bussiere, P., Characterization of a promoted precipitated iron catalyst for Fischer-Tropsch synthesis, *Appl. Catal. A* **1988**, *40*, 197–218.
- [2] Bub, G.; Baerns, M., Prediction of the performance of catalytic fixed bed reactors for Fischer-Tropsch synthesis, *Chem. Eng. Sci.* **1980**, *35*, 348–355.
- [3] Bukur, D.B.; Patel, S.A.; Lang, X., Fixed bed and slurry reactor studies of Fischer-Tropsch synthesis on precipitated iron catalyst, *Appl. Catal. A* **1990**, *61*, 329–349.
- [4] Wojciechowski, B.W., The kinetics of the Fischer Tropsch synthesis, *Catal. Rev. - Sci. Eng.* **1988**, *30*, 629–702.
- [5] Sarup, B.; Wojciechowski, B.W., Studies of the Fischer-Tropsch synthesis on a cobalt catalyst. I. Evaluation of product distribution parameters from experimental data, *Can. J. Chem. Eng.* **1988**, *66*, 831–842.
- [6] Shen, W.J.; Zhou, J.L.; Zhang, B.J., Kinetics of Fischer-Tropsch synthesis over precipitated iron catalyst, *J. Nat. Gas Chem.* **1994**, *4*, 385–400.
- [7] Breman, B.B.; Beenackers, A.A.C.M.; Rietjens, E.W.J.; Stege, R.J.H., Gas-liquid solubilities of carbon monoxide, carbon dioxide, hydrogen, water, 1-alcohols ($1 \leq n \leq 6$), and n-paraffins ($1 \leq n \leq 6$) in hexadecane, octacosane, 1-hexadecanol, phenantrene, and tetraethylene glycol at pressures up to 5.5 MPa and temperatures from 293 to 552 K, *J. Chem. Eng. Data* **1994**, *39*, 647–666.
- [8] Ledakowicz, S.; Nettelhoff, H.; Kokuun, R.; Deckwer, W.-D., Kinetics of the Fischer-Tropsch synthesis in the slurry phase on a potassium-promoted iron catalyst, *Top. Catal.* **1985**, *24*, 1043–1049.
- [9] Tajbl, D.G., Kinetics of catalytic ethane hydrogenolysis: stirred reactor study of commercial nickel catalyst, *Can. J. Chem. Eng.* **1969**, *47*, 154–156.
- [10] Nettelhoff, H.; Kokuun, R.; Ledakowicz, S.; Deckwer, W.-D., Studies on the kinetics of Fischer-Tropsch synthesis in slurry phase, *Ger. Chem. Eng.* **1985**, *8*, 177–185.
- [11] Frohning, C.D.; Kölbl, H. Ralek, M.; Rottig, W.; Schuur, F.; Schulz, H., Fischer-Tropsch-Synthese, in J. Falbe, ed., *Chemierohstoffe aus Kohle*, Georg Thieme Verlag, Stuttgart, 1977 pp. 219–299.
- [12] Bukur, D.B.; Okabe, K.; Rosynek, M.P.; Li, C.; Wang, D.; Rao, K.R.P.M.; Huffman, G.P., Activation studies with a precipitated iron catalyst for Fischer-Tropsch synthesis. 1. Characterization studies, *J. Catal.* **1995**, *155*, 353–365.

- [13] Donnelly, T.J.; Satterfield, C.N., Product distributions of the Fischer-Tropsch synthesis on precipitated iron catalysts, *Appl. Catal. A* **1989**, *52*, 93–114.
- [14] Nijs, H.H.; Jacobs, P.A., On-line single run analysis of effluents from a Fischer-Tropsch reactor, *J. Chromatogr. Sci.* **1981**, *19*, 40–45.
- [15] Lox, E.S.; Froment, G.F., Kinetics of the Fischer-Tropsch reaction on a precipitated promoted iron catalyst. 1. Experimental procedure and results, *Ind. Eng. Chem. Res.* **1993**, *32*, 61–70.
- [16] Huff, Jr., G.A.; Satterfield, C.N., Stirred autoclave apparatus for study of the Fischer-Tropsch synthesis in a slurry bed. 2. Analytical procedures, *Ind. Eng. Chem. Fundam.* **1983**, *22*, 258–263.
- [17] Marsman, J.H.; Breman, B.B.; Beenackers, A.A.C.M., On-line single column capillary gas chromatographic analysis of all reactants and products in the synthesis of fuel methanol from hydrogen and oxides of carbon, *J. High Resolut. Chromatogr.* **1993**, *16*, 141–147.
- [18] Snel, R., On-line gas chromatographic analysis of light Fischer-Tropsch synthesis products, *Chromatographia* **1986**, *21*, 265–268.
- [19] Dictor, R.A.; Bell, A.T., On-line analysis of Fischer-Tropsch synthesis products, *Ind. Eng. Chem. Fundam.* **1984**, *23*, 252–256.
- [20] Hackett, J.P.; Gibbon, G.A., Capillary gas chromatographic characterization of Fischer-Tropsch liquefaction products: on-line analysis, *J. Chromatogr. Sci.* **1989**, *27*, 405–412.
- [21] Marsman, J.H.; Ede van, C.J.; Breman, B.B.; Stamhuis, E.J.; Beenackers, A.A.C.M., Applications of the deferred standard technique in process gas chromatography, *Anal. Chim. Acta* **1990**, *238*, 129–137.
- [22] Dierickx, J.L.; Plehiers, P.M.; Froment, G.F., On-line gas chromatographic analysis of hydrocarbon effluents. Calibration factors and their correlation, *J. Chromatogr.* **1986**, *362*, 155–174.
- [23] Caldwell, L.; van Vuuren, D.S., On the formation and composition of the liquid phase in Fischer-Tropsch reactors, *Chem. Eng. Sci.* **1986**, *41*, 89–96.
- [24] Bukur, D.B.; Nowicki, L.; Manne, R.K.; Lang, X., Activation studies with a precipitated iron catalyst for Fischer-Tropsch synthesis 2. Reaction studies, *J. Catal.* **1995**, *155*, 366–375.
- [25] Marano, J.J.; Holder, G.D., Characterization of Fischer-Tropsch liquids for vapor-liquid equilibria calculations, *Fluid Phase Equilib.* **1997**, *138*, 1–21.
- [26] Post, M.F.M.; van't Hoog, A.C.; Minderhoud, J.K.; Sie, S.T., Diffusion limitations in Fischer-Tropsch catalysts, *AIChE J.* **1989**, *35*, 1107–1114.

- [27] Zimmerman, W.H.; Bukur, D.B., Effect of particle size on the activity of a fused iron Fischer-Tropsch catalyst, *Ind. Eng. Chem. Res.* **1989**, *28*, 406–413.
- [28] Westerterp, K.R.; van Swaaij, W.P.M.; Beenackers, A.A.C.M., *Chemical reactor design and operation*, Wiley & Sons, second edn. **1984**.
- [29] Press, W.H.; Flannery, B.P.; Teukolsky, S.A.; Vetterling, W.T., *Numerical recipes in Pascal*, Cambridge University Press, New York **1989**.
- [30] Jonker, G.H.; Veldsink, J.-W.; Beenackers, A.A.C.M., Intrinsic kinetics of 9-monoenic fatty acid methyl ester hydrogenation over nickel-based catalysts, *Ind. Eng. Chem. Res.* **1997**, *36*, 1567–1579.
- [31] Fisher, R.A., *Statistical methods for research workers*, Macmillan, 14th edn. **1970**.
- [32] Dry, M.E., The Fischer-Tropsch synthesis, in J.R. Anderson; M. Boudart, eds., *Catalysis-Science and technology*, vol. 1, Springer-Verlag, New York, 1981 pp. 160–255.
- [33] Sault, A.G., An Auger electron spectroscopy study of the activation of iron Fischer-Tropsch catalyst. I Hydrogen activation, *J. Catal.* **1993**, *140*, 121–135.

4

α -Olefin Readsorption Product Distribution Model for the Gas-Solid Fischer-Tropsch Synthesis

Abstract

The kinetics of the gas-solid Fischer-Tropsch synthesis over a commercial Fe-Cu-K-SiO₂ catalyst was studied in a continuous spinning basket reactor. Experimental conditions were varied as follows: reactor pressure of 0.8-4.0 MPa, H₂/CO feed ratio of 0.25-4.0, and space velocity of 0.5-2.0 10⁻³ Nm³ kg_{cat}⁻¹ s⁻¹ at a constant temperature of 523 K. A new product distribution model for linear hydrocarbons is proposed. Deviations from conventional Anderson-Schulz-Flory distribution can be quantitatively described with an α -Olefin Readsorption Product Distribution Model. The experimentally observed relatively high yield of methane, relatively low yield of ethene and both the exponential decrease of the olefin to paraffin ratio and the change of the chain growth parameter with chain length can all be predicted from this new model. It combines a mechanistic model of olefin readsorption with kinetics of chain growth and termination on the same catalytic sites. The hydrocarbon formation is based on the surface carbide mechanism by CH₂ insertion. The olefin readsorption rate depends on chain length due to increasing physisorption strength on the catalyst surface and increasing solubility in FT-wax inside the catalyst pores with increasing chain length. Interfacial concentrations of reactive olefins near the gas-wax and wax-catalyst surface are used in the kinetic model. By optimizing three parameters per experimental product distribution, the olefin readsorption product distribution model proved to predict product selectivities accurately over the entire range of experimental conditions. The relative deviations are 10.1 % and 9.1 % for the selectivity to paraffins and olefins with carbon number smaller than 11, respectively.

4.1 Introduction

The FT synthesis has been recognized as a polymerization reaction [1]. The reactants, CO and H₂, adsorb and dissociate at the surface of the catalyst and react to form chain initiator (CH₃), and methylene monomer (CH₂) and H₂O. The most important growth mechanism for the hydrocarbon formation is the surface carbide mechanism by CH₂ insertion into adsorbed alkyl chains. Termination can take place by dehydrogenation to an α -olefin or hydrogenation to form a paraffin [2–4].

The product yield decreases exponentially with increasing chain length. The so-called Anderson-Schulz-Flory (ASF) distribution describes the entire product range by a single parameter, α , the probability of the addition of a carbon intermediate to a chain [2, 5]. However, significant deviations from the ASF distribution are reported in literature. The usual deviations of the distribution of α -olefins and paraffins are a relatively high yield of methane [6–9] and a relatively low yield of ethene [6, 7, 10] in comparison to the ASF distribution. Higher surface mobility or reactivity of C₁ and C₂ precursors and rapid readsorption of ethene give the most reasonable explanation for the deviations of the short-chain hydrocarbons from the ASF distribution (Chapter 2). Furthermore, an exponential decrease of the α -olefin to paraffin ratio and change in chain growth parameter, α_n , with increasing chain length is observed. These deviations are caused by secondary reactions, readsorption and hydrogenation, of α -olefins [7, 11–13]. However, secondary hydrogenation is strongly inhibited by CO and H₂O in comparison to readsorption [12]. Readsorption of α -olefins leads to chain initiation and will result in a decrease of the olefin to paraffin ratio and increase of the chain growth parameter with chain length. The olefin readsorption rate depends on chain length due to increasing physisorption on the catalyst surface and increasing solubility in FT-wax with chain length [7, 13].

Models for the hydrocarbon selectivity of products obtained on iron catalysts are usually based on the ASF distribution; the total hydrocarbon yield is calculated with a single chain growth factor, α [2, 14]. The "break" or increase of the chain growth factor in the ASF distribution of the total hydrocarbon yield was observed on iron catalysts [15–20]. Some authors described the total hydrocarbon yield with two different catalytic sites with different chain growth probabilities, since the total hydrocarbon distribution could be fitted by addition of two individual ASF distributions [19, 20]. However, such double- α models cannot explain the decrease of the olefin to paraffin ratio.

More comprehensive models taking into account the readsorption of olefins during

the FT synthesis have been published, mostly for non-iron catalysts only. Zimmerman et al. [21] proposed a kinetic model for both the formation of linear olefins and paraffins and for the water gas shift reaction over iron catalysts. Their model takes into account olefin readsorption on FT sites and secondary hydrogenation of olefins on separate hydrogenation sites. Their model predicts a decrease of the olefin to paraffin ratio and an increase of the chain growth factor with increasing carbon number. The decrease of the olefin content is ascribed to high olefin concentrations in the liquid phase. However, the model was tested for one experiment only and showed significant deviations between model prediction and experimental mole fractions, specially for methane and ethene. The major differences between the new model proposed here and the model of Zimmerman et al. [21] will be discussed below. The model of Iglesia and co-workers, see for example Iglesia et al. [12], is based on diffusion-enhanced olefin readsorption due to a decrease of diffusion coefficients with increasing carbon number. As discussed below, it is more likely that preferential physisorption and increase of the solubility with increasing chain length result in a high surface concentration of adsorbed olefins. Komaya and Bell [7] measured the dynamic and steady-state Fischer-Tropsch synthesis over Ru/TiO₂ and determined the pseudo reaction rate constants of the chain growth, termination, and readsorption of olefins. The authors accounted for the effect of chain length dependent readsorption of olefins due to increasing physisorption with increasing carbon number, as well as depolymerization of ethene and dehydrogenation of methyl. However, they did not specify separate termination reactions for the formation of paraffins and olefins from adsorbed alkyl species, but lumped these termination reactions in a single termination rate constant. Therefore, no complete description of the product distribution could be obtained using their model. Kuipers et al. [13] modeled experimental data of the olefin to paraffin ratio synthesized on wax-coated and uncoated cobalt foils at low CO conversions at atmospheric pressures and a temperature of 493 K. Their model predicts an exponential decrease of the olefin to paraffin ratio with carbon number due to increased physisorption and solubility with increasing chain length. This model was extended by Kuipers et al. [9] in order to incorporate hydrogenation and cracking on Co/SiO₂ wafers and Co foils. In contrast to Kuipers et al. [13], they concluded that the deviations from the ASF distribution on Co foils were completely due to hydrogenation instead of readsorption of olefins.

The aim of this chapter is to develop and test a new product distribution model, called α -Olefin Readsorption Product Distribution Model (ORPDM) based on the results of kinetic experiments at industrially relevant conditions over a precipitated iron

catalyst to explain the deviations from the ASF distribution. The new model combines a mechanistic model of olefin readsorption with kinetics of chain growth and termination on the same catalytic sites. In this chapter, the emphasis is placed on the selectivity to linear olefins and paraffins.

4.2 α -Olefin Readsorption Product Distribution Model

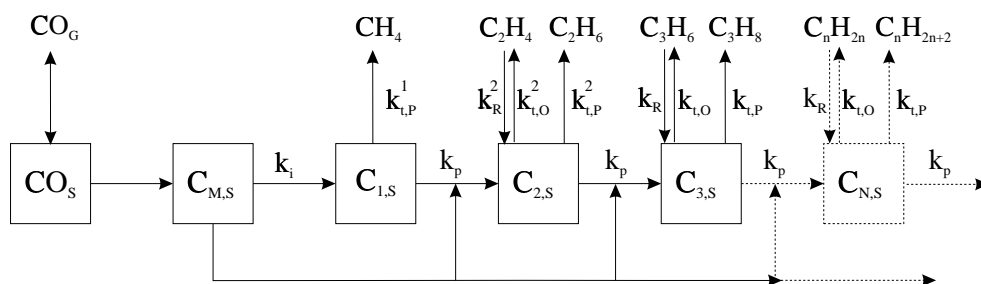


Figure 4.1 Reaction network α -Olefin Readsorption Product Distribution Model. The model reduces to ASF model when k_R^2 , and $k_R = 0$.

The α -Olefin Readsorption Product Distribution Model (ORPDM) accounts for secondary readsorption of α -olefins on FT growth sites on the precipitated iron catalyst (see Figure 4.1). Here, CO_G and CO_S denote the gas phase and the adsorbed CO, respectively. $C_{M,S}$ refers to adsorbed monomeric building units ($CH_{2,S}$), and $C_{n,S}$ is an adsorbed alkyl species with carbon number n . Conversion of CO to $C_{M,S}$ follows a sequence of elementary reaction steps, but is shown as a single step. Table 4.1 shows the reactions for the chain growth and termination of alkyl chains. Chain growth initiates by hydrogenation of $C_{M,S}$ to $CH_{3,S}$, while chain propagation proceeds via insertion of $C_{M,S}$ into adsorbed alkyl chains. Chain termination by dehydrogenation of adsorbed alkyl chains gives olefins, whereas paraffins are formed by hydrogenation of alkyl species [7, 22]. Based on the reaction network shown in Figure 4.1, α -olefins may readsorb on growth sites and continue to grow via propagation with monomers or terminate as hydrocarbon product [7, 11].

Steady state mass balances for C_2 and alkyl species with carbon number, n , can be derived to account for readsorption:

$$k_p\theta_M\theta_1 = (k_{t,O}^2\theta_v + k_{t,P}^2\theta_H + k_p\theta_M)\theta_2 - k_R^*C_{C_2H_4} \quad (4.1)$$

$$k_p\theta_M\theta_{n-1} = (k_{t,O}\theta_v + k_{t,P}\theta_H + k_p\theta_M)\theta_n - k_R^*C_{C_nH_{2n}} \quad (4.2)$$

Table 4.1 Proposed mechanism of the chain growth and termination reactions [3, 11].

Elementary reactions	Reaction rates
1 $H_2 + 2s \rightleftharpoons 2Hs$	
2 ¹ $CO + 2H_2 + s \rightarrow CH_2S + H_2O$	
3 $CH_2S + Hs \rightarrow CH_3S + s$	
4 $CH_3S + Hs \rightarrow CH_4 + 2s$	$k_{t,p}^1 \theta_1 \theta_H$
5 $CH_3S + CH_2S \rightarrow C_2H_5S + s$	$k_p \theta_1 \theta_M$
6 $C_2H_5S + s \rightleftharpoons C_2H_4 + Hs + s$	$k_{t,o}^2 \theta_2 \theta_v - k_R^2 C_{C_2H_4} \theta_H \theta_v$
7 $C_2H_5S + Hs \rightarrow C_2H_6 + 2s$	$k_{t,p}^2 \theta_H \theta_2$
8 $C_2H_5S + CH_2S \rightarrow C_3H_7S + s$	$k_p \theta_2 \theta_M$
9 $C_n H_{2n+1} S + s \rightleftharpoons C_n H_{2n} + Hs + s$	$k_{t,o} \theta_n \theta_v - k_R C_{C_n H_{2n}} \theta_H \theta_v$
10 $C_n H_{2n+1} S + Hs \rightarrow C_n H_{2n+2} + 2s$	$k_{t,p} \theta_n \theta_H$
11 $C_n H_{2n+1} S + CH_2S \rightarrow C_{n+1} H_{2n+3} + s$	$k_p \theta_n \theta_M$
etc.	

¹ Overall reaction for methylene formation.

where θ_H is the surface coverage of adsorbed hydrogen and θ_v is the fraction of vacant catalytic sites, and $k_R^* = k_R \theta_v \theta_H$ is a pseudo kinetic constant for the readsorption path. Since the readsorption reaction path of olefins is built up from several consecutive elementary surface reactions it is simplified as a single kinetic reaction rate constant (k_R^*). The actual concentration of the olefin on the catalyst surface, $C_{C_n H_{2n}}$, can be related to the reaction rate:

$$R_{C_n H_{2n}} = k_{t,o} \theta_n \theta_v - k_R^* C_{C_n H_{2n}} \quad (4.3)$$

It is assumed that the olefins leave the reactor in the gas phase. The same assumption was made by Iglesia et al. [11] and Kuipers et al. [13]. Liquid products are predominantly paraffins, which are unreactive under Fischer-Tropsch conditions. The steady-state mass balance for α -olefins in an ideally mixed continuous reactor is

$$R_{C_n H_{2n}} = \frac{\Phi_{v,R} P_{C_n H_{2n}}}{WRT} \quad (4.4)$$

where $P_{C_n H_{2n}}/RT$ is the gas phase concentration of olefins in the reactor with carbon number n , $\Phi_{v,R}$ is the volumetric flow rate of the gas phase at reactor conditions, and W is the weight of the unreduced supported catalyst.

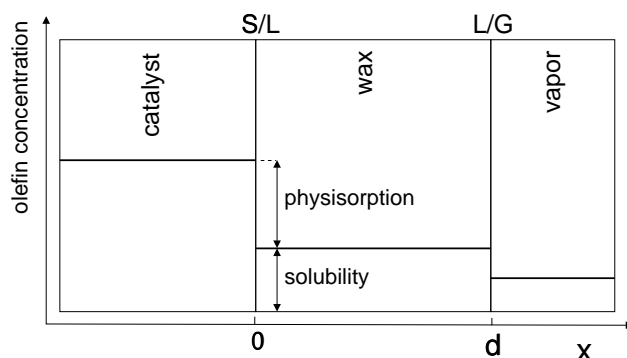


Figure 4.2 Olefin concentration profile near a Fischer-Tropsch catalyst.

The interfacial effects of reactive olefins at the gas-wax and wax-catalyst surface should be taken into account. Figure 4.2 gives a schematic representation of the olefin concentration profile in a wax-filled catalyst pore. The concentration in the wax phase (at $0 \leq x \leq d$) can be related to the vapor-phase concentration by Henry's law. Several authors stated that a greater solubility of larger hydrocarbons results in an increase of readsorption rates for larger olefins [13, 23, 24]. Vapor-liquid equilibria [25–28] show that the solubility of hydrocarbons increases exponentially with the chain length.

Data on the adsorption of hydrocarbons on solids show that the enthalpy of adsorption increases linearly with carbon number [29–31]. Adsorption equilibria constants increase exponentially with chain length [7, 30, 32, 33]. This increase results from an increase of the contact area between hydrocarbons and catalytic surface, which enhance Van der Waals attraction forces responsible for physisorption effects. Since physisorption is the precursor step to chemisorption, this increase is essential for readsorption of olefins. In multi-component mixtures (Fischer-Tropsch product spectrum) these effects result in a physisorbed layer with mainly long-chain hydrocarbons, while shorter chains are further away from the surface.

Iglesia and co-workers studied the influence of chain-length dependent diffusion coefficients on secondary reactions [11, 12, 34–37]. They reported an empirical equation describing a strong influence of chain length on diffusivity for olefins and paraffins $D_n \propto e^{-0.3n}$, which was not verified by experimental data. This carbon number dependency is a factor of three higher than experimentally determined by Erkey et al. [38]. Furthermore, the Wilke-Chang correlation [39] predicts a chain length dependence proportional to $n^{-0.5}$. Therefore, increase of readsorption rates of olefins with

chain length can hardly be due to diffusion effects only. More likely, preferential physisorption and increase of the solubility with chain length result in a high surface concentration of adsorbed olefins. Therefore we assume the olefin gas phase pressure to relate to the concentration at the catalyst surface as:

$$\frac{C_{C_n H_{2n}}}{P_{C_n H_{2n}}/RT} \propto e^{c n} \quad (4.5)$$

where c is a constant depending on the exponential increase of the physisorption and solubility with chain length.

Rearranging and solving eqs 4.1 - 4.5 yields:

$$\frac{\theta_2}{\theta_1} = \frac{k_p \theta_M}{k_{t,O}^2 \theta_v / (1 + k_R^2) + k_{t,P}^2 \theta_H + k_p \theta_M} = \frac{p}{t_O^2 / (1 + k_R^2) + t_P^2 + p} = \alpha_2 \quad (4.6)$$

and for $n > 2$:

$$\frac{\theta_n}{\theta_{n-1}} = \frac{k_p \theta_M}{k_{t,O} \theta_v / (1 + k_R e^{c n}) + k_{t,P} \theta_H + k_p \theta_M} = \frac{p}{t_O / (1 + k_R e^{c n}) + 1 + p} = \alpha_n \quad (4.7)$$

where $k_R = k_R^* W P / (\Phi_{v,0} P_0)$ (P = reactor pressure and $\Phi_{v,0}$ = flow rate at normal conditions), $p = k_p \theta_M / k_{t,P} \theta_H$, $t_P^2 = k_{t,P}^2 / k_{t,P}$, and $t_O^2 = t_P^2 t_O$, and $t_O = k_{t,O} \theta_v / k_{t,P} \theta_H$. These model parameters are pseudo kinetic rate constants, incorporating true kinetic rate constants, surface concentrations and process conditions. The surface fractions of alkyl chains with carbon number n can be determined by successive calculation of the chain growth parameter with increasing carbon number:

$$\frac{\theta_n}{\theta_1} = \prod_{i=2}^n \alpha_i = \alpha_2 \alpha_3 \cdots \alpha_n \quad (4.8)$$

The formation rate of paraffins with $n > 2$ (see Table 4.1) is equal to:

$$R_{C_n H_{2n+2}} = k_{t,P} \theta_H \theta_n \quad (4.9)$$

Normalizing eq 4.9 with respect to the termination to paraffins and substitution of eq 4.8 yields:

$$m_{C_n H_{2n+2}} = \theta_1 \prod_{i=2}^n \alpha_i \quad (4.10)$$

Similarly, solving eqs 4.3 and 4.4 gives the following reaction rates and molar selectivities for olefins:

$$R_{C_nH_{2n}} = \frac{k_{t,O}\theta_v\theta_n}{1 + k_R e^{c n}} \quad (4.11)$$

$$m_{C_nH_{2n}} = \frac{t_O}{1 + k_R e^{c n}} \theta_1 \prod_{i=2}^n \alpha_i \quad (4.12)$$

The selectivity to product i is calculated from the experimental mole fractions relative to all products (n) considered:

$$m_i = \frac{y_i}{\sum_{j=1}^n y_j} \quad (4.13)$$

The molar selectivities of the C_1 and C_2 products are calculated differently:

$$m_{CH_4} = t_P^1 \theta_1 \quad (4.14)$$

$$m_{C_2H_6} = t_P^2 \theta_2 = t_P^2 \alpha_2 \theta_1 \quad (4.15)$$

$$m_{C_2H_4} = \frac{t_O^2}{1 + k_R^2} \theta_2 \quad (4.16)$$

with $t_P^1 = k_{t,P}^1/k_{t,P}$. The optimization constraint for the selectivities is:

$$\sum_i^n m_i = 1 \quad (4.17)$$

This model reduces to the ASF distribution model when olefins can not adsorb, i.e. $k_R = 0$. Therefore, eqs 4.7- 4.12 can also be used for the ASF distribution with substitution of $k_R = 0$.

$$\frac{\theta_n}{\theta_{n-1}} = \frac{k_p \theta_M}{k_{t,O} \theta_v + k_{t,P} \theta_H + k_p \theta_M} = \frac{p}{t_O + 1 + p} = \alpha \quad (4.18)$$

The product selectivities are equal to:

$$m_{C_nH_{2n}} = t_O \left(\frac{p}{p + 1 + t_O} \right)^{n-1} = t_O \alpha^{n-1} \quad (4.19)$$

and for paraffins:

$$m_{C_n H_{2n+2}} = \left(\frac{p}{p+1+t_O} \right)^{n-1} = \alpha^{n-1} \quad (4.20)$$

It can easily be seen from eq 4.19 and 4.20 that the predicted olefin to paraffin ratio is equal to t_O and independent of chain length.

The α -olefin readsorption product distribution model (ORPDM) accounts for the chain-length dependent readsorption of olefins on FT sites. The readsorption step depends on carbon number, resulting in a net decrease of the termination to olefins. α_n increases with increasing chain length until no olefins are formed. At high carbon numbers, the chain growth parameter, α_n , approaches a maximum constant value of $\alpha_\infty = p/(1+p)$ (see eq 4.7). The increased readsorption of long-chain olefins results in a decreasing olefin/paraffin ratio with chain length.

4.3 Experimental

Fischer-Tropsch experiments were carried out with a gas-continuous Spinning Basket Reactor (SBR). Details about the experimental set-up, the catalyst, and the analysis sections are described in Chapter 3. The catalyst applied was a commercial precipitated iron catalyst (type LP 33/81) synthesized by Ruhrchemie AG. The baskets were loaded with 2.34 g of unreduced catalyst particles with $0.125 \leq d_p \leq 0.160$ mm. The catalyst was pretreated with hydrogen with a flow rate of $0.83 \cdot 10^{-3} \text{ Nm}^3 \text{ kg}_{cat}^{-1} \text{ s}^{-1}$ according to Bukur et al. [40]. The gas space velocity was based on the total mass of the unreduced catalyst. The reactor temperature, T , was increased linearly from 293 K to 553 K by 0.017 K s^{-1} . T remained at 553 K for 24 hours at atmospheric pressure. After reduction, synthesis gas was fed to the reactor at reference conditions of 523 K, 1.50 MPa, $F=2$ and a space velocity of $1.51 \cdot 10^{-3} \text{ Nm}^3 \text{ kg}_{cat}^{-1} \text{ s}^{-1}$. Long-chain products have filled the catalyst pores with a liquid phase during the initial stage of the FT experiments.

Liquid products were accumulated in both high-pressure and low-pressure condensers for a typical period of 6-8 hours during steady state of the reactor system. The products were collected and weighed before analysis. Several on-line GC analyses were performed during this period. After changing the process conditions the reactor operated about 24 hours undisturbed before a new mass balance period was started. Deviations of the mass and element balances remained below 5 %.

Reportedly, internal diffusion is insignificant for $d_p < 0.16$ mm [41, 42]. Checking the criteria of Weisz and Prater [43] for the reactants CO and H₂ confirmed that no

intra-particle diffusion limitations could have occurred at even the highest conversion rates observed, and under the conservative assumption that the catalyst pores are filled with long-chain (C₂₈) hydrocarbon waxes.

The experimental conditions were varied as follows: $P = 0.8 - 4.0$ MPa, $F = 0.25 - 4.0$, and $\Phi_{v,0}^i/W = 0.5 - 2.0 \cdot 10^{-3} \text{ Nm}^3 \text{ kg}_{cat}^{-1} \text{ s}^{-1}$ at a constant temperature of 523 K. The standard deviation of the experimental selectivities was determined for various products by repeating the analysis of the experimental mole fractions:

$$\sigma^2 = \sum_i (m_i - \bar{m})^2 / (n - 1) < 4 \cdot 10^{-4} \bar{m} \quad (4.21)$$

The reference experiment was repeated 6 times to determine possible deactivation effects on the activity and selectivity of the catalyst. A summary of relevant experimental data is given in Appendix A.

4.4 Results and Discussion

24 kinetic experiments were carried out in the SBR with the Ruhrchemie precipitated iron catalyst at 523 K (see Appendix A). Four experiments were excluded for product distribution modeling due to analytical problems of the on-line analysis of hydrocarbons. Mono-methyl paraffins and β -olefins were below the detection limit in this range and were not taken into account. Potassium promoters in iron catalysts suppress isomerization reactions of α -olefins [20].

Figure 4.3 shows various typical distributions of the hydrocarbon products. Generally, we observed a decrease of the α -olefin/paraffin ratio with increasing carbon number and a curved line for the distribution of paraffins alone and paraffins and olefins combined.

4.4.1 Reactant Composition Effects

Figure 4.4a shows the effect of the (H₂/CO) ratio at the reactor outlet on the hydrocarbon selectivity. The product distribution of the on-line analysis is lumped in three groups of hydrocarbons: methane (w_1), C₂-C₄ (w_{2-4}) (light gases), and C₅-C₁₀ (w_{5-10}) (gasoline) and expressed in mass percentages of the on-line analyzed hydrocarbons. In an ideally mixed reactor, the composition at the reactor outlet equals the reactor composition. The feed ratio differs from the exit ratio, due to the stoichiometry of the FT reactions and the water gas shift reaction [14, 44]. The product distribution

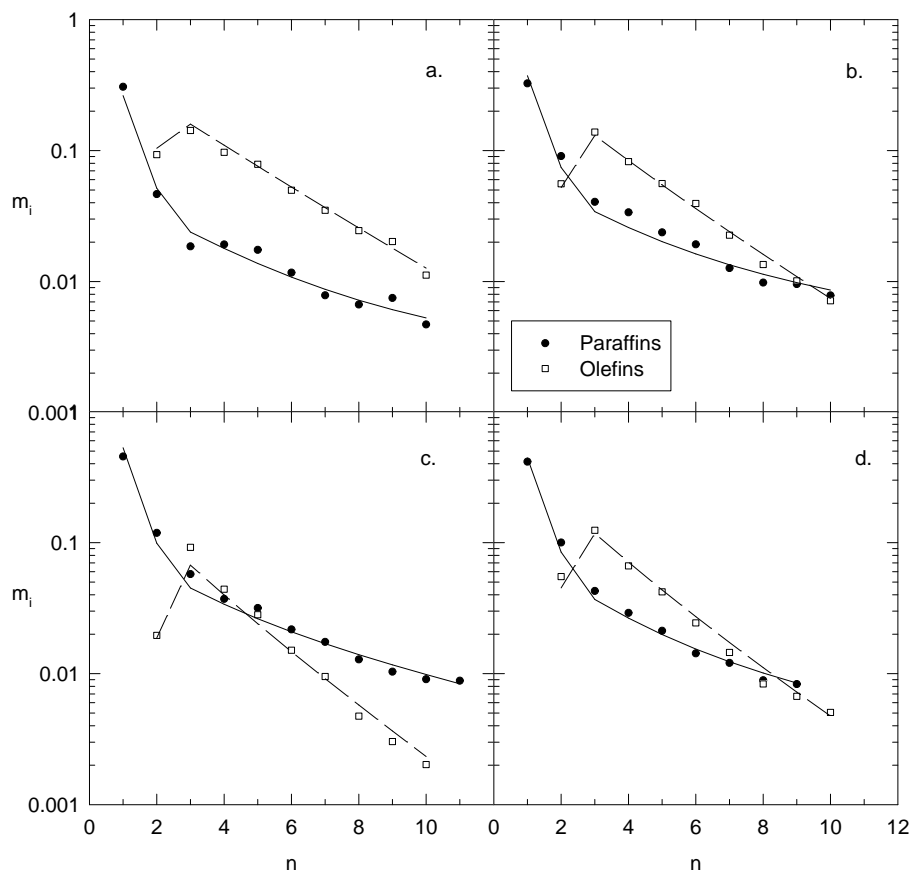


Figure 4.3 Product distribution for various experiments of Appendix A

Experimental conditions:

a. Low H_2/CO feed ratio, $P=1.2$ MPa, $F=0.5$, $\Phi_{v,0}^{in}/W=1.0 \cdot 10^{-3} \text{ Nm}^3 \text{ kg}^{-1} \text{ s}^{-1}$ (Run A2).

b. High H_2/CO feed ratio, $P=3.2$ MPa, $F=1$, $\Phi_{v,0}^{in}/W=1.0 \cdot 10^{-3} \text{ Nm}^3 \text{ kg}^{-1} \text{ s}^{-1}$ (Run A8).

c. Low space velocity, $P=2.4$ MPa, $F=2$, $\Phi_{v,0}^{in}/W=0.5 \cdot 10^{-3} \text{ Nm}^3 \text{ kg}^{-1} \text{ s}^{-1}$ (Run A10).

d. High space velocity, $P=2.4$ MPa, $F=2$, $\Phi_{v,0}^{in}/W=2.0 \cdot 10^{-3} \text{ Nm}^3 \text{ kg}^{-1} \text{ s}^{-1}$ (Run A11).

Lines are model ORPDM predictions. Symbols are experimental selectivities.

shifts to lower molecular weight products with an increase of the H_2/CO ratio. Donnelly and Satterfield [20] and Bukur et al. [45] have reported the same effect for the same commercial precipitated iron catalyst.

Figure 4.4b shows that in agreement with Donnelly and Satterfield [20] the olefin content for the light gases decreases sharply from 85 to 45 wt% as the H_2/CO exit ratio increases from 0.5 to 4.5. Low hydrogen concentrations in the feed and in the reactor result in low hydrogen surface concentrations and termination to olefins instead of saturated paraffins. The pressures of both synthesis gas components were varied independently between 0.1 and 1.3 MPa. The measured ratio of the mole fractions of olefin to paraffin (O/P) as function of carbon number for several H_2/CO ratios is shown in Figure 4.5. The O/P ratio shows a minimum at carbon number 2, a maximum for the propene to propane ratio and decreases exponentially. Figure 4.5 shows that the ratio of 1-butene to butane decreased from about 5 to 1 with increasing H_2/CO ratios from 0.5 to 4.5. Similar results were reported by Donnelly and Satterfield [20] and Bukur et al. [45].

4.4.2 Space Velocity Effects

The effect of space velocity on the O/P ratio is plotted in Figure 4.6. The O/P ratio increases with increased space velocity at a H_2/CO feed ratio of 2. The same trend was observed by Dictor and Bell [17] on Fe_2O_3 powders, Bukur et al. [45] on the commercial Ruhrchemie catalyst, and Kuipers et al. [13] on uncoated and wax-coated Co foils. Donnelly and Satterfield [20] found no dependence of the space velocity on the 1-butene to butane ratio in their experiments. Iglesia and co-workers measured the effect of space velocity on the selectivity to olefins and paraffins extensively on Ru-catalysts [36] and Co-catalysts [11]. They observed the olefin selectivities to increase with increasing space velocity, whereas selectivity to paraffins remained constant for C_2 to C_4 and decreased for larger paraffins. Figure 4.7 shows the effect of space velocity on the selectivities of C_1 , C_2 , and C_4 products. The methane selectivity decreases with increasing space velocity. In agreement with the studies on Co- and Ru- catalysts, olefin selectivities increase with increasing space velocity, while paraffin selectivities decrease. The ethene selectivity increases sharper than the selectivity to ethane decreases. Selectivities of C_4 products show similar behavior. Thus, the decreasing paraffin selectivity cannot result from secondary hydrogenation of olefins alone. The hydrocarbon fraction of C_{20+} consists merely of paraffins, therefore paraffins are formed in primary chain termination reactions. The observed selectivities result from olefin readsorption, causing a decrease of the O/P ratio and increase of the

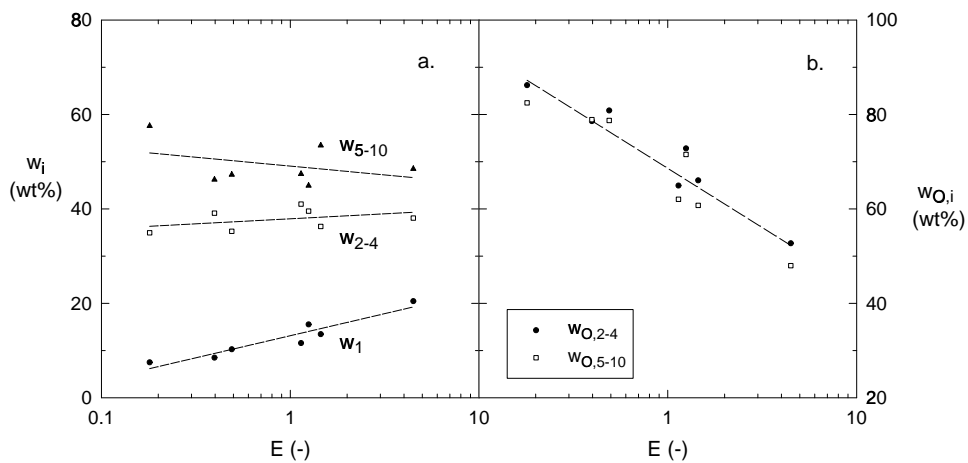


Figure 4.4 Effect of H₂/CO exit ratio (E) on hydrocarbon selectivity (a) and olefin selectivity (b) ($T=523$ K). Experimental data, see Appendix A.

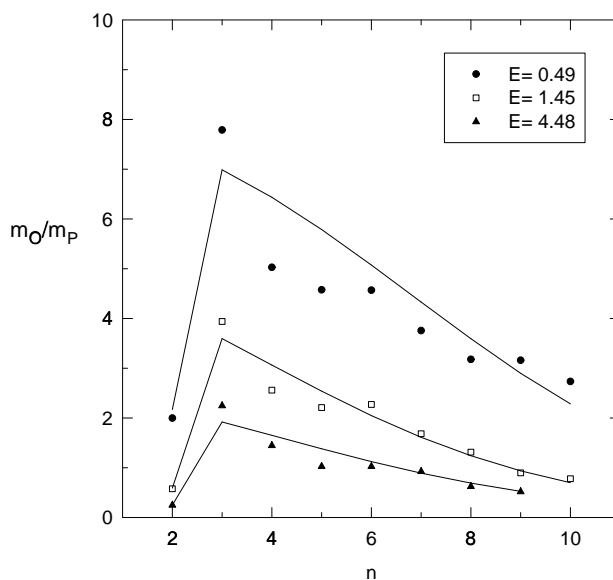


Figure 4.5 Effect of the reactor H₂/CO ratio on molar olefin/paraffin ratio as a function of carbon number. Lines are model predictions with model ORPDM ($T=523$, $\Phi_{v,0}^{in}/W=1.0$ 10^{-3} $\text{Nm}^3 \text{kg}^{-1} \text{s}^{-1}$, Run: A2, A3, A4).

chain growth probability [11, 13, 36]. The increasing paraffin selectivity with decreasing space velocity results from an increased surface concentration of (smaller) alkyl chains due to readsorption of olefins.

4.4.3 Product Distribution Models

Both the Anderson-Schulz-Flory (ASF) model as well as the Olefin Readsorption Product Distribution Model (ORPDM) were tested to our experiments at 523 K. The model parameters were optimized for each experiment with the Levenberg-Marquardt method [46].

The ASF model was optimized with two model parameters (p and t_O , see eqs 4.18 - 4.20), within each experiment. The number of parameters in model ORPDM was equal to 7: p , t_O , k_R , c , t_P^1 , t_P^2 , and k_R^2 (see eqs 4.7-4.16). Simultaneous optimization of these parameters within each experiment showed four parameters to be independent of the experimental conditions. The average values of these parameters are shown in Table 4.2. The value of the exponential coefficient c of 0.29 corresponds to the value of 0.30 reported by Iglesia et al. [34] for the dependence of diffusion coefficients and the exponential decrease of the molar O/P ratio with $0.55n$ at 493 K [13].

Introduction of these mean model parameters at 523 K for both the increased readsorption of ethene relative to other olefins and for the termination to C_1 and C_2 products and the exponential increase of the readsorption rate reduces the number of parameters to be optimized from 7 to 3 within each experiment. At high readsorption rates, for example, low space velocity, ($k_R e^{c n} \gg 1$) t_O becomes strongly correlated to k_R and cannot be determined separately (see eq 4.12):

$$t_O / (1 + k_R e^{c n}) \quad (4.22)$$

In experiments with strongly correlated parameters (t_O and k_R) the ratio of t_O/k_R is

Table 4.2 Optimized model parameters for ORPDM at 523 K that are independent of $\Phi_{v,0}$, P , H_2/CO ratio.

model parameter	value
t_P^1	6.62 ± 1.92
t_P^2	1.59 ± 0.29
k_R^2	$(12.58 \pm 3.55) k_R e^{2c}$
c	0.29 ± 0.07

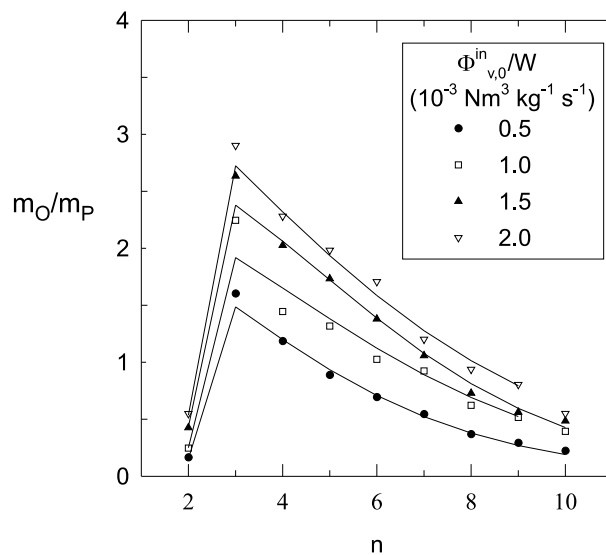


Figure 4.6 Space velocity effects on molar olefin/paraffin ratio as a function of carbon number. Lines are model predictions with model ORPDM ($T=523 \text{ K}$, $F=2$, $P=2.4 \text{ MPa}$, Run: A10, A4, A12, A11).

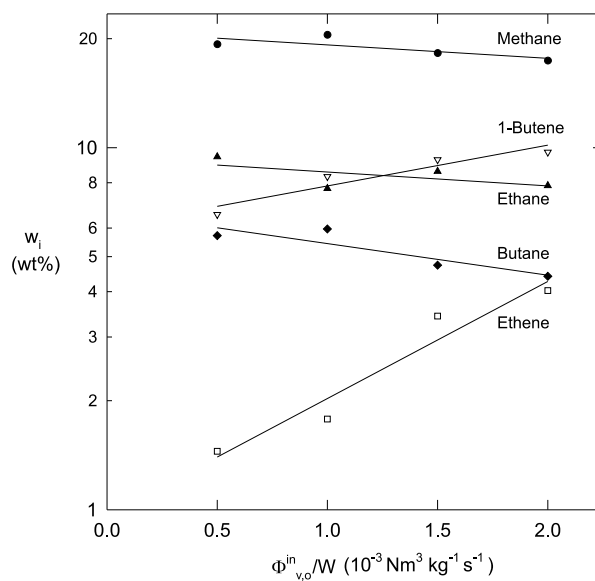


Figure 4.7 Space velocity effects on C_1 , C_2 , and C_4 selectivity. Experimental conditions, see Figure 4.6.

Table 4.3 Optimized model parameters ORPDM.

Run	p	t_O	k_R	n	s_{rel}
A1	11.64	6.28	0.364	19	9.5
A2	21.40	9.11	0.156	19	11.4
A3	12.55	9.46	0.632	19	6.4
A4	6.97	6.47 ¹	—	18	18.6
A6	9.27	7.87	0.500	19	9.4
A8	13.13	7.94	0.457	19	10.5
A9	20.24	7.33	0.123	15	7.5
A10	6.69	4.22 ¹	—	20	10.8
A11	9.42	7.73	0.600	18	10.3
A12	6.73	6.91	0.701	19	14.1
A13	7.09	8.20	0.470	19	16.8
A14	8.41	5.74	0.252	20	10.7
A15	6.01	6.53 ¹	—	19	10.1
A16	10.19	13.99	0.572	18	13.7
A17	21.23	7.69	0.107	19	10.2
A18	19.46	5.50	0.076	19	14.2
A19	7.18	9.18	0.779	20	7.1
A21	5.00	6.87	1.253	19	11.1
A23	12.92	6.85	0.245	15	7.5
A24	8.29	5.68	0.397	17	9.1

¹ t_O/k_R

modeled. The optimized model parameter values for each experiment are given in Table 4.3.

Table 4.4 shows the accuracies of the optimized models expressed with the relative standard deviation s_{rel} and the $MARR$ function for the paraffins and olefins, respectively, both for the complete set of experimental values at 523 K. The total number of selectivities n as well as the total number of optimized parameters m are also included in this table.

The ASF model observes large deviations between model and experiment. The accuracy of the ASF-model is improved, if hydrocarbons with $n=1-2$ are excluded from that model. Figure 4.8a shows a typical product distribution for the on-line hydrocarbon products with the predicted model values with model ASF. The relative residuals of the model appear to be a strong function of the carbon number and product type (see Figure 4.9a). The mean values of the relative residuals (\overline{RR}) as a function of

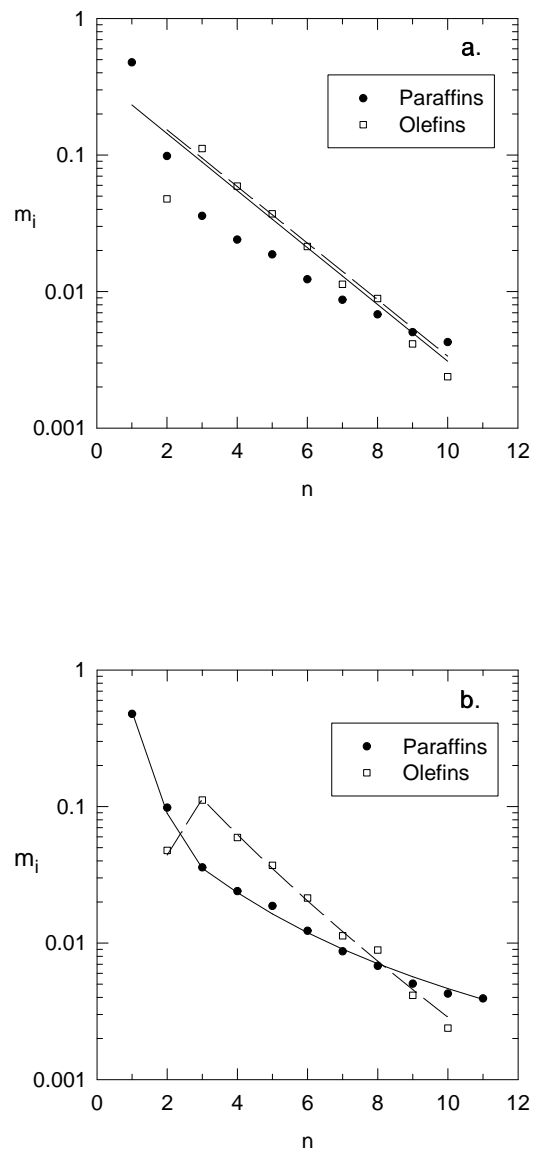
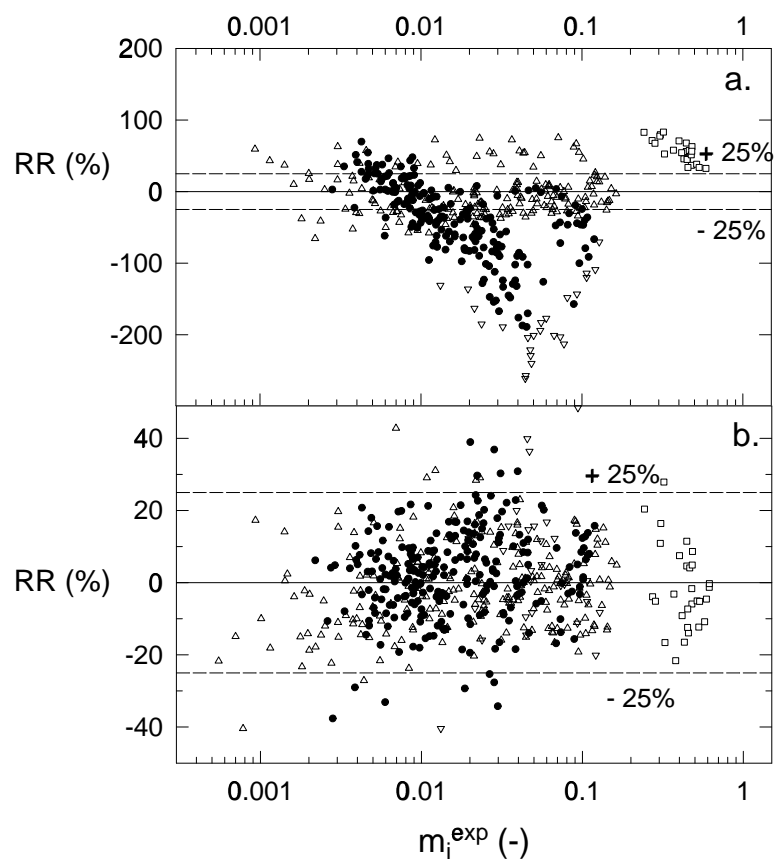


Figure 4.8 Product distribution as a function of carbon number (Run A19: $T=523$ K, $P=1.50$ MPa, $F=2$, $\Phi_{v,0}^{in}/W=1.50 \cdot 10^{-3}$ Nm³ kg⁻¹ s⁻¹). Lines are model predictions. Symbols are experimental selectivities. a) Model ASF; b) Model ORPDM ($p=7.18$, $t_O=9.18$, $k_R=0.779$).

Table 4.4 Accuracies of the Product Distribution Models.

Model	<i>MARR</i> %		<i>s_{rel}</i> %	<i>n</i>	<i>m</i>
	paraffins	olefins			
ASF	49.9	42.5	70.1	370	40
ORPDM	10.1	9.1	13.3	370	57

**Figure 4.9** Relative residuals versus experimental selectivities. (●: paraffins, □: methane, △: olefins, ▽: ethene) a) Model ASF. b) Model ORPDM.

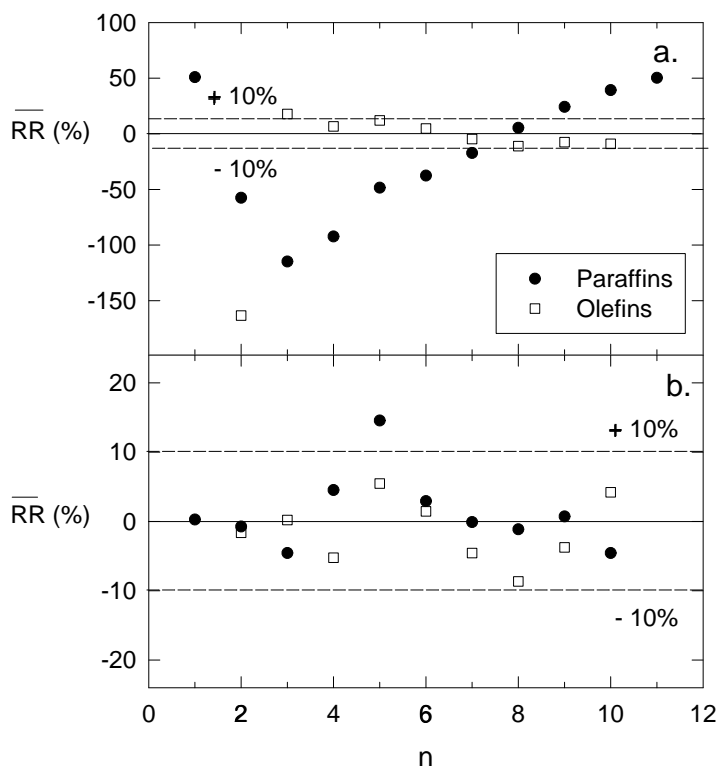


Figure 4.10 Mean relative residuals versus carbon number. a) Model ASF; b) Model ORPDM.

carbon number are plotted in Figure 4.10a. The ASF model appears to give a strong deviation for the selectivity to methane and ethene. Furthermore, a significant trend in the mean deviations of paraffins as function of carbon number was observed (Figure 4.10a). Also, the curved paraffin distribution cannot be described with the ASF model.

The Olefin Readsorption Product Distribution Model, ORPDM, describes n -dependent readsorption of olefins, resulting in a curved distribution of paraffins and a decreasing O/P ratio with carbon number. Examples of product distributions with the predicted model values from model ORPDM are shown in Figure 4.3a-d and 4.8b. The modeled product distribution shows a good prediction of the experimental selectivities. The deviations for C_1 and C_2 products, as well as the increasing paraffin

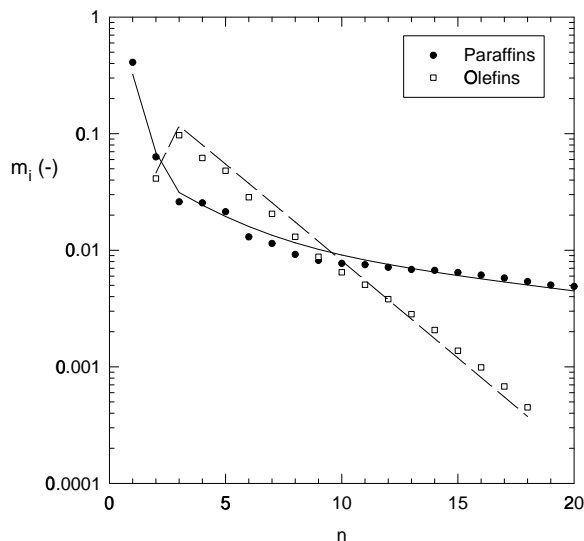


Figure 4.11 Product distribution. Symbols are experimental selectivities of on-line and off-line products. Lines are model predictions of model ORPDM (Run A1: $T=523$ K, $P=1.50$ MPa, $F=2$, $\Phi_{v,0}^{in}/W=1.50 \cdot 10^{-3} \text{ Nm}^3 \text{ kg}^{-1} \text{ s}^{-1}$).

content of the products are described accurately. The predicted O/P ratios for several experiments are plotted in Figure 4.5 and 4.6. The O/P ratio follows the experimental values accurately, with the exception of $n=3$. The model underestimates the O/P ratio slightly at this carbon number.

Figure 4.9b shows that the relative residuals between model ORPDM and experiment are almost always within 25 %, while the mean RR shows no significant trend with carbon number (see Figure 4.10b). The observed deviations from the ASF model are accurately described by our model, resulting in a lower relative variance ($s_{rel}=13.3$ %) relative to the ASF model ($s_{rel}=70.1$ %). The accuracy of the new model is demonstrated in Figure 4.11. Here, the hydrocarbon distribution obtained from taking both the on-line and off-line products into account, is compared with model ORPDM. This figure shows that the optimal values of the model parameters are not affected when taking the off-line product composition into account.

The model parameters of model ORPDM are pseudo kinetic rate constants, incorporating true kinetic rate constants, surface concentrations of intermediates, hydrogen

Table 4.5 Effect of process variables on model parameters.

Parameter	Power law
k_R	$3.3210^{-4} \frac{P_{H_2}^{1.4} P_{CO}^{-0.49}}{\Phi_{v,0}/W}$
t_O	$6.1686 P_{H_2}^{-0.5}$
p	$13.8 P_{H_2}^{-0.47} P_{CO}^{0.43}$

Pressures in MPa, $\Phi_{v,0}/W$ in $\text{Nm}^3 \text{kg}^{-1} \text{s}^{-1}$

and vacant sites. Therefore, the model parameters vary with the adjusted process variables, P_{CO} , P_{H_2} , and space velocity. The effect of process variables on the model parameters is shown in Table 4.5. The model parameters, p and k_R were fitted to the experimental conditions with appropriate empirical equations. If it is assumed that the hydrogen adsorption is dissociative [3]:



the relative olefin termination probability, t_O , can be expressed as:

$$t_O = \frac{k_{t,O}\theta_v}{k_{t,P}\theta_H} = \frac{k_{t,O}}{k_{t,P}K_{H_2}^{0.5}P_{H_2}^{0.5}} \propto P_{H_2}^{-0.5} \tag{4.24}$$

The ratio of the termination rates to olefins and paraffins (t_O) decreases with increasing H_2 pressure, whereas the ratio of the chain growth rate to the paraffin termination rate (p) increases with CO pressure and decreases with H_2 pressure. These observations correspond with the experimental results discussed above. The readsorption parameter, k_R , increases with increasing H_2 pressure and decreases with increasing CO pressure and space velocity. CO inhibits readsorption rates, while a high H_2/CO ratio is favorable for readsorption of olefins. The accuracy of the equations presented in Table 4.5 is illustrated in Figure 4.12.

Figure 4.13 shows the effect of carbon number on the chain growth parameter (α_n) calculated with eq 4.6 and 4.7 according to model ORPDM with the optimized parameters from the experiments in Figure 4.5. The chain growth parameter, α_n , is high at $n = 2$ due to rapid readsorption of ethene (k_R^2) and increased termination to C_2 products (t_p^2), minimal for C_3 and increases to the asymptotical value of $\alpha_\infty = p/(1 + p)$. Some authors stated that this behavior results from two different catalytic

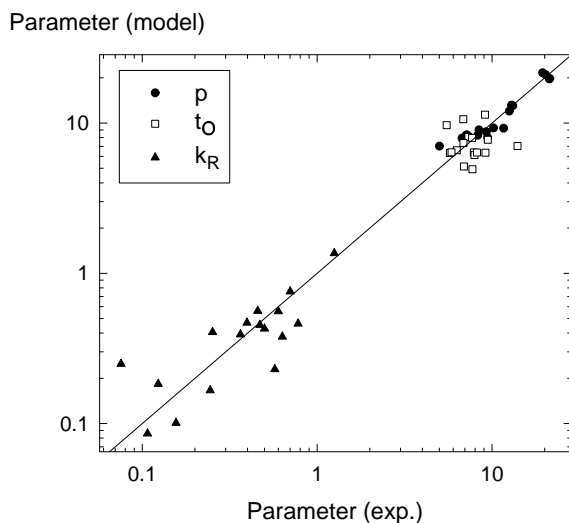


Figure 4.12 Parity graph of experimental (Table 4.3) and modeled parameters (Table 4.5) of model ORPDM.

sites with different chain growth probabilities, since the total hydrocarbon distribution could be fitted by addition of two individual ASF distributions [16, 18, 19]. However such a double- α model cannot explain the following experimental results observed both by us and by, for example, Donnelly and Satterfield [20]: 1) Decrease of the O/P ratio with increasing carbon number. 2) Decrease of the O/P ratio with decreasing space velocity. 3) Decrease of the O/P ratio and mean carbon number with increasing H_2/CO ratios.

Comparison between the model proposed by Zimmerman et al. [21] and ORPDM shows the following major differences: 1) The model of Zimmerman et al. [21] does not account for the increase of the physisorption strength with carbon number. Several studies showed that even in gas-solid reactors, without solubility effects, strong chain length dependencies occur [7, 13]; 2) The strong deviations of C_1 and C_2 products relative to the other hydrocarbons are described accurately with our model in comparison to the model of Zimmerman et al. [21]; 3) Our model describes the complete product distribution accurately without the assumption of secondary hydrogenation on separate hydrogenation sites; 4) ORPDM is tested for a large number of experiments at industrially relevant process conditions, whereas the model of Zimmerman et al. [21]

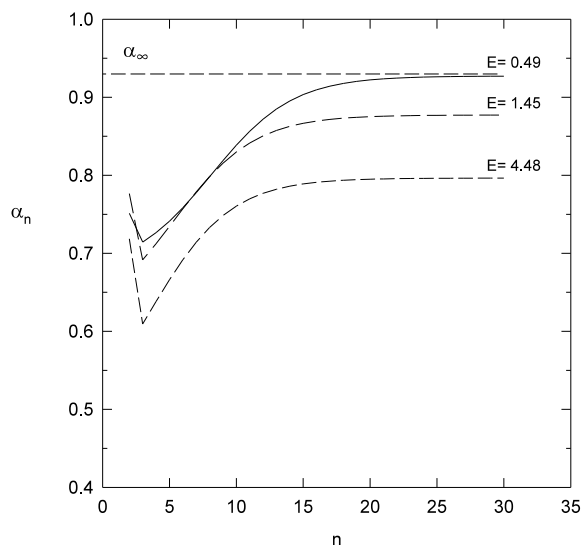


Figure 4.13 Chain growth parameter as function of carbon number. Lines are model predictions of model ORPDM for experiments mentioned in Figure 4.5.

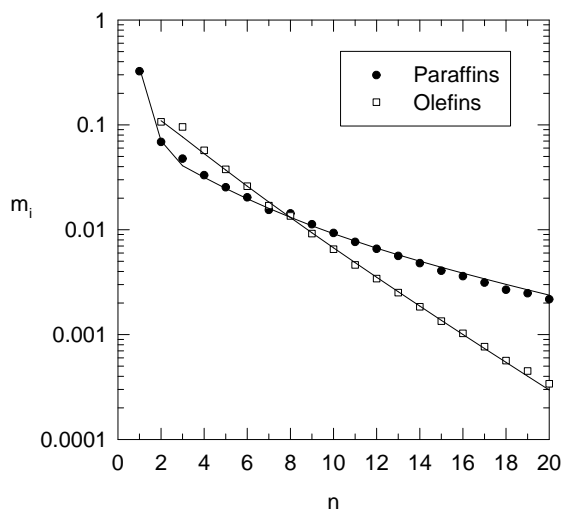


Figure 4.14 Selectivity for Fe-Cu-K ($T=489\text{K}$, $P=1.62\text{MPa}$, $\text{H}_2/\text{CO}=2$), data from Madon et al. [35]. Lines are model predictions of model ORPDM ($p=9.15$, $t_O=4.12$, $k_R=0.66$, $c=0.19$, $t_P^1=4.78$, $t_P^2=1.31$, $k_R^2=1.69e^{2c}$).

has been tested for one experiment only.

To check model ORPDM further, we applied it to interpret selectivity data given by Madon et al. [35] for a Fe-Cu-K precipitated catalyst in a fixed bed plug flow reactor. The selectivity data for paraffins and olefins with the optimized values with model ORPDM are given in Figure 4.14. Our readsorption model proves to describe the observed product distribution accurately. The optimal exponential factor, c , of the readsorption term in eq 4.7 on Fe of 0.19 at $T= 489$ K is lower than the optimized factor in the current study ($c= 0.29$ at $T= 523$ K). The asymptotical value of α on Fe appears to be $\alpha_{\infty}= 0.901$.

ORPDM accounts for secondary readsorption of α -olefins on iron catalysts. In contrast to iron, cobalt catalysts can easily hydrogenate olefins in a secondary reaction [9, 13]. In general, the extent of secondary reactions increases in the order: Fe, Ru, Co [35, 36]. Because of the relatively low tendency of Fe to catalyze secondary hydrogenation, high olefin yields can be obtained with alkali promoted iron catalysts. The present model is applicable for catalysts with no catalytic activity for secondary hydrogenation. However, the model can easily be extended to reaction networks including secondary hydrogenation.

4.5 Conclusions

A new product distribution model, which accounts for n -dependent olefin readsorption, proves to be able to describe accurately the deviations in the observed product distributions, obtained on a precipitated iron catalysts in a gas-solid spinning basket reactor, in both olefins and paraffins from ASF distributions: i.e., a relatively high yield of methane, a relatively low yield of ethene and an exponential decrease of the olefin to paraffin ratio and change of the chain growth parameter with chain length.

For each experimental product distribution three parameters (p , t_O , and k_R) were optimized containing kinetic parameters and surface concentrations of intermediates and vacant sites, whereas four model parameters (c , t_P^1 , t_P^2 , and k_R^2) were optimized for the entire set of experiments. The effects of the process conditions on the product selectivity and model parameters were investigated. The model parameters could be described successfully with equations depending only on the experimental conditions.

The superior accuracy of the new model in predicting experimentally observed product distributions is obtained from adding one extra parameter only (k_R) in comparison to the Anderson-Schulz-Flory model, without assuming of multiple catalytic chain growth sites.

References

- [1] Adesina, A.A., Hydrocarbon synthesis via Fischer-Tropsch reaction: travails and triumphs, *Appl. Catal. A* **1996**, *138*, 345–367.
- [2] Anderson, R.B., *Catalysts for the Fischer-Tropsch synthesis*, vol. 4, Van Nostrand Reinhold, New York **1956**.
- [3] Bell, A.T., Catalytic synthesis of hydrocarbons over group VIII metals. A discussion on the reaction mechanism, *Catal. Rev.-Sci. Eng.* **1981**, *23*, 203–232.
- [4] Dry, M.E., The Fischer-Tropsch synthesis, in J.R. Anderson; M. Boudart, eds., *Catalysis-Science and technology*, vol. 1, Springer-Verlag, New York, 1981 pp. 160–255.
- [5] Glebov, L.S.; Kliger, G.A., The molecular weight distribution of the products of the Fischer-Tropsch synthesis, *Russ. Chem. Rev.* **1994**, *63*, 185–194.
- [6] Wojciechowski, B.W., The kinetics of the Fischer Tropsch synthesis, *Catal. Rev.-Sci. Eng.* **1988**, *30*, 629–702.
- [7] Komaya, T.; Bell, A.T., Estimates of rate coefficients for elementary processes occurring during Fischer-Tropsch synthesis over Ru/TiO₂, *J. Catal.* **1994**, *146*, 237–248.
- [8] Schulz, H.; Van Steen, E.; Claeys, M., Olefin formation, hydrogenation and isomerization in the kinetic regime of Fischer-Tropsch synthesis, in *Selective hydrogenation and dehydrogenation*, DGMK, Kassel, Germany, 1993 .
- [9] Kuipers, E.W.; Scheper, C.; Wilson, J.H.; Oosterbeek, H., Non-ASF product distributions due to secondary reactions during Fischer-Tropsch synthesis, *J. Catal.* **1996**, *158*, 288–300.
- [10] Novak, S.; Madon, R.J.; Suhl, H., Models of hydrocarbon product distributions in Fischer-Tropsch synthesis, *J. Chem. Phys.* **1981**, *74*, 6083–6091.
- [11] Iglesia, E.; Reyes, S.C.; Soled, S.L., Reaction-transport selectivity models and the design of Fischer-Tropsch catalysts, in E.R. Becker; C.J. Pereira, eds., *Computer-aided design of catalysts*, Marcel Dekker, New York, 1993 pp. 199–257.
- [12] Iglesia, E.; Reyes, S.C.; Madon, R.J.; Soled, S.L., Selectivity control and catalyst design in the Fischer-Tropsch synthesis: sites, pellets, and reactors, in E.E. Eley; H. Pines; P.B. Weisz, eds., *Advances in Catalysis*, vol. 39, Academic Press, New York, 1993 pp. 221–302.
- [13] Kuipers, E.W.; Vinkenburg, I.H.; Oosterbeek, H., Chain length dependence of α -olefin readsorption in Fischer-Tropsch synthesis, *J. Catal.* **1995**, *152*, 137–146.

- [14] Satterfield, C.N.; Huff, Jr., G.A., Carbon number distribution of Fischer-Tropsch products formed on an iron catalyst in a slurry reactor, *J. Catal.* **1982**, *73*, 187–197.
- [15] König, L.; Gaube, J., Fischer-Tropsch-Synthese. Neuere Untersuchungen und Entwicklungen, *Chem.-Ing.-Tech.* **1983**, *55*, 14–22.
- [16] Huff, Jr., G.A.; Satterfield, C.N., Evidence for two chain growth probabilities on iron catalysts in the Fischer-Tropsch synthesis, *J. Catal.* **1984**, *85*, 370–379.
- [17] Dictor, R.A.; Bell, A.T., Fischer-Tropsch synthesis over reduced and unreduced iron oxide catalysts, *J. Catal.* **1986**, *97*, 121–136.
- [18] Egiebor, N.O.; Cooper, W.C.; Wojciechowski, B.W., Carbon number distribution of Fischer-Tropsch CO-hydrogenation products from precipitated iron catalysts, *Can. J. Chem. Eng.* **1985**, *63*, 826–834.
- [19] Donnelly, T.J.; Yates, I.C.; Satterfield, C.N., Analysis and prediction of product distributions of the Fischer-Tropsch synthesis, *Energy Fuels* **1988**, *2*, 734–739.
- [20] Donnelly, T.J.; Satterfield, C.N., Product distributions of the Fischer-Tropsch synthesis on precipitated iron catalysts, *Appl. Catal. A* **1989**, *52*, 93–114.
- [21] Zimmerman, W.H.; Bukur, D.B.; Ledakowicz, S., Kinetic model of Fischer-Tropsch selectivity in the slurry phase, *Chem. Eng. Sci.* **1992**, *47*, 2707–2712.
- [22] Krishna, K.R.; Bell, A.T., Estimates of the rate coefficients for chain initiation, propagation, and termination during Fischer-Tropsch synthesis over Ru/TiO₂, *J. Catal.* **1993**, *139*, 104–118.
- [23] Schulz, H.; Beck, K.; Erich, E., Kinetics of Fischer-Tropsch selectivity, *Fuel Process. Technol.* **1988**, *18*, 293–304.
- [24] Tau, L.-M.; Dabbagh, A.; Davis, B.H., Fischer-Tropsch synthesis: ¹⁴C tracer study of alkene incorporation, *Energy Fuels* **1990**, *4*, 94–99.
- [25] Breman, B.B.; Beenackers, A.A.C.M.; Rietjens, E.W.J.; Stege, R.J.H., Gas-liquid solubilities of carbon monoxide, carbon dioxide, hydrogen, water, 1-alcohols ($1 \leq n \leq 6$), and n-paraffins ($1 \leq n \leq 6$) in hexadecane, octacosane, 1-hexadecanol, phenantrene, and tetraethylene glycol at pressures up to 5.5 MPa and temperatures from 293 to 552 K, *J. Chem. Eng. Data* **1994**, *39*, 647–666.
- [26] Chappelow, C.C.; Prausnitz, J.M., Solubilities of gases in high-boiling hydrocarbon solvents, *AIChE J.* **1974**, *20*, 1097–1103.
- [27] Donohue, M.C.; Shah, D.S.; Connally, K.G.; Venkatachalam, V.R., Henry's constants for C₅ to C₉ hydrocarbons in C₁₀ and larger hydrocarbons, *Ind. Eng. Chem. Fundam.* **1985**, *24*, 241–246.
- [28] Caldwell, L.; van Vuuren, D.S., On the formation and composition of the liquid

- phase in Fischer-Tropsch reactors, *Chem. Eng. Sci.* **1986**, *41*, 89–96.
- [29] Ruthven, D.M., *Principles of adsorption and adsorption processes*, Wiley & Sons, New York **1984**.
- [30] Rybolt, T.R.; Wall, M.D.; Thomas, H.E.; Bramblett, J.W.; Phillips, M., Gas-solid chromatography and virial analysis of hydrocarbon adsorption on 13X zeolite, *J. Colloid Interface Sci.* **1990**, *138*, 113–121.
- [31] Keldsen, G.L.; Nicholas, J.B.; Carrado, K.A.; Winans, R.E., Molecular modeling of the enthalpies of hydrocarbons on smectite clay, *J. Phys. Chem.* **1994**, *98*, 279–284.
- [32] Miyabe, K.; Suzuki, M., Chromatographic study on liquid-phase adsorption on octadecylsilyl-silica gel, *AIChE J.* **1995**, *41*, 548–558.
- [33] Miyabe, K.; Suzuki, M., Solvent effect on adsorption phenomena in reversed-phase liquid chromatography, *AIChE J.* **1995**, *41*, 536–547.
- [34] Iglesia, E.; Reyes, S.C.; Madon, R.J., Transport-enhanced α -olefin readsorption pathways Ru-catalyzed hydrocarbon synthesis, *J. Catal.* **1991**, *129*, 238–256.
- [35] Madon, R.J.; Iglesia, E.; Reyes, S.C., Non-Flory product distributions in Fischer-Tropsch synthesis catalyzed by Ruthenium, Cobalt, and Iron, in S.L. Suib; M.E. Davis, eds., *Selectivity in Catalysis*, ACS Symposium Series, American Chemical Society, 1993 pp. 382–396.
- [36] Madon, R.J.; Reyes, S.C.; Iglesia, E., Primary and secondary reaction pathways in ruthenium-catalyzed hydrocarbon synthesis, *J. Phys. Chem.* **1991**, *95*, 7795–7804.
- [37] Madon, R.J.; Iglesia, E., The importance of olefin readsorption and H₂/CO reactant ratio for hydrocarbon chain growth on ruthenium catalysts, *J. Catal.* **1993**, *139*, 576–590.
- [38] Erkey, C.; Rodden, J.B.; Akgerman, A., Diffusivities of synthesis gas and n-alkanes in Fischer-Tropsch wax, *Energy Fuels* **1990**, *4*, 275–276.
- [39] Reid, R.C.; Prausnitz, J.M.; Poling, B.E., *The properties of gases and liquids*, McGraw-Hill, New York, fourth edn. **1987**.
- [40] Bukur, D.B.; Nowicki, L.; Manne, R.K.; Lang, X., Activation studies with a precipitated iron catalyst for Fischer-Tropsch synthesis 2. Reaction studies, *J. Catal.* **1995**, *155*, 366–375.
- [41] Post, M.F.M.; van't Hoog, A.C.; Minderhoud, J.K.; Sie, S.T., Diffusion limitations in Fischer-Tropsch catalysts, *AIChE J.* **1989**, *35*, 1107–1114.
- [42] Zimmerman, W.H.; Bukur, D.B., Effect of particle size on the activity of a fused iron Fischer-Tropsch catalyst, *Ind. Eng. Chem. Res.* **1989**, *28*, 406–413.

- [43] Westerterp, K.R.; van Swaaij, W.P.M.; Beenackers, A.A.C.M., *Chemical reactor design and operation*, Wiley & Sons, second edn. **1984**.
- [44] Nettelhoff, H.; Kokuun, R.; Ledakowicz, S.; Deckwer, W.-D., Studies on the kinetics of Fischer-Tropsch synthesis in slurry phase, *Ger. Chem. Eng.* **1985**, *8*, 177–185.
- [45] Bukur, D.B.; Patel, S.A.; Lang, X., Fixed bed and slurry reactor studies of Fischer-Tropsch synthesis on precipitated iron catalyst, *Appl. Catal. A* **1990**, *61*, 329–349.
- [46] Press, W.H.; Flannery, B.P.; Teukolsky, S.A.; Vetterling, W.T., *Numerical recipes in Pascal*, Cambridge University Press, New York **1989**.

5

Intrinsic Kinetics of the Gas-Solid Fischer-Tropsch and Water Gas Shift Reactions

Abstract

The kinetics of the gas-solid Fischer-Tropsch synthesis over a commercial Fe-Cu-K-SiO₂ catalyst was studied in a continuous spinning basket reactor. Experimental conditions were varied as follows: reactor pressure of 0.8-4.0 MPa, H₂/CO feed ratio of 0.25-4.0, and space velocity of 0.5-2.0 10⁻³ Nm³ kg_{cat}⁻¹ s⁻¹ at a constant temperature of 523 K. A number of rate equations were derived on the basis of a detailed set of possible reaction mechanisms originating from the carbide mechanism for the hydrocarbon formation and the formate mechanism for the water gas shift reaction, respectively. 14 models for the Fischer-Tropsch reaction rate and 2 water gas shift reaction rate models were fitted to the experimental reaction rates. Bartlett's test was used to reduce the set of Fischer-Tropsch rate equations to 3 models, which were statistically indistinguishable. It could be concluded that the reaction rate of the Fischer-Tropsch synthesis is controlled by the formation of the monomer species (methylene) by hydrogenation of molecularly adsorbed CO, whereas the carbon dioxide formation rate (water gas shift) is determined by the formation of a formate intermediate species from adsorbed CO and dissociated hydrogen. Simulations using the optimal kinetic models derived showed good agreement both with experimental data and with some kinetic models from literature.

5.1 Introduction

The Fischer-Tropsch synthesis can be simplified as a combination of the FT reaction and the water gas shift (WGS) reaction. Water is a primary product of the FT reaction, and CO_2 can only be produced by the WGS reaction ($R_{\text{WGS}} = R_{\text{CO}_2}$). The water gas shift reaction is a reversible parallel-consecutive reaction with respect to CO (see Figure 5.1).

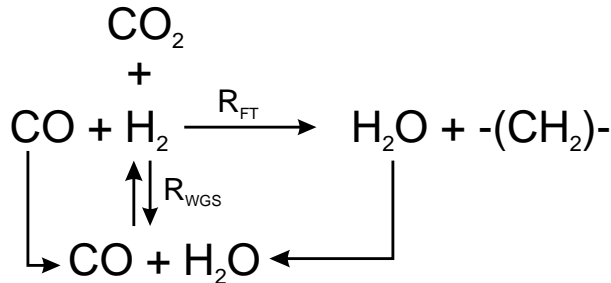


Figure 5.1 Scheme of the reaction of carbon monoxide and hydrogen.

The major problem in describing Fischer-Tropsch reaction kinetics is the complexity of its reaction mechanism and the large number of species involved. Literature on the kinetics of the Fischer-Tropsch synthesis can be divided into two classes. Most studies aim at catalyst improvement and postulate empirical power law kinetics for the carbon monoxide rates [1, 2]:

$$-R_{\text{CO}} = k P_{\text{H}_2}^a P_{\text{CO}}^b \quad (5.1)$$

and carbon dioxide formation or water gas shift reaction [3, 4]:

$$R_{\text{CO}_2} = k P_{\text{H}_2\text{O}}^c P_{\text{CO}}^d \quad (5.2)$$

Relatively few studies aim at understanding the reaction mechanisms. Some authors derived Langmuir-Hinshelwood- Hougen-Watson (LHHW) rate expressions for the reactant consumption [5, 6]. In most cases the rate determining step was assumed to be the formation of the building block or monomer, methylene [7–14]. Simultaneous modeling of the WGS and FT reactions on iron catalysts with WGS activity has hardly been reported. Zimmerman and Bukur [9] and Shen et al. [15] fitted kinetic expressions to their data, but their rate expressions for the WGS were largely empirical.

Our objective is to develop intrinsic rate expressions for the CO conversion to Fischer-Tropsch products and for the water gas shift (WGS) reaction over a precip-

itated iron catalyst on the basis of realistic mechanisms. It also appeared that several existing literature models can be derived from the same limited set of mechanisms [7–14]. A reactor model will be used to predict the reaction rates and conversions as a function of experimental conditions. Comparison between the new rate expressions and available literature models is included as well. The kinetics of the gas-solid Fischer-Tropsch synthesis over a commercial Fe-Cu-K-SiO₂ catalyst were studied in a continuous spinning basket reactor (CSTR) at industrially relevant conditions. Product distributions at the same reaction conditions are reported in Chapter 4.

5.2 Theory

5.2.1 Active Sites on Precipitated Iron Catalysts

The composition of iron-based catalysts changes during Fischer-Tropsch synthesis. Zhang and Schrader [16] concluded that two active sites operate simultaneously on the surface of iron catalysts: Fe⁰/Fe-carbides and magnetite (Fe₃O₄). The carbide phase is active towards dissociation of CO and formation of hydrocarbons, while the oxide phase adsorbs CO associatively and produces predominantly oxygenated products. Lox et al. [17] and Shroff et al. [18] concluded that the magnetite phase has negligible catalytic activity towards FT reactions whereas carbide formation results in a high FT activity.

Several authors proposed that magnetite (Fe₃O₄) is the most active phase for the WGS reaction [4, 5, 16, 19, 20] on iron catalysts. Rao et al. [19] studied the iron phase of Fe/Cu/K/SiO₂ catalysts from the demonstration unit at LaPorte, Texas (August, 1992) with Mössbauer spectroscopy. The changes of the magnetite phase corresponded with the WGS reaction activity during time-on-stream. Lox et al. [17] showed that Fe₃O₄ coexists with various iron carbides on the catalyst during synthesis gas reactions. It is generally accepted that the WGS and FT reactions proceed on different active sites on precipitated iron catalysts [5, 19].

5.2.2 Hydrocarbon Formation

5.2.2.1 Elementary Reactions

The mechanism of the hydrocarbon formation during the FTS has been reviewed and discussed by several authors [1, 21–24]. Recent reviews were given by Hindermann et al. [25], Dry [26], Dry [27], and Adesina [28] and in Chapter 2. The most important

growth mechanism for the hydrocarbon formation is the surface carbide mechanism by CH_2 insertion [1, 6, 29, 30]. The presence of adsorbed methylene has been identified with isotopic-tracer techniques on $\text{Fe}/\text{Al}_2\text{O}_3$ [31].

The formation of the methylene species will be discussed in more detail. Hydrogen reacts via either the dissociative adsorbed state or in the molecular state [32]. Dissociative adsorption of hydrogen proceeds on two free active sites:



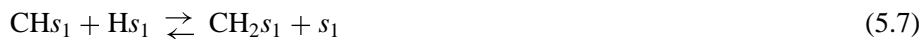
s_1 denotes a catalytic site where hydrocarbons can be formed. Carbon monoxide adsorbs associatively on an active site [32]:



Adsorbed CO can be dissociated in a second step:



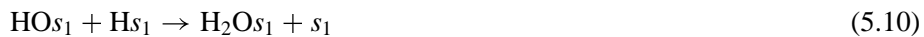
Surface carbon reacts with adsorbed dissociated hydrogen,



or with molecular hydrogen,



Oxygen is removed irreversibly and rapidly from the surface by consecutive hydrogenation reactions [24, 33, 34],



or with molecular hydrogen according to an Eley-Rideal mechanism [8, 24, 33],



Another possible mechanism starts with molecularly adsorbed carbon monoxide and successive hydrogen assisted dissociation with dissociated hydrogen [6, 8],



or molecular hydrogen,



Based on these elementary reactions, we defined four different possible mechanisms. See Table 5.1 for the conventions and state of the reactants in the elementary formation reactions of methylene. The complete set of elementary reactions for each model is given in Table 5.2.

Table 5.1 The various kinetic models considered, together with the presence of the reactants in the rate determining step.

Model	CO	H ₂
FT-I	Dissociative	Dissociative
FT-II	Dissociative	Molecular
FT-III	Associative	Dissociative
FT-IV	Associative	Molecular

5.2.2.2 Kinetic Rate Equations

In order to derive rate equations, we used the Langmuir-Hinshelwood-Hougen-Watson approach, see, for example, Graaf et al. [35]. For each model, the possible rate determining steps were identified, while all other steps were assumed to be at quasi-equilibrium. The following assumptions, all based on literature, were taken into account:

1. Reaction path for the CO consumption to the monomer methylene, CH₂, contains one irreversible rate determining step, in analogy with Ref. [35].
2. Steady state concentrations of all intermediates on the catalyst surface [35, 36].

Table 5.2 Elementary reactions for FT synthesis.

Model	Number	Elementary reaction
FT-I	1	$\text{CO} + \text{s}_1 \rightleftharpoons \text{COs}_1$
	2	$\text{COs}_1 + \text{s}_1 \rightleftharpoons \text{Cs}_1 + \text{Os}_1$
	3	$\text{Cs}_1 + \text{Hs}_1 \rightleftharpoons \text{CHs}_1 + \text{s}_1$
	4	$\text{CHs}_1 + \text{Hs}_1 \rightleftharpoons \text{CH}_2\text{s}_1 + \text{s}_1$
	5	$\text{Os}_1 + \text{Hs}_1 \rightarrow \text{HOs}_1 + \text{s}_1$
	6	$\text{HOs}_1 + \text{Hs}_1 \rightarrow \text{H}_2\text{Os}_1 + \text{s}_1$
	7	$\text{H}_2\text{O} + \text{s}_1 \rightleftharpoons \text{H}_2\text{Os}_1$
	8	$\text{H}_2 + 2\text{s}_1 \rightleftharpoons 2\text{Hs}_1$
FT-II	1	$\text{CO} + \text{s}_1 \rightleftharpoons \text{COs}_1$
	2	$\text{COs}_1 + \text{s}_1 \rightleftharpoons \text{Cs}_1 + \text{Os}_1$
	3	$\text{Cs}_1 + \text{H}_2 \rightleftharpoons \text{CH}_2\text{s}_1$
	4	$\text{Os}_1 + \text{H}_2 \rightarrow \text{H}_2\text{Os}_1$
	5	$\text{H}_2\text{O} + \text{s}_1 \rightleftharpoons \text{H}_2\text{Os}_1$
FT-III	1	$\text{CO} + \text{s}_1 \rightleftharpoons \text{COs}_1$
	2	$\text{COs}_1 + \text{Hs}_1 \rightleftharpoons \text{HCOs}_1 + \text{s}_1$
	3	$\text{HCOs}_1 + \text{Hs}_1 \rightleftharpoons \text{Cs}_1 + \text{H}_2\text{Os}_1$
	4	$\text{Cs}_1 + \text{Hs}_1 \rightleftharpoons \text{CHs}_1 + \text{s}_1$
	5	$\text{CHs}_1 + \text{Hs}_1 \rightleftharpoons \text{CH}_2\text{s}_1 + \text{s}_1$
	6	$\text{H}_2 + 2\text{s}_1 \rightleftharpoons 2\text{Hs}_1$
	7	$\text{H}_2\text{O} + \text{s}_1 \rightleftharpoons \text{H}_2\text{Os}_1$
FT-IV	1	$\text{CO} + \text{s}_1 \rightleftharpoons \text{COs}_1$
	2	$\text{COs}_1 + \text{H}_2 \rightleftharpoons \text{H}_2\text{COs}_1$
	3	$\text{H}_2\text{COs}_1 + \text{H}_2 \rightleftharpoons \text{CH}_2\text{s}_1 + \text{H}_2\text{O}$
	4	$\text{H}_2\text{O} + \text{s}_1 \rightleftharpoons \text{H}_2\text{Os}_1$

¹Equilibrium constant, e.g. reaction step FT-II: $K_1 = \frac{\theta_{\text{COs}_1}}{P_{\text{CO}}\theta_{\text{s}_1}}$

Table 5.3 Reaction rate expressions considered for the Fischer-Tropsch synthesis, R_{FT} ($\text{mol kg}_{cat}^{-1} \text{s}^{-1}$).

Model	Kinetic equation
FT-I3	$\frac{k P_{CO}^{1/2} P_{H_2}^{1/2}}{(1 + a P_{CO}^{1/2} + b P_{H_2O})^2}$
FT-I4	$\frac{k P_{CO}^{1/2} P_{H_2}^{3/4}}{(1 + a P_{CO}^{1/2} P_{H_2}^{-1/4} + b P_{H_2O})^2}$
FT-II3	$\frac{k P_{CO}^{1/2} P_{H_2}}{1 + a P_{CO}^{1/2} + b P_{H_2O}}$
FT-III2	$\frac{k P_{CO} P_{H_2}^{1/2}}{(1 + a P_{CO} + b P_{H_2O})^2}$
FT-III3	$\frac{k P_{CO} P_{H_2}}{(1 + a P_{CO} + b P_{H_2O})^2}$
FT-IV2	$\frac{k P_{CO} P_{H_2}}{1 + a P_{CO} + b P_{H_2O}}$
FT-IV3	$\frac{k P_{CO} P_{H_2}^2}{1 + a P_{CO} + b P_{H_2O}}$

- Catalyst sites of type 1 are active towards hydrocarbon formation, which are uniform and homogeneously distributed [35, 36].
- Initial adsorption of hydrogen and carbon monoxide is in quasi-equilibrium with the gas phase concentrations [24].
- Water is removed irreversibly after CO dissociation [24, 33, 37].
- CO is adsorbed more strongly than H_2 on iron catalysts, resulting in a high surface concentration of CO or dissociated CO relative to H_2 [21, 38].
- H_2O adsorbs strongly and may inhibit the FT reaction rate [9].

With these assumptions, 7 different kinetic models remain possible. These are summarized in Table 5.3. The development of the kinetic equations will be illustrated for model FT-II3. The model codes refer to the set of elementary reactions and the elementary reaction not at equilibrium (that is the rate determining step, so in this case

Table 5.4 Parameters for the FT kinetic models.

Model	k (x) (mol kg ⁻¹ s ⁻¹ MPa ^x)	a (x) (MPa ^x)	b (MPa ⁻¹)
FT-I3	$(k_3 k_5 K_1 K_2 K_8)^{1/2} (-1)$	$(K_1 K_2 k_5 / k_3)^{1/2} (-1/2)$	K_7
FT-I4	$(k_4 k_5 K_1 K_2 K_3)^{1/2} K_8^{3/4} (-5/4)$	$(K_1 K_2 K_3 K_8^{1/2} k_5 / k_4)^{1/2} (-1/4)$	K_7
FT-II3	$(k_3 k_4 K_1 K_2)^{1/2} (-3/2)$	$(k_4 K_1 K_2 / k_3)^{1/2} (-1/2)$	K_5
FT-III2	$k_2 K_1 K_6^{1/2} (-3/2)$	$K_1 (-1)$	K_7
FT-III3	$k_3 K_1 K_2 K_6 (-2)$	$K_1 (-1)$	K_7
FT-IV2	$k_2 K_1 (-2)$	$K_1 (-1)$	K_4
FT-IV3	$k_3 K_1 K_2 (-3)$	$K_1 (-1)$	K_4

reaction 3). The set of elementary reactions for model FT-II3 is shown in Table 5.2. The reaction rate of the rate determining step is:

$$R_{\text{FT-II3}} = k_3 \theta_{C_{s_1}} P_{H_2} = k_4 \theta_{O_{s_1}} P_{H_2} \quad (\text{mol kg}_{\text{cat}}^{-1} \text{s}^{-1}) \quad (5.18)$$

The surface fraction of carbon can be calculated from the site balance, the preceding reaction steps which are at quasi-equilibrium and the reaction rate for water formation:

$$K_1 = \frac{\theta_{C_{s_1}}}{P_{CO} \theta_{s_1}}, \quad K_2 = \frac{\theta_{C_{s_1}} \theta_{O_{s_1}}}{\theta_{CO_{s_1}} \theta_{s_1}} \quad (5.19)$$

$$\theta_{C_{s_1}} = \frac{k_4}{k_3} \theta_{O_{s_1}} = \left(\frac{K_1 K_2 k_4}{k_3} \right)^{1/2} P_{CO}^{1/2} \theta_{s_1} \quad (5.20)$$

From assumptions 6 and 7 it follows that only surface carbon and water occupy a significant fraction of the total number of sites, the site balance becomes:

$$\theta_{s_1} + \theta_{C_{s_1}} + \theta_{H_2 O_{s_1}} = 1 \quad (5.21)$$

Substitution of the surface fraction of carbon in eq 5.18:

$$R_{\text{FT-II3}} = \frac{(k_3 k_4 K_1 K_2)^{1/2} P_{CO}^{1/2} P_{H_2}}{1 + (K_1 K_2 k_4 / k_3)^{1/2} P_{CO}^{1/2} + K_5 P_{H_2 O}} = \frac{k P_{CO}^{1/2} P_{H_2}}{1 + a P_{CO}^{1/2} + b P_{H_2 O}} \quad (5.22)$$

Table 5.3 summarizes the final form of the various rate expressions for the 7 possible kinetic models considered, whereas Table 5.4 shows the kinetic and adsorption parameters for the different kinetic models. It can be seen that the pressure dependency of CO and H₂ in the numerator ranges from 1/2 to 1, and 1/2 to 2, respectively. The denominator is quadratic in case of a dual site elementary reaction, in contrast to a single

site rate determining step. The denominator consists of the individual contributions of significantly abundant species on the catalyst surface.

The concentration of free sites θ_{s_1} is determined from a site balance. It is assumed that the total number of sites is constant:

$$\theta_{s_1} + \sum_{i=1}^n \theta_{i s_1} = 1 \quad (5.23)$$

where θ_{s_1} is the fraction free sites and $\theta_{i s_1}$ are the surface fractions occupied with adsorbed species such as carbon, carbon monoxide, hydrogen, alkyl chains, water, carbon dioxide, and so forth. The addition of several inhibition terms in the denominator can not be justified statistically due to a high degree of covariance or correlation [39, 40]. The derived kinetic expressions have a maximum of two inhibition terms: one term for CO or a carbidic species ($\theta_{C s_1}$) and the other for H₂O inhibition.

5.2.2.3 Literature Models

Reviews of kinetic equations for iron-based catalysts were published by Huff and Satterfield [8], Zimmerman and Bukur [9], and Van der Laan and Beenackers [45], enclosed in slightly revised form as Chapter 2. Kinetic studies of the FTS on iron and cobalt catalysts are summarized in Table 5.5. The corresponding operating conditions are given in Chapter 2 (Table 2.7).

It can be shown that all these literature models can be derived from the set of mechanisms considered in this study and which are summarized in Table 5.2. Appropriate assumptions for the inhibitor effects in the site balance of the kinetic rate expressions in table 5.3 result in similar mathematical expressions. The mechanistic implications of the available FT kinetic models are summarized in Table 5.5.

5.2.3 Water Gas Shift Reaction

5.2.3.1 Reaction Mechanism

Several mechanisms for the water gas shift reaction were proposed in the literature. Single studies of the water gas shift reaction over supported metals suggest the appearance of formate species [4, 5, 20, 35]. The formate species can be formed by the reaction between either a hydroxy species or water and carbon monoxide either in the gas phase or in the adsorbed state. The hydroxy intermediate can be formed by the decomposition of water. The formate intermediate can be reduced to either adsorbed or gaseous carbon dioxide (see Table 5.6). Rethwisch and Dumesic [20] studied the water gas shift reaction on several supported and unsupported iron oxide and zinc

Table 5.5 Reaction rate equations overall synthesis gas consumption rate. See Table 2.7 for experimental conditions, reactor type and catalyst applied.

	Kinetic expression	References	Mechanistic implications
(a)	$k P_{H_2}$	[9, 22, 41]	FT-II3 ($b=0, a P_{CO} \gg 1$) FT-IV2 ($b=0, a P_{CO} \gg 1$)
(b)	$k P_{H_2}^a P_{CO}^b$	[3]	-
(c)	$\frac{k P_{H_2} P_{CO}}{P_{CO} + K P_{H_2O}}$	[7, 9, 10, 15, 22]	FT-IV2 ($a P_{CO}$ and $b P_{H_2O} \gg 1$)
(d)	$\frac{k P_{H_2}^2 P_{CO}}{P_{CO} P_{H_2} + K P_{H_2O}}$	[8, 15, 42, 43]	FT-II3 (water formation is reversible)
(e)	$\frac{k P_{H_2}^2 P_{CO}}{1 + a P_{CO} P_{H_2}^2}$	[22]	-
(f)	$\frac{k P_{H_2} P_{CO}}{P_{CO} + K P_{CO_2}}$	[9, 11, 12, 43]	FT-IV2 ($a P_{CO} \gg 1$ and CO_2 inhibition)
(g)	$\frac{k P_{H_2} P_{CO}}{P_{CO} + K_1 P_{H_2O} + K_2 P_{CO_2}}$	[9, 11, 12]	FT-IV2 ($a P_{CO} \gg 1, CO_2$ and H_2O inhibition)
(h)	$\frac{k P_{CO}^{1/2} P_{H_2}^{1/2}}{\left(1 + K_1 P_{CO}^{1/2} + K_2 P_{H_2}^{1/2}\right)^2}$	[14]	FT-I3 (H_2 inhibition, $b P_{H_2O} = 0$)
(i)	$\frac{k P_{CO} P_{H_2}^{1/2}}{\left(1 + K_1 P_{CO} + K_2 P_{H_2}^{1/2}\right)^2}$	[6]	FT-III2 (H_2 inhibition, $b P_{H_2O} = 0$)
(j)	$\frac{k P_{CO} P_{H_2}}{(1 + K P_{CO})^2}$	[13, 40, 44]	FT-III3 ($b P_{H_2O} = 0$)

Table 5.6 Elementary reactions for the water gas shift reaction.

Model	Number	Elementary reaction
WGS-I	1	$\text{CO} + \text{s}_2 \rightleftharpoons \text{COs}_2$
	2	$\text{CO}_2 + \text{s}_2 \rightleftharpoons \text{CO}_2\text{s}_2$
	3	$\text{H}_2\text{O} + \text{s}_2 \rightleftharpoons \text{H}_2\text{Os}_2$
	4	$\text{H}_2 + 2\text{s}_2 \rightleftharpoons 2\text{Hs}_2$
	5	$\text{COs}_2 + \text{H}_2\text{Os}_2 \rightleftharpoons \text{HCOOs}_2 + \text{Hs}_2$
	6	$\text{HCOOs}_2 + \text{s}_2 \rightleftharpoons \text{Hs}_2 + \text{CO}_2\text{s}_2$
WGS-II	1	$\text{CO} + \text{s}_2 \rightleftharpoons \text{COs}_2$
	2	$\text{CO}_2 + \text{s}_2 \rightleftharpoons \text{CO}_2\text{s}_2$
	3	$\text{H}_2\text{O} + \text{s}_2 \rightleftharpoons \text{H}_2\text{Os}_2$
	4	$\text{H}_2\text{Os}_2 + \text{s}_2 \rightleftharpoons \text{OHs}_2 + \text{Hs}_2$
	5	$\text{H}_2 + 2\text{s}_2 \rightleftharpoons 2\text{Hs}_2$
	6	$\text{COs}_2 + \text{OHs}_2 \rightleftharpoons \text{HCOOs}_2 + \text{s}_2$
	7	$\text{HCOOs}_2 + \text{s}_2 \rightleftharpoons \text{Hs}_2 + \text{CO}_2\text{s}_2$

oxide catalysts. They suggested that the WGS reaction over unsupported magnetite proceeds via a direct oxidation mechanism, while all supported iron catalysts operate via a mechanism with formate species due to limited change of oxidation state of the iron cations.

5.2.3.2 Kinetic Expressions

Several assumptions were made in order to derive the LHHW rate expressions:

- Steady state for the adsorbed species.
- One rate determining step in the sequence of elementary reactions over the complete range of experimental conditions.
- Surface concentrations of intermediate species are negligible [35].
- Active sites for the WGS (type 2) are different than the sites for the hydrocarbon forming reactions (type 1) [5].

- Rate determining step is a dual-site elementary reaction between two adsorbed species [5].
- Adsorption of reactants and desorption of products are at equilibrium.

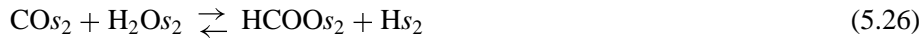
With the mentioned assumptions two rate determining steps are possible. First, the rate determining step is (WGS-II6):



The hydroxyl species is formed by dissociation of water:



Second, the reaction between adsorbed water and carbon monoxide (WGS-I5) can be rate determining:



On basis of the formate mechanism and the mentioned assumptions, two kinetic rate equations were developed. The expressions are given in Table 5.7. The adsorption of H_2 and CO_2 are assumed to be negligible relative to CO and H_2O [5, 9, 38]. Thus, the mass balance of the catalytic sites, s_2 , is:

$$\theta_{s_2} + \theta_{\text{H}_2\text{O}s_2} + \theta_{\text{CO}s_2} = 1 \quad (5.27)$$

Derivation of other kinetic expressions based on adsorption of more components is possible from the above equations. Since the WGS reaction is an equilibrium reaction, the reverse reaction has to be taken into account. For the temperature dependency of the equilibrium constant of the WGS reaction, K_P , the following relation was used (Graaf et al. [46]):

$$\log K_P = \log \left(\frac{P_{\text{CO}_2} P_{\text{H}_2}}{P_{\text{H}_2\text{O}} P_{\text{CO}}} \right)_{eq} = \left(\frac{2073}{T} - 2.029 \right) \quad (5.28)$$

Kinetic studies of the WGS reaction under FT conditions on iron-based catalysts are summarized in Chapter 2 (Table 2.8).

Table 5.7 Rate expressions considered for the water gas shift reaction, R_{CO_2} (mol kg_{cat}⁻¹ s⁻¹).

Model	Kinetic equation	Site balance
WGS-I5	$\frac{k_w (P_{CO} P_{H_2O} - P_{CO_2} P_{H_2} / K_P)}{(1 + K_1 P_{CO} + K_3 P_{H_2O})^2}$ $k_w = k_5 K_1 K_3 \text{ (mol kg}^{-1} \text{ s}^{-1} \text{ MPa}^{-2}\text{)}$	s ₂ , COs ₂ , H ₂ O s ₂
WGS-II6	$\frac{k_w (P_{CO} P_{H_2O} / P_{H_2}^{1/2} - P_{CO_2} P_{H_2}^{1/2} / K_P)}{(1 + K_1 P_{CO} + K_3 P_{H_2O})^2}$ $k_w = k_5 K_1 K_3 K_4 K_5^{-1/2} \text{ (mol kg}^{-1} \text{ s}^{-1} \text{ MPa}^{-1.5}\text{)}$	s ₂ , COs ₂ , H ₂ O s ₂

5.3 Experimental

The kinetics of both the Fischer-Tropsch synthesis and the water gas shift reaction over a commercial precipitated iron catalyst (Ruhchemie LP33/81) were unraveled by relevant experiments in a Spinning Basket Reactor (SBR). For a detailed description of the experimental set-up, the catalyst applied, the analytic and the experimental procedures, see Chapter 3.

The baskets were loaded with 2.34 g of catalyst, with particle diameters between 0.125 and 0.160 mm. The catalyst was pretreated with a hydrogen flow rate of $8.33 \cdot 10^{-4} \text{ Nm}^3 \text{ kg}_{cat}^{-1} \text{ s}^{-1}$ according to Bukur et al. [47]. The reactor temperature was linearly increased from 293 to 553 K by 0.017 K /s. The reactor temperature was kept at 553 K for 24 hrs at atmospheric pressure. After catalyst reduction, synthesis gas was fed to the reactor which at standard conditions operated at 523 K, 1.50 MPa, $(H_2/CO)_{feed}=2$ and a space velocity of $1.51 \cdot 10^{-3} \text{ Nm}^3 \text{ kg}_{cat}^{-1} \text{ s}^{-1}$.

Checking the criteria of Weisz and Prater [48] for the reactants CO and H₂ showed that no intraparticle diffusion limitations occurred at relevant experimental conditions, even not at the highest conversion rates. Here, it was conservatively assumed that the catalyst pores were filled with long-chain hydrocarbon waxes.

24 kinetic experiments were carried out in the SBR with the Ruhchemie precipitated iron catalyst. The experimental conditions were varied as follows: $P=0.8 - 4.0$ MPa, H_2/CO feed ratio= 0.25 - 4.0, and $\Phi_{v,0}^{in}/W=0.5 \cdot 10^{-3} - 2.0 \cdot 10^{-3} \text{ Nm}^3 \text{ kg}_{cat}^{-1} \text{ s}^{-1}$ at a temperature of 523 K. At regular intervals, the standard experiment was repeated to

determine possible deactivation effects of the catalyst. A summary of the experimental results and operating conditions is given in Appendix A.

5.4 Results and Discussion

After an initial period of 100 hrs, a steady state was more or less obtained. The catalyst activity, reaction rate to hydrocarbon products (R_{FT}) and the rate of the water gas shift (R_{WGS}) did not change much over 1200 hrs time on stream (see Chapter 3; Figure 3.10a). The reaction rates were not corrected for catalyst aging due to the small effect of time on stream on the catalyst activity.

The preliminary screening of the Fischer-Tropsch kinetic expressions was performed with a maximum of two adsorbed species in the site balance. Every kinetic model was optimized with two different mathematical forms of the site balance:

$$\theta_{s_1} + (\theta_{C_{s_1}} \text{ or } \theta_{CO_{s_1}}) + \theta_{H_2O_{s_1}} = 1 \quad (5.29)$$

$$(\theta_{C_{s_1}} \text{ or } \theta_{CO_{s_1}}) + \theta_{H_2O_{s_1}} = 1 \quad (5.30)$$

For models based on the carbide mechanism (FT-I, FT-II), the carbidic species is surface carbon $\theta_{C_{s_1}}$, formed by dissociation of CO. Models FT-III and FT-IV are based on associative adsorbed CO species $\theta_{CO_{s_1}}$. The 7 kinetic equations were optimized with a non-linear optimization routine using both eqs 5.29 and 5.30 for the site balance. Contributions of species in the site balance were eliminated if the fitted adsorption coefficients were not significantly different from zero or had a significantly negative value. Table 5.8 shows the results of the kinetic models with the relative variance and their ranking. Four models are able to describe the experimental FT reaction rates with a relative variance less than 35 % and a maximum of three optimized parameters.

Bartlett's test was applied to investigate whether the differences in accuracy of the various models were statistically significant [49, 50]. This test compares a critical calculated χ_c^2 value (for details, see Chapter 3 or Jonker et al. [49]) with a tabulated χ_t^2 value [51]. If χ_c^2 exceeds the tabulated value, the model with the largest deviation was rejected and χ_c^2 was recalculated. Models were subsequently rejected, until χ_c^2 was below the tabulated value. Table 5.9 compares χ_c^2 with the tabulated χ_t^2 value for $H - 1$ degrees of freedom. The table shows that the best five models ($H = 5$) passed the test and are statistically indistinguishable. The best five models are, in succeeding order: FT-IV2 (eq 5.29), FT-III2, FT-III3, FT-IV2 (eq 5.30), FT-II3. Model FT-II3 was rejected from list of best models, because the optimized parameters of this model were unrealistic and the model just passed the Bartlett's test due to the large relative

Table 5.8 FT kinetic model screening.

Model	Site balance (eq)	s_{rel} (%)	Rank	Remarks
FT-I3	5.30	63.7	6	
FT-I4	5.30	65.9	9	
FT-II3	5.30	45.2	5	
FT-III2	5.29	30.0	2	
FT-III2	5.30	64.4	8	
FT-III3	5.29	30.9	3	
FT-III3	5.30	63.8	7	
FT-IV2	5.29	29.6	1	
FT-IV2	5.30	32.4	4	
FT-IV3	5.29, 5.30	-	-	$a < 0$

FT-I3, FT-I4, FT-II3 with site balance 5.29 results in $a < 0$

variance. The site balances of models FT-IV2 (eq 5.29) and FT-IV2 (eq 5.30) vary slightly only. Consequently, the model with the highest relative variance was rejected, i.e. FT-IV2 (eq 5.30).

Four experiments were found to be outliers in the three remaining models (Runs: 5, 17, 20, 23). The remaining models were fitted again with the reduced data set of 20 experimental reaction rates. Table 5.10 gives the optimized values of the parameters in these three models: FT-III2, FT-III3, FT-IV2. The three remaining kinetic expressions (FT-III2, FT-III3, and FT-IV2) are all based on the combined enol/carbide mechanism. The mathematical form of the equations is very similar, indicating a difficult discrimination procedure. Figure 5.2 compares the experimental and calculated reaction rates of these three models.

Kinetic expression FT-IV2 is similar to several literature models [7, 9, 10, 22] for iron catalysts (see Table 5.5). In this model, the rate determining step is a single site reaction between undissociated adsorbed CO and gaseous H₂. However, the literature models were developed from experiments in slurry phase or packed bed reactors. The major difference between these literature models and optimized model FT-IV2 is a significant number of free sites in the latter model. In our experiments, the catalyst particles are located in spinning baskets with a small amount of high-boiling hydrocarbons present in the catalyst pores.

Kinetic expressions FT-III2 and FT-III3 are also able to describe our experiments accurately. These models are also developed from the combined enol/carbide mecha-

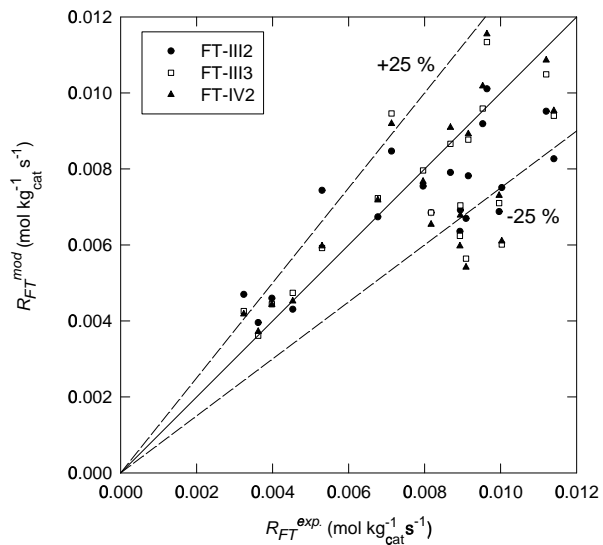


Figure 5.2 Parity graph of experimental and optimized Fischer-Tropsch reaction rates.

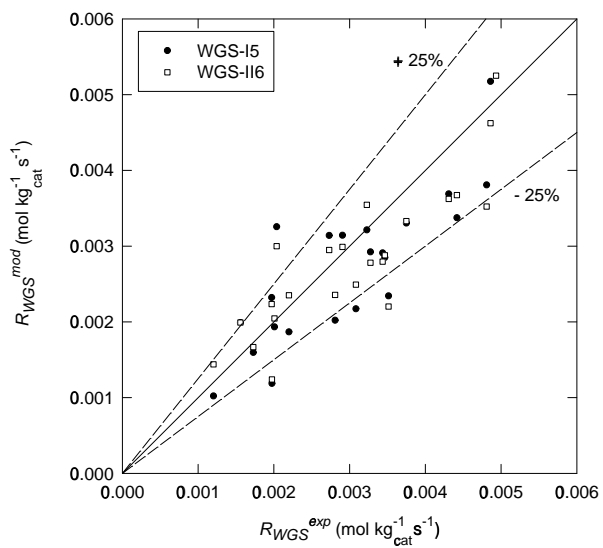


Figure 5.3 Parity graph of experimental and optimized WGS reaction rates.

Table 5.9 Bartlett's test for FT models¹.

H^2	χ_c^2	χ_t^2
9	42.2	15.5
8	38.2	14.1
7	32.6	12.6
6	23.6	11.1
5	6.03	9.49
4	0.206	7.81
3	0.040	5.99
2	0.0037	3.84

¹ χ_c^2 : critical χ^2 according to Bartlett's test [49]; χ_t^2 : tabulated χ^2 [51]

² H : number of models under consideration

nism: rate determining steps are the dual site surface reaction between undissociated adsorbed CO and dissociated H₂ (FT-III2) and between adsorbed formyl and dissociated H₂ (FT-III3). Model FT-III2 is similar to the optimal equation of Sarup and Wojciechowski [14] for a precipitated cobalt catalyst in a Bertly reactor, whereas FT-III3 was found to be the best model by Yates and Satterfield [40] on cobalt measured in a slurry reactor. The kinetic model of Sarup and Wojciechowski [14] was developed with the assumption that the site balance consists of free sites, adsorbed CO and dissociated H₂, while Yates and Satterfield [40] only included CO inhibition.

The WGS reaction rate was optimized with the kinetic expressions in Table 5.7. Due to a high degree of similarity between equations WGS-I5 and WGS-II6, the relative variances are almost equal, 25.0 % and 23.0 %, respectively. The Bartlett's test is unable to discriminate between these models. A parity plot between the experimental and model values of the WGS reaction rates is shown in Figure 5.3. Reaction rate expression WGS-II6 is similar to the optimal model of Lox and Froment [5]. Both models assume that the rate of the WGS reaction is determined by the reaction of adsorbed carbon monoxide and hydroxyl towards a formate intermediate. Our model assumes adsorption of CO and water to be dominant in the site balance, whereas Lox and Froment [5] included inhibition of hydroxyl species only. The corresponding model parameters are also given in Table 5.10.

Both the experimental and the calculated rates of the Fischer-Tropsch and the water gas shift reaction are compared in Figures 5.4- 5.5 at various experimental conditions. The calculated rates stem from models FT-III2 and WGS-II6 with the input

Table 5.10 Final estimates for the parameters of the FT and WGS kinetic models.

Parameter	Dimension	Estimate
WGS-I5 (s_{rel} 21.0 %)		
k_w	$\text{mol kg}^{-1} \text{s}^{-1} \text{MPa}^{-2}$	1.77 ± 0.04
K_1	MPa^{-1}	2.10 ± 0.04
K_3	MPa^{-1}	24.19 ± 3.14
WGS-II6 (s_{rel} 21.5 %)		
k_w	$\text{mol kg}^{-1} \text{s}^{-1} \text{MPa}^{-1.5}$	1.13 ± 0.01
K_1	MPa^{-1}	2.78 ± 0.04
K_3	MPa^{-1}	12.27 ± 0.94
FT-III2 (s_{rel} 23.7 %)		
k	$\text{mol kg}^{-1} \text{s}^{-1} \text{MPa}^{-1.5}$	0.0488 ± 0.0049
a	MPa^{-1}	0.563 ± 0.094
b	MPa^{-1}	4.05 ± 0.77
FT-III3 (s_{rel} 22.4 %)		
k	$\text{mol kg}^{-1} \text{s}^{-1} \text{MPa}^{-2}$	0.0556 ± 0.0056
a	MPa^{-1}	0.125 ± 0.069
b	MPa^{-1}	7.00 ± 0.87
FT-IV2 (s_{rel} 22.7 %)		
k	$\text{mol kg}^{-1} \text{s}^{-1} \text{MPa}^{-2}$	0.0779 ± 0.0157
a	MPa^{-1}	0.536 ± 0.333
b	MPa^{-1}	32.27 ± 8.69

values of the H_2/CO feed ratio and the flow rate, $\Phi_{v,0}^{in}/W$ based on stoichiometry and mass balances of the components present (CO , CO_2 , H_2 , H_2O). The product composition was determined from gas chromatographic analysis of the gas and from liquid hydrocarbon product samples. The values of n and m were determined from the product composition. In this study, n varied between 2.86-5.04. The ratio of m/n varied between 2.14-2.42. The effluent flow rate was estimated with the average contraction factor calculated at m/n of 2.30. Since the variation of m/n with process conditions is minor, this assumption seems justified.

The effect of the flow rate on the overall rate and rates of the water gas shift and Fischer-Tropsch reaction is demonstrated in Figure 5.4a. As expected, the reaction rates increase with increasing space velocity. There is good agreement between the model calculations and the experimental values. Overall conversion of synthesis gas,

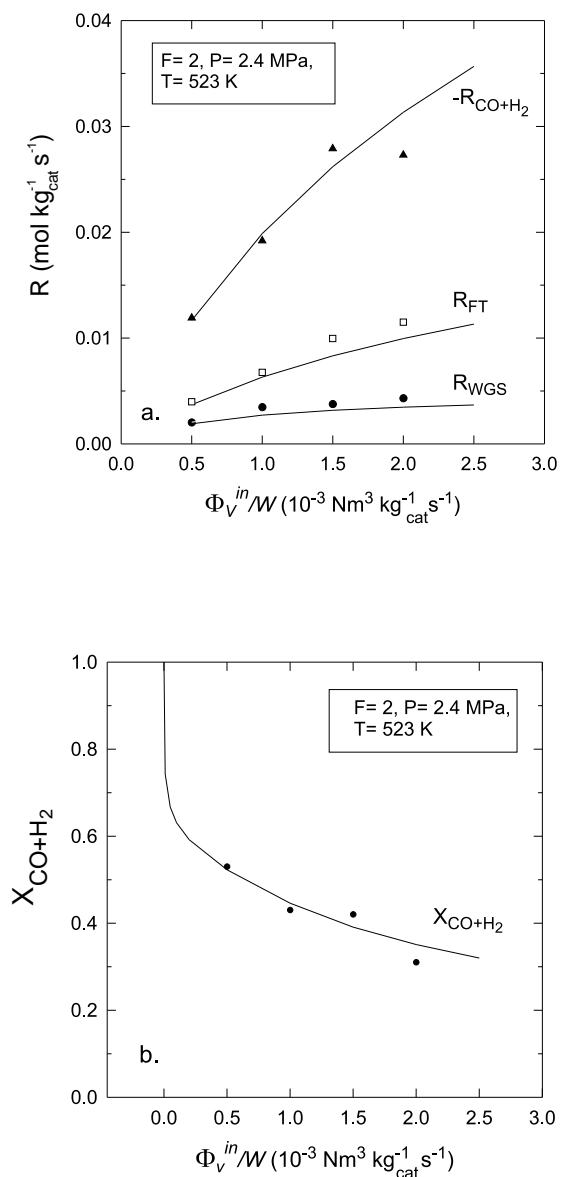


Figure 5.4 Reaction rates for the WGS and FT and total conversion of CO and H₂ (a) and overall conversion of synthesis gas (X_{CO+H_2}) versus space velocity (b). Symbols are experimental values. Lines are model predictions (FT-III2 and WGS-II6).

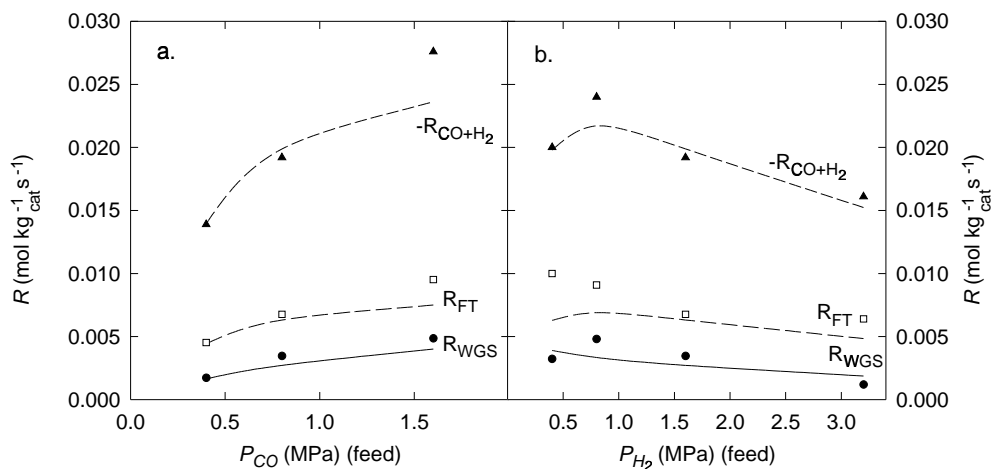


Figure 5.5 Reaction rates for the WGS and FT and total conversion of CO and H₂ versus reactant feed pressures. Symbols are experimental values. Lines are model predictions (FT-III2 and WGS-II6). a: Feed pressure $P_{CO} = 0.8$ MPa, $T = 523$ K, $\Phi_v^{in}/W = 1.0 \cdot 10^{-3} \text{ kg}_{cat}^{-1} \text{ s}^{-1}$; b: Feed pressure $P_{H_2} = 0.8$ MPa, $T = 523$ K, $\Phi_v^{in}/W = 1.0 \cdot 10^{-3} \text{ kg}_{cat}^{-1} \text{ s}^{-1}$.

X_{CO+H_2} , at the same conditions is accurately predicted with the optimized kinetic expressions and a CSTR reactor model (see Figure 5.4b).

The effect of the individual reactant pressures (P_{CO} and P_{H_2}) in the feed stream is shown in Figures 5.5a-b. The models appear to predict the trends of varying reactant pressures satisfactory. Both the water gas shift as well as the Fischer-Tropsch reaction rate increase with increasing feed pressure of CO (Figure 5.5a). The water pressure decreases with increasing CO pressure causing an increase of the Fischer-Tropsch reaction rate. Figure 5.5b shows that the space time yield and the Fischer-Tropsch reaction rate increase slightly and then decrease monotonically. This is caused by an increase of the hydrogen and water pressure in the reactor with increasing feed pressure of hydrogen. Water is a strong inhibitor on the catalyst and reduces the reaction rates of the hydrocarbon-forming reactions.

5.5 Conclusions

Experiments for the kinetics of the hydrocarbon formation and water gas shift reaction over an iron catalyst were obtained over a wide range of industrially relevant reaction conditions. A number of rate equations were derived on the basis of a detailed set of possible reaction mechanisms. The following conclusions can be made:

1. Two different sites are present on iron catalysts. The iron carbides are active towards hydrocarbon forming reactions, whereas magnetite (Fe_3O_4) seems to be the most active site for the water gas shift reaction.
2. The reaction rate of the Fischer-Tropsch synthesis is determined by the formation of the monomer species (methylene). The best models assume that the rate determining step proceeds via hydrogenation of associative adsorbed CO.
3. Carbon dioxide is formed by the water gas shift reaction. The rate determining step is the formation of a formate intermediate species.

Simulations using the kinetic models derived show good agreement with both experimental data and with some kinetic models from literature.

References

- [1] Dry, M.E., The Fischer-Tropsch synthesis, in J.R. Anderson; M. Boudart, eds., *Catalysis-Science and technology*, vol. 1, Springer-Verlag, New York, 1981 pp. 160–255.
- [2] Ribeiro, F.H.; Schach von Wittenau, A.E.; Bartholemew, C.H.; Somorjai, G.A., Reproducibility of turnover rates in heterogeneous metal catalysis: compilation of data and guidelines for data analysis, *Catal. Rev.-Sci. Eng.* **1997**, *39*, 49–76.
- [3] Bub, G.; Baerns, M., Prediction of the performance of catalytic fixed bed reactors for Fischer-Tropsch synthesis, *Chem. Eng. Sci.* **1980**, *35*, 348–355.
- [4] Newsome, D.S., The water-gas shift reaction, *Catal. Rev.-Sci. Eng.* **1980**, *21*, 275–318.
- [5] Lox, E.S.; Froment, G.F., Kinetics of the Fischer-Tropsch reaction on a precipitated promoted iron catalyst. 2. Kinetic modeling, *Ind. Eng. Chem. Res.* **1993**, *32*, 71–82.
- [6] Wojciechowski, B.W., The kinetics of the Fischer Tropsch synthesis, *Catal. Rev.-Sci. Eng.* **1988**, *30*, 629–702.
- [7] Dry, M.E., Advances in Fischer-Tropsch chemistry, *Ind. Eng. Chem. Prod. Res. Dev.* **1976**, *15*, 282–286.
- [8] Huff, Jr., G.A.; Satterfield, C.N., Intrinsic kinetics of the Fischer-Tropsch synthesis on a reduced fused-magnetite catalyst, *Ind. Eng. Chem. Process Des. Dev.* **1984**, *23*, 696–705.
- [9] Zimmerman, W.H.; Bukur, D.B., Reaction kinetics over iron catalysts used for the Fischer-Tropsch synthesis, *Can. J. Chem. Eng.* **1990**, *68*, 292–301.

- [10] Atwood, H.E.; Bennett, C.O., Kinetics of the Fischer-Tropsch reaction over iron, *Ind. Eng. Chem. Process Des. Dev.* **1979**, *18*, 163–170.
- [11] Nettelhoff, H.; Kokuun, R.; Ledakowicz, S.; Deckwer, W.-D., Studies on the kinetics of Fischer-Tropsch synthesis in slurry phase, *Ger. Chem. Eng.* **1985**, *8*, 177–185.
- [12] Ledakowicz, S.; Nettelhoff, H.; Kokuun, R.; Deckwer, W.-D., Kinetics of the Fischer-Tropsch synthesis in the slurry phase on a potassium-promoted iron catalyst, *Top. Catal.* **1985**, *24*, 1043–1049.
- [13] Dixit, R.S.; Tavlarides, L.L., Kinetics of the Fischer-Tropsch synthesis, *Ind. Eng. Chem. Process Des. Dev.* **1983**, *22*, 1–9.
- [14] Sarup, B.; Wojciechowski, B.W., Studies of the Fischer-Tropsch synthesis on a cobalt catalyst. II. Kinetics of carbon monoxide conversion to methane and to higher hydrocarbons, *Can. J. Chem. Eng.* **1989**, *67*, 62–74.
- [15] Shen, W.J.; Zhou, J.L.; Zhang, B.J., Kinetics of Fischer-Tropsch synthesis over precipitated iron catalyst, *J. Nat. Gas Chem.* **1994**, *4*, 385–400.
- [16] Zhang, H.-B.; Schrader, G.L., Characterisation of a fused iron catalyst for Fischer-Tropsch synthesis by in situ laser Raman spectroscopy, *J. Catal.* **1985**, *95*, 325–332.
- [17] Lox, E.S.; Marin, G.B.; de Graeve, E.; Bussiere, P., Characterization of a promoted precipitated iron catalyst for Fischer-Tropsch synthesis, *Appl. Catal. A* **1988**, *40*, 197–218.
- [18] Shroff, M.D.; Kalakkad, D.S.; Coulter, K.E.; Köhler, S.D; Harrington, M.S.; Jackson, N.B.; Sault, A.G.; Datye, A.K., Activation of iron precipitated Fischer-Tropsch catalysts, *J. Catal.* **1995**, *156*, 185–207.
- [19] Rao, K.R.P.M.; Huggins, F.E.; Mahajan, V.; Huffman, G.P.; Rao, V.U.S.; Bhatt, B.L.; Bukur, D.B.; Davis, B.H.; O'Brien, R.J., Mössbauer spectroscopy study of iron-based catalysts used in Fischer-Tropsch synthesis, *Top. Catal.* **1995**, *2*, 71–78.
- [20] Rethwisch, D.G.; Dumesic, J.A., Adsorptive and catalytic properties of supported metal oxides. III. Water-gas shift over supported iron and zinc oxides, *J. Catal.* **1986**, *101*, 35–42.
- [21] Ponec, V., Some aspects of the methanation and Fischer-Tropsch synthesis, *Catal. Rev.-Sci. Eng.* **1978**, *18*, 151–171.
- [22] Anderson, R.B., *Catalysts for the Fischer-Tropsch synthesis*, vol. 4, Van Nostrand Reinhold, New York **1956**.
- [23] Anderson, R.B., *The Fischer-Tropsch synthesis*, Academic Press, New York

1984.

- [24] Bell, A.T., Catalytic synthesis of hydrocarbons over group VIII metals. A discussion on the reaction mechanism, *Catal. Rev.-Sci. Eng.* **1981**, *23*, 203–232.
- [25] Hindermann, J.P.; Hutchings, G.J.; Kiennemann, A., Mechanistic aspects of the formation of hydrocarbons and alcohols from CO hydrogenation, *Catal. Rev.-Sci. Eng.* **1993**, *35*, 1–127.
- [26] Dry, M.E., Conversion of syngas to fuels and chemicals, in *Int. Conf. on Catal. & Catal. Proc.*, Cape Town, South Africa, 1993 pp. 57–66.
- [27] Dry, M.E., Practical and theoretical aspects of the catalytic Fischer-Tropsch process, *Appl. Catal. A* **1996**, *138*, 319–344.
- [28] Adesina, A.A., Hydrocarbon synthesis via Fischer-Tropsch reaction: travails and triumphs, *Appl. Catal. A* **1996**, *138*, 345–367.
- [29] Fischer, F.; Tropsch, H., Über die Herstellung synthetischer ölgemische (Synthol) durch Aufbau aus Kohlenoxyd und Wasserstoff, *Brennst. Chem.* **1923**, *4*, 276–285.
- [30] Schulz, H.; Van Steen, E.; Claeys, M., Olefin formation, hydrogenation and isomerization in the kinetic regime of Fischer-Tropsch synthesis, in *Selective hydrogenation and dehydrogenation*, DGMK, Kassel, Germany, 1993 .
- [31] Bianchi, D.; Tau, L.M.; Borcar, S.; Bennett, C.O., Nature of the species on supported iron during CO/H₂ reaction, *J. Catal.* **1983**, *84*, 358–374.
- [32] Ponc, V.; Van Barneveld, W.A., The role of chemisorption in Fischer-Tropsch synthesis, *Ind. Eng. Chem. Prod. Res. Des.* **1979**, *4*, 268–271.
- [33] Kellner, C.S.; Bell, A.T., The kinetics and mechanism of carbon monoxide hydrogenation over alumina-supported ruthenium, *J. Catal.* **1981**, *70*, 418–432.
- [34] Hovi, J.-P.; Lahtinen, J.; Liu, Z.S.; Nieminen, R.M., Monte Carlo study of CO hydrogenation on cobalt model catalysts, *J. Chem. Phys.* **1995**, *102*, 7674–7682.
- [35] Graaf, G.H.; Winkelman, J.G.M.; Stamhuis, E.J.; Beenackers, A.A.C.M., Kinetics of the three-phase methanol synthesis, *Chem. Eng. Sci.* **1988**, *43*, 2161–2168.
- [36] Froment, G.F.; Hosten, L.H., Catalytic kinetics: modelling, in J.R. Anderson; M. Boudart, eds., *Catalysis. Science and technology*, vol. 2, Springer-Verlag, New York, 1981 pp. 98–170.
- [37] Biloen, P.; Sachtler, W.M.H., Mechanism of hydrocarbon synthesis over Fischer-Tropsch catalysts, *Adv. Catal.* **1981**, *30*, 165–216.
- [38] Dry, M.E.; Shingles, T.; Boshoff, L.J.; Oosthuizen, G.J., Heats of adsorption on promoted iron surfaces and the role of alkali in Fischer-Tropsch synthesis, *J. Catal.* **1969**, *15*, 190–199.

- [39] Yates, I.C.; Satterfield, C.N., Effect of carbon dioxide on the kinetics of the Fischer-Tropsch synthesis on iron catalysts, *Ind. Eng. Chem. Res.* **1989**, *28*, 9–12.
- [40] Yates, I.C.; Satterfield, C.N., Intrinsic kinetics of the Fischer-Tropsch synthesis on a cobalt catalyst, *Energy Fuels* **1991**, *5*, 168–173.
- [41] Dry, M.E.; Shingles, T.; Boshoff, L.J.; Oosthuizen, G.J., Rate of the Fischer-Tropsch reaction over iron catalysts, *J. Catal.* **1972**, *25*, 99–104.
- [42] Whitters, Jr., H.P.; Eleizer, K.F.; Mitchell, J.W., Slurry-phase Fischer-Tropsch synthesis and kinetic studies over supported cobalt carbonyl derived catalysts, *Ind. Eng. Chem. Res.* **1990**, *29*, 1807–1814.
- [43] Deckwer, W.-D.; Kokuun, R.; Sanders, E.; Ledakowicz, S., Kinetic studies of Fischer-Tropsch synthesis on suspended Fe/K catalyst. Rate inhibition by CO₂ and H₂O, *Ind. Eng. Chem. Process Des. Dev.* **1986**, *25*, 643–649.
- [44] Chanenchuk, C.A.; Yates, I.C.; Satterfield, C.N., The Fischer-Tropsch synthesis with a mechanical mixture of a cobalt catalyst and a copper-based water gas shift catalyst, *Energy Fuels* **1991**, *5*, 847–855.
- [45] Van der Laan, G.P.; Beenackers, A.A.C.M., Kinetics and selectivity of the Fischer-Tropsch synthesis. A literature review, Accepted for publication in *Catal. Rev.-Sci. Eng.*
- [46] Graaf, G.H.; Sijtsema, P.J.J.M.; Stamhuis, E.J.; Joosten, G.E.H., Chemical equilibria in methanol synthesis, *Chem. Eng. Sci.* **1986**, *41*, 2883–2890.
- [47] Bukur, D.B.; Nowicki, L.; Manne, R.K.; Lang, X., Activation studies with a precipitated iron catalyst for Fischer-Tropsch synthesis 2. Reaction studies, *J. Catal.* **1995**, *155*, 366–375.
- [48] Westerterp, K.R.; van Swaaij, W.P.M.; Beenackers, A.A.C.M., *Chemical reactor design and operation*, Wiley & Sons, second edn. **1984**.
- [49] Jonker, G.H.; Veldsink, J.-W.; Beenackers, A.A.C.M., Intrinsic kinetics of 9-monoenic fatty acid methyl ester hydrogenation over nickel-based catalysts, *Ind. Eng. Chem. Res.* **1997**, *36*, 1567–1579.
- [50] Graaf, G.H., *The synthesis of methanol in gas-solid and gas-slurry reactors*, Ph.D. thesis, University of Groningen, The Netherlands **1988**.
- [51] Fisher, R.A., *Statistical methods for research workers*, Macmillan, 14th edn. **1970**.

6

Kinetics and Selectivity of the Gas-Slurry Fischer-Tropsch Synthesis

Abstract

The kinetics of the Fischer-Tropsch (FT) synthesis over a commercial Fe-Cu-K-SiO₂ catalyst was studied in a continuous gas-slurry reactor. A novel product distribution model, recently developed to describe the product selectivity of a gas-solid FT synthesis was applied to model the product distributions obtained at industrially relevant conditions (reactor pressure of 1.2-4.0 MPa, H₂/CO feed ratio of 0.25-4.0, space velocity of 0.25-0.77 10⁻³ Nm³ kg_{cat}⁻¹ s⁻¹, and a constant temperature of 523 K) over a precipitated iron catalyst in the slurry phase. The new model, called Olefin Readsorption Product Distribution Model (ORPDM), combines a mechanistic model of olefin readsorption with kinetics of chain growth and termination on the same catalytic sites. In the slurry phase, this model appears to describe the deviations from the classical Anderson-Schulz-Flory distribution accurately. The selectivity to paraffins and olefins could be predicted with average deviations of 10.6 % and 8.7 %, respectively. The presence of the slurry liquid appeared to affect both the model parameters and the product selectivity relative to the gas-solid kinetics. The slurry-phase system shows a higher olefin content at comparable reaction conditions. The corresponding model parameters, the readsorption constant and the termination constant to olefins, are all lower at similar process conditions than the corresponding model parameters for the gas-solid kinetics. The intrinsic kinetics is also influenced by the slurry liquid. At H₂/CO ratios < 2, both the Fischer-Tropsch and the water gas shift reaction rates are lower than for the gas-solid system. The slurry liquid influences the adsorption of CO₂ on FT sites and causes a complete coverage of the water gas shift sites.

6.1 Introduction

The Fischer-Tropsch (FT) synthesis converts synthesis gas into a multicomponent mixture of predominantly hydrocarbons. The Fischer-Tropsch synthesis in slurry bubble columns is very attractive relative to fixed bed reactors [1]. The advantages are: 1) Low pressure drop over the reactor. 2) Excellent heat transfer characteristics resulting in stable reactor temperatures. 3) No diffusion limitations. 4) Possibility of continuous refreshment of catalyst particles. 5) Relatively simple construction and low investment costs.

Recently, we developed a novel product selectivity model for linear paraffins and α -olefins (see Chapter 4). The α -Olefin Readsorption Product Distribution Model (ORPDM) accounts for secondary readsorption of α -olefins on FT growth sites on the precipitated iron catalyst. The proposed reaction network is shown in Figure 4.1. The readsorption rates of the olefins are supposed to increase exponentially with carbon number due to the increase of both physisorption effects and solubility with increasing chain length. ORPDM accounts for chain-length dependent readsorption of olefins on FT sites. The readsorption step depends on carbon number, resulting in a net decrease of the termination probability to olefins. α_n increases with increasing chain length until no olefins are formed anymore. At high carbon numbers, the chain growth parameter, α_n , approaches a maximum constant value. The increased readsorption of long-chain olefins results in a decreasing olefin/paraffin ratio with increasing chain length.

Intrinsic rate expressions for the Fischer-Tropsch (FT) reaction and the water gas shift (WGS) reaction on the same precipitated iron catalyst in a gas-solid system are reported in Chapter 5. These kinetic equations are based on the Langmuir-Hinshelwood-Hougen-Watson and the Eley-Rideal approach using a detailed scheme of potentially possible reaction mechanisms. The same set of kinetic equations will be tested for the description of the gas-slurry kinetics. The liquid-phase may influence heterogeneous reaction kinetics (Van der Laan et al. [2]):

1. The rate of reaction may be significantly affected by introducing any non-"ideal" (interacting) liquids.
2. Competitive adsorption of a slurry liquid on active catalytic sites will reduce the reaction rates.
3. The slurry liquid can interact with weakly adsorbed surface species.
4. Differences in solubility of reactants and products in various solvents explains the difference in liquid-phase concentration.

Several studies concerning both the Fischer-Tropsch, the methanol, and the methanol-higher alcohol synthesis are of special interest. Stenger and Satterfield [3, 4] measured the effect of the nature of an inert liquid on the reaction rate and on the selectivity of the Fischer-Tropsch synthesis on a reduced fused magnetite catalyst. They observed that the reaction rate of the Fischer-Tropsch synthesis in presence of phenantrene is nearly twice as fast as in n-octacosane and triphenylmethane, even though the solubility is slightly lower in phenantrene. The presence of phenantrene caused reduction of deposit formation (catalyst deactivation) and readsorption of primary olefins onto the catalyst and hence inhibited secondary reactions. Bukur et al. [5] measured the activity and selectivity of a Ruhrchemie LP 33/81 catalyst both in gas-solid (tubular fixed bed) and in slurry systems. The initial activity and selectivity was about the same for both systems. However, catalyst aging affected the hydrocarbon distribution differently. In the slurry system the olefin selectivity decreased, while the internal olefins and oxygenated production rates increased with time on stream, whereas the opposite changes were observed in the gas-solid system. Bukur et al. [5] reported similar effects of changes in the process conditions (temperature, pressure, H_2/CO feed ratio and space velocity) on the product selectivities. The initial FT activity was the same in both systems, whereas the WGS selectivity (carbon dioxide production relative to the carbon monoxide consumption) was somewhat higher in gas-solid system [5].

Graaf et al. [6] observed a significant contribution of the methanol formation via CO_2 by introducing squalane as a solvent, relative to the two-phase system. The three-phase methanol synthesis in squalane is much less sensitive to the temperature. Van der Laan et al. [2] measured the kinetics of the three-phase methanol synthesis both in an apolar solvent, squalane, and in a polar solvent, tetra ethylene glycol dimethylether (TEGDME). The slurry liquid appears to affect both the activation energy and the kinetic rate constant by interactions between adsorbed species and solvent and by competitive adsorption of the solvent on the catalyst surface. The rate of reaction to methanol observed in TEGDME appeared to be 10 times lower than in squalane.

The kinetics of both the gas-solid and gas-slurry (n-octacosane) methanol-higher alcohol synthesis from $CO/CO_2/H_2$ was investigated by Breman et al. [7]. The presence of n-octacosane as a slurry liquid appeared to affect the product distributions and the activity of the catalyst relative to the gas-solid system: lower $CO+CO_2$ reaction rates, lower higher alcohol to methanol selectivities, higher hydrocarbon yields, and lower water gas shift reaction rates.

The aim of this study is to test the Olefin Readsorption Product Distribution Model,

recently developed for the gas-solid system, for predicting gas-slurry product distributions at industrially relevant conditions on a precipitated iron catalyst. The gas-slurry kinetics will be modeled starting from a comprehensive set of equations proposed elsewhere (Chapter 5). Furthermore, the effects of process conditions on the kinetics and the selectivity of the gas-slurry Fischer-Tropsch synthesis are investigated experimentally and the results are compared with the performance of a gas-solid system.

6.2 Experimental

6.2.1 Slurry Reactor

The Fischer-Tropsch experiments were carried out in a gas-continuous slurry reactor. A detailed description of the experimental setup and analysis sections is given in Chapter 3. The slurry reactor is a 1.8 dm³ autoclave ($H=18.2$ cm, $D=12.0$ cm) made by Medimex (see Figure 3.3). During the Fischer-Tropsch reaction, liquid products can be formed. The level of the slurry was maintained constant using a home-made filtering unit. The liquid products were removed via a filter (sintered metal 5 μm), whereas the catalyst particles remained inside the reactor. The liquid and gas phase volumes applied were 730 and 985 cm³, respectively.

6.2.2 Experimental Procedure

The slurry reactor was loaded with 7.3 g of unreduced catalyst particles with $40 \leq d_p \leq 50 \mu\text{m}$. The catalyst applied was a commercial precipitated iron catalyst (type LP 33/81) synthesized by Ruhrchemie AG (Oberhausen, Germany). Details of this catalyst are given in Chapter 3. The catalyst was pretreated with hydrogen at a flow rate of $0.83 \cdot 10^{-3} \text{ Nm}^3 \text{ kg}_{cat}^{-1} \text{ s}^{-1}$ according to Bukur et al. [8]. The gas space velocity was based on the total mass of the unreduced supported catalyst. The reactor temperature, T , was increased linearly from 293 K to 553 K by 0.017 K s^{-1} . T remained at 553 K for 24 hours at an increased pressure of 1.0 MPa to prevent excessive solvent evaporation. After reduction, synthesis gas was fed to the reactor at reference conditions of 523 K, 1.50 MPa, $F=0.67$ and a space velocity of $0.25 \cdot 10^{-3} \text{ Nm}^3 \text{ kg}_{cat}^{-1} \text{ s}^{-1}$.

Liquid products were accumulated in high and low-pressure condensers for a typical period of 8-12 hours during steady state of the reactor system. The products were collected and weight before analysis. Several on-line GC analysis were performed during this period. Mass and atomic balances were typically $100 \pm 10 \%$. After changing

the process conditions the reactor operated at least 48 hours undisturbed before a new mass balance period was started.

The variation of the experimental conditions at a constant temperature of 523 K are given in Chapter 3. The reference experiment was repeated 6 times to determine possible deactivation effects on the activity and selectivity of the catalyst. A summary of relevant experimental data is given in Appendix B. 27 kinetic experiments were carried out in the slurry reactor with the Ruhrchemie precipitated iron catalyst at 523 K in two separate catalyst tests, series B and series C.

6.3 Results and Discussion

6.3.1 Product Distribution Modeling

The olefin readsorption product distribution model (ORPDM) was tested to our experiments at 523 K. The model parameters were optimized for each experiment with the Levenberg-Marquardt method [9]. The number of parameters in model ORPDM was equal to 7: p , t_O , k_R , c , t_P^1 , t_P^2 , and k_R^2 . Similar to a previous study (Chapter 4), the number of optimized parameters could be reduced because four parameters appeared to be independent of the experimental conditions. The average values of these parameters are shown in Table 6.1. For comparison, the corresponding values for the gas-solid study (Chapter 4) are also given in this table. Introduction of these mean model parameters at 523 K for both the increased readsorption of ethene relative to other olefins ($k_R^2/k_R e^{2c}$) and for the termination to C_1 (t_P^1) and C_2 products (t_P^2) and the exponential increase of the readsorption rate (c) reduces the number of parameters to be optimized from 7 to 3 within each experiment. Remarkably, both the readsorption rate of ethene and the exponential factor c are higher in both gas-slurry experimental series than observed for the gas-solid system.

Table 6.1 Optimized model parameters for ORPDM at 523 K that are independent of $\Phi_{v,0}$, P , H_2/CO ratio.

model parameter	G-S (A)	G-L-S (B)	G-L-S (C)
t_P^1	6.6	5.4	6.5
t_P^2	1.6	1.3	1.7
$k_R^2/k_R e^{2c}$	12.6	25.4	17.6
c	0.29	0.36	0.35

Table 6.2 Optimized model parameters ORPDM.

Run	p	t_O	k_R	n	s_{rel}	Run	p	t_O	k_R	n	s_{rel}
B1	17.92	6.39	0.037	19	8.9	C1	11.42	4.25	0.112	17	11.7
B2	14.08	6.59	0.063	19	16.4	C2	12.69	3.34	0.047	18	12.8
B3	12.04	5.63	0.075	19	10.8	C3	9.38	4.22	0.301	19	14.0
B4	15.90	5.25	0.040	18	13.5	C4	5.43	4.52 ¹	-	19	19.9
B5	8.17	3.62	0.197	18	13.9	C5	12.62	4.12	0.098	19	12.2
B6	7.27	2.92	0.247	19	9.1	C6	11.83	4.65	0.119	18	13.0
B7	14.22	4.71	0.059	19	8.3	C7	21.48	7.05	0.087	19	12.3
B8	15.20	5.49	0.030	18	20.3	C8	9.55	5.90	0.339	19	14.8
B9	15.46	5.48	0.026	19	11.8	C9	7.28	7.26	0.869	19	18.0
B10	19.55	6.47	0.020	19	11.0	C10	14.54	5.15	0.070	16	14.7
B11	8.86	2.95	0.110	17	18.5	C11	23.12	7.62	0.085	18	11.9
B12	13.60	4.76	0.038	19	16.1	C12	17.05	6.32	0.113	19	8.7
						C13	5.99	5.70	0.631	19	17.8
						C14	16.33	8.47	0.056	16	17.7
						C15	19.26	7.28	0.056	15	7.9

¹ t_O/k_R

The three remaining model parameters (p , t_O , k_R) to be optimized within each experiment and the number of selectivities and s_{rel} for both experimental gas-slurry series B and C are given in Table 6.2. Table 6.3 shows the accuracies of the optimized models expressed with the relative standard deviation s_{rel} and the $MARR$ function for the paraffins and olefins, respectively, both for the gas-solid as well as the gas-slurry experiments at 523 K. The total number of selectivities n as well as the total number of optimized parameters m within a catalyst test are also included in this table. Figure 6.1a-b shows that the relative residuals between model ORPDM and experiments are almost always within 25 % in both catalyst tests.

Table 6.3 Accuracies of the Olefin Readsorption Product Distribution Models.

model	$MARR$ %		s_{rel} %	n	m
	paraffins	olefins			
G-S (A)	10.1	9.1	13.3	370	57
G-L-S (B)	9.4	8.4	12.5	223	36
G-L-S (C)	11.8	9.0	14.0	270	44

The model parameters of model ORPDM are pseudo kinetic rate constants, incorporating true kinetic rate constants, surface concentrations of intermediates, hydrogen

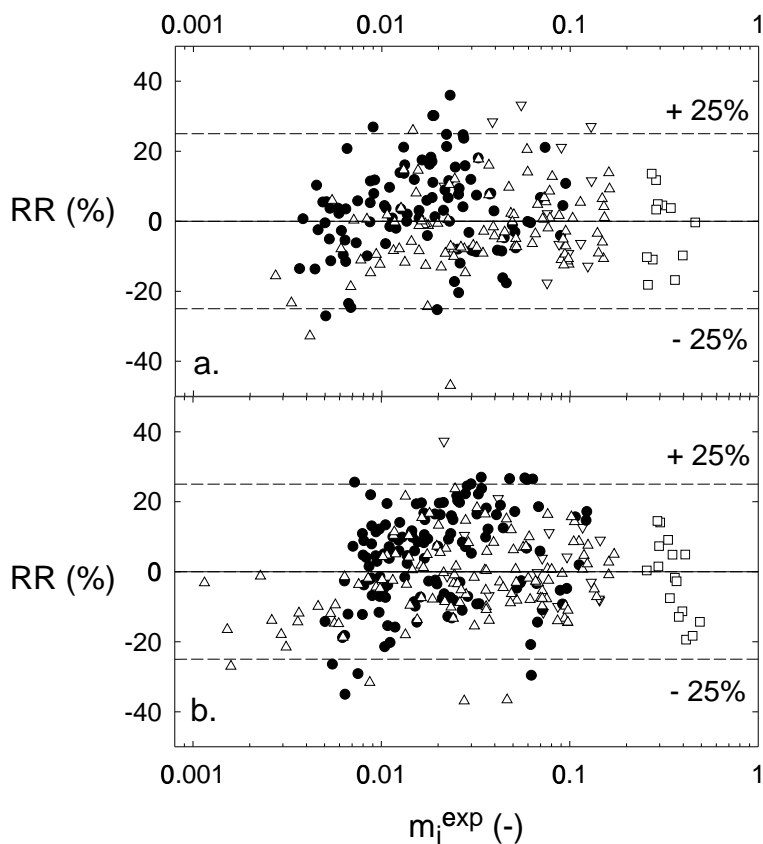


Figure 6.1 Relative residuals versus experimental selectivities. (●: paraffins, □: methane, △: olefins, ▽: ethene) Model ORPDM. a. Gas-slurry series B; b. Gas-slurry series C.

and vacant sites. Therefore, the model parameters vary with the adjusted process variables, P_{CO} , P_{H_2} , and space velocity. The effect of the process variables on the model parameters (p , t_O , k_R) was described with the same equations as in Table 6.4 (Chapter 4). The readsorption parameter, k_R , increases with H_2 pressure and decreases with CO pressure. CO inhibits readsorption rates, while a high H_2/CO ratio is favorable for readsorption of olefins. The accuracy of the equations presented in Table 6.4 is shown in Figure 6.2. Remarkably, the readsorption constant (k_R) and the termination constant to olefins (t_O) appear to be lower at similar process conditions than the corresponding model parameters for the gas-solid system. Both effects will result in a higher predicted olefin selectivity for the gas-slurry reactor.

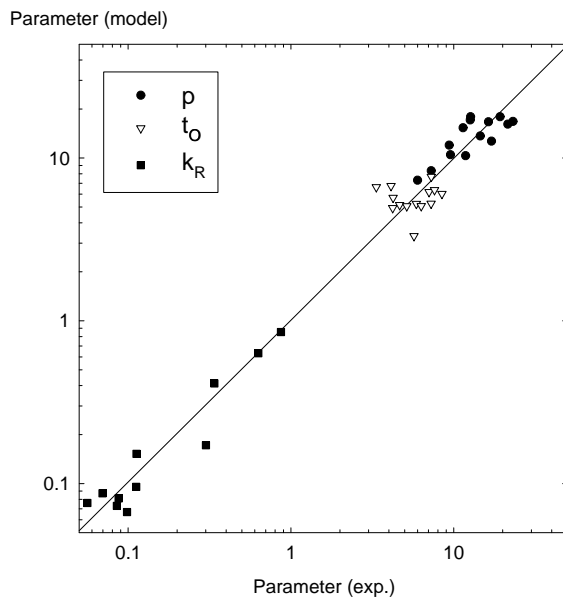


Figure 6.2 Parity graph of experimental (Table 6.2) and modeled parameters (Table 6.4) of model ORPDM.

Table 6.4 Model parameters ORPDM at 523 K in gas-solid (Chapter 4) and gas-slurry (C) experiments.

Parameter	G-S (A)	G-L-S (C)
p	$13.8 P_{H_2}^{-0.47} P_{CO}^{0.43}$	$14.4 P_{H_2}^{-0.26} P_{CO}^{0.40}$
t_O	$6.17 P_{H_2}^{-0.5}$	$3.71 P_{H_2}^{-0.5}$
k_R	$3.32 \cdot 10^{-4} \frac{P_{H_2}^{1.4} P_{CO}^{-0.49}}{\Phi_{v,0}/W}$	$8.00 \cdot 10^{-5} \frac{P_{H_2}^{1.2} P_{CO}^{-0.47}}{\Phi_{v,0}/W}$

ORPDM describes n-dependent readsorption of olefins, resulting in a curved distribution of paraffins and a decreasing O/P ratio with carbon number. Examples of product distributions with the predicted model values from model ORPDM are shown in Figure 6.3a-b and Table 6.5. The modeled product distributions appeared to predict the experimentally observed selectivities accurately. The deviations for C₁ and C₂

products, as well as the increasing paraffin content of the products are also described accurately. These figures also compare product distributions between two experiments from this study and gas-solid system experiments at comparable conditions (Chapter 4). Figure 6.3a-b and Table 6.5 show that the slurry liquid influences the product distribution obtained. It should be noted that the experimental conditions inside the reactor are not completely similar. The olefin content of the hydrocarbon mixture is higher in both gas-slurry experiments as a result of the model parameters (see Table 6.5 for p , t_O , and k_R). In accordance with Stenger and Satterfield [4], the readsorption of olefins is reduced in presence of the slurry liquid resulting in an increase of the olefin selectivity. In both comparisons, the selectivity to olefins is higher in the gas-slurry reactor. The selectivity to low molecular weight hydrocarbons appears to be decreased in the slurry system relative to the gas-solid system.

Table 6.5 Model parameters ORPDM, experimental conditions and selectivities (wt%) for Figure 6.3.

	Figure 6.3a		Figure 6.3b	
	Gas-solid	Gas-slurry	Gas-solid	Gas-slurry
Run	A16	B8	A8	B11
F	0.5	0.5	2.0	2.0
H_2/CO	0.38	0.30	6.19	4.71
$\Phi_{v,0}/W$ ($10^{-3} \text{ Nm}^3 \text{ kg}_{cat} \text{ s}^{-1}$)	0.36	0.39	0.35	0.34
p	19.46	15.20	6.69	8.86
t_O	5.50	5.49	4.22 ¹	2.95
k_R	0.076	0.030	-	0.110
w_1	9.0	8.4	16.6	12.8
w_{2-4}	36.6	41.3	34.4	37.6
w_{5-10}	48.8	50.2	34.9	49.6
$w_{O,2-4}$	75.3	80.9	45.5	58.6
$w_{O,5-10}$	72.9	75.0	35.0	57.1

¹ t_O/k_R

6.3.2 Reaction Kinetics

The reaction rates of the Fischer-Tropsch synthesis (R_{FT}) and the water gas shift reaction (R_{WGS}) were calculated from the experimental results of experimental series C in Appendix B. The kinetic models applied were optimized for series C. The set of

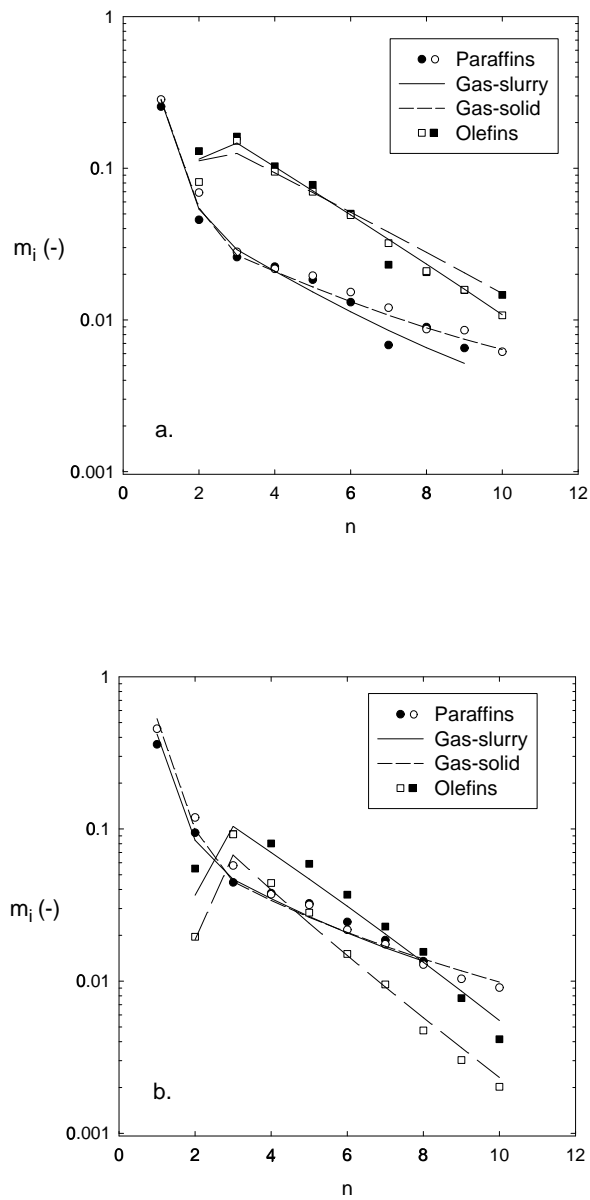


Figure 6.3 Product distributions as a function of carbon number for both the gas-slurry system (solid symbols, solid lines) and the gas-solid study (Chapter 4) (open symbols, dashed lines). Symbols are experimental selectivities. Lines are model predictions from ORPDM. Optimized parameters and the experimental conditions are shown in Table 6.5.

rate expressions developed in Chapter 5 were used for kinetic modeling in this study. These Langmuir-Hinshelwood-Hougen-Watson type of intrinsic rate expressions were derived on the basis of a detailed set of reaction mechanisms for the hydrocarbon formation as well as for the water gas shift equation. The same set of assumptions given in Chapter 5 was used for the development of the kinetic equations. In addition, however, it was assumed that carbon dioxide adsorbed strongly on the catalytic sites active for the Fischer-Tropsch reaction whereas the adsorption of water was assumed to be negligible. This, because of the experimental observations of high carbon dioxide concentrations in the reactor effluent (see Appendix B, series C) relative to water. Kinetic equations with carbon dioxide inhibition were also reported by Ledakowicz et al. [10], Nettelhoff et al. [11], and Deckwer et al. [12]. As a result, the site balances for the FT catalytic sites read:

$$\theta_{s_1} + (\theta_{C_{s_1}} \text{ or } \theta_{CO_{s_1}}) + \theta_{CO_{2s_1}} = 1 \quad (6.1)$$

$$(\theta_{C_{s_1}} \text{ or } \theta_{CO_{s_1}}) + \theta_{CO_{2s_1}} = 1 \quad (6.2)$$

with $\theta_{C_{s_1}}$ relevant for dissociative and $\theta_{CO_{s_1}}$ relevant for associative CO adsorption, respectively.

The final form of the kinetic equations is presented in Table 6.6. These equations were optimized with both site balances (eqs 6.1-6.2). The relative variances of these optimizations and the appropriate ranking are shown in Table 6.7. The statistical significance of the differences in accuracy was tested with Bartlett's test (Chapter 3) [13]. For a number of competitive models H , the Bartlett's test compares a critical calculated χ_c^2 value (for details, see Chapter 3 or Jonker et al. [13]) with a tabulated χ_t^2 value [14]. If χ_c^2 exceeds the tabulated value, the model with the largest deviation was rejected and χ_c^2 was recalculated. Models were subsequently rejected, until χ_c^2 was below the tabulated value. Table 6.8 compares χ_c^2 with the tabulated χ_t^2 value for $H - 1$ degrees of freedom. The table shows that the best two models ($H = 2$) passed the test and are statistically indistinguishable. These best models are, in succeeding order: FT-I3 (eq 6.1) and FT-III2 (eq 6.2). Table 6.9 shows the optimized model parameters. The 95 % confidence limits show that the adsorption constant of CO_2 is rather inaccurate. The adsorption constant of CO (a) for model FT-I3 is not significantly different from zero. Therefore, we prefer model FT-III2 for the description of the FT reaction rate. This model is also one of the optimal kinetic equations of the gas-solid system (Chapter 5). Parity graphs of the FT kinetic equations are shown in Figure 6.4.

Based on the formate mechanism and the assumptions mentioned in Chapter 5, two kinetic rate equations for the water gas shift reaction are possible. The expressions are

Table 6.6 Reaction rate expressions considered for the Fischer-Tropsch synthesis, R_{FT} ($\text{mol kg}_{\text{cat}}^{-1} \text{s}^{-1}$).

Model ¹	Kinetic equation
FT-I3	$\frac{k P_{\text{CO}}^{1/2} P_{\text{H}_2}^{1/2}}{\left(1 + a P_{\text{CO}}^{1/2} + b P_{\text{CO}_2}\right)^2}$
FT-I4	$\frac{k P_{\text{CO}}^{1/2} P_{\text{H}_2}^{3/4}}{\left(1 + a P_{\text{CO}}^{1/2} P_{\text{H}_2}^{-1/4} + b P_{\text{CO}_2}\right)^2}$
FT-II3	$\frac{k P_{\text{CO}}^{1/2} P_{\text{H}_2}}{1 + a P_{\text{CO}}^{1/2} + b P_{\text{CO}_2}}$
FT-III2	$\frac{k P_{\text{CO}} P_{\text{H}_2}^{1/2}}{\left(1 + a P_{\text{CO}} + b P_{\text{CO}_2}\right)^2}$
FT-III3	$\frac{k P_{\text{CO}} P_{\text{H}_2}}{\left(1 + a P_{\text{CO}} + b P_{\text{CO}_2}\right)^2}$
FT-IV2	$\frac{k P_{\text{CO}} P_{\text{H}_2}}{1 + a P_{\text{CO}} + b P_{\text{CO}_2}}$
FT-IV3	$\frac{k P_{\text{CO}} P_{\text{H}_2}^2}{1 + a P_{\text{CO}} + b P_{\text{CO}_2}}$

¹ See Chapter 5 for a description of these models.

Table 6.7 FT kinetic model screening.

Model	Site balance (eq)	s_{rel} (%)	Rank
FT-I3	6.1	12.9	1
FT-I3	6.2	29.5	6
FT-I4	6.2	27.3	4
FT-II3	6.2	29.2	5
FT-III2	6.1	13.3	2
FT-III2	6.2	32.3	7
FT-III3	6.2	42.5	9
FT-IV2	6.2	25.0	3
FT-IV3	6.2	41.8	8

FT-I4, FT-II3, FT-III2, FT-III3, FT-IV2, FT-IV3 with site balance 6.1 results in $a < 0$ or $b < 0$

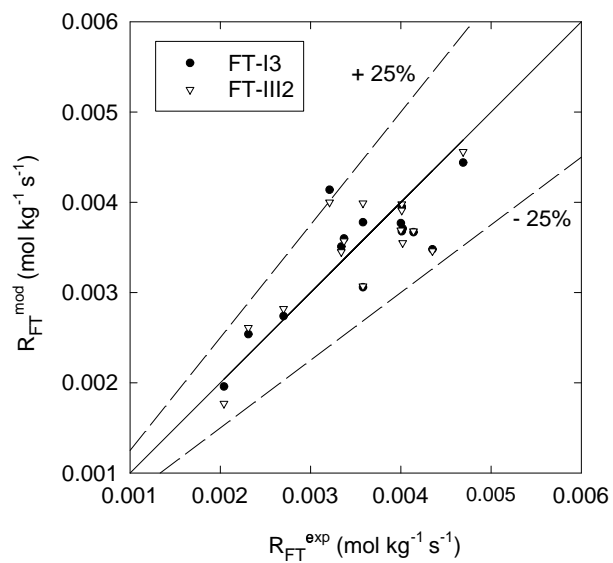


Figure 6.4 Parity graph of the best FT rate equations.

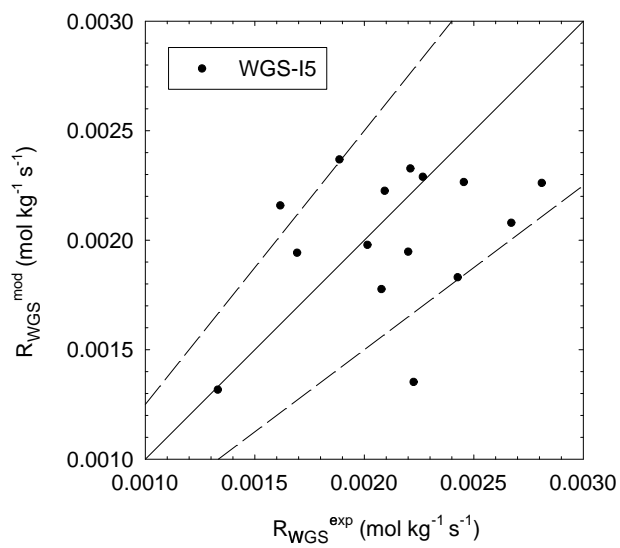


Figure 6.5 Parity graph of the WGS rate equation.

Table 6.8 Bartlett's test for FT models¹.

H	χ_c^2	χ_t^2
9	37.6	15.5
8	31.4	14.1
7	22.0	12.6
6	17.9	11.1
5	13.9	9.49
4	10.7	7.81
3	7.24	5.99
2	0.0107	3.84

¹ χ_c^2 : critical χ^2 according to Bartlett's test [13]; χ_t^2 : tabulated χ^2 [14]

given in Chapter 5 (Table 5.7). The adsorption of both H_2 and CO_2 is assumed to be negligible relative to CO and H_2O [15–17]. Thus, the mass balance of the catalytic sites, s_2 , is:

$$\theta_{s_2} + \theta_{H_2O s_2} + \theta_{CO s_2} = 1 \quad (6.3)$$

$$\theta_{H_2O s_2} + \theta_{CO s_2} = 1 \quad (6.4)$$

For the temperature dependency of the equilibrium constant of the WGS reaction, K_P , the following relation was used (Graaf et al. [18]):

$$\log K_P = \log \left(\frac{P_{CO_2} P_{H_2}}{P_{H_2O} P_{CO}} \right)_{eq} = \left(\frac{2073}{T} - 2.029 \right) \quad (6.5)$$

The agreement between the experiments and the kinetic models is not impressive. Model WGS-I5 with site balance eq. 6.4 fitted the experimental rates the best ($s_{rel} = 20.5\%$).

$$R_{WGS-I5} = \frac{k_w / K_1^2 (P_{CO} P_{H_2O} - P_{CO_2} P_{H_2} / K_P)}{\left(P_{CO} + \frac{K_3}{K_1} P_{H_2O} \right)^2} \quad (6.6)$$

The relative variance of the other kinetic models exceeded 30 % or the values of the optimized parameters were unrealistic. The corresponding model parameters are given in Table 6.9 and the parity graph is shown in Figure 6.5.

Table 6.9 Final estimates of the parameters of the FT and WGS kinetic models.

Parameter	Dimension	Estimate
FT-I3 (s_{rel} 12.9 %)		
k	$\text{mol kg}^{-1} \text{s}^{-1} \text{MPa}^{-1.25}$	0.011 ± 0.004
a	MPa^{-1}	0.175 ± 0.204
b	MPa^{-1}	0.485 ± 0.365
FT-III2 (s_{rel} 13.3 %)		
k	$\text{mol kg}^{-1} \text{s}^{-1} \text{MPa}^{-1.5}$	0.034 ± 0.011
a	MPa^{-1}	1.185 ± 0.357
b	MPa^{-1}	0.656 ± 0.456
WGS-I5 (s_{rel} 20.5 %)		
k_w/K_1^2	$\text{mol kg}^{-1} \text{s}^{-1}$	0.030 ± 0.003
K_3/K_1	-	3.07 ± 0.31

A comparison between the experimental and the calculated reaction rates of the Fischer-Tropsch and the water gas shift reaction is presented in Figure 6.6a-b. The calculated rates are based on the optimal kinetic models FT-III2 and WGS-I5. The behavior of the kinetic reactor was calculated with a CSTR model (see Chapter 5 for details). Figure 6.6a shows the effect of the flow rate on the overall synthesis gas consumption rate and on reaction rates of the both Fischer-Tropsch reaction and the water gas shift reaction. There appears to be good agreement between the experimental and the calculated reaction rates over the measured range of space velocity. The reaction rates increase with increasing space velocity due to decreasing inhibitor concentrations (FT: CO_2 ; WGS: H_2O).

The effect of the feed ratio of H_2/CO at a constant reactor pressure of 1.5 MPa is shown in Figure 6.6b. Both the Fischer-Tropsch and the water gas shift reaction rate decrease slightly towards lower H_2/CO ratios. The overall synthesis gas consumption rate decreases strongly due to the reaction stoichiometry. Figure 6.6b also compares the reaction rates observed with the gas-slurry system and in the gas-solid system (Chapter 5). The model lines for the gas-solid system were calculated at comparable conditions with the optimal kinetic equations: FT-III2 and WGS-I6 (Chapter 5; see Table 5.10). At high feed ratios ($F > 2$), the reaction rates in the gas-slurry and the gas-solid systems are nearly the same. However, at low H_2/CO ratios, the reaction rates in the gas-solid system are significantly higher than in the gas-slurry system. The main difference between the reaction rate equations for two systems is in the inhibitor

term. Both optimal models for the gas-slurry system contain CO_2 inhibition in contrast to H_2O inhibition for the gas-solid system, see Chapter 5. Consequently, the gas-slurry reaction rates are inhibited at low H_2/CO ratios due to CO_2 formed via the water gas shift reaction. The water gas shift reaction is rather slow in the slurry phase relative to the gas-solid system. In case of the gas-slurry system, the WGS catalytic sites are completely covered. Apparently, the presence of the liquid phase affects the adsorption strength of the components present.

6.4 Conclusions

- The product selectivity model ORPDM, previously developed to describe gas-solid selectivity, also appears to describe accurately the selectivities over a precipitated iron catalyst in the slurry phase. The average deviation of the selectivity to paraffins and olefins is 10.6 % and 8.7 %, respectively.
- The presence of the slurry liquid appears to affect the product selectivity relative to the gas-solid system. The slurry-phase system yields a higher olefin fraction at comparable reaction conditions. The corresponding model parameters, the readsorption constant and the termination constant to olefins, are lower at similar conditions.
- The reaction kinetics of both the Fischer-Tropsch and the water gas shift reaction in the gas-slurry system can be described with the same set of reaction mechanisms found previously to describe the gas-solid system. The reaction rates appear to be comparable at high H_2/CO feed ratios. However, the reaction rate of the FT synthesis appears to be lower at H_2/CO ratios below 2 due to inhibition of CO_2 in the slurry system. The water gas shift reaction rate is also lower at these low H_2/CO ratios due to complete occupation of the WGS catalytic sites.

References

- [1] Saxena, S.C.; Rosen, M.; Smith, D.N.; Ruether, J.A., Mathematical modeling of Fischer-Tropsch slurry bubble column reactors, *Chem. Eng. Commun.* **1986**, *40*, 97–151.
- [2] Van der Laan, G.P.; Beenackers, A.A.C.M.; Ding, B.; Strikwerda, J.C., Liquid-

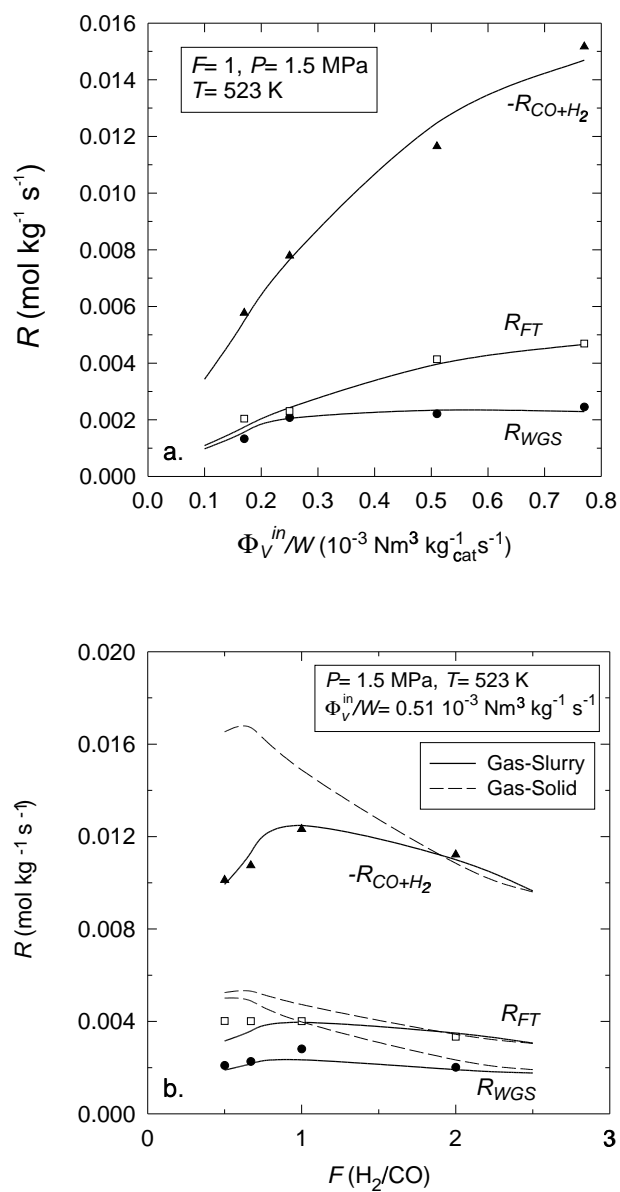


Figure 6.6 Reaction rates for the FT, WGS, and total conversion of CO and H₂ versus space velocity (a) and feed ratio H₂/CO (b). Dotted lines are model predictions of the optimal kinetic equations for the gas-solid system (FT-III2 and WGS-II6, see Chapter 5). Symbols are experimental values. Solid lines are model predictions (FT-III2 and WGS-I5).

- phase methanol synthesis in apolar (squalane) and polar (tetraethylene glycol dimethylether) solvents, *Catal. Today* **1999**, *48*, 93–100.
- [3] Stenger, H.G.; Satterfield, C.N., Effect of liquid composition on the slurry Fischer-Tropsch synthesis. 1. Rate of reaction, *Ind. Eng. Chem. Process Des. Dev.* **1985**, *24*, 407–411.
- [4] Stenger, H.G.; Satterfield, C.N., Effect of liquid composition on the slurry Fischer-Tropsch synthesis. 2. Product selectivity, *Ind. Eng. Chem. Process Des. Dev.* **1985**, *24*, 411–415.
- [5] Bukur, D.B.; Patel, S.A.; Lang, X., Fixed bed and slurry reactor studies of Fischer-Tropsch synthesis on precipitated iron catalyst, *Appl. Catal. A* **1990**, *61*, 329–349.
- [6] Graaf, G.H.; Winkelman, J.G.M.; Stamhuis, E.J.; Beenackers, A.A.C.M., Kinetics of the three-phase methanol synthesis, *Chem. Eng. Sci.* **1988**, *43*, 2161–2168.
- [7] Breman, B.B.; Beenackers, A.A.C.M.; Schuurman, H.A.; Oesterholt, E., Kinetics of the gas-slurry methanol-higher alcohol synthesis from CO/CO₂/H₂ over a Cs-Cu/ZnO/Al₂O₃ catalyst, including simultaneous formation of methyl esters and hydrocarbons, *Catal. Today* **1995**, *24*, 5–14.
- [8] Bukur, D.B.; Nowicki, L.; Manne, R.K.; Lang, X., Activation studies with a precipitated iron catalyst for Fischer-Tropsch synthesis 2. Reaction studies, *J. Catal.* **1995**, *155*, 366–375.
- [9] Press, W.H.; Flannery, B.P.; Teukolsky, S.A.; Vetterling, W.T., *Numerical recipes in Pascal*, Cambridge University Press, New York **1989**.
- [10] Ledakowicz, S.; Nettelhoff, H.; Kokuun, R.; Deckwer, W.-D., Kinetics of the Fischer-Tropsch synthesis in the slurry phase on a potassium-promoted iron catalyst, *Top. Catal.* **1985**, *24*, 1043–1049.
- [11] Nettelhoff, H.; Kokuun, R.; Ledakowicz, S.; Deckwer, W.-D., Studies on the kinetics of Fischer-Tropsch synthesis in slurry phase, *Ger. Chem. Eng.* **1985**, *8*, 177–185.
- [12] Deckwer, W.-D.; Kokuun, R.; Sanders, E.; Ledakowicz, S., Kinetic studies of Fischer-Tropsch synthesis on suspended Fe/K catalyst. Rate inhibition by CO₂ and H₂O, *Ind. Eng. Chem. Process Des. Dev.* **1986**, *25*, 643–649.
- [13] Jonker, G.H.; Veldsink, J.-W.; Beenackers, A.A.C.M., Intrinsic kinetics of 9-monoenic fatty acid methyl ester hydrogenation over nickel-based catalysts, *Ind. Eng. Chem. Res.* **1997**, *36*, 1567–1579.
- [14] Fisher, R.A., *Statistical methods for research workers*, Macmillan, 14th edn. **1970**.

- [15] Dry, M.E.; Shingles, T.; Boshoff, L.J.; Oosthuizen, G.J., Heats of adsorption on promoted iron surfaces and the role of alkali in Fischer-Tropsch synthesis, *J. Catal.* **1969**, *15*, 190–199.
- [16] Zimmerman, W.H.; Bukur, D.B., Reaction kinetics over iron catalysts used for the Fischer-Tropsch synthesis, *Can. J. Chem. Eng.* **1990**, *68*, 292–301.
- [17] Lox, E.S.; Froment, G.F., Kinetics of the Fischer-Tropsch reaction on a precipitated promoted iron catalyst. 2. Kinetic modeling, *Ind. Eng. Chem. Res.* **1993**, *32*, 71–82.
- [18] Graaf, G.H.; Sijtsema, P.J.J.M.; Stamhuis, E.J.; Joosten, G.E.H., Chemical equilibria in methanol synthesis, *Chem. Eng. Sci.* **1986**, *41*, 2883–2890.

7

Multicomponent Reaction Engineering Model for Fischer-Tropsch Synthesis in Commercial Scale Slurry Bubble Column Reactors

Abstract

A multicomponent mathematical model is presented for a large scale slurry bubble column reactor operating in the heterogeneous or churn-turbulent flow regime. The model accounts for both the Fischer-Tropsch reaction as well as the water gas shift reaction and the individual paraffin and olefin formation rates. It provides all the data necessary for reliable scale up, process optimization, and prediction of the performance of industrial scale Fischer-Tropsch bubble column reactors.

7.1 Introduction

Synthesis gas (CO and H₂) from coal or natural gas can be converted in the Fischer-Tropsch (FT) process to a multicomponent mixture of predominantly linear hydrocarbons. The FT synthesis in slurry bubble column reactors (SBCR) is very attractive relative to fixed bed reactors [1]. The advantages are: 1) Low pressure drop over the reactor. 2) Excellent heat transfer characteristics resulting in stable reactor temperatures. 3) No diffusion limitations. 4) Possibility of continuous refreshment of catalyst particles. 5) Relatively simple construction and low investment costs. Mathematical modeling of a FT SBCR was reviewed by Saxena et al. [1] and more recently by Saxena [2]. The bottleneck appears to be the lack of reliable kinetic equations for all products and reactants based on realistic reaction mechanisms.

A summary of previous slurry bubble column reactor models for the Fischer-Tropsch synthesis is given in Table 7.1. Most models are only applicable in small scale slurry bubble columns operating in the homogeneous regime. However, the churn-turbulent or heterogeneous regime is the most optimal one for the FT synthesis [13]. In this regime, there is a range of bubble sizes. The gas bubbles can be divided into two classes: 1) the small bubbles with a constant bubble diameter less than 0.01 m, and 2) the large bubbles: bubbles larger than 0.01 m with irregular shape and varying size. The mixing behavior of both classes is completely different due to the difference in rise velocity. Krishna and co-workers modeled a slurry bubble column containing cobalt catalyst particles with the use of flow patterns for the large and small bubbles [13, 16, 17].

Appropriate rate equations for both the Fischer-Tropsch and the water gas shift reaction are needed for modeling of bubble columns operated with iron catalysts. Kuo [9], Stenger and Satterfield [10], Prakash and Bendale [11], Prakash [12], and Inga and Morsi [15] included rate expressions for the FT and WGS reactions to obtain accurate hydrogen and carbon monoxide axial concentration profiles. Until now, none of the available literature models can describe the complete product distribution of the FT synthesis at industrial conditions (high temperature and pressure) as a function of overall consumption of synthesis gas components and operating conditions.

This study will investigate an iron-based Fischer-Tropsch SBCR operating in the heterogeneous flow regime. The model takes into account both the water gas shift and the FT reactions, as well as individual hydrocarbon product formation rates. Here, multicomponent vapor-liquid equilibria (VLE) with detailed kinetic expressions for all reactants and hydrocarbon products are combined with SBCR hydrodynamics and

Table 7.1 Comparison of reaction engineering models for the Fischer-Tropsch synthesis in slurry bubble column reactors.

Reference	Gas phase	Liquid phase	Catalyst distribution	Energy balance	Components	FT	WGS
Calderbank et al. [3]	PF	PF	uniform	isothermal	H ₂	1	-
Satterfield and Huff [4]	PF	PM	uniform	isothermal	H ₂	1	-
Deckwer et al. [5]	PF	PM	uniform	isothermal	H ₂	1	-
Deckwer et al. [6]	AD	AD	non-uniform	non-isothermal	H ₂	1	-
Bukur [7]	PF	PF, PM	uniform	isothermal	H ₂	1	-
Stern et al. [8]	PF	PM	uniform	isothermal	H ₂ , CO, CO ₂ , H ₂ O, CH ₄ , C ₅ H ₁₀	1	-
Kuo [9]	PF	PM, PF, AD	non-uniform	isothermal	H ₂	1	-
Kuo [9]	PF	PF	non-uniform	isothermal	H ₂ , CO, CO ₂ , H ₂ O	2	2
Stenger and Satterfield [10]	AD	AD	non-uniform	isothermal	H ₂ , CO, CO ₂ , H ₂ O, C ₅ H ₁₀	1	1
Prakash and Bendale [11]	AD	AD	non-uniform	isothermal	H ₂ , CO, CO ₂ , H ₂ O, C ₁₋₃	2	2
Prakash [12]	AD	AD	non-uniform	isothermal	H ₂ , CO, CO ₂ , H ₂ O, C ₁₋₃	2	2
De Swart [13] ¹	AD	AD	non-uniform	non-isothermal	H ₂	1	-
De Swart [13] ²	PF	PM	uniform	isothermal	H ₂	1	-
Mills et al. [14]	AD	AD	non-uniform	non-isothermal	H ₂	1	-
Inga and Morsi [15]	PF	MC	uniform	isothermal	H ₂ , CO, H ₂ O	1, 3	2
Krishna and Maretto [16] ²	PF	PM	uniform	isothermal	H ₂ , CO	3	-
Our model ²	PF	PM	uniform	isothermal	H ₂ , CO, CO ₂ , H ₂ O, N ₂ , C ₁₋₁₀₀		

PF: plug flow, PM: perfectly mixed, MC: mixing cells, AD: axial dispersion

¹ Heterogeneous flow regime: Large bubbles: PF, Small bubbles and liquid: AD

² Heterogeneous flow regime: Large bubbles: PF, Small bubbles and liquid: PM

mass transfer characteristics to predict the detailed product composition of both gas and liquid phase as a function of operating conditions.

Table 7.2 Kinetic models for Table 7.1.

	FT kinetic expressions		WGS kinetic expressions
1	$kC_{H_2,L}$	1	$k(C_{CO,L}C_{H_2O,L} - C_{CO_2,L}C_{H_2,L}/K_P)$
2	$\frac{kC_{H_2,L}C_{CO,L}}{C_{CO,L} + aC_{H_2O}}$	2	$\frac{k(C_{CO,L}C_{H_2O,L} - C_{CO_2,L}C_{H_2,L}/K_P)}{P_{CO} + aP_{H_2O}}$
3	$\frac{kC_{H_2,L}C_{CO,L}}{(1 + aC_{CO,L})^2}$		

7.2 Kinetics and Hydrocarbon Selectivity

The rate expression for the FT reaction on a precipitated iron catalyst in the slurry phase proposed in Chapter 6 was used (Table 7.3):

$$R_{FT} = \frac{kP_{CO}P_{H_2}^{1/2}}{(1 + aP_{CO} + bP_{CO_2})^2} \quad (7.1)$$

The water gas shift reaction is an exothermic and reversible reaction proceeding simultaneously with the Fischer-Tropsch reaction. Due to the WGS reaction, synthesis gas with a H_2/CO ratio below 2 can be used because excess of carbon monoxide is converted with water to carbon dioxide and hydrogen. The equilibrium constant K_P was obtained from Graaf et al. [18] and the following rate expression was used for the kinetics of the WGS (see Table 7.3 and Chapter 6):

$$R_{WGS} = \frac{k_{WGS}(P_{CO}P_{H_2O} - P_{CO_2}P_{H_2}/K_P)}{(P_{CO} + K P_{H_2O})^2} \quad (7.2)$$

The product selectivity to α -olefins and paraffins was calculated using a recently developed selectivity model for iron catalysts, called α -Olefin Readsorption Product Distribution Model (ORPDM) (see Chapters 4 and 6). This model allows for a chain-length dependent chain growth factor due to readsorption of α -olefins. The appropriate model parameters are shown in Table 7.3 as a function of process variables (P_{CO} , P_{H_2} , $\Phi_{v,0}/W$) at a constant temperature of 523 K.

Table 7.3 Kinetic and selectivity model parameters at 523 K (Chapter 6).

Parameter	Value	Parameter	Value
t_P^1	6.5	k (mol kg ⁻¹ s ⁻¹ MPa ^{-1.5})	0.0339
t_P^2	1.7	a (MPa ⁻¹)	1.185
c	0.35	b (MPa ⁻¹)	0.656
k_R^2	$17.6 k_R e^{2c}$	k_{WGS} (mol kg ⁻¹ s ⁻¹)	0.0292
p	$14.0 P_{H_2}^{-0.26} P_{CO}^{0.40}$	K (-)	3.07
t_O	$3.71 P_{H_2}^{-0.5}$	K_P	85.81
k_R	$8.00 \cdot 10^{-5} \frac{P_{H_2}^{1.2} P_{CO}^{-0.47}}{\Phi_{v,0}/W}$		

Pressures in MPa, space velocity $\Phi_{v,0}/W$ in Nm³ kg_{cat}⁻¹ s⁻¹

7.3 Model Equations

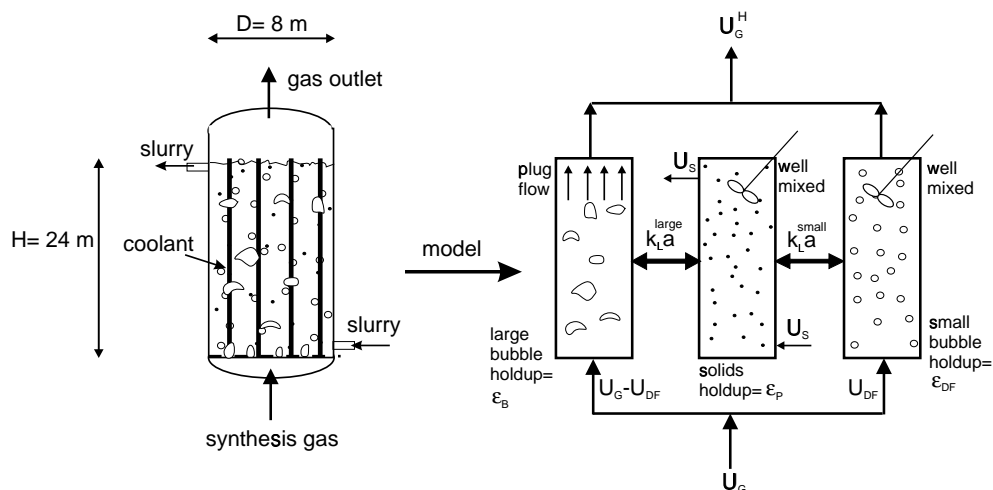


Figure 7.1 Hydrodynamic model of slurry bubble column reactor in the heterogeneous flow regime.

A mathematical description for the simulation of an industrial Fischer-Tropsch SBCR is presented. The reactor model can be applied in the heterogeneous or churn-turbulent regime (see Figure 7.1). The large bubbles are assumed to be in plug flow with a superficial gas velocity of $U_G - U_{DF}$. The superficial velocity of the gas present in the well mixed small bubbles is U_{DF} , which is equal to the total superficial gas ve-

locity at regime transition. The mathematical model for the Fischer-Tropsch synthesis is based on the following assumptions: 1) Gas-liquid mass transfer resistance is located in the liquid phase. 2) Large gas bubbles are in plug flow due to high rise velocities, typically $1\text{-}2\text{ m s}^{-1}$. 3) The gas phase in the small gas bubbles, and the liquid phase are each completely mixed, due to the large reactor diameter of 8 m [6]. Catalyst distribution is uniform due to upflow of the slurry phase, the large reactor diameter and the turbulence created by the fast-rising large bubbles. 4) Hydrocarbon products, paraffins and olefins only, in the gas and liquid phase of the reactor outlet are assumed to be in equilibrium at the reactor outlet. 5) The reactor operates isothermally due to the completely mixed liquid phase. 6) The slurry velocity is constant. 7) The reactor operates at steady state conditions. 8) The effectiveness factor of the catalyst particles is equal to unity and mass and heat transfer resistances between catalyst and liquid are negligible due to the small particle size applied ($50\text{ }\mu\text{m}$).

The gas phase mass balance for component i in the *large* bubbles, rising in plug flow is:

$$\frac{d(U_G - U_{DF}) C_{i,G}^{large}}{dh} + (k_L a)_i^{large} \left(\frac{C_{i,G}^{large}}{m_i^{GL}} - C_{i,L} \right) = 0 \quad (7.3)$$

with concentrations in mol m^{-3} subject to the boundary conditions at the reactor entrance: $h=0$: $C_{i,G}^{large} = C_{i,G}^{in}$. The gas phase mass balance for component i in the *small* bubbles (completely mixed) is:

$$\frac{U_{DF}}{H} (C_{i,G}^{in} - C_{i,G}^{small}) = (k_L a)_i^{small} \left(\frac{C_{i,G}^{small}}{m_i^{GL}} - C_{i,L} \right) \quad (7.4)$$

The mass balance for component i in the completely mixed liquid phase can be written as:

$$\begin{aligned} 1/H \int_0^H (k_L a)_i^{large} \left(\frac{C_{i,G}^{large}}{m_i^{GL}} - C_{i,L} \right) dh + (k_L a)_i^{small} \left(\frac{C_{i,G}^{small}}{m_i^{GL}} - C_{i,L} \right) + \\ + \varepsilon_L \varepsilon_P \rho_P \sum_{j=1}^n v_{ij} R_j - \frac{U_S}{H} C_{i,L} = 0 \quad (7.5) \end{aligned}$$

where ε_L is the liquid holdup ($\text{m}_L^3 \text{ m}_R^{-3}$), ε_P is the solids holdup ($\text{m}_P^3 \text{ m}_L^{-3}$), ρ_P is the catalyst density, R_j is the FT ($j=1$) or WGS ($j=2$) reaction rate ($\text{mol kg}_{cat}^{-1} \text{ s}^{-1}$), v_{ij} is the stoichiometric coefficient for component i in the j -th reaction. The reaction heat

is removed with vertical cooling tubes of 1.5 inch diameter at a constant steam temperature T_c of 495 K. The overall heat transfer coefficient α_{eff} from slurry to coolant is estimated from the correlation of Deckwer et al. [19]:

$$\alpha_{eff} = 0.1 U_G^{0.25} \rho_S^{0.75} C_{p,S}^{0.5} g^{0.25} \eta_S^{-0.25} \lambda_S^{0.5} \quad (7.6)$$

At gas velocities higher than 0.10 m s^{-1} the heat transfer coefficient does not increase any more and is calculated from eq 7.6 with U_G equal to 0.10 m s^{-1} .

The energy balance for the slurry phase reads, assuming the catalyst and the liquid temperature to be equal:

$$\begin{aligned} \varepsilon_L \varepsilon_P \rho_P \sum_{j=1}^n (-\Delta H_{R,j}) R_j - \alpha_{eff} a_c (T - T_c) + \\ + \frac{U_S}{H} ((\rho_S C_{p,S} T)_{in} - (\rho_S C_{p,S} T)_{out}) = 0 \end{aligned} \quad (7.7)$$

where a_c is the specific heat transfer area (m^{-1}), $C_{p,S}$ is the heat capacity of the slurry phase, ρ_S is the slurry density and $-\Delta H_{R,j}$ is the reaction heat of reaction j (J mol^{-1}).

The molar flow rate of the gas phase will change due to reaction. The superficial velocity is assumed to be a linear function of the overall synthesis gas conversion, X_{CO+H_2} [14]:

$$U_G = (1 + \alpha_c X_{CO+H_2}) U_G^{in} = (1 + \alpha_c (1 + U)/(1 + F) X_{H_2}) U_G^{in}, \quad (7.8)$$

where α_c is the contraction factor, defined as:

$$\alpha_c = \frac{U_G(X_{CO+H_2} = 1) - U_G(X_{CO+H_2} = 0)}{U_G(X_{CO+H_2} = 0)} \quad (7.9)$$

U is the usage ratio of hydrogen to carbon monoxide ($-R_{H_2}/-R_{CO}$) and F is the feed ratio of H_2 to CO . The reported values of α are between -0.5 and -0.65 [6]. The contraction factor α_c is determined by the product selectivity (m and n).

7.4 Hydrodynamic Parameters

The most important hydrodynamic parameters are the gas holdup of the large and small bubbles in presence of solids under Fischer-Tropsch reaction conditions. The rise velocity of the small bubbles will increase with increasing solids holdup due to enhanced coalescence according to:

$$V_{small} = V_{small}^{ref} \left(1 + 0.8 \varepsilon_P / V_{small}^{ref} \right) \quad (7.10)$$

with $V_{small}^{ref} = 0.095 \text{ m s}^{-1}$ [20]. The gas holdup at the transition from homogeneous to churn turbulent regime in the presence of a high solids loading follows from Krishna et al. [20]:

$$\varepsilon_{DF} = \varepsilon_{DF}^{ref} \left(\rho_G / \rho_G^{ref} \right)^{0.48} \left(1 - 0.7 \varepsilon_P / \varepsilon_{DF}^{ref} \right) \quad (7.11)$$

where the small bubble holdup in solids-free liquid is $\varepsilon_{DF}^{ref} = 0.27$ and the atmospheric density is $\rho_G^{ref} = 1.3 \text{ kg m}^{-3}$. The corresponding superficial gas velocity at regime transition is calculated from $U_{DF} = V_{small} \varepsilon_{DF}$. The model of Krishna and Ellenberger [21] is used to predict the gas holdup of the *large* bubbles. This model is corrected for the influence of gas density according to a recent study of Letzel et al. [22]. For large bubble columns ($D > 1 \text{ m}$) and high slurry concentrations ($\varepsilon_P > 0.16$), the large bubble holdup can be estimated from a combination of the correlations given by Letzel et al. [22] and Krishna et al. [20]:

$$\varepsilon_B = 0.3 (U_G - U_{DF})^{0.58} \left(\rho_G / \rho_G^{ref} \right)^{0.5} \quad (7.12)$$

The total gas holdup in the heterogeneous regime is calculated from:

$$\varepsilon_G = \varepsilon_B + \varepsilon_{DF} (1 - \varepsilon_B) \quad (7.13)$$

The volumetric mass transfer coefficient of *large* bubbles is obtained from the relation proposed by Vermeer and Krishna [23] and more recently by Letzel et al. [22]:

$$k_L a_{ref}^{large} / \varepsilon_B = 0.5 \quad (7.14)$$

which is corrected for the mass transfer coefficient of component i by the factor:

$$k_{L,i}^{large} / k_{L,ref}^{large} = (D_i / D_{ref})^{0.5} \quad (7.15)$$

where $D_{ref} = 2 \cdot 10^{-9} \text{ m}^2 \text{ s}^{-1}$. In the same way, the volumetric mass transfer coefficient for component i of the small bubbles is defined as [16]:

$$k_L a_{ref}^{small} / \varepsilon_{DF} = 1.0 \quad (7.16)$$

7.5 Physical Properties and Flash Calculations

For calculating the physical properties of the liquid, it was assumed that the FT wax consisted of n-paraffins with a carbon number of 28 ($\text{C}_{28}\text{H}_{58}$). The physical properties at 523 K were estimated with the asymptotical behavior correlations developed by

Table 7.4 Operation conditions and physical properties.

Reactor configuration		
reactor diameter	$D=8$	m
reactor height	$H=30$ (20% disengagement zone)	m
dispersion height	$H=24$	m
Operating conditions		
pressure	$P=30 \cdot 10^5$	Pa
temperature	$T=523$	K
catalyst concentration	$\varepsilon_P=0.20 - 0.35$	$m^3_P m_L^{-3}$
superficial gas velocity	$U_G=0.15-0.40$	$m s^{-1}$
superficial slurry velocity	$U_S=0.01$	$m s^{-1}$
cooling tube diameter	$d_c = 0.0381$	m
coolant temperature	$T_c=495$	K
feed composition	$F=0.5 - 2.0, y_{CO_2}=0.05, y_{inert}=0.05$	-
Liquid phase (L)		
liquid viscosity	$\eta_L=5.95 \cdot 10^{-4}$	Pa s
liquid density	$\rho_L=656.7$	$kg m^{-3}$
surface tension	$\sigma=0.017$	$N m^{-1}$
liquid heat capacity	$C_{p,L}=2721$	$J kg^{-1} K^{-1}$
liquid heat conductivity	$\lambda_L=0.181$	$W m^{-1} K^{-1}$
Catalyst phase (P)		
catalyst diameter	$d_P=50 \cdot 10^{-6}$	m
catalyst density	$\rho_P=1957$ (Lox et al. [24])	$kg m^{-3}$
catalyst heat capacity	$C_{p,P}=993$	$J kg^{-1} K^{-1}$
catalyst heat conductivity	$\lambda_P=1.7$	$W m^{-1} K^{-1}$
Slurry phase (S)		
catalyst weight fraction	$w_P = \frac{\varepsilon_P \rho_P}{\varepsilon_P (\rho_P - \rho_L) + \rho_L}$ [6]	-
slurry density	$\rho_S = \varepsilon_P \rho_P + (1 - \varepsilon_P) \rho_L$ [6]	$kg m^{-3}$
slurry viscosity	$\eta_S = \eta_L (1 + 4.5 \varepsilon_P)$ [19]	Pa s
slurry heat capacity	$C_{p,S} = w_P C_{p,P} + (1 - w_P) C_{p,L}$ [6]	$J kg^{-1} K^{-1}$
slurry heat conductivity	$\lambda_S = \lambda_L \frac{2\lambda_L + \lambda_P - 2\varepsilon_P(\lambda_L - \lambda_P)}{2\lambda_L + \lambda_P + \varepsilon_P(\lambda_L - \lambda_P)}$ [25]	$W m^{-1} K^{-1}$

Marano and Holder [26, 27] (see Table 7.4). Henry constants for CO, CO₂, H₂, H₂O, N₂ and light hydrocarbons (C₁- C₃) were obtained from Marano and Holder [28]. Diffusivities at high temperatures and pressures, necessary for calculating mass transfer coefficients, were estimated using correlations of Erkey et al. [29] based on the rough hard sphere theory. The multicomponent VLE model of Marano and Holder [28] was applied. However, we assumed ideal gas behavior of the gas phase because under the reaction conditions applied, the fugacity coefficients (upto C₃₀) as calculated with the Peng-Robinson equation of state are between 0.95 and 1.01. The equilibrium constants between vapor and liquid for non-hydrocarbons and C₁₋₃ hydrocarbons were calculated from:

$$K_i \equiv y_i/x_i = H_i^\infty \Phi_i / P \quad (7.17)$$

where K_i is the K -value for component i , H_i^∞ is the Henry constant for component i at infinite dilution, and Φ_i is the Poynting-factor. For the other hydrocarbons, the K -value is given by:

$$K_i = \gamma_i^\infty P_{i,sat} \Phi_i / P \quad (7.18)$$

where γ_i^∞ is an activity coefficient, and $P_{i,sat}$ is the vapor pressure of pure component i . The appropriate parameter values were obtained from Marano and Holder [28]. A flash calculation using these K -values gives the final composition of the liquid and gas phase outlet of the SBCR:

$$\rho_p \bar{\varepsilon}_L \varepsilon_P V_R R_{FT} \frac{m_i}{\sum_i n m_i} = U_G^H A y_i C_G + U_S A x_i C_L \quad (7.19)$$

where m_i is the molar selectivity to product i with carbon number n , and C_G and C_L are the total gas and liquid concentration, respectively.

7.6 Results and Discussion

A commercial scale SBCR with diameter $D= 8$ m, dispersion height $H= 24$ m, pressure $P= 3.0$ MPa and temperature $T= 523$ K is used in our simulations. The superficial slurry velocity U_S is 0.01 m s⁻¹. The slurry enters the reactor with an inlet temperature of 423 K. The properties of the catalyst applied (Ruhrchemie LP 33/81 Fe/Cu/K on SiO₂) are: catalyst particle diameter $50 \cdot 10^{-6}$ m, catalyst density $\rho_p= 1957$ kg m⁻³. The properties of the slurry were determined using the relations of Deckwer et

Table 7.5 Physical properties and concentrations of the components in the SBCR mentioned in Figure 7.2. Operating conditions: $F=1$, $U_G^{in}=0.20$ m s⁻¹, $\varepsilon_P=0.25$, $D=8$ m, $H=24$ m, $T=523$ K.

Component	m_i^{GL} (C_G/C_L)	D_i (10^{-8} m ² s ⁻¹)	$C_{i,G}^{in}$	$C_{i,G,out}^{large}$	$C_{i,G}^{small}$	$C_{i,L}$
			(mol m ⁻³)			
H ₂	5.83	3.85	310.5	152.6	155.1	26.2
CO	4.86	1.53	310.5	125.2	129.2	25.8
CO ₂	2.32	1.26	34.5	150.3	149.0	64.9
H ₂ O	0.85	1.89	0	53.5	53.3	62.9
N ₂	5.65	1.54	34.5	44.5	44.3	7.9

al. [6, 19] (see Table 7.4). The complete reactor model consists of a system of ordinary differential equations and algebraic equations, with the corresponding boundary conditions. The set of equations was solved numerically using a backward differentiation scheme with 60 grid points using the gPROMS software package (Version 1.6a, Process Systems Enterprise, London).

The concentration gradients of CO, H₂, CO₂, H₂O and N₂ are large in the bottom of the slurry reactor. Particularly at the top of the reactor, the liquid phase is in equilibrium with the gas phase ($C_{i,L} = C_{i,G}^{large}/m_i^{GL}$, see Table 7.5). Resulting from the difference in solubility, the H₂/CO ratio in the liquid phase is larger than that in the gas feed. The liquid phase concentrations of H₂ and CO influence the chain length and olefin content of the products formed. The axial concentration profiles of CO, H₂, CO₂, H₂O and N₂ in the large gas bubbles are plotted in Figure 7.2.

Figure 7.3 shows the corresponding productivity of each individual paraffin and olefin, both in the gas and liquid phase. The model predicts the FT product distribution between the vapor and liquid phases. The lighter products with a high olefin yield are in the gas phase, and the heavier products, mainly paraffins, leave the reactor in the liquid or wax phase. Our model predicts the effect of the process conditions on the selectivity and composition of the individual phases.

The major results of our simulations on the reactor performance are shown in Figure 7.4a-b for a range of catalyst concentrations ε_P between 0.2 and 0.35, feed ratios of H₂ to CO (F) in the synthesis gas between 0.67 and 2, with a constant mole fraction of CO₂ and N₂ in the feed of 0.05 and superficial inlet gas velocity U_G^{in} from 0.15 to 0.4 m s⁻¹ (see Table 7.4). Increase of the inlet gas velocity causes a decrease of the synthesis gas conversion, as expected. At low gas velocities, $U_G^{in} < 0.15$ m s⁻¹,

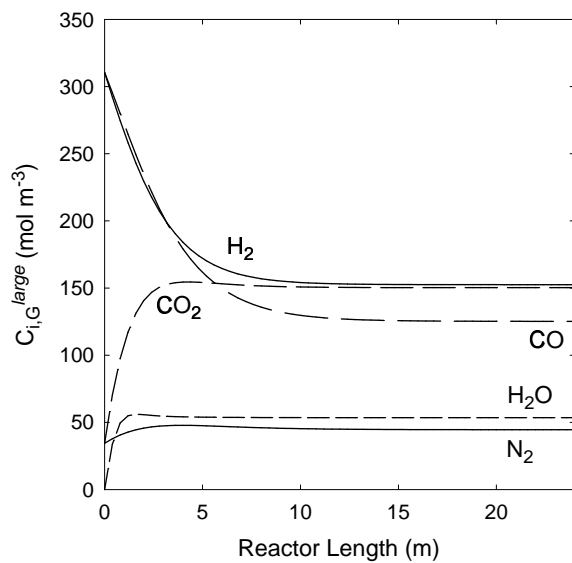


Figure 7.2 Axial concentration profiles for CO, H₂, CO₂, H₂O and N₂. Operating conditions: $F=1$, $U_G^{in} = 0.20 \text{ m s}^{-1}$, $\varepsilon_P=0.25$, $D=8 \text{ m}$, $H=24 \text{ m}$, $T=523 \text{ K}$. See also Table 7.5.

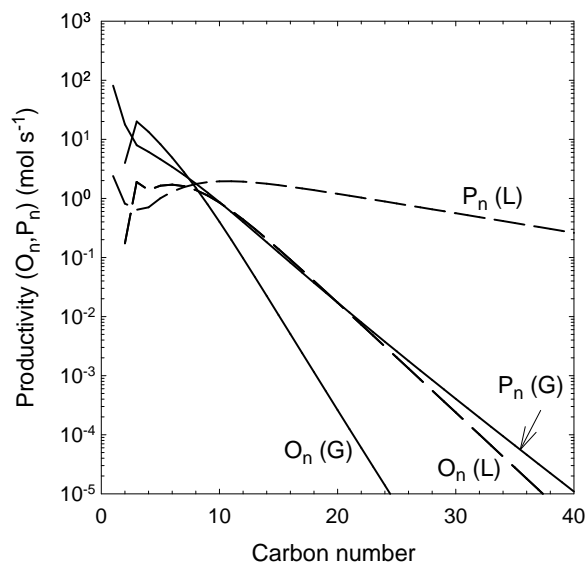


Figure 7.3 Paraffin (P_n) and olefin (O_n) production rates in the gas and liquid outlet streams ($p=12.6$, $t_O=4.6$, $k_R=0.27$). Operating conditions: $F=1$, $U_G^{in} = 0.20 \text{ m s}^{-1}$, $\varepsilon_P=0.25$, $D=8 \text{ m}$, $H=24 \text{ m}$, $T=523 \text{ K}$.

the synthesis gas conversion reaches a constant level of about 80 % as a consequence of the kinetic expressions with product (CO_2) inhibition. Higher conversions can be obtained when the operating conditions (P , T) or catalyst are changed or when the dispersion height is increased to, for example, $H = 30$ m. The reactor productivity, expressed as total hydrocarbon production in $\text{kg h}^{-1} \text{m}_R^{-3}$, shows an increase with increasing gas velocity. The effect of catalyst concentration on the reactor performance at $F = 1$ is shown in Figure 7.4a. Increasing the catalyst concentration (ϵ_P) shows an

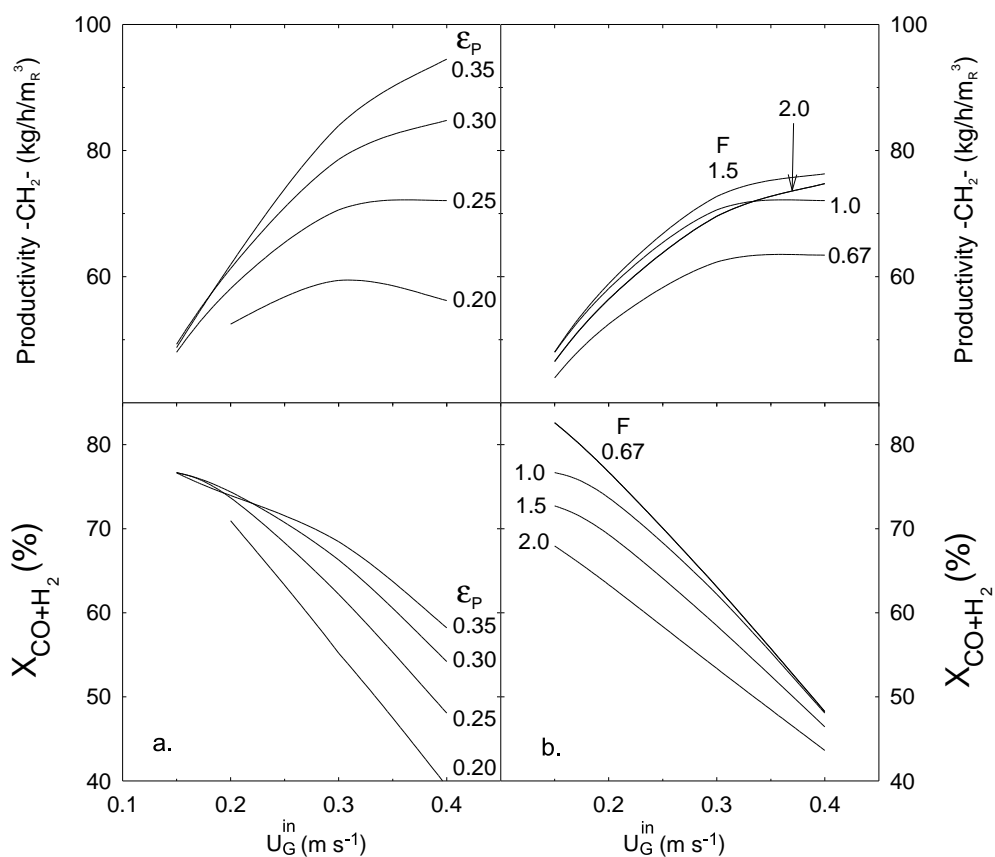


Figure 7.4 a. Effect of catalyst concentration and gas velocity on the synthesis gas conversion and productivity ($F=1$, $T= 523$ K). b. Effect of the H_2/CO feed ratio F and gas velocity on the same ($\epsilon_P=0.25$, $T= 523$ K).

increase of the conversion and productivity. The catalyst concentration influences the concentration levels as well as ε_{DF} according to eq 7.11. The highest productivity is obtained at high catalyst concentrations ($\varepsilon_P=0.35$) and gas velocities up to 0.4 m s^{-1} . The effect of the feed ratio F at a constant catalyst concentration of $\varepsilon_P=0.25$ is given in Figure 7.4b. The decrease of the synthesis gas conversion with increasing F is mainly caused by the kinetics. At low feed ratios, conversions of CO are large due to the high water gas shift reaction rate. The optimal productivity is obtained at a feed ratio of $F=1.5$. The feed ratio influences the gas holdup due to changing gas density. Significantly lower gas holdup values were observed with increasing F . The number of cooling tubes required strongly depends on the productivity and varies between 600 and 1700 cooling tubes. The corresponding pitch distance varies from 0.33 to 0.20 m, which is large enough not to influence the hydrodynamics of the SBCR [16].

The effect of the feed ratio on the selectivity to several product classes is shown in Table 7.6. The total hydrocarbon (paraffin and olefin) selectivities in mass percentages were lumped in four groups: methane (w_1), light gases C_{2-4} (w_{2-4}), gasoline C_{5-10} (w_{5-10}), and a diesel/wax fraction C_{10-100} (w_{10+}). The olefin content is shown for the C_2 products ($w_{O,2}$), C_{3-4} products ($w_{O,3-4}$) and the total olefin yield of all products (w_O). The selectivities in Table 7.6 were calculated with the model parameters in Table 7.3. Increasing F has a pronounced effect on the increasing selectivity to methane and a decreasing olefin content of the product spectrum. The hydrogen concentration in the liquid bulk increases, which causes an increase of the termination to paraffins relative to olefins and a decrease of the chain growth parameter.

Table 7.6 Selectivity parameters and product selectivities (wt%) as a function of the H_2/CO feed ratio F ($U_G^{in} = 0.20 \text{ m s}^{-1}$, $\varepsilon_P = 0.25$, $T = 523 \text{ K}$).

F	p	t_O	k_R	Product selectivity (wt%)						
				w_1	w_{2-4}	w_{5-10}	w_{10+}	$w_{O,2}$	$w_{O,3-4}$	w_O
0.67	17.4	5.6	0.17	3.7	17.5	26.5	52.3	43.0	85.3	37.7
1.0	12.6	4.6	0.27	5.7	18.9	27.2	48.2	28.5	79.3	33.5
1.5	9.6	3.9	0.41	8.2	20.5	28.4	43.0	19.0	72.7	29.6
2.0	7.9	3.6	0.56	10.6	21.8	29.3	38.3	13.9	66.8	26.5

7.7 Conclusions

A mathematical design model for a large scale Fischer-Tropsch SBCR is developed. The model takes into account the water gas shift and Fischer-Tropsch reactions as well as individual hydrocarbon product formation rates. Under the operating conditions investigated the FT SBCR is mainly reaction controlled. This is caused by the limited activity of Fe catalysts on the one hand and the large value of the volumetric mass transfer coefficient of the large bubbles due to frequent bubble coalescence and breakup on the other hand. The model predicts the composition of the gaseous and liquid streams of a large scale bubble column operating in the churn-turbulent regime as a function of the operating parameters. It provides all the data necessary for reliable scale up, process optimization and prediction of the performance of industrial scale FT bubble column reactors.

List of Symbols

A	reactor area, m^2
a_c	specific cooling area, m^{-1}
C	concentration, mol m^{-3}
C_p	heat capacity, $\text{J kg}^{-1} \text{K}^{-1}$
D	reactor diameter, m
D	diffusion coefficient, $\text{m}^2 \text{s}^{-1}$
F	H_2/CO feed ratio
g	gravity acceleration factor, 9.81 m s^{-2}
h	axial position, m
H	dispersion height, m
H_i^∞	Henry constant, Pa
K_i	equilibrium constant (y_i/x_i)
k_{La}	volumetric mass transfer coefficient, s^{-1}
m_i^{GL}	solubility coefficient C_G/C_L
m_i	molar selectivity
n	carbon number
P	pressure, Pa
P_i^{sat}	vapor pressure, Pa
R	gas constant, $8.314 \text{ J mol}^{-1} \text{K}^{-1}$
R_j	reaction rate, $\text{mol kg}_{cat}^{-1} \text{s}^{-1}$

T	temperature, K
U	H ₂ /CO consumption ratio ($-R_{H_2}/-R_{CO}$)
U	superficial velocity, m s ⁻¹
V_R	reactor volume, m ³
V_{small}	rise velocity small bubbles, m s ⁻¹
w_i	weight fraction of product i
X_{CO+H_2}	synthesis gas conversion
X_{H_2}	hydrogen conversion
x_i	mole fraction in liquid phase
y_i	mole fraction in gas phase

Greek Letters

α_{eff}	effective heat transfer coefficient, W m ⁻² K ⁻¹
α_c	contraction factor
γ_i^∞	liquid phase activity coefficient
$\Delta H_{R,j}$	reaction enthalpy, J mol ⁻¹
ε	holdup
η_L	liquid viscosity, Pa s
λ	heat conductivity, W m ⁻¹ K ⁻¹
ν_{ij}	stoichiometric coefficient
ρ	density, kg m ⁻³
σ	surface tension, N m ⁻¹
Φ_i	Poynting factor
$\Phi_{v,0}/W$	space velocity, Nm ³ kg _{cat} ⁻¹ s ⁻¹

Sub- and Superscripts

B	large bubbles	<i>large</i>	referring to large bubbles
c	coolant	<i>out</i>	outlet conditions
DF	dense phase	P	catalyst phase
G	gas phase	R	reactor
i	component	<i>ref</i>	reference conditions
<i>in</i>	inlet conditions	S	slurry phase
j	reaction	<i>small</i>	referring to small bubbles
L	liquid phase		

Kinetic and selectivity parameters (see List of Symbols for Chapters 2-6):

$a, b, k, K_P, k_{WGS}, K, t_P^1, t_P^2, k_R^2, p, t_O, k_R, c, \alpha_n, \theta_n$

References

- [1] Saxena, S.C.; Rosen, M.; Smith, D.N.; Ruether, J.A., Mathematical modeling of Fischer-Tropsch slurry bubble column reactors, *Chem. Eng. Commun.* **1986**, *40*, 97–151.
- [2] Saxena, S.C., Bubble column reactors and Fischer-Tropsch synthesis, *Catal. Rev.-Sci. Eng.* **1995**, *37*, 227–309.
- [3] Calderbank, P.H.; Evans, F.; Farley, R.; Jepson, G.; Poll, A., Rate processes in the catalyst-slurry Fischer-Tropsch reaction, *Catal. in Practice* **1963**, 66–74.
- [4] Satterfield, C.N.; Huff, G.A., Effects of mass transfer on Fischer-Tropsch synthesis in slurry reactors, *Chem. Eng. Sci.* **1980**, *35*, 195–202.
- [5] Deckwer, W.-D.; Serpemen, Y.; Ralek, M.; Schmidt, B., On the relevance of mass transfer limitations in the Fischer-Tropsch slurry process, *Chem. Eng. Sci.* **1981**, *36*, 765–771.
- [6] Deckwer, W.-D.; Serpeman, Y.; Ralek, M.; Schmidt, B., Modeling the Fischer-Tropsch synthesis in the slurry phase, *Ind. Eng. Chem. Process Des. Dev.* **1982**, *21*, 231–241.
- [7] Bukur, D.B., Some comments on models for Fischer-Tropsch reaction in slurry bubble column reactors, *Chem. Eng. Sci.* **1983**, *38*, 441–446.
- [8] Stern, D.; Bell, A.T.; Heinemann, H., Effects of mass transfer on the performance of slurry reactors used for Fischer-Tropsch synthesis, *Chem. Eng. Sci.* **1983**, *38*, 597–605.
- [9] Kuo, J.C.W., Slurry Fischer-Tropsch/Mobil two stage process of converting syngas to high octane gasoline, Final report DOE-PC-3022-10, DOE **1983**.
- [10] Stenger, H.G.; Satterfield, C.N., Effects of sulfur poisoning of a reduced fused magnetite catalyst in the Fischer-Tropsch synthesis, *Ind. Eng. Chem. Process Des. Dev.* **1985**, *24*, 415–420.
- [11] Prakash, A.; Bendale, P.G., Design of slurry reactor for indirect liquefaction applications, Final report DE-AC22-89PC89870, DOE **1991**.
- [12] Prakash, A., On the effects of syngas composition and water-gas-shift reaction rate on FT synthesis over iron based catalyst in a slurry reactor, *Chem. Eng. Commun.* **1994**, *1280*, 143–158.
- [13] De Swart, J.W.A., *Scale-up of a Fischer-Tropsch reactor*, Ph.D. thesis, University of Amsterdam, Amsterdam, The Netherlands **1996**.
- [14] Mills, P.L.; Turner, J.R.; Ramachandran, P.A.; Dudukovic, M.P., The Fischer-Tropsch synthesis in slurry bubble column reactors: analysis of reactor perfor-

- mance using the axial dispersion model, in K.D.P. Nigam; A. Schumpe, eds., *Three-phase sparged reactors*, Gordon & Breach, Amsterdam, 1996 pp. 339–386.
- [15] Inga, J.R.; Morsi, B.I., A novel approach for the assessment of the rate-limiting step in Fischer-Tropsch slurry process, *Energy Fuels* **1996**, *10*, 566–572.
- [16] Krishna, R.; Maretto, C., Scale up of a bubble column slurry reactor for Fischer-Tropsch synthesis, *Stud. Surf. Sci. Catal.* **1998**, *119*, 197–202.
- [17] De Swart, J.W.A.; Krishna, R.; Sie, S.T., Selection, design and scale up of the Fischer-Tropsch reactor, *Stud. Surf. Sci. Catal.* **1997**, *107*, 213–218.
- [18] Graaf, G.H.; Sijtsema, P.J.J.M.; Stamhuis, E.J.; Joosten, G.E.H., Chemical equilibria in methanol synthesis, *Chem. Eng. Sci.* **1986**, *41*, 2883–2890.
- [19] Deckwer, W.-D.; Louisi, Y.; Zaidi, A.; Ralek, M., Hydrodynamic properties of the Fischer-Tropsch slurry process, *Ind. Eng. Chem. Process Des. Dev.* **1980**, *19*, 699–708.
- [20] Krishna, R.; De Swart, J.W.A.; Ellenberger, J.; Martina, G.B.; Maretto, C., Gas holdup in slurry bubble columns: effect of column diameter and slurry concentrations, *AIChE J.* **1997**, *43*, 311–316.
- [21] Krishna, R.; Ellenberger, J., Gas holdup in bubble column reactors operating in the churn-turbulent regime, *AIChE J.* **1996**, *42*, 2627–2634.
- [22] Letzel, M.H.; Schouten, J.C.; Krishna, R.; Van den Bleek, C.M., Gas holdup and mass transfer in bubble column reactors operated at elevated pressure, *Chem. Eng. Sci.* **1999**, in press.
- [23] Vermeer, D.J.; Krishna, R., Hydrodynamics and mass transfer in bubble columns operating in the churn-turbulent regime, *Ind. Eng. Chem. Process Des. Dev.* **1981**, *20*, 475–482.
- [24] Lox, E.S.; Marin, G.B.; de Graeve, E.; Bussiere, P., Characterization of a promoted precipitated iron catalyst for Fischer-Tropsch synthesis, *Appl. Catal. A* **1988**, *40*, 197–218.
- [25] Tareef, M., *Colloid J. USSR* **1940**, *6*, 545, cited in *Ind. Eng. Chem. Process Des. Dev.* **1980**, *19*, 699–708.
- [26] Marano, J.J.; Holder, G.D., General equation for correlating the thermophysical properties of n-paraffins, n-olefins, and other homologous series. 2. Asymptotic behavior correlations for PVT properties, *Ind. Eng. Chem. Res.* **1997**, *36*, 1895–1907.
- [27] Marano, J.J.; Holder, G.D., General equation for correlating the thermophysical properties of n-paraffins, n-olefins, and other homologous series. 3. Asymptotic

- behavior correlations for thermal and transport properties, *Ind. Eng. Chem. Res.* **1997**, *36*, 2399–2408.
- [28] Marano, J.J.; Holder, G.D., Characterization of Fischer-Tropsch liquids for vapor-liquid equilibria calculations, *Fluid Phase Equilib.* **1997**, *138*, 1–21.
- [29] Erkey, C.; Rodden, J.B.; Akgerman, A., A correlation for predicting diffusion coefficients in alkanes, *Can. J. Chem. Eng.* **1990**, *68*, 661–665.

8

Conclusions and Epilogue

The major objective of this thesis is to develop a kinetic model that can predict Fischer-Tropsch conversion and product selectivities over a commercial precipitated iron catalyst with improved accuracy relative to existing models. A detailed multicomponent reaction engineering model for a commercial scale slurry bubble column reactor with use of these new kinetic and selectivity models is the final aim of this thesis. The work reported in this thesis consisted of: a) critical literature review on the kinetics and selectivity of the Fischer-Tropsch synthesis (Chapter 2), b) kinetic and selectivity modeling of experimental data obtained over a commercial precipitated Fe/Cu/K/SiO₂ catalyst both in a spinning basket reactor and a slurry reactor (Chapters 3-6) and c) reactor modeling of a large scale Fischer-Tropsch slurry bubble column reactor (Chapter 7). Data on the hydrodynamic behavior and mass transfer characteristics of the bubble column under the operating conditions applied were selected from literature. The major conclusions and suggestions for further research are summarized below.

Product Selectivity

The product selectivity to linear olefins and paraffins was studied both in a gas-solid spinning basket reactor (Chapter 4) and in a gas-slurry reactor (Chapter 6.3.1) over a wide range of industrially relevant process conditions on a precipitated iron catalyst. A new product selectivity model for linear hydrocarbons, the α -Olefin Readsorption Product Distribution Model (ORPDM), was developed. This model combines readsorption of α -olefins and chain growth on the same catalytic site. ORPDM predicts the selectivity to olefins and paraffins accurately at a constant temperature of 523 K. The ORPDM parameters (chain growth parameter p , olefin termination parameter t_O and readsorption parameter k_R) were described successfully by equations depending on the operating conditions only. In contrast to most literature models, the experimentally observed relatively high yield of methane, relatively low yield of ethene and the changing olefin to paraffin ratio and chain growth factor with chain length can all be

predicted from this model.

The current model is a basis for more advanced kinetic models which do take into account the effect of temperature. Ultimately, a small set of kinetic parameters must be obtained which are able to describe the synthesis gas consumption as well as the product selectivity over a wide range of feed component pressures, residence time and temperature. The main problem is to obtain the experimental kinetic data without severe catalyst deactivation. If necessary, the new model can be extended to describe the selectivity to minor amounts of oxygenated products (1-alcohols) or isomers (β -olefins, branched hydrocarbons) on iron catalysts. On cobalt catalysts, product selectivity models should include secondary hydrogenation of α -olefins to paraffins [1].

Reaction Kinetics

The reaction kinetics of both the Fischer-Tropsch and the water gas shift reactions over a precipitated iron catalyst were measured and modeled for both gas-solid and gas-slurry systems. A number of rate equations were derived on the basis of a detailed set of realistic reaction mechanisms. It was assumed that the formation of methylene, originating from the carbide mechanism, is the rate determining step in the Fischer-Tropsch reaction. 14 models for the FT reaction rate and 2 WGS reaction rate equations were fitted to the experimental data. Bartlett's test was applied to reduce the set of possible Fischer-Tropsch rate equations to 3 models for the gas-solid system (Chapter 5) and to 2 models for the gas-slurry system (Chapter 6.3.2), which were statistically indistinguishable. The rate equations for the water gas shift reaction are all based on the formate mechanism. Simulations using the optimal kinetic models derived showed good agreement both with experimental data and with some literature models. The slurry liquid appeared to affect the kinetic parameters and the adsorption constants. At low H_2/CO ratios, both the Fischer-Tropsch and the water gas shift reaction appeared to be lower than for the gas-solid kinetics.

The reaction kinetics were determined at a constant temperature of 523 K only. Further research should investigate the influence of the temperature and test the validity of the activation and adsorption energies according to the guidelines of Boudart [2].

The preferred way to present catalytic rate data is in the form of specific activity, such as turnover rates (TOR) or turnover frequencies (TOF) [3]. This way, different catalysts can be compared appropriately. Measurements of the surface area and the

metal dispersion are complicated on precipitated iron catalyst operating under industrial conditions in the slurry-phase due to wax-filled pores and changing composition of the iron phases. In this thesis, the reaction rates are given per mass unit of catalyst. These reaction rates can directly be applied in reaction engineering models, such as presented in Chapter 7.

Reaction Engineering Model for an FT Slurry Bubble Column Reactor

A reaction engineering model was developed for a commercial scale Fischer-Tropsch slurry bubble column reactor (Chapter 7). The model incorporates new hydrodynamic insights with respect to gas holdup and mass transfer in the heterogeneous flow regime [4] and improved kinetic models for the selectivity and the reaction rates based on own measurements (Chapter 6). The reactor model assumes plug flow for the large gas bubbles and ideal mixing for both the liquid, the small bubbles and the catalyst phase. The assumption of complete mixing of the small bubbles (dense phase) is conservative, because these bubbles can also be entrained by the large bubbles. The assumption on ideal mixing results in a conservative reactor design with respect to conversions and hydrocarbon production. However, the overall contribution of the dense phase is small in comparison to the large bubbles, especially at high gas velocities. The main novel aspect of this model is the prediction of the composition of both the gaseous and the liquid product streams of a slurry reactor operating in the heterogeneous flow regime as a function of process conditions. It provides information for reliable scale up, design and prediction of the performance of an industrial scale FT slurry reactor.

A number of patents deal with modifications of Fischer-Tropsch slurry bubble column reactors to reduce the back-mixing of both the liquid and the gas phase [5–7]. Arcuri [5] described the influence of various degrees of back-mixing on the selectivity and the productivity based on kinetic data obtained over a Co/TiO₂ catalyst, both in plug flow (fixed bed), bubble column and completely mixed reactors (CSTR). Arcuri [5] claimed that the productivity in a slurry bubble column is equal to or greater than for plug flow, and that the same selectivity is obtained for the completely mixed system. Koros [6] (Exxon Research) reported the invention of a slurry bubble column with plug flow in either the gas phase and the liquid phase. The patent describes a multi-tubular slurry bubble column reactor with cooling medium around the tubes. The presented example shows a reaction tube of 0.15 m mounted inside a 0.30 m pipe that served as a cooling jacket. According to our opinion, this reactor configuration has several disadvantages: 1) possibility of slug flow conditions, 2) large gas holdup

due to the influence of the column diameter on the large gas bubble holdup [8], 3) possibility of maldistribution of the gas, the liquid and the catalyst phases, and 4) low specific cooling area relative to, for example, 1.5 inch cooling tubes. A better option is staging the slurry bubble column horizontally as proposed earlier by Graaf [9] for slurry phase methanol synthesis. Maretto and Piccolo [7] reported the effect of staging a slurry bubble column. The temperature in each stage could be controlled separately. Their model assumed plug flow of the gas phase and complete mixing of the slurry in each stage. Maretto and Piccolo [7] claimed that the liquid phase in the multistage reactor may approach plug flow behavior, resulting in an increase of the synthesis gas conversion with increasing the number of stages. Our model can easily be extended to incorporate the effect of staging of a slurry bubble column. In addition to the study of Maretto and Piccolo [7], extension of the model presented will also predict the effect of staging on the product selectivity. Maretto and Piccolo [7] did not report on the engineering details of staging bubble columns. One of the possibilities would be the application of horizontal gauzes or perforated plates [10, 11]. These plates decrease the bubble size of large gas bubbles and slugs which results in a higher gas holdup and improvement of the plug flow characteristics of the gas and liquid phase.

Epilogue

With the current, extremely low, oil prices, the process economy of Fischer-Tropsch is unfavorable. Under certain conditions and in specific situations, FT processes are interesting: 1) availability of cheap natural gas (for example, Malaysia, Alaska, Qatar) or coal (South Africa); 2) production of chemicals or high-value clean diesel and gas oil; 3) governmental regulations on flaring of natural gas or on emissions in the transport sector.

The main barrier for Fischer-Tropsch technology is in the high costs of producing synthesis gas. A challenging development in this area is the ceramic membrane technology, which allows oxygen to transport from air to the natural gas, where it produces synthesis gas via partial oxidation. However, after a successful research stadium, commercial application is still more than 10 years away.

The optimal Fischer-Tropsch reactor for high molecular weight products is the slurry bubble column reactor. Good temperature control due to the excellent heat transfer allows the use of highly active catalysts. Major problem is the necessary catalyst-wax separation step. Cost reduction may be accomplished by increase of the reactor size to 10,000 - 20,000 bbl/day.

Parallel to the process development, catalytic design of Fischer-Tropsch catalysts remains important. Special aspects are the improvement of activity, selectivity, and resistance to attrition and deactivation. Most recent research deals with cobalt-based catalysts. Under certain conditions, the activity of iron catalysts is equal to or greater than that of cobalt catalysts [12, 13]. Cobalt catalysts are preferred at high CO conversions with a synthesis gas feed from natural gas ($H_2/CO=2$). Synthesis gas from coal or other carbon resources is preferably converted with iron catalysts because of their high water gas shift activities.

References

- [1] Kuipers, E.W.; Scheper, C.; Wilson, J.H.; Oosterbeek, H., Non-ASF product distributions due to secondary reactions during Fischer-Tropsch synthesis, *J. Catal.* **1996**, *158*, 288–300.
- [2] Boudart, M., Two-step catalytic reactions, *AIChE J.* **1972**, *18*, 465–478.
- [3] Ribeiro, F.H.; Schach von Wittenau, A.E.; Bartholemew, C.H.; Somorjai, G.A., Reproducibility of turnover rates in heterogeneous metal catalysis: compilation of data and guidelines for data analysis, *Catal. Rev.-Sci. Eng.* **1997**, *39*, 49–76.
- [4] Letzel, M.H.; Schouten, J.C.; Krishna, R.; Van den Bleek, C.M., Gas holdup and mass transfer in bubble column reactors operated at elevated pressure, *Chem. Eng. Sci.* **1999** (in press).
- [5] Arcuri, K.B., Process for hydrocarbon synthesis using slurry Fischer-Tropsch process with Co/TiO₂ catalyst, *Eur. Patent EP 0 450 861 A2* **1991**.
- [6] Koros, R.M., Bubble column, tube-slide slurry process and apparatus, *Eur. Patent EP 0 592 176 A1* **1992**.
- [7] Maretto, C.; Piccolo, V., Fischer-Tropsch process with a multistage bubble column reactor, *Eur. Patent EP 0823470 A1* **1998**, AGIP, Institut Francais du Petrole.
- [8] Krishna, R.; De Swart, J.W.A.; Ellenberger, J.; Martina, G.B.; Maretto, C., Gas holdup in slurry bubble columns: effect of column diameter and slurry concentrations, *AIChE J.* **1997**, *43*, 311–316.
- [9] Graaf, G.H., *The synthesis of methanol in gas-solid and gas-slurry reactors*, Ph.D. thesis, University of Groningen, The Netherlands **1988**.
- [10] Chen, B.H.; Yang, N.S., Characteristics of a cocurrent multistage bubble column, *Ind. Eng. Chem. Res.* **1989**, *28*, 1405–1410.
- [11] Voigt, J.; Schugerl, K., Absorption of oxygen in countercurrent multistage bubble columns – I, *Chem. Eng. Sci.* **1979**, *34*, 1221–1229.

- [12] Xu, L.; Bao, S.; R.J., O'Brien; Raje, A.; Davis, B.H., Don't rule out iron catalysts for Fischer-Tropsch synthesis, *CHEMTECH* **1998**, *8*, 47–53.
- [13] Berge van, P.J.; Everson, R.C., Cobalt as an alternative Fischer-Tropsch catalyst to iron for the production of middle distillates, *Stud. Surf. Sci. Catal.* **1997**, *107*, 207–212.

Appendix A Spinning Basket Reactor, Run A

Table A1 Summary of the experimental conditions and analysis.

Run	TOS (h)	P (MPa)	F	$\Phi_{v,0}^{in}/W$ ($10^{-3} \text{ Nm}^3 \text{ kg}^{-1} \text{ s}^{-1}$)	$\Phi_{v,0}/W$	y_i			
						H ₂	CO	CO ₂	H ₂ O
A1 ¹	240	1.5	2	1.5	1.19	0.584	0.226	0.0537	0.0880
A2	265	1.2	0.5	1.0	0.7	0.245	0.500	0.0978	0.0239
A3	292	1.6	1	1.0	0.69	0.397	0.274	0.1568	0.0537
A4	313	2.4	2	1.0	0.75	0.621	0.138	0.1034	0.0582
A5	361	4.0	4	1.0	0.79	0.771	0.037	0.0341	0.0702
A6 ¹	387	1.5	2	1.5	1.23	0.623	0.213	0.0498	0.0407
A7	410	2.0	4	1.0	0.82	0.767	0.073	0.0473	0.0453
A8	450	3.2	1	1.0	0.64	0.317	0.277	0.1699	0.0900
A9	496	3.0	0.5	1.0	0.70	0.194	0.489	0.1593	0.0452
A10	552	2.4	2	0.5	0.34	0.581	0.094	0.1304	0.0569
A11	581	2.4	2	2.0	1.65	0.653	0.191	0.0585	0.0599
A12	622	2.4	2	1.5	1.14	0.599	0.170	0.0739	0.0648
A13 ¹	653	1.5	2	1.5	1.24	0.625	0.188	0.0644	0.0502
A14 ¹	862	1.5	2	1.5	1.27	0.634	0.233	0.0359	0.0352
A15	889	1.2	2	0.5	0.41	0.624	0.154	0.0912	0.0383
A16	914	1.2	2	2.0	1.80	0.641	0.247	0.0255	0.0205
A17	961	2.4	0.5	2.0	1.65	0.250	0.541	0.0635	0.0251
A18	982	2.4	0.5	0.5	0.36	0.169	0.439	0.2219	0.0562
A19 ¹	1011	1.5	2	1.5	1.21	0.630	0.194	0.0626	0.0406
A20	1080	1.2	0.5	2.0	1.70	0.275	0.547	0.0392	0.0117
A21	1101	1.2	2	0.5	0.38	0.586	0.117	0.1243	0.0255
A22	1151	2.0	0.25	1.0	0.81	0.115	0.657	0.0648	0.0072
A23	1177	0.8	1	1.0	0.81	0.423	0.339	0.0919	0.0298
A24 ¹	1224	1.5	2	1.5	1.19	0.622	0.188	0.0682	0.0537

¹ Reference experiment

Table A2 On-line mole fractions of paraffins.

Run	Paraffins $10^3 y_i$ (-)									
	1	2	3	4	5	6	7	8	9	10
A1	10.8	1.67	0.687	0.658	0.542	0.382	0.281	0.223	0.187	0.136
A2	5.68	0.861	0.338	0.356	0.318	0.202	0.172	0.142	0.118	0.082
A3	17.6	3.97	1.55	1.44	1.29	0.720	0.613	0.536	0.471	0.431
A4	25.5	5.13	2.27	2.05	1.65	1.15	0.663	0.473	0.387	0.190
A5	18.5	2.90	1.76	1.56	1.19	0.786	0.424	0.351	-	-
A6	11.4	1.88	0.780	0.756	0.573	0.287	0.242	0.196	0.171	0.132
A7	23.85	3.60	1.83	1.60	1.14	0.815	0.386	0.244	0.156	0.114
A8	17.2	4.80	2.15	1.79	1.26	1.02	0.672	0.519	0.506	0.415
A9	6.47	1.32	0.658	0.576	0.502	0.252	0.233	0.195	-	-
A10	31.2	8.14	3.94	2.55	2.17	1.49	1.20	0.880	0.709	0.620
A11	14.3	3.44	1.47	0.998	0.729	0.490	0.384	0.279	0.234	0.189
A12	17.3	4.34	1.84	1.24	0.913	0.645	0.443	0.332	0.269	0.220
A13	14.8	3.33	1.29	0.983	0.687	0.392	0.333	0.273	0.257	-
A14	10.3	1.81	0.713	0.508	0.358	0.249	0.172	0.133	0.115	0.094
A15	24.3	4.96	1.90	1.26	1.02	0.701	0.474	0.336	0.266	0.222
A16	7.44	1.12	0.442	0.276	0.207	0.143	0.107	0.083	0.062	0.063
A17	5.21	0.895	0.430	0.324	0.222	0.162	0.154	0.113	0.105	0.095
A18	9.83	2.39	0.974	0.752	0.678	0.529	0.417	0.301	0.244	0.214
A19	15.6	3.20	1.17	0.784	0.610	0.401	0.284	0.222	0.164	0.139
A20	3.16	0.378	0.192	0.137	0.123	0.080	0.069	0.056	0.052	-
A21	33.3	6.84	2.87	1.82	1.48	0.974	0.697	0.518	0.347	0.294
A22	2.19	0.269	0.165	0.123	0.133	0.094	0.076	0.068	0.054	0.052
A23	11.8	2.20	0.740	0.552	0.487	0.357	0.282	0.264	0.245	-
A24	17.6	3.40	1.28	0.898	0.702	0.461	0.363	0.327	-	-

Table A3 On-line mole fractions of olefins.

Run	Olefins $10^3 y_i$ (-)								
	2	3	4	5	6	7	8	9	10
A1	1.09	2.56	1.63	1.27	0.751	0.542	0.344	0.232	0.178
A2	1.72	2.63	1.73	1.45	0.921	0.648	0.453	0.374	0.224
A3	2.29	6.10	3.68	2.85	1.63	1.03	0.704	0.423	0.336
A4	1.27	5.11	2.97	2.18	1.18	0.613	0.295	0.200	0.090
A5	0.286	1.98	1.05	0.720	0.348	0.120	0.081	-	-
A6	1.24	2.94	1.87	1.34	0.757	0.433	0.284	0.165	0.101
A7	0.535	2.89	1.48	0.933	0.494	0.185	0.123	0.046	0.037
A8	2.95	7.32	4.35	2.96	2.08	1.19	0.714	0.536	0.377
A9	2.53	3.86	2.50	1.88	1.25	0.852	0.599	0.557	-
A10	1.34	6.30	3.02	1.93	1.03	0.651	0.324	0.207	0.138
A11	1.89	4.26	2.28	1.45	0.837	0.440	0.257	0.153	0.107
A12	1.85	4.85	2.50	1.58	0.890	0.468	0.242	0.151	0.088
A13	1.64	3.95	2.04	1.31	0.694	0.402	0.223	0.154	-
A14	1.49	2.62	1.44	0.922	0.524	0.304	0.167	0.115	0.079
A15	1.52	4.79	2.35	1.47	0.777	0.372	0.202	0.119	0.077
A16	1.19	1.84	1.01	0.632	0.371	0.206	0.125	0.077	0.059
A17	1.78	2.40	1.53	1.07	0.738	0.572	0.351	-	0.262
A18	2.81	5.25	3.28	2.42	1.70	1.11	0.727	0.547	0.371
A19	1.56	3.64	1.93	1.21	0.697	0.368	0.290	0.135	0.078
A20	1.19	1.40	0.930	0.687	0.478	0.332	0.228	0.186	0.158
A21	1.34	5.54	2.69	1.66	0.897	0.447	0.259	0.125	0.089
A22	1.15	1.34	0.935	0.744	0.544	0.391	0.282	0.225	0.184
A23	2.13	3.81	2.33	1.66	1.04	0.638	0.428	0.302	-
A24	1.62	3.99	2.25	1.46	0.857	0.512	0.297	0.255	-

Table A4 On-line mole fractions of oxygenates.

Run	1-alcohols $10^3 y_i$ (-)			
	1	2	3	4
A1	1.07	0.662	0.166	-
A2	0.691	0.468	0.101	-
A3	1.05	1.12	0.345	-
A4	2.83	2.34	0.561	0.196
A5	4.42	1.53	-	-
A6	1.16	0.735	0.205	-
A7	1.42	0.922	-	-
A8	1.16	1.30	0.549	0.382
A9	0.882	0.755	0.227	-
A10	4.62	3.89	1.30	0.249
A11	1.55	1.37	0.484	-
A12	1.55	1.51	0.460	0.131
A13	1.11	1.12	0.302	-
A14	1.00	0.854	0.204	-
A15	1.68	1.53	0.387	-
A16	0.793	0.509	-	-
A17	0.552	0.592	0.155	-
A18	0.752	1.14	0.346	-
A19	1.01	1.09	0.285	-
A20	0.247	0.296	0.063	-
A21	1.23	1.50	0.393	-
A22	0.424	0.318	0.076	-
A23	0.690	0.771	0.206	-
A24	1.00	1.10	0.284	-

Appendix B Slurry Reactor, Run B and C

Table B1 Summary of experimental conditions and results.

Run	TOS (h)	P (MPa)	F	$\Phi_{v,0}^n/W$ ($10^{-3} \text{ Nm}^3 \text{ kg}^{-1} \text{ s}^{-1}$)	$\Phi_{v,0}/W$	y_i			
						H ₂	CO	CO ₂	H ₂ O
B1 ¹	156	1.5	0.67	0.51	0.41	0.311	0.503	0.093	0.038
B2	183	1.5	0.67	0.25	0.18	0.270	0.434	0.196	0.035
B3	228	1.5	1	0.51	0.43	0.482	0.390	0.097	0.031
B4 ¹	289	1.5	0.67	0.51	0.41	0.310	0.520	0.098	0.030
B5	349	1.5	2	0.51	0.37	0.552	0.174	0.085	0.104
B6	452	2.4	3	0.51	0.39	0.681	0.097	0.071	0.077
B7	520	2.4	1	0.51	0.36	0.340	0.370	0.119	0.079
B8	571	2.4	0.5	0.51	0.39	0.182	0.606	0.100	0.055
B9 ¹	643	1.5	0.67	0.51	0.39	0.269	0.512	0.103	0.044
B10	694	1.2	0.5	0.51	0.40	0.220	0.592	0.099	0.026
B11	760	2.4	2	0.51	0.34	0.537	0.114	0.149	0.108
B12	904	2.4	0.5	0.51	0.37	0.165	0.550	0.198	0.034
C1 ¹	345	1.5	0.67	0.51	0.38	0.282	0.448	0.136	0.104
C2	385	1.5	0.5	0.51	0.43	0.209	0.542	0.123	0.108
C3	443	1.5	1.0	0.51	0.39	0.378	0.295	0.178	0.076
C4	506	1.5	2.0	0.51	0.40	0.579	0.135	0.122	0.086
C5 ¹	552	1.5	0.67	0.51	0.39	0.202	0.475	0.119	0.154
C6	614	1.5	1.0	0.25	0.16	0.346	0.192	0.242	0.143
C7 ¹	802	1.5	0.67	0.51	0.39	0.240	0.458	0.136	0.118
C8	875	1.5	1.0	0.25	0.16	0.334	0.194	0.299	0.034
C9	950	1.5	1.0	0.17	0.10	0.332	0.110	0.306	0.163
C10	1001	1.5	1.0	0.77	0.61	0.358	0.393	0.096	0.087
C11	1057	1.5	0.67	0.51	0.39	0.226	0.486	0.148	0.057
C12	1094	1.5	1.0	0.51	0.38	0.357	0.327	0.167	0.057
C13	1139	2.4	2.0	0.51	0.35	0.519	0.090	0.149	0.125
C14 ¹	1396	1.5	0.67	0.51	0.41	0.252	0.515	0.093	0.092
C15	1487	1.2	0.5	0.51	0.39	0.195	0.560	0.128	0.075

¹ Reference experiment

Table B2 On-line mole fractions of paraffins.

Run	Paraffins $10^3 y_i$ (-)									
	1	2	3	4	5	6	7	8	9	10
B1	3.98	0.686	0.352	0.316	0.254	0.158	0.120	0.087	0.073	0.068
B2	7.90	1.88	0.741	0.696	0.589	0.319	0.234	0.156	0.113	0.093
B3	7.29	1.48	0.657	0.589	0.470	0.268	0.178	0.137	0.126	0.108
B4	4.92	0.864	0.430	0.385	0.311	0.318	0.220	0.112	0.107	0.098
B5	15.3	3.53	1.67	1.44	1.14	1.04	0.669	0.527	0.426	-
B6	18.3	3.52	1.74	1.56	1.26	1.02	0.759	0.624	0.590	0.415
B7	6.86	1.54	0.793	0.674	0.540	0.394	0.297	0.258	0.216	0.186
B8	3.25	5.83	3.31	2.87	2.35	1.67	0.872	1.14	0.833	-
B9	4.70	0.836	0.398	0.348	0.294	0.217	0.149	0.083	0.082	0.074
B10	3.42	0.519	0.248	0.220	0.207	0.133	0.110	0.068	0.058	0.048
B11	17.9	4.69	2.21	1.88	1.61	1.22	0.925	0.672	-	-
B12	4.60	1.06	0.532	0.454	0.392	0.331	0.196	0.130	0.115	0.094
C1	4.41	0.673	0.355	0.280	0.259	0.190	0.155	0.121	0.085	-
C2	3.13	0.537	0.372	0.205	0.202	-	0.142	0.108	0.081	0.055
C3	7.47	1.68	0.963	0.694	0.618	0.429	0.386	0.322	0.204	0.193
C4	11.7	2.67	1.51	0.969	0.809	0.605	0.401	0.347	0.231	0.210
C5	3.54	0.701	0.498	0.334	0.270	0.157	0.138	0.112	0.093	0.097
C6	3.32	0.641	0.288	0.251	0.211	0.151	0.137	-	0.088	0.056
C7	3.56	0.650	0.287	0.232	0.175	0.161	0.122	0.111	0.098	0.093
C8	13.1	3.70	1.53	1.04	0.964	0.738	0.580	0.429	0.340	0.222
C9	18.8	5.59	2.69	1.62	1.54	1.14	0.872	0.622	0.479	0.340
C10	4.17	0.789	0.340	0.254	0.191	0.132	0.130	0.127	-	-
C11	3.44	0.615	0.265	0.227	0.173	0.123	0.115	0.102	0.104	0.103
C12	6.01	1.25	0.484	0.380	0.279	0.271	0.233	0.186	0.155	0.120
C13	16.3	4.43	2.09	1.30	1.03	0.735	0.524	0.400	0.292	0.199
C14	3.09	0.713	0.312	0.177	0.121	0.084	0.075	-	-	-
C15	2.61	0.478	0.203	0.156	0.103	0.095	0.078	0.062	-	-

Table B3 On-line mole fractions of olefins.

Run	Olefins $10^3 y_i$ (-)								
	2	3	4	5	6	7	8	9	10
B1	1.34	2.07	1.37	1.09	0.718	0.480	0.353	0.246	0.176
B2	1.93	3.84	2.48	1.90	1.11	0.702	0.437	0.295	0.175
B3	1.61	3.01	1.91	1.43	0.843	0.514	0.336	0.209	0.151
B4	1.47	2.35	1.58	1.23	1.00	0.585	0.390	0.286	0.197
B5	1.50	4.38	2.53	1.83	1.26	0.643	0.413	0.235	0.128
B6	0.851	3.46	2.01	1.47	0.970	0.491	0.331	0.216	0.108
B7	2.24	3.69	2.36	1.82	1.21	0.764	0.562	0.359	0.234
B8	1.66	2.06	1.31	0.991	0.640	0.295	0.263	0.201	0.186
B9	1.87	2.48	1.55	1.17	0.810	0.524	0.357	0.268	0.214
B10	1.57	1.92	1.24	0.965	0.656	0.495	0.332	0.250	0.192
B11	2.73	4.59	3.99	2.93	1.84	1.13	0.773	0.384	0.206
B12	2.30	2.86	1.63	1.12	0.800	0.494	0.312	0.236	0.155
C1	0.724	1.26	0.767	0.609	0.381	0.233	0.153	0.108	-
C2	0.838	0.975	0.619	0.511	0.313	0.226	0.162	0.118	0.081
C3	0.788	1.98	1.14	0.871	0.457	0.307	0.201	0.106	0.068
C4	0.510	1.82	0.862	0.585	0.320	0.128	0.070	0.038	0.027
C5	0.808	1.24	0.802	0.633	0.372	0.243	0.169	0.119	0.079
C6	0.641	1.11	0.678	0.525	0.354	0.252	0.120	0.104	0.053
C7	1.02	1.64	1.11	0.900	0.613	0.324	0.299	0.232	0.165
C8	1.29	4.33	2.36	1.69	1.00	0.578	0.340	0.221	0.126
C9	1.01	4.79	2.34	1.61	0.912	0.531	0.259	0.141	0.104
C10	1.08	1.72	1.08	0.752	0.504	0.335	0.261	0.195	-
C11	1.13	1.70	1.15	0.945	0.616	0.424	0.313	0.242	0.165
C12	1.31	2.45	1.56	1.19	0.800	0.562	0.386	0.263	0.184
C13	0.998	3.68	1.81	1.17	0.651	0.308	0.167	0.095	0.055
C14	1.49	1.80	0.992	0.644	0.391	0.253	0.162	0.091	0.065
C15	1.14	1.41	0.857	0.614	0.429	0.316	0.214	-	-

Table B4 On-line mole fractions of oxygenates.

Run	1-alcohols $10^3 y_i$ (-)			
	1	2	3	4
B1	1.25	5.83	1.42	0.800
B2	2.08	1.13	0.299	0.184
B3	1.76	0.930	0.256	0.162
B4	0.986	0.637	0.177	-
B5	2.20	1.28	0.387	0.292
B6	2.43	1.18	0.288	0.086
B7	1.71	0.757	0.225	0.144
B8	0.978	0.394	0.116	0.077
B9	0.992	0.495	0.142	0.108
B10	0.683	0.369	0.091	-
B11	2.13	2.63	0.596	0.235
B12	1.20	0.794	0.091	-
C1	0.315	0.468	0.126	-
C2	0.196	0.394	0.075	-
C3	0.241	0.795	0.206	-
C4	0.338	0.828	0.228	-
C5	0.176	0.461	0.097	-
C6	0.406	0.470	0.120	-
C7	0.150	0.404	0.094	-
C8	0.451	0.976	0.287	-
C9	0.513	1.10	0.331	-
C10	0.198	0.418	0.104	-
C11	0.120	0.346	0.086	-
C12	0.240	0.482	0.126	-
C13	0.536	1.14	0.323	-
C14	0.130	0.387	0.084	-
C15	0.119	0.329	0.083	-

List of Symbols

Included in the following list are common symbols employed throughout this thesis. An additional list of symbols is added for Chapter 7.

A_i	integrated GC peak area of component i	counts
a, a_∞	kinetic parameters	-
b	kinetic parameter	-
c	kinetic parameter	-
c	exponential constant, eq 4.5	-
C	constant	-
C	concentration	mol m^{-3}
C_n^s	saturated vapor phase concentration	mol m^{-3}
C_i	calibration factor GC	-
d	kinetic parameter	-
D	diffusion coefficient	$\text{m}^2 \text{s}^{-1}$
D	diameter	m
D_n	diffusivity hydrocarbon with chain length n	$\text{m}^2 \text{s}^{-1}$
d_p	diameter of catalyst particle	m
d	diameter or film thickness	m
df	degrees of freedom	-
E_A	activation energy	kJ mol^{-1}
E	molar exit ratio H_2 to CO	-
ΔE	potential energy	kJ mol^{-1}
F	molar feed ratio H_2 to CO	-
f	fugacity	Pa
F	molar flow reactor outlet	mol s^{-1}
H	number of competitive models	-
ΔH	reaction enthalpy	kJ mol^{-1}
ΔH_{ad}	heat of adsorption	kJ mol^{-1}
H	height	m
H	Henry's solubility constant	$\text{mol Pa}^{-1} \text{m}^{-3}$ or Pa
$\Delta G_{1 \text{ phys}}$	free energy change of physisorption	kJ mol^{-1}
ΔG_{ox}	free energy change of oxidation	kJ mol^{-1}

k, k_{∞}	reaction rate constant	-
k_0	reaction rate constant in ideal state	-
k_{dp}	reaction rate constant for depolymerization	-
k_i, k_{ir}	reaction rate for (reverse) initiation	-
k_w	WGS reaction rate constant	-
K_p	equilibrium constant water gas shift	-
K_i	adsorption constant	-
k_R, k_R^*	reaction rate constant readsorption of olefins	-
k_R^2	reaction rate constant readsorption of ethene	-
K_{H_2}	adsorption constant hydrogen	MPa ⁻¹
K_i	equilibrium constant (y_i/x_i)	-
L	molar flow liquid phase	mol s ⁻¹
m	number of model parameters	-
m	average number of hydrogen atoms	-
m_i	molar selectivity of component i , eq 3.17	-
m_i^{GL}	solubility constant (C_G/C_L)	-
m_n	molar selectivity of hydrocarbon with carbon number n	-
m_O	molar olefin selectivity	-
m_P	molar paraffin selectivity	-
$MARR$	Mean Absolute Relative Residual, eq 3.21	-
M	molecular weight	kg mol ⁻¹
n	carbon number	-
n	number of experimental data points	-
N	constant	-
O_n	olefin fraction carbon number n	-
P_n	paraffin fraction carbon number n	-
p	propagation probability	-
P	pressure	Pa
P_n	hydrocarbon vapor pressure with carbon number n	Pa
P_0	vapor pressure constant	Pa
R	reaction rate	mol kg _{cat} ⁻¹ s ⁻¹
R_{FT}	overall Fischer-Tropsch reaction rate	mol kg _{cat} ⁻¹ s ⁻¹
R_{WGS}	water gas shift reaction rate	mol kg _{cat} ⁻¹ s ⁻¹
R	gas constant	8.314 J mol ⁻¹ K ⁻¹
RMR	Relative Molar Response factor	-

RR	Relative Residual, eq 3.23	-
s	catalytic surface site	-
s_{rel}	relative variance, eq 3.22	-
S_{av}^2	average variance of H models	-
S_h^2	total variance of model h	-
STY	space time yield, $-R_{H_2+CO}$	$\text{mol kg}_{cat}^{-1} \text{s}^{-1}$
t	time	s
t_O	relative olefin termination probability	-
t_O^2	relative termination probability to ethene	-
t_P^1	relative termination probability to methane	-
t_P^2	relative termination probability to ethane	-
T	temperature	K
V	volume	m^3
V	molar volume	mol m^{-3}
V	molar flow gas phase	mol s^{-1}
$V_{n wax}^m$	molar volume waxeous hydrocarbons	mol m^{-3}
w_i	mass component selectivity, eq 3.18	-
w_n	hydrocarbon weight selectivity with carbon number n	-
W	weight of unreduced supported catalyst	kg
X_i	conversion component i	-
X_{CO+H_2}	total synthesis gas conversion	-
x	distance	m
x_i	mole fraction liquid phase	-
y_i	mole fraction gas phase	-
z_i	mole fraction	-

Greek symbols

α	chain growth probability	-
α_∞	asymptotical chain growth probability	-
β	termination probability	-
β	vapor pressure coefficient	-
γ	activity coefficients	-
γ_0	relative transport rates of H_2 and CO	-
γ_n	relative transport rates of olefins	-
δ	solubility parameter	-

δ	film thickness	m
θ_i	surface fraction occupied with component i	-
μ	viscosity	N s m^{-2}
ρ_L	liquid density	kg m^{-3}
σ^2	function for optimization, eq 4.21	-
$\Phi_{v,0}$	gas flow rate at normal conditions	$\text{Nm}^3 \text{s}^{-1}$
χ^2	function for optimization, eq 3.20	-
χ_c^2	critical χ^2 for Bartlett's test	-
χ_t^2	tabulated χ^2 for Bartlett's test	-

Superscripts and Subscripts

A	component A
B	component B
CH_2	methylene
CH_3	methyl
DS	deferred standard
eq	equilibrium
exp	experimental value
G	gas phase
H	hydrogen
i	component, interface, initiation or index
I	activated complex
in	inlet conditions
L	liquid
M	monomer methylene (CH_2)
mod	predicted value
n	carbon number
O	olefins
P	paraffins
p	propagation
ps	physisorption
R	readsorption
R	reactor
S	adsorbed state
s_1	FT catalytic site

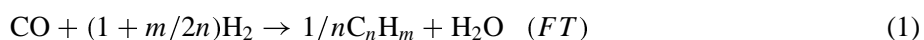
s_2	WGS catalytic site
t	termination
v	vacant or free catalytic sites
0	normal conditions, $T_0=273$ K, $P_0=0.1013$ MPa
1	solute
2	solvent
1	carbon number $n=1$
2	carbon number $n=2$

Samenvatting

Met de Fischer-Tropsch synthese is het mogelijk om benzine, diesel en chemicaliën te produceren uit steenkool of aardgas. Het proces is al 75 jaar bekend, maar wordt momenteel alleen door het Zuid-Afrikaanse bedrijf Sasol en door Shell in Maleisië commercieel toegepast. De belangstelling voor het proces neemt de laatste tijd sterk toe. In dit proefschrift worden metingen vermeld van de reactiesnelheid en de selectiviteit van het Fischer-Tropsch proces. Deze informatie wordt gebruikt om commerciële reactoren te optimaliseren.

Door de afname van de wereldvoorraad van aardolie staan alternatieve energiebronnen steeds meer in de belangstelling. Eén van de mogelijkheden is het gebruik van steenkool of aardgas, die nog in relatief grote hoeveelheden aanwezig zijn. Steenkool en aardgas kunnen worden gebruikt als grondstof voor de chemische industrie en voor de fabricage van brandstoffen. Vooral omzetting van aardgas naar vloeibare brandstoffen op verafgelegen plaatsen (bijv. Qatar, Saudi-Arabië, Alaska) staat momenteel sterk in de belangstelling. Eén van de processen voor deze omzetting is de zogenaamde Fischer-Tropsch synthese. Het Fischer-Tropsch proces bestaat globaal uit drie stappen: i) Omzetten van steenkool of aardgas naar synthesegas. Dit is een mengsel van koolmonoxide (CO) en waterstof (H₂). ii) De daadwerkelijke omzetting van synthesegas naar een veelvoud van producten, zoals gasolie, nafta, kerosine, grondstoffen voor de chemische industrie en paraffinewassen met behulp van de Fischer-Tropsch reactie. iii) Scheiden en optimalisatie van de verschillende productstromen. Het proces dankt zijn naam aan de uitvinders Franz Fischer en Hans Tropsch, die in 1923 ontdekten dat de gasvormige componenten koolmonoxide en waterstof bij hoge temperatuur (180-250 °C) met een katalysator kunnen worden omgezet in vloeibare producten. Momenteel worden zowel ijzer als kobalt toegepast als het katalytisch actieve materiaal.

De reacties van de Fischer-Tropsch synthese kunnen op de volgende manier vereenvoudigd worden weergegeven:

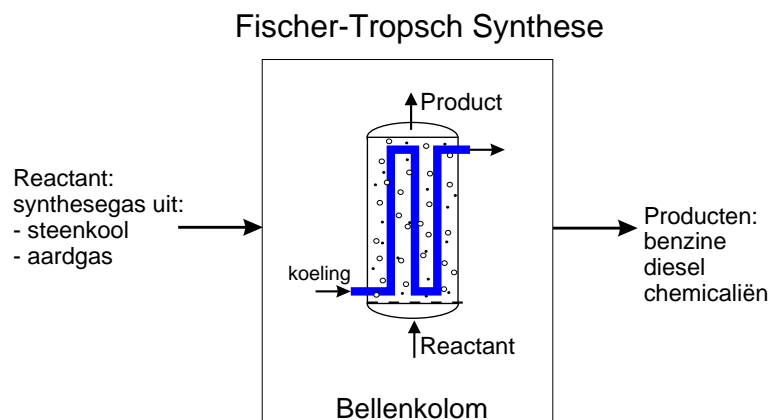


In deze formule is n het gemiddelde koolstofgetal en m het gemiddelde aantal waterstofatomen van de koolwaterstoffen. Water is een primair product van de Fischer-Tropsch reactie, dat op ijzerkatalysatoren kan worden omgezet naar CO_2 en H_2 via de *water gas shift* (WGS) reactie (vergelijking 2).

De belangstelling voor het Fischer-Tropsch proces is sterk afhankelijk van economische en politieke omstandigheden. In de jaren dertig en veertig werden in Duitsland brandstoffen geproduceerd vanuit steenkool. Na de Tweede Wereldoorlog werd de productie stopgezet. Door de ontdekking en exploratie van grote oliebronnen in het Midden-Oosten in de jaren vijftig nam de interesse voor het Fischer-Tropsch proces sterk af. Politieke oorzaken en grote voorraden van goedkope steenkool leidden echter tot de bouw van een commerciële Fischer-Tropsch fabriek in Sasolburg, Zuid-Afrika in 1955. Tijdens de oliecrisis en door een olieboycot van de OPEC in 1973 werd besloten om de productie te vergroten. In het begin van de jaren tachtig zijn de fabrieken Sasol 2 en Sasol 3 in Secunda in bedrijf genomen. De totale productiecapaciteit van Sasol is momenteel ca. 130.000 vaten brandstof en chemicaliën per dag (1 vat = 160 liter). Recentelijk hebben Sasol, Phillips Petroleum en Qatar General Petroleum Corp. contracten getekend voor de bouw van een fabriek in Qatar die vanaf 2002, per dag 20.000 vaten brandstof zal gaan maken vanuit aardgas.

In 1993 heeft Shell in Bintulu (Maleisië) een commerciële fabriek opgestart waar aardgas wordt omgezet in zuivere diesel en hoogwaardige wassen (capaciteit 12.000 vaten/dag). De vaste paraffinewassen zijn terug te vinden in tal van producten: onder andere in kaarsen, waskrijt, drukinkt en in de verpakkings- en geneesmiddelenindustrie. Als brandstoffen, zoals diesel en benzine, worden gemaakt in een conventionele raffinaderij, gebaseerd op aardolie, bevat het product verontreinigingen zoals zwavel, aromaten en naftenen. Verbranding geeft emissie van onder andere zwavelverbindingen, onverbrande koolwaterstoffen, stikstofoxiden en roetdeeltjes. De brandstoffen van het Fischer-Tropsch proces zijn echter volledig vrij van zwavel en aromaten en worden daardoor veel beter en schoner verbrand dan de conventionele brandstoffen.

De optimale reactor voor de Fischer-Tropsch synthese is een drie-fasen (of slurrie, gas-vloeistof-vast) bellenkolom. In deze reactor (zie Figuur 1) wordt synthesegas goed verdeeld onder in een kolom toegevoerd. De kolom is gevuld met vloeistof (Fischer-Tropsch producten) en kleine katalysator deeltjes (ca. 0.05 mm) die in suspensie worden gehouden. De gasbellen stijgen omhoog, waarbij de reactanten oplossen in de vloeistof. Op het oppervlak van de katalysator vindt de omzetting plaats naar de verschillende producten. Afhankelijk van de ketenlengte van het product, verlaat deze de reactor via de gasfase of de vloeistoffase. In de reactor bevinden zich verticale



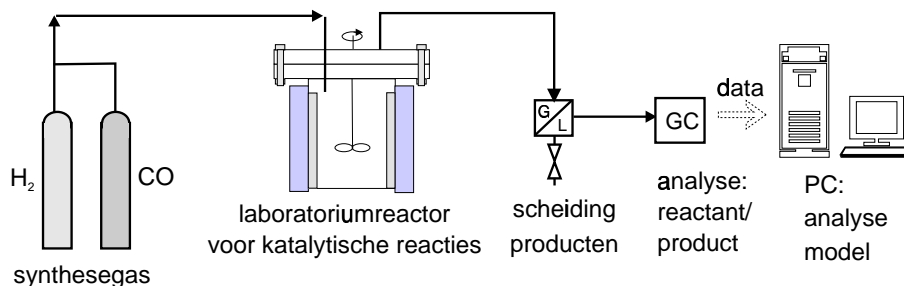
Figuur 1 Schema van een industriële bellenkolom.

buizen met bijv. stoom, die de grote reactiewarmte kunnen afvoeren. Door de goede warmteoverdracht is de temperatuurbeheersing in een bellenkolom zeer gemakkelijk in vergelijking met bijvoorbeeld de vast bed reactoren, die nu nog voornamelijk worden toegepast.

Voor een betrouwbaar ontwerp en optimalisatie van de reactor zijn gegevens nodig over het reactiemechanisme en de snelheid waarmee de reactanten kunnen worden omgezet (kinetiek). Het doel van dit proefschrift is inzicht te verkrijgen in de kinetiek en de selectiviteit naar de verschillende producten. Het uiteindelijke doel van dit proefschrift is de simulatie van een industriële bellenkolom met een gedetailleerd reactortecnologisch model.

Hoofdstuk 2 van het proefschrift geeft een kritisch literatuuroverzicht over de kinetiek en selectiviteit van het Fischer-Tropsch proces. Uit dit overzicht blijkt dat de beschikbare literatuurmodellen voor de productselectiviteit niet in staat zijn om het volledige productmengsel nauwkeurig te voorspellen als functie van de procescondities. Ook vertonen de kinetische vergelijkingen uit de literatuur geen uniform beeld en zijn de meeste kinetiekmodellen voor ijzerkatalysatoren onvolledig, omdat de vorming van CO_2 via de WGS reactie vaak niet wordt meegenomen.

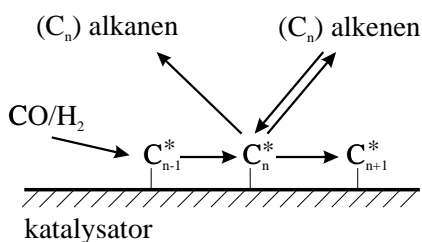
Voor het meten van de kinetiek en selectiviteit zijn verschillende laboratoriumreactoren gebruikt (zie schema in Figuur 2). De gebruikte katalysator is een commerciële geprecipiteerde ijzerkatalysator (type Ruhrchemie LP 33/81) met koper en kalium promotors op silica dragermateriaal (Fe/Cu/K/SiO_2). Er is gebruik gemaakt van een gas-vast reactor, waarbij de katalysatordeeltjes in mandjes aan de roerderas



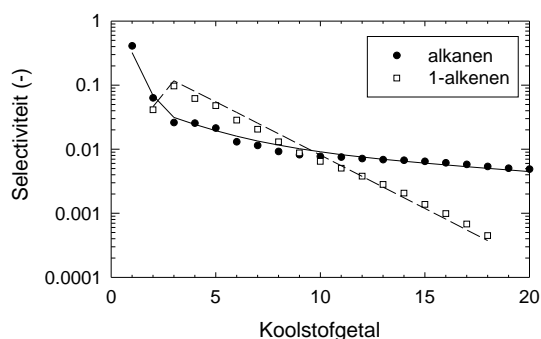
Figuur 2 Schematische weergave van de laboratoriumopstelling voor het meten van de kinetiek en selectiviteit van de Fischer-Tropsch synthese.

zijn bevestigd, en van een gas-slurrie reactor, waarin kleine katalysatordeeltjes in de vloeistof zijn gesuspenderd. In de verschillende laboratoriumreactoren is de invloed van de procesomstandigheden (druk, temperatuur, verblijftijd en samenstelling van het synthesegas) op de kinetiek en de selectiviteit bestudeerd.

Er is een kinetisch model ontwikkeld, waarmee de selectiviteit naar de tientallen verschillende producten, variërend in ketenlengte en soort (voornamelijk alkanen en alkenen), nauwkeurig kan worden beschreven. In Figuur 3 staat een schema van het mechanisme van de vorming van de diverse producten afgebeeld en in Figuur 4 wordt een voorbeeld gegeven van de modelbeschrijving van de gemeten selectiviteit in één van de experimenten. De selectiviteit wordt onder andere beïnvloed door de gebruikte katalysator en door de procescondities. De reactanten CO en H₂ reageren op het katalysatoroppervlak en vormen de bouwsteen (monomeer) methyleen. Deze bouwstenen zorgen voor de groei van de koolwaterstofketens. Met dit model is het mogelijk



Figuur 3 Reactienetwerk voor de productvorming.



Figuur 4 Modelbeschrijving (lijnen) van experimenteel gevonden selectiviteiten (symbolen).

om de selectiviteit naar de gevormde producten nauwkeurig te beschrijven. Hierbij is aangenomen dat de onverzadigde producten (alkenen) opnieuw kunnen reageren op het katalysatoroppervlak (Figuur 3). In tegenstelling tot de meeste literatuurmodellen is dit selectiviteitsmodel in staat om de productverdeling van lineaire koolwaterstoffen nauwkeurig te beschrijven. De belangrijkste kenmerken van de productverdeling, die nu goed worden beschreven zijn: i) hoge selectiviteit naar methaan; ii) lage selectiviteit naar etheen; iii) afname van de verhouding tussen alkenen en alkanen met toenemende ketenlengte.

De reactiesnelheid van de reactantconsumptie en van de vorming van CO_2 is beschreven met modellen die zijn afgeleid vanuit reactiemechanismen die de katalytische elementaire reactiestappen op het katalysatoroppervlak beschrijven. Uit de literatuur is bekend dat de FT reactie en de CO_2 vorming (WGS) op verschillende katalytisch actieve plaatsen optreedt. Voor de FT reactie is het carbide mechanisme aangenomen en voor de CO_2 vorming is het mechanisme gebaseerd op een formaat-intermediair. Simulaties waarbij de beste kinetische vergelijkingen zijn gebruikt blijken goed overeen te komen met de experimentele gegevens. Zowel de selectiviteit als de kinetiek van de FT en de WGS reactie worden beïnvloed door de aanwezigheid van de vloeistoffase (slurrie-medium). In het gas-slurrie systeem bleek de selectiviteit naar alkenen, bij overeenkomstige reactieomstandigheden, hoger te zijn dan in het gas-vast systeem. Ook is de reactiesnelheid van de FT en de WGS reacties lager in het slurrie-systeem.

Met behulp van deze gegevens is een commerciële reactor gemodelleerd. In dit model zijn de nieuwste inzichten met betrekking tot de hydrodynamica uit de literatuur gecombineerd met de nieuwe modellen voor de selectiviteit en de kinetiek. Bellenkolommen op commerciële schaal worden in het heterogene stromingsregime bedreven, waar de gasfase is verdeeld over "grote" en "kleine" gasbellen. De kleine bellen zijn slechts enkele millimeters groot, terwijl de diameter van de grote bellen kan oplopen tot 5-10 centimeter. Het stromingspatroon van de grote en de kleine bellen is dan ook volledig anders. De grote bellen stijgen met zeer hoge snelheid in enkele secondes door een bellenkolom van bijv. 24 meter. De kleine bellen, de vloeistoffase en de katalysatordeeltjes worden door de turbulentie goed gemengd. Met de modellen gepresenteerd in dit proefschrift is het nu mogelijk om de samenstelling van de gas- en vloeistoffase nauwkeurig te voorspellen. Het model levert dan ook alle gegevens die noodzakelijk zijn voor een betrouwbaar FT reactor ontwerp en voor de voorspelling van het gedrag van slurrie-bellenkolommen.

Na de ontdekking van Fischer en Tropsch, 75 jaar geleden, is het Fischer-Tropsch

proces opnieuw volop in de belangstelling. Dit proefschrift geeft een literatuuroverzicht en nieuwe experimentele gegevens betreffende de kinetiek en de selectiviteit. De gedetailleerde modellen ontwikkeld in dit proefschrift kunnen worden gebruikt voor de optimalisatie van industriële Fischer- Tropsch processen.

List of Abbreviations

AGC 21	Advanced Gas Conversion 21st century
ASF	Anderson-Schulz-Flory
BET	Braun-Emmett-Teller
CFB	Circulating Fluidized Bed
CSTR	Continuous Stirred Tank Reactor
FT	Fischer-Tropsch
GC	Gas Chromatograph
GTL	Gas-To-Liquids
HTFT	High Temperature Fischer-Tropsch
LNG	Liquefied Natural Gas
LPG	Liquefied Petroleum Gas
LTFT	Low Temperature Fischer-Tropsch
MS	Mass Spectrometer
ORPDM	α -Olefin Readsorption Product Distribution Model
SAS	Sasol Advanced Synthol
SBR	Spinning Basket Reactor
SMDS	Shell Middle Distillate Synthesis
SR	Slurry Reactor
SBCR	Slurry Bubble Column Reactor
SSPD	Sasol Slurry Phase Distillate
TOS	Time On Stream
WGS	Water Gas Shift

List of Publications

- Van der Laan, G.P.; Beenackers, A.A.C.M., Kinetics and selectivity of the Fischer-Tropsch synthesis. A literature review. Accepted for publication in *Catal. Rev. Sci.-Eng.* **1999**.
- Van der Laan, G.P.; Beenackers, A.A.C.M., α -Olefin readsorption product distribution model for the gas-solid Fischer-Tropsch synthesis, *Stud. Surf. Sci. Catal.* **1998**, *119*, 179–184.
- Van der Laan, G.P.; Beenackers, A.A.C.M., Hydrocarbon selectivity model for the gas-solid Fischer-Tropsch synthesis on precipitated iron catalysts, Submitted for publication in *Ind. Eng. Chem. Res.* **1999**.
- Van der Laan, G.P.; Beenackers, A.A.C.M., Intrinsic kinetics of the Fischer-Tropsch and water gas shift reactions over a precipitated iron catalyst, Submitted for publication in *Appl. Catal. A* **1999**.
- Van der Laan, G.P.; Beenackers, A.A.C.M., Hydrocarbon selectivity model for the gas-slurry Fischer-Tropsch on precipitated iron catalysts, Accepted for *AIChE Spring Meeting*, March 14-18, Houston TX **1999**.
- Van der Laan, G.P.; Beenackers, A.A.C.M.; Krishna, R., Multicomponent reaction engineering model for Fe-catalyzed Fischer-Tropsch synthesis in commercial scale slurry bubble column reactors, Accepted for oral presentation at Gas-Liquid and Gas-Liquid-Solid Reactor Engineering 1999 and for publication in *Chem. Eng. Sci.* **1999**.
- Van der Laan, G.P.; Beenackers, A.A.C.M.; Ding, B.; Strikwerda, J.C., Liquid-phase methanol synthesis in apolar (squalane) and polar (tetraethylene glycol dimethylether) solvents, *Catal. Today* **1999**, *48*, 93–100.
- Marsman, J.H.; Van der Laan, G.P.; Beenackers, A.A.C.M., On-line gas sampling and pre-concentration of volatile components directly on the analytical capillary column: quantification and identification with GC/MS, Accepted for publication in *J. Process Anal. Chem.* **1999**.

Dankwoord

Een groot aantal mensen heeft een bijdrage geleverd aan de totstandkoming van dit proefschrift. Ik wil hierbij iedereen bedanken en enkele van hen speciaal vermelden.

Allereerst wil ik mijn promotor, professor Ton Beenackers, bedanken voor de gelegenheid om bij zijn onderzoeksgroep een promotieonderzoek uit te voeren. In het bijzonder dank ik Ton voor de goede adviezen en vele discussies, maar bovenal voor de plezierige samenwerking in de afgelopen vier en half jaar. De leden van de beoordelingscommissie professor De Jong, professor Krishna en professor Moulijn wil ik bedanken voor de snelle en deskundige beoordeling van het proefschrift en de vele waardevolle suggesties. Prof. Krishna wordt tevens bedankt voor het overleg en de medewerking aan het artikel gebaseerd op hoofdstuk 7. I am grateful to Dr. Ding Baiquan (present address: East China University of Science and Technology, Shanghai) for his contribution to the research concerning the kinetic effects of several solvents in the three-phase methanol synthesis.

De bijdrage van afstudeerstudenten is onmisbaar bij het uitvoeren van tijdrovende en complexe experimenten en mathematische modelvorming van o.a. het Fischer-Tropsch proces. Johan Strikwerda, Eduard Kalsbeek, Bas Monhemius, Tycho van der Plas, Reinier Brul en Udo Meijer ben ik zeer dankbaar voor hun persoonlijke inbreng en inzet. Tycho en Eduard wil ik alvast bedanken voor hun taken als paranimf. Ook de studenten die hun klein werkbezoek bij mij hebben uitgevoerd wil ik bedanken voor hun bijdrage: Jelle Holwerda, Filips Jager, Bernd de Jonge en nogmaals Tycho van der Plas.

Jan Henk Marsman, Ronald Veenhuis en alle stagiairs bedank ik hierbij voor hun inzet bij het ontrafelen en optimaliseren van de ingewikkelde analyses. De experimentele opstellingen zijn gerealiseerd door de inbreng van Oetze Staal, Jan Willem Post, Jan Bolhuis en Marcel de Vries. Jullie hebben oplossingen gevonden voor het bouwen van nieuwe en het modificeren van oude, niet meer werkende, opstellingen. Ook hebben jullie diverse tweedehands apparatuur en reactoren opgehaald bij bedrijven (met dank aan Unilever Research en Shell Research), zodat deze in Groningen een tweede leven hebben gekregen. Frans van den Berg (Universiteit Utrecht) wil ik bedanken voor het karakteriseren en produceren van verschillende katalysatormonsters.

Naast mijn kamergenoot en Unix-expert Martin Bouma wil ik in het bijzonder

enkele (oud-)collega's bedanken voor de leuke tijd en goede samenwerking: Gerald Jonker, Joost Demmink, Iris van Paasen, Marga Dijkstra, José Tijsen en Jildert Visser. Met Martin Bouma en Gerald Jonker heb ik veel interessante en gezellige discussies gehad over kinetische modellering, parameteroptimalisatie en numerieke methoden. Alle AIO's, OIO's, TWAIO's, secretaresses en overige medewerkers bij Technische Scheikunde bedankt voor de leuke tijd.

Mijn ouders en schoonouders ben ik dankbaar voor hun steun en stimulans tijdens mijn studie en promotie. En tenslotte wil ik Loeki bedanken voor haar steun, luisterend oor en motivatie in de afgelopen tijd. Aan haar wil ik dit proefschrift opdragen.

Gerard

Curriculum Vitae

Gerard Pieter van der Laan werd op 15 juni 1971 geboren in Hoogeveen. Hij behaalde in 1988 het H.A.V.O. diploma aan het Menso Alting College te Hoogeveen. Vanaf september 1988 studeerde hij aan de H.T.S., afdeling Chemische Technologie te Groningen. Hij behaalde in 1992 zijn diploma met een afstudeeronderzoek bij de Gasunie naar twee-fasen stroming in T-stukken. Van september 1992 tot augustus 1994 studeerde hij Technische Scheikunde aan de Rijksuniversiteit Groningen. Deze studie werd cum laude afgesloten met als afstudeeronderwerp gasontzwaveling in gestructureerde pakkingen binnen de onderzoeksgroep van prof. dr. ir. A.A.C.M. Beenackers. Aansluitend begon hij bij dezelfde onderzoeksgroep met een promotieonderzoek naar de kinetiek, selectiviteit en industriële beschrijving van het Fischer-Tropsch proces. Daarnaast onderzocht hij de invloed van het oplosmiddel op de kinetiek van de methanolsynthese.